Computational Modeling of Non-idealities in Gaseous and Multiphase Detonating Flows

by

Supraj Prakash

A dissertation submitted in partial fulfillment
of the requirements for the degree of
Doctor of Philosophy
(Aerospace Engineering)
in The University of Michigan
2022

Doctoral Committee:

Professor Venkat Raman, Chair
Professor James F. Driscoll
Associate Professor Mirko Gamba
Professor Margaret Wooldridge

Supraj Prakash
suprajp@umich.edu
ORCID iD: 0000-0001-7172-5824

To my parents, Prakash & Sujatha, and my sister, Tejashree.

ACKNOWLEDGEMENTS

First and foremost, I wish to thank my advisor and mentor, Professor Venkat Raman. I am grateful for having been selected to join your research group and have enjoyed my time immensely. I could not have achieved this dissertation without your patience, motivation, encouragement, and support. I have learned so much from you, and have become a more inquisitive and critical thinker with your guidance. I am always impressed by your knowledge on any given topic either about research or something beyond. I always enjoyed our conversations and appreciate that I could come to you for advice about research or my career at any time, especially during this last year when I probably bothered you quite a bit! I felt you had my best interests in mind and could always trust your advice.

I would like to thank my dissertation committee members, Professors Mirko Gamba, Margaret Wooldridge, and James Driscoll, for their constructive feedback, guidance, and time dedicated to serving on my committee. I truly appreciate all of your support. In particular, I thank Professor Gamba for our discussions on research and career goals, starting from my first year at Michigan.

I would like to thank the NASA Aeronautics Research Mission Directorate (ARMD) Fellowship program (grant No. 80NSSC18K1735) for their financial support of this research, and Dr. Tomasz Drozda for serving as my technical adviser, supporting my work, and offering research advice. Special thanks to the generous allocation of computing resources from the NASA High-End Computing Capability (HECC) and Advanced Supercomputing (NAS) facilities, Oak Ridge Leadership Computing Fa-

cility (OLCF), and the DoD High Performance Computing Modernization Program (HPCMP) which enable the state-of-the-art massively-parallel calculations presented within this dissertation.

I am eternally grateful for the excellent research group colleagues and friends. Thank you to Malik and Romain for getting me up and running as soon as I joined the research group, and for answering all my questions about CFD, physics, or code. Malik, I could always come to you for advice and guidance during my first few years as a doctoral student and we enjoyed quite a bit outside of work. Romain, I particularly appreciate you for always taking the time to discuss UTCOMP with me, even when you were 6 hours ahead in Europe. Alex, our shared enthusiasm for all things cars and motorsport kept me going during the first year of coursework and preliminary exams. Thank you, Andy, Smriti, and Chris for making the first year of graduate school more welcoming – especially Chris for your encouragement every time we met. Yihao, thank you for answering all my questions about combustion, algorithms, and life in general and for always being willing to help and provide detailed explanations. Thank you, Takuma for training me as a detonations researcher as I could always come to you for help with anything. Also, thank you for your friendship as we traveled the country and the world for conferences – I could always count on you to find the best restaurant in any city! Negin, thank you for being a wonderful friend and making our time in the office more enjoyable. I enjoyed all of our conversations as we took a break from research and the walks in Ann Arbor to get out and relax, especially during the pandemic.

Thank you, Caleb, Ral, Michael, and Connor for your friendship and discussions on research. Ral, I truly admire your dedication and work ethic. Thank you for your help in the development of the solver that enabled the work discussed within this dissertation, and for always being available when I want to chat and discuss research. Connor, thank you for your help on the RDE modeling work and the conversations

we've had. More recently, thank you Vansh and Shivank for your friendship and willingness to always meet up, talk, and relax. And last but certainly not least, Shivam: what a journey we've had - from when we met during the first week of undergrad at UT Austin to now as we graduate with our doctoral degrees nine years later! I am privileged and honored to have had such a great friend over the past decade. I am so grateful for your work on the GPU solver that allows some of the simulations that made this dissertation possible. Thank you for sharing some of the best and some of the most chaotic memories with me, from our international conference adventures and enjoying Ann Arbor summers to late nights studying for exams, working on papers and proposals, and endlessly debugging code.

Most importantly, I wish to thank my family for their never-ending love, support, and encouragement during this long journey. When confronted with the question "where do you see yourself in 20 years?" all the way back in middle school, I answered that I wanted to be an aerospace engineer with a Ph.D. I always had my family's blessing and was able to realize this goal 15 years later. Special thank you to my parents that were always there for me, whether I needed help moving all over the country for my undergraduate and graduate education and different internships each year, or just someone to talk to and ask for advice. I want to thank my sister for always being there to cheer me up and for all our enjoyable times, no matter how old we get.

TABLE OF CONTENTS

LIST OF FIGURES

Figure

LIST OF TABLES

Table

LIST OF ABBREVIATIONS

AFRL Air Force Research Laboratory

AI Artificial intelligence

ANN Artificial neural network

AMR Adaptive mesh refinement

BR Buffer region

CB Contact burning

CC Commensal combustion

CFD Computational fluid dynamics

CJ Chapman-Jouguet

CPU Central processing unit

CS Contact surface

CTAP Capillary tube average pressure

DDT Deflagration-to-detonation transition

DNS Direct numerical simulation

EAP Equivalent available pressure

FJ Fickett-Jacobs

FVM Finite volume method

GPU Graphical processing unit

HLLC Harten-Lax-van Leer contact

HPC High-performance computing / high-performance computer

IPM Induction parameter model

KNP Kurganov, Noelle, and Petrova

LES Large eddy simulation

LMDE Linearized model detonation engine

MAP Maximum a posteriori

MCMC Markov chain Monte Carlo

ML Machine learning

MLE Maximum likelihood estimate

MPI Message passing interface

MSE Mean-squared error

MUSCL Monotonic upstream-centered scheme for conservation laws

NASA National Aeronautics and Space Administration

ODE Ordinary differential equation

PC Parasitic combustion

PDE Partial differential equation

PDE Pulse detonation engine

PGC Pressure gain combustion

QoI Quantity of interest

RH Rankine-Hugoniot

RDE Rotating detonation engine

RDC Rotating detonation combustor

RK Runge-Kutta

ROM Reduced-order model

TVD total variation diminishing

U of M/UM University of Michigan

ZND Zeldovich-von Neumann-Döring

ABSTRACT

To enhance the efficiency and capability of aeropropulsion platforms, step changes in thermal efficiency and fuel burn, particulate emissions, and device thrust-to-weight ratio are of paramount importance. Such fundamental efficiency improvements may be attained through detonation-based combustion, in contrast to deflagration-based combustion traditionally found in gas turbines, rockets, and scramjets today. The rotating detonation engine (RDE) is one realization of detonation-based combustion, where a propagating detonation wave confined within a combustion chamber produces shock-based compression with rapid chemical heat release. The complex flow field within an RDE is fraught with non-idealities, ranging from incomplete propellant mixing and stratification, unsteady injector dynamics, secondary combustion, and multiple detonation waves. The goal of this dissertation was to 1) develop an understanding of the non-idealities within RDEs and their effects on device operation, 2) contribute high-fidelity data on detonation physics and RDE operation to the community, and 3) establish a framework for the assimilation of data from numerical and experimental campaigns and reduced-physics models for RDE performance estimation.

The numerical simulations were used to provide unprecedented insight into the physics of gaseous and multiphase detonating flows in RDE combustors. Canonical detonating flows revealed that discrete injection and mixture preburning result in detonation waves with diminished strengths, slower propagation speeds, and broader spatial structure than the theoretical expectation. The simulations of full-scale gas- and liquid-fueled RDEs performed here represent some of the highest fidelity com-

putational studies of these systems, with advancements in the modeled degrees of freedom through increased cell resolutions, larger computational domains, high-order detailed chemical kinetics of hydrocarbon mixtures, and extended simulation times. These studies revealed that parasitic combustion ahead of the wave results in commensal combustion behind the wave; most of the heat released within an RDE is through slow and distributed deflagrative combustion processes ($> 60\%$) as opposed to detonation. However, this secondary combustion, while decreasing the achievable thermal efficiency, may improve operability and the overall combustion efficiency of the system due to the complex interaction of unsteady turbulent mixing and detonation wave propagation. Furthermore, multiple competing detonation and secondary waves influence the flow structure by altering local heat release and fuel-oxidizer mixing and are integral to RDE operation.

While small-scale processes are important for operational stability and dictate how heat is released within the system, variations at the small-scale do not produce propulsive performance changes of the same order. The operating mode cannot be determined *a priori* as it is a manifestation of the equilibrium between small- and large-scale processes. Due to this challenge, a modeling framework to construct a surrogate model for RDE performance using limited and disparate data sets was proposed and demonstrated on a characteristic detonation combustor. In essence, the modeling approach establishes a pathway to unravel the connection between RDE operating conditions and the propulsive performance of the device: a high-dimensional coupling. The multi-fidelity fit of a performance quantity of interest, such as specific thrust, yielded a solution with a tighter confidence interval than a standard Gaussian process fit using the information contained within data at different fidelity levels, such as experiments, numerical simulations, and reduced-physics models. Further, additional experiments and simulations can be commissioned to reduce model uncertainty in an iterative design loop. The outcomes from the studies within this dissertation

help shape the community's current understanding of reacting flows within detonation engines.

CHAPTER I

Rotating Detonation Engines (RDEs) for Aeropropulsion

1.1 The Current State of Aeropropulsion

The field of high-speed propulsion is at a crossroads: the aspiration to reach distances farther and faster than ever before is faced with increasingly more stringent environmental regulations and the obligation towards sustainable aviation. These endeavors for more efficient and sustainable propulsion systems are primarily driven by economic motives. Current public sentiment has also heavily shifted towards the reduced environmental impact of human travel. In most airborne platforms, the onboard fuel is the primary contributor to the systems' weight, often three to four times the maximum payload capacity. The following form of the Breguet range equation [206] highlights the importance of the overall efficiency of the mission range of a simplified aircraft system:

$$\text{Range} = \eta_{overall} \frac{\Delta H_{fuel}}{g} \frac{L}{D} \ln\left(1 + \frac{W_{fuel}}{W_a}\right), \tag{1.1}$$

where $\eta_{overall} = \eta_{thermal}\, \eta_{propulsive}\, \eta_{combustion}$, ΔH_{fuel} is the heat of combustion, L/D is the lift-to-drag ratio of the aircraft, and W_{fuel} and W_a are the weights of the onboard fuel and aircraft, respectively.

For a platform with a given aerodynamic lift-to-drag capability, the tremendous value of lower fuel consumption and increased propulsion system efficiency, along with reduced fuel weight, is clear: a more efficient propulsion system will 1) reduce the required fuel quantity for the same mission range and 2) allow for longer ranges with current fuel quantities. Additionally, these platforms are constructed around the propulsion system, as the engines themselves are of the same order of weight as the payload. Increased payload capability is possible through reductions in vehicle components, namely improvements to the propulsion system thrust-to-weight ratio. Furthermore, aeropropulsion systems within the defense industry must adapt to counter emerging threats abroad. Propulsion systems with reduced fuel consumption and increased thrust density (increased thrust-to-weight ratio) will provide a tactical advantage in countless environments.

Among the multitude of ground-breaking technological innovations within the aerospace industry over the past few decades, namely in materials science, control algorithms, and software systems, propulsion system performance advancement is crucial and motivates this dissertation. In current aerospace applications, gas turbine technology is the primary form of energy conversion, transforming chemical energy stored within hydrocarbon or hydrogen-based fuels into usable work. Here, the combustion of the fuel occurs through deflagration, a relatively slow oxidation process. However, the design of these combustors is optimized to encourage turbulence-dominated flows, which intensify the mixing and transport of chemical species, fluid momentum, and fluid energy significantly. The dynamics of these turbulent processes occur across a wide range of length and time scales. As a result, understanding the physics of turbulence within a complex reacting environment is a challenging task, and the successful optimization of these combustors mandates that the interaction between the large- and small-scale processes is resolved entirely.

Decades of refinement of gas turbine technology have led to reliable and highly

mature technology, with practical implementations operating at near-theoretical efficiencies due to the optimization of flow paths, materials advancements, and electronic control capability. A range of technologies derived from efficient fuel mixing and combustion strategies for low-emission combustors are currently being developed [172], such as Rich-Quench-Lean (RQL) combustors, premixing swirlers, and direct fuel injection. These approaches integrate with traditional industry-standard fuels as well as sustainable aviation fuels (SAFs) [203, 339], fuel mixtures with increased hydrogen content [55, 336], and syngas [324]. Advancements to the turbomachinery within gas turbines are being studied through the geared turbofan [161] and open rotor [304] concepts to improve the thermodynamic efficiency of aircraft engines.

Longer-term or lower technology readiness level (TRL) methods are also being studied. Pure liquid hydrogen fuel is being considered for aerospace applications – in modified gas turbine engines and rocket propellant settings [24, 35, 338] – due to the potential elimination of all particulate emissions, with the exception of NOx derivatives. Hydrogen is a clean-burning fuel that eradicates carbon emission, although its highly reactive nature changes the combustion dynamics within the engine (i.e., flame flashback, flame holding, and flapping) and requires additional safeguards for safe operation in a practical setting. The reader is referred to Ref. [225] for further details of hydrogen fuel applications and challenges. Similarly, ammonia (NH_3) has been recognized as an alternative sustainable fuel that burns without carbon emissions while offering a higher energy density than liquid hydrogen [303]. Ammonia can be blended with hydrocarbon-based traditional fuels and hydrogen to retain their combustion properties enabling their use in gas turbine systems. Hybrid-electric propulsion systems (HEPSs) are also being considered, pairing hydrogen and SAF-powered combustion engines with electric motors to supplement the energy demand of airborne systems [11]. Additionally, liquid hydrogen can be used to generate electrical power that augments the gas turbine using hydrogen fuel cell technology [337].

HEPSs can support the electrical demands of kW-class general aviation and MW-class regional aircraft [66], with a reduction in fuel consumption, noise, and emissions in dense urban environments. Furthermore, a HEPS platform can power emerging technologies onboard unmanned aircraft systems (UAS) for defense applications [90].

1.2 Detonative Combustion

The drive to meet upcoming efficiency and environmental goals implores a step change in fuel burn and particulate emissions, namely CO_2 and NOx. Gas turbine engine operation is defined by deflagrative combustion through the Brayton thermodynamic cycle. To provide this fundamental efficiency change, detonation-based combustion, dictated by the more efficient Fickett-Jacobs cycle, is an alternative approach [176]. In this detonation cycle, Zeldovich-von Neumann-Döring (ZND) theory states that a detonation wave (DW) traveling at the Chapman-Jouguet (CJ) velocity releases energy through a fundamentally unsteady process [174]. The reactant gases are initially compressed by the shock wave (leading component of the DW system), driving energy release through a constant volume chemical reaction process. Deflagration-based combustion occurs nominally at constant pressure, although losses may result in a small pressure drop. In detonation-based combustion, gas expansion by heat release is spatially constrained, leading to a rise in the stagnation pressure. In the limit of infinite wave speed, an instantaneous conversion of reactants into products occurs in a constant-volume process. Thus, devices exploiting detonative combustion are classified as pressure gain combustion (PGC) systems. Ultimately, the rapid conversion of reactants in the detonation cycle (through speeds two orders of magnitude higher than corresponding deflagration speeds) lends to a more intense heat release process, allowing for a compact combustor with a greater thrust density than traditional deflagrative devices. This quality can provide a substantial reduction in propulsion system size and weight, with enhanced thermodynamic efficiency.

The T-s (temperature-entropy) diagram for the Fickett-Jacobs (FJ) detonation cycle, in comparison to the Brayton and Humphrey cycles, are depicted in Fig. 1.1. The Humphrey cycle is a modification of the Brayton cycle where the constant-pressure heat addition process is replaced by a constant-volume heat addition process, also resulting in PGC. The detonation cycle is identical to the Brayton cycle outside of the heat addition process. The initial shock compression leads to entropy rise, and combustion occurs through the constant volume reaction. At the end of heat addition, the local Mach number is one (sonic or choked), defining a sonic plane in multi-dimensional detonation wave systems. Following the end of reaction, the product gases are isentropically expanded. The total entropy rise induced by the unsteady propagating detonation wave is lower than that of deflagration-based combustion. As such, the FJ cycle is thermodynamically more efficient than either the Humphrey or Brayton cycles, namely about 20% greater than a Brayton cycle with the same compression pressure ratio [317].

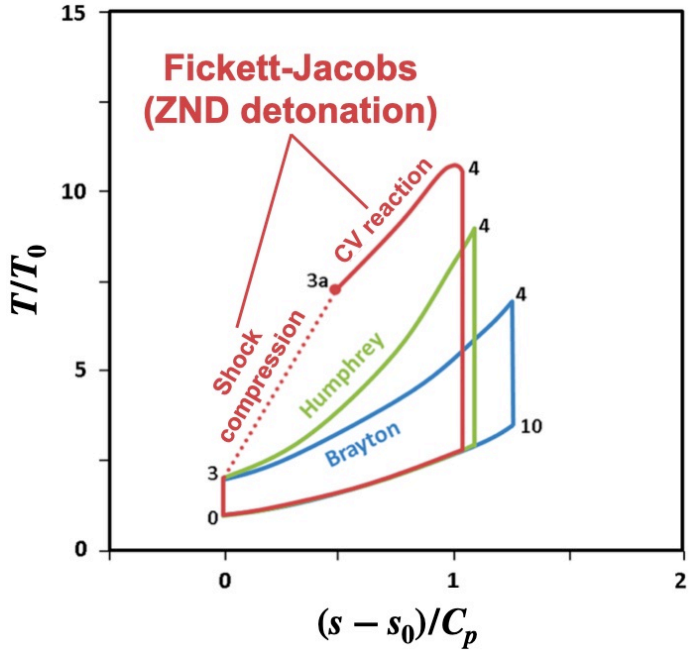

Figure 1.1: T-s (Temperature-entropy) diagram comparing the Brayton, Humphrey, and Fickett-Jacobs thermodynamic cycles. Adapted from Refs. [121] and [69].

It must be noted that the thermal efficiency gains of the FJ cycle in comparison to the Brayton cycle can be computed through thermodynamic analysis for an unsteady propagating detonation wave, but the thermal efficiency of a steady detonation-based engine is lower than that of a deflagration-based system [318]. This is because detonations produce the maximum amount of irreversible entropy rise which was shown to control the system's thermal efficiency. In these steady air-breathing engines, the initial stagnation state is fixed, and the total entropy rise is maximized through detonation-based combustion as opposed to the deflagration solution [270]. In general, high combustion thermal efficiency corresponds to low entropy increase. In PGC systems, such as a pulse detonation engine or rotating detonation engine, an unsteady, propagating wave operating near the CJ velocity can be thermodynamically represented through a constant-volume process starting from a fixed initial thermodynamic state that is at rest. The Rankine-Hugoniot relationship:

$$h_2 - h_1 = \frac{1}{2}\left(\frac{1}{\rho_1} + \frac{1}{\rho_2}\right)(P_2 - P_1) \tag{1.2}$$

provides the thermodynamic state across a combustion wave (deflagration or detonation) for a given initial state and energy release q_c. The solution for the second state must fall on the Rayleigh line defined by:

$$\frac{P_2 - P_1}{\left(1/\rho_2 - 1/\rho_1\right)} = -(\rho_1 u_1)^2 \tag{1.3}$$

The pressure versus specific volume plot with the general form of the Rankine-Hugoniot curve and Rayleigh lines for different levels of combustion energy release is illustrated in Fig. 1.2. The points where the Rayleigh line is tangent to the Hugoniot curve are the CJ points, of which there are two: the upper CJ point on the detonation branch and the lower CJ point on the deflagration point. The CJ points represent

states where the flow downstream of the combustion wave is sonic and correspond to the entropy extrema of the post-combustion gases. Courant and Friedrichs have shown that the upper CJ point corresponds to an entropy minimum and the lower CJ point corresponds to an entropy maximum [63]. While this result may seem unexpected due to the additional entropy generation associated with a normal shock wave implicit in the detonation process, the entropy generation during combustion is minimal because the heat addition occurs at a temperature higher than in a deflagration process. This relationship for a given one-dimensional detonation wave with a prescribed energy release q_c is depicted in Fig. 1.3. These analyses utilize premixed representations of combustion waves and losses associated with shock waves, mixing, and heat transfer will further reduce the thermal efficiency of deflagration and detonation combustion waves.

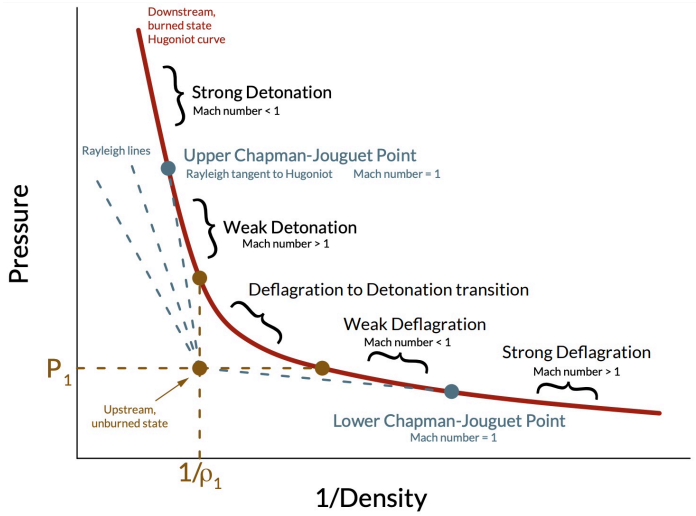

Figure 1.2: Pressure versus specific volume plot with the Rankine-Hugoniot relation for the thermodynamic states across a combustion wave (deflagration or detonation) for a perfect gas with a given combustion energy release q_c. Reproduced from Ref. [297].

In the pressure-specific volume diagram of Fig. 1.4, the pressure rise from a detonation (with an operating pressure ratio (OPR) of 2 in this case) results in such high pressure rise that more work can be extracted through flow expansion than from a

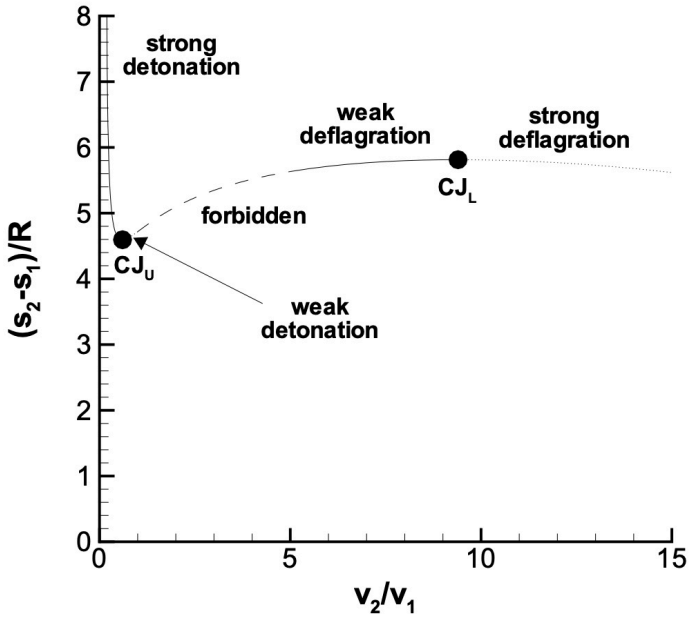

Figure 1.3: The variation of total entropy rise along the Rankine-Hugoniot curve for a perfect gas with a given combustion energy release q_c. Reproduced from Ref. [270].

gas turbine with an OPR of 10 [262]. Analysis by Paxson [217] highlights that for a given specific thrust, employing PGC with a nominal pressure ratio of 4% in a gas turbine results in a specific fuel consumption reduction of approximately 2.4% and 3.6% for both turbojet and turbofan applications, respectively. The pressure gain attributed to the detonation process allows for integration with existing propulsion systems with downstream turbomachinery. Furthermore, the shock compression also reduces the size of the required turbomachinery by needing a lower pre-compression of the reactant gases along with limited high-pressure turbine components.

1.2.1 The rotating detonation engine (RDE) concept

Pressure gain and namely detonation-based combustion devices have been studied for more than six decades starting most prominently with the work of Nicholls and colleagues in the 1960s [204]. However, advancements in materials engineering along with diagnostic and numerical simulation capabilities have led to a recent resurgence

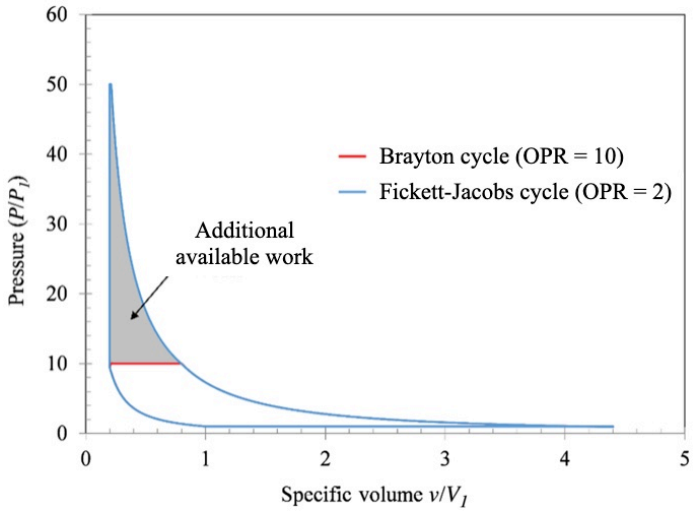

Figure 1.4: P-v (Pressure-specific volume) diagram comparing the available work between the Brayton (OPR = 10) and Fickett-Jacobs (OPR = 2) thermodynamic cycles. Adapted from Ref. [286] and [262].

in the technology. PGC in the form of resonant pulse combustors [171], fast deflagration wave rotor combustors [1], pulse detonation engines (PDEs) [e.g., 141], and rotating detonation engines [e.g., 3, 44, 174, 323] have been studied as implementation strategies. The dynamics of detonative combustion within RDEs will be explored in this dissertation. The primary advantage of the use of RDEs as opposed to PDEs is in the near-uniform thrust provided by continuously propagating DWs, confined within a detonation chamber. In a PDE, the well-mixed reactant gases are filled within a detonator tube, and a detonation is formed through a deflagration-to-detonation transition (DDT) event that combusts the mixture. The product gases are evacuated from the tube and provide thrust for the system. However, the finite time needed to purge and refill the detonation chamber before detonations can be initialized leads to a mechanically-limited frequency for thrust generation. This behavior is detrimental to downstream turbomachinery which relies on continuous thrust. While RDEs also generate variations in thrust due to the presence of shock structures, such variations occur at a very high frequency (as shown in Fig. 1.5). This variation can be greatly reduced when coupled with exit nozzles [243].

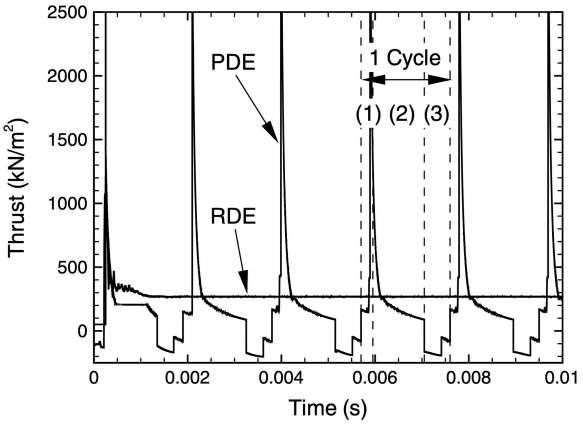

Figure 1.5: Comparison of the temporal evolution of thrust per unit area between PDE and RDE. Reproduced from [334].

Apart from the high frequency of operation, the nature of DW propagation allows for novel RDE combustor flowpaths that open up the design space, with radial [130], planar [328], and even various non-circular combustors [202]. Figure 1.7 shows sample designs and applications related to RDEs. The most common form of RDE is the annular design with concentric inner and outer bodies separated by a narrow annular combustion chamber, as shown by the schematic in Fig. 1.6. The RDE/RDC/RDRE refers to the combustion chamber as well as the injection flowpath and the exit geometry attached downstream of the combustor. Fuel and oxidizer are injected from the bottom face into the combustor, often through discrete injection ports. The design and placement of these injectors have a first-order effect on performance. The reactant streams then mix inside the annulus, mostly by shear-driven turbulence processes. One or more DWs propagate azimuthally through the annulus, which both compress and ignite the fuel/oxidizer mixture. The spatial structure of this heat release determines the strength of the propagating shock, which in turn affects the detonation process. The expansion behind the DW accelerates the product gases, which might be processed by another oblique shock formed above the height of the DW. The flow then turns and is accelerated towards the exit of the combustion chamber. The high operating frequency of these systems ensures continuous flow at the

exit. This is an important property that essentially leads to drop-in integration with existing power generation systems and their turbomachinery.

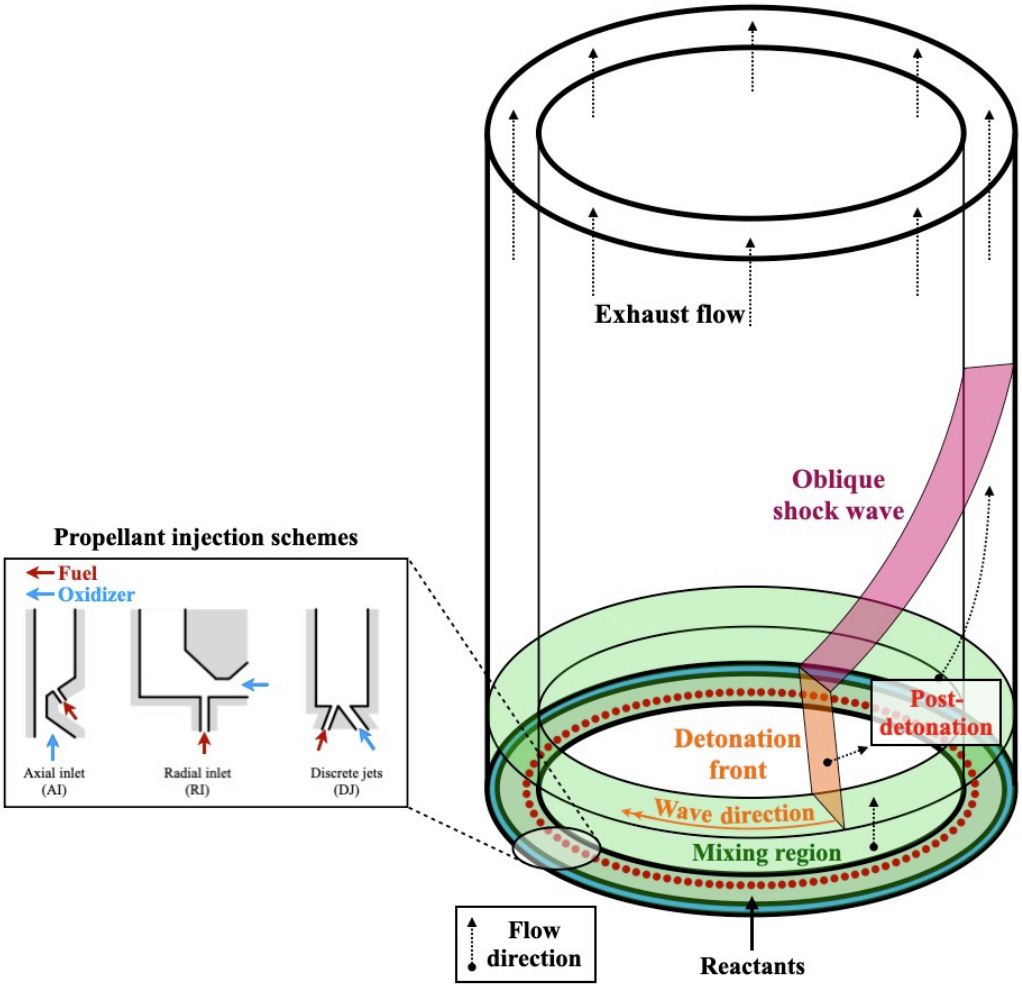

Figure 1.6: Schematic of a typical RDE configuration showing the DW, reactant gases, post-detonation products, and typical propellant injection configurations.

Within an RDE, the number of detonation waves is a key feature ascribed to the operating condition of the device. More than one DW may be present, traveling in co-rotating or counter-propagating modes. Such annular RDEs have been studied using a variety of injector designs, such as axial [e.g., 53, 151], radial [e.g., 5, 247], and discrete impinging schemes [e.g., 45, 122]. Further, different fuel and oxidizer compositions including H_2/air [91, 247], hydrocarbon/air [e.g., 46, 170, 183, 254, 316, 344] and hydrocarbon/O_2 [e.g., 94, 112, 309] have been considered. Studies of RDE dynamics

have focused on gas-phase propellants but initial investigations into the operability of liquid fuels have also been considered [160, 184, 342]. In order to practically realize this RDE concept, industry-standard liquid fuels for aviation applications (e.g., liquid methane, jet fuels, and rocket propellants) must be implemented and their influence understood.

Due to the nature of DWs, combustion can be sustained in a wide range of non-conventional designs. One such configuration is the radial RDE [118, 130, 199], where the DW is sustained between two concentric disks – refer to Fig. 1.7b. Fuel and oxidizer are fed radially from the outer wall between the disks, and the exhaust flow is removed through a port near the center of one of the disks. Such devices can be readily integrated into turbomachinery for gas turbines [130]. Another design is the shuttling reflective configuration, where the DW is sustained over a linear array of injectors [268, 328, 329] – refer to Fig. 1.7c. The DW repeatedly moves across this row of injectors, sustained by wave reflections at the ends of the domain. Interestingly, Slabaugh and co-workers [268] have shown that even when only one of the ends of this linear array is physically bounded, the DWs can be sustained through wave reflects across a choked flow boundary. This phenomenon has been identified numerically with its dynamics explained in Ref. [300]. Several additional configurations that either improve diagnostic abilities [51, 56, 174, 248] or performance [202] have been considered.

The RDE concept can be integrated into a variety of propulsion and energy conversion systems described in Sec 1.1. For instance, RDEs have been integrated into gas turbines for aircraft [87, 124, 201, 322] and power generation [173, 279], scramjets [343], augmentors [127, 200] and rockets [21, 96, 105, 164]. The main challenges of integration stem from the impact of shock waves on the upstream and downstream components: passing shock waves can introduce large pressure fluctuations that are not contained within the detonation chamber, but travel across the flowpath. Typ-

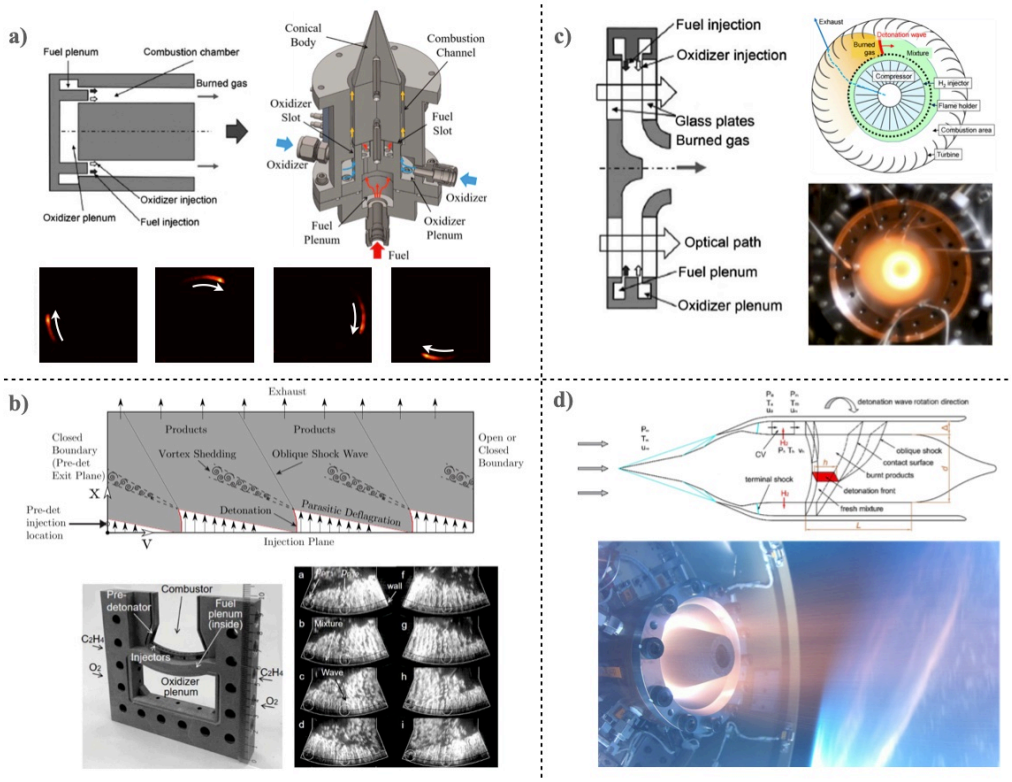

Figure 1.7: Example configurations of detonation combustors and integration in practical systems: A) annular detonation and its implementation in a rocket configuration; B) radial detonation and a visualization of the exhaust flow from experimental operation; C) shuttling planar combustor and a schematic and experimental imaging of multiple DWs during operation; and D) annular detonation and its implementation in a scramjet implementation. Adapted from: A) (upper left) [130], (upper right) [112], and (lower) [73]; B) [130]; C) (left) [268] and (right) [328]; and D) (left) [343] and (right) [106].

ically, some form of isolation such as a nozzle to reduce exit flow periodicity [243] is necessary to reduce this impact. Fig. 1.7d shows two practical applications: (upper) integration into a scramjet flowpath [343], and (lower) a recent demonstration of RDEs for rocket propulsion applications [106]. Hence, when considering RDE usage, the design should take into account system-level integration and its implications.

These demonstrations in practical systems show the usability of RDEs. Theoretical studies based on thermodynamic analysis have shown that the detonation cycle can provide roughly 20% increase in efficiency compared to Brayton cycle-based

devices [269]. To realize these potential gains, addressing the integration issues previously mentioned is necessary. For instance, experimental studies have provided some evidence that the theoretical gains can be realized [93, 320], including a reduction in specific fuel consumption. But these designs are not optimized to the extent of conventional gas turbines [93]. A critical gap remains between detonation theory and the practical realization of RDEs. Much of detonation theory, and hence the expected efficiency gain, is based on wave propagation through homogeneous fuel/air mixtures. Practical designs preclude this flow-field homogeneity, where the DW propagates through a highly unsteady and inhomogeneous environment. As a result, other physical processes, termed here as *non-idealities*, can emerge and lead to spurious losses. For RDEs to be adopted in these applications, it is necessary to understand the physics of non-idealities and to manage them for realizing the potential gains.

1.2.2 RDE flow features

RDE design is characterized by the design and positioning of the injectors, plenum conditions, the detonation chamber geometry, and the exit configuration. While macroscopic features of RDE flow structure can be obtained from simplified configurations, including two-dimensional representations [261], the performance of such systems depends on the complex interactions between the aforementioned components [3]. Figure 1.8 shows a rendered snapshot from a three-dimensional simulation of a practical RDE configuration. Most RDE designs feature fuel and air being injected separately into the detonation chamber for safety and operability, where turbulent mixing prepares the gas phase for the passing DW. While there has been considerable focus on premixed detonations [e.g., 98], RDEs fall under the category of mixing-limited detonation devices, where the strength and structure of the detonation process depend on fuel/air mixing. In order to understand the key features, Fig. 1.9 shows instantaneous snapshots of the flow field from a two-dimensional representation-based

simulation of RDEs as well as a full three-dimensional simulation. The main features of the RDEs are described in the discussion below.

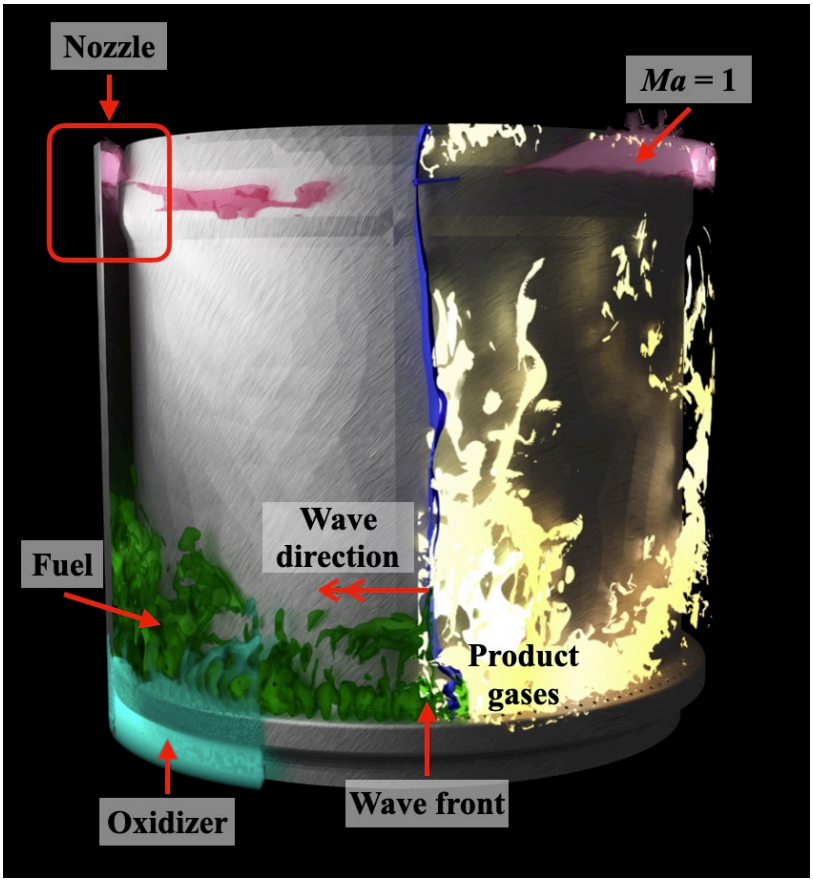

Figure 1.8: General flow features of a typical annular RDE with non-premixed injection.

- The fuel and air are injected separately for safety and operability, and through discrete ports located at the base of the chamber [e.g., 247]. In some cases, the oxidizer may be injected as a continuous feed, for instance through slots [e.g., 331]. Some of the main injection configurations are provided schematically in the inset image of Fig. 1.6, but additional options such as side-wall injection have also been considered [104]. The location of these injectors and the feed pressures play a critical role in ensuring adequate mixing of fuel and oxidizer prior to the arrival of the DW. Additionally, the choking of the injectors is used to limit the flashback of the combustion process and the reverse flow of post-combustion and

partially-burnt product gases into the feed plenums. In rocket-type combustors, micro-nozzles ensure highly stiff injectors at the expense of increased pressure drop across these injectors.

- The DW comprises of a leading shock, a reaction zone trailing this shock where heat release occurs, and a sonic point that separates this shock-reaction complex from the flow downstream of the wave. Unlike detonations over premixed mixtures, the waves observed in RDEs are thicker in nature, primarily due to the inhomogeneities caused by discrete injection [e.g., 218, 235]. These waves generally travel at speeds that are lower than the theoretical C-J speed. In fact, wave speeds of up to 50% lower than C-J speed have been observed, although 60-80% of ideal value is typically seen in most RDE configurations [e.g., 3].

- Since the DW is associated with a large pressure rise, the flow through a set of injectors may be reduced or even completely blocked as the wave passes over [e.g., 237, 261]. As the pressure is relieved through expansion behind the wave, the injector flow will recover over a timescale, determined by the strength of the DW, the upstream injection pressure, and the thickness of the post-detonation high-pressure region [261, 272]. Further, in many practical systems, a single plenum or manifold will feed all the fuel or oxidizer injectors. As a result, when the flow is blocked at certain injectors, it might be rerouted through the other remaining injectors. This process has the net effect of increasing the pressure in the manifold or plenum region [e.g., 247]. In other words, there is a critical injection pressure needed to sustain a given mass flow rate, which is important in the design process [139]. This recovery process provides the characteristic triangular fill region (Fig. 1.9, region II).

- In many RDE applications, multiple DWs have been observed [e.g., 44, 99]. Currently, there is not a complete description and understanding of the pres-

ence, effects, and coupling of multiple competing waves, although the review of [3] has a drawn a parallel to rocket combustor instabilities. The presence of multiple waves changes the time available for injector recovery and fuel/air mixing. Further, the penetration of the fresh gases into the detonation chamber is also reduced. These effects alter the quality of the detonation process, with either reduced fuel participation in the process or secondary losses such as deflagration being augmented.

- Contraction of the flowpath near the exit of the chamber leads to choked mass flow, which also raises the baseline pressure in the chamber [5]. There are two key pressures in an RDE which control its operating performance: 1) the feed pressure of the injectors and 2) the pressure at the exit of the combustion chamber. These two conditions dictate the usable pressure gain of the combustor. With a choked or partially choked condition at the exit, [88] concluded that stagnation pressure rise must be present within the combustor. It was observed to be a function of the global equivalence ratio and ranged from 3-7% for the conditions tested. Similarly, [333] found that with divergent nozzles, the nozzle characteristics had a relatively negligible effect on the propulsive performance, but significantly influenced the system's total pressure loss.

The basic structure of the RDE flow field has been elucidated from two-dimensional simulations [126, 261], both of which consider premixed fuel/air injection. There are many differences with the 3D RDE operation, but its certain key features are useful to discuss. The upper illustration of Fig. 1.9 shows the key features from two-dimensional calculations, which include: I) detonation front, II) fresh reactant gases, III) product gases, IV) contact surface between reacted and unreacted gases, and V) oblique shock wave. The detonation front features a characteristic wrinkled and curved structure. Extending behind the wave front, cellular structure indicative of unsteady detonation propagation is visible. Ahead of the wave is the fresh reactant fill region, repre-

sented by a triangular profile. A similar structure is observed in 3D systems with the following key features: A1 and A2 - contact burning surfaces between fresh and partially-deflagrated gases, region B - localized autoignition of injected gases, region C - secondary combustion at low pressure, D - detonation wave, region E - entrainment of post-detonation gases, region R - recirculation due to injector recovery, U - induced velocity, and W - detonation wave speed. In non-premixed systems, the refill region (region II in 2D flow) may be triangular or parabolic, depending on the injector response and wave motion within the combustor. The peak height of the refill region is strongly correlated with the DW height. The refill region is separated from the post-combustion product gases by a slip line. The DW itself features an oblique shock wave that extends above, and a shear-layer type contact surface with vortical structures separates post-detonation gases and shocked residual gases. The DW locally suppresses the injection of fresh reactants, which recover in a linear, uniform manner.

Practical RDEs differ from the ideal representation above in multiple ways, as outlined by the unwrapped projection of a three-dimensional RDE simulation shown in the lower portion of Fig. 1.9. The unsteady injector flow, due to periodic blockage by the passing DW, creates striated structures in the temperature profile. Even in relatively narrow channels, the injector design can result in large-scale recirculation patterns and turbulent shear layers. Since detonation itself is weaker than ideal premixed waves, these turbulence-induced inhomogeneities can lead to highly corrugated wave fronts and a distributed reaction zone behind the wave. These features can augment mixing with post-detonation gases above the fresh reactant mixture (denoted by the contact burning (A2) surface in Fig. 1.9), which can cause deflagrative combustion before the arrival of the DW. While the details of the flow structures depend on the injector scheme [e.g., 96, 213, 237, 254], the general flow regions identified above exist in all the configurations. It is recognized now that the deflagration, either

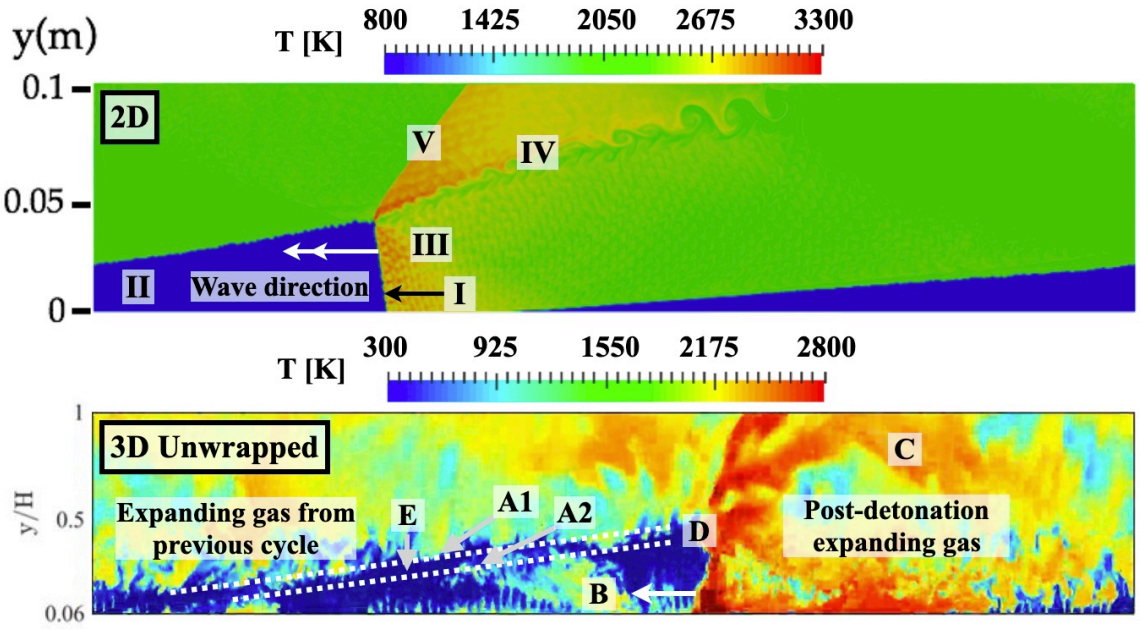

Figure 1.9: Two-dimensional structure of a propagating detonation wave: the top schematic shows a two-dimensional DW through premixed reactants, highlighting key flow components, and the bottom image highlights the temperature profile at the mid-channel plane of a 3D RDE, unwrapped and projected onto two-dimensions.

ahead of the wave or through mixing in the shear layers, can have a critical impact on the performance and operability of the RDE.

1.2.3 Mechanisms driving RDE performance

To practically realize RDEs, it is necessary to estimate performance as a function of operating conditions. In a design optimization workflow, an understanding of the RDE's operability across the required envelope is crucial. Macroscopic performance metrics, such as thrust or feed plenum pressure, are dependent on the so-called operating mode, which contains key information such as the number of detonation waves and the velocity and pressure rise associated with each wave. This operating mode is controlled by the quality and state of the reactant mixture presented to the detonation waves. Thus, RDE operation is defined by a strong complex coupling between large-

and small-scale physical processes, as outlined in Fig. 1.10. Small-scale features are local mechanisms that occur within the combustion chamber uncontrollably during operation whereas large-scale processes are mechanisms that occur at the device scale and are operationally controllable.

The small-scale features that drive mixture stratification (such as mixing inhomogeneity, gas entrainment, and secondary combustion) control the pre-detonation mixture. This mixture subsequently controls the small-scale generation of triple points and transverse shock waves and their motions through the RDE. The strength and stability of the detonation waves regulate the large-scale injector dynamics through the blockage of the injectors. The reactant fill height is an outcome of these interactions, which determines the number and speed of the detonation waves. The injector dynamics feed back into the preparation of the stratified and partially-combusted pre-detonation mixture state. At present, the operating mode cannot be predicted *a priori*, but only observed *a posteriori* – one of the key limitations in the understanding of RDE dynamics. The current view is that operation may be closely related to rocket combustion instabilities [3] and that the timescales of different processes, such as injector response, mixing, auto-ignition, etc., must overlap to sustain operation [23, 284].

In general, properties such as wave speed are macroscopically observable and are used to characterize large-scale features of the system. For instance, τ_w represents a large timescale that is related to operational mode [319, 325]. τ_w is defined based on the perimeter l, wave velocity W, and the number of detonation waves n_w as $\tau_w = l/(n_w W)$. Experimental measurements [e.g., 23] and CFD computations [e.g., 237] show that the injector recovery time τ_r is roughly $0.3 - 0.5\tau_w$. Similarly, the ignition time-scale in the pre-detonation mixture should be longer than τ_w for the detonation wave to be stable [284] but should be short enough in the post-shock state for substantial heat release to occur before reaching the sonic plane. *A priori*,

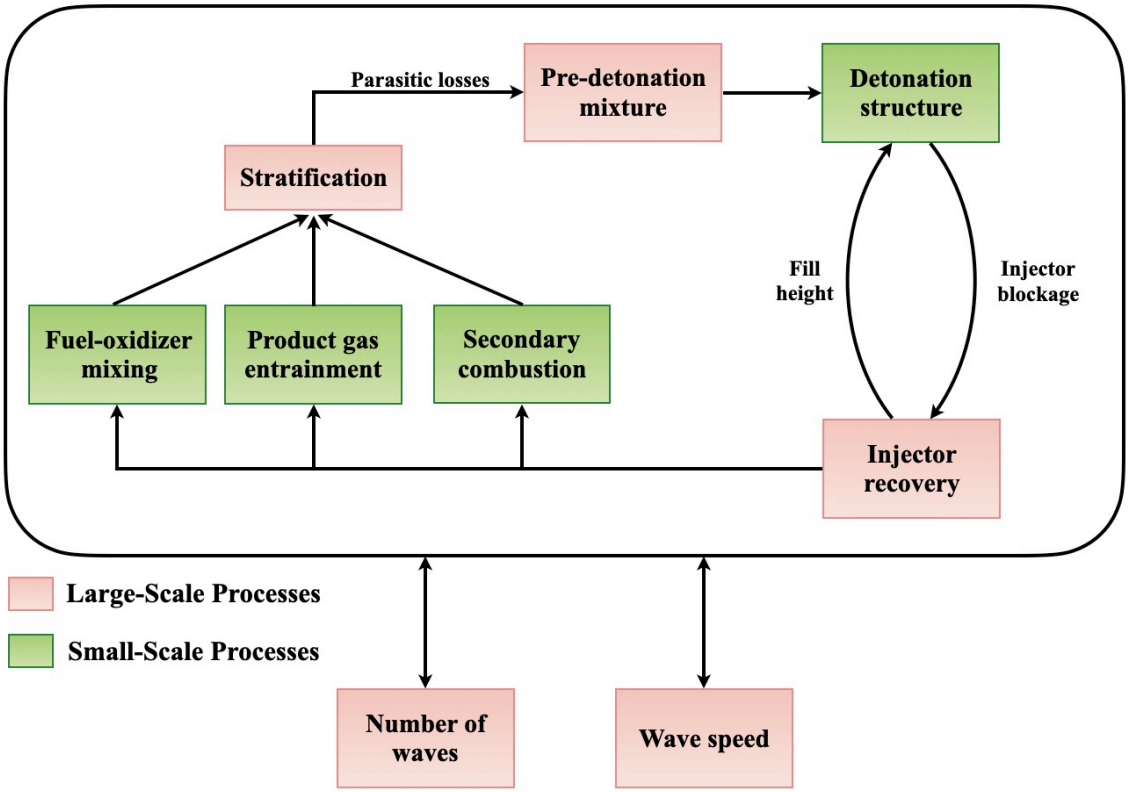

Figure 1.10: Diagram of the coupling between the large- and small-scale processes defining RDE operation.

this timescale cannot be predicted, since n_w and W cannot be predicted. Hence, the operational equilibrium cannot currently be predicted.

Based on these timescales, two different viewpoints are possible. In the first view, the RDC operation is mediated by large-scale processes which drive the small-scale processes toward an operational equilibrium. This view is similar to that used for thermoacoustic instabilities in rocket engines or gas turbines and is discussed extensively in [3]. A second perspective is that small-scale phenomena define the structure and characteristics of large-scale operation. Hence, they ultimately define the operation mode. The propagation of DWs is linked to the formation and evolution of triple points and transverse shock waves [e.g., 129, 162]. However, these DWs propagate into inhomogeneous mixtures, and the exact link between inhomogeneity and DW stability is not known. Fill height, which denotes the maximum penetration of the

fresh fuel/air mixture before encountering a detonation wave, is known to play a role in determining the number of waves [319]. However, the splitting of waves and the development of multiple detonation waves depend on the triple point structure and wave propagation in a partially deflagrated and fuel-stratified mixture. The injector response drives unsteady mixing and entrainment with post-combustion gases, creating a stratified mixture that undergoes different degrees of localized autoignition. It is thus increasingly evident that the pre-detonation mixture state plays a crucial role in defining the structure of the DW [e.g., 232]. As a consequence, the temporal and spatial inhomogeneities have a first-order impact on the performance and realization of the theoretical gains.

Recent experimental and computational studies [e.g., 21, 48, 62, 325] have started to explore the role of small-scale processes. Non-ideal phenomena in a practical RDE operated as a non-premixed system drive these small-scale processes. As described in Fig. 1.10, the non-idealities are manifested through three primary components: 1) inhomogeneities in the reactant mixture due to the varying dynamics of the fuel and oxidizer injection streams and entrainment of product gases; 2) secondary deflagrative combustion within the combustion chamber; and 3) detonative wave dynamics due to the effects of multiple competing waves. The deflagrative combustion results in heat release separate and secondary to the primary DW system. The additional competing waves (either of detonation or acoustic wave strength) are secondary waves that additionally alter the dynamics of the primary DWs. The secondary deflagrative combustion and the secondary waves are sources of losses within the system and manifest as a deviation in the DW properties of the system (e.g., reduction in wave speed and detonation pressure rise) and loss in performance of the combustor (e.g., reduced thrust and effective pressure gain). The characteristics of RDE operation are a result of the detonation wave system and the dynamic response of the propellant injection system in the presence of secondary combustion and waves. Although some

of these non-ideal phenomena have been identified and studied, their details and interrelations across scales are not fully known presently. Investigation of the impact of non-ideal phenomena on the DW structure and RDE operation is the primary focus of this dissertation. The details of each non-ideal phenomenon will be discussed in the subsequent chapters as relevant.

1.3 Experimental Approaches to Investigate RDEs

The RDE concept and the detonation process have been studied in a range of configurations. These include 1) linearized or simplified systems to understand wave propagation through inhomogeneous mixtures and injector response (similar to the unwrapped structure shown in Fig. 1.9) [e.g., 19, 40]; 2) laboratory-scale RDEs to investigate the effects of operating conditions, fuel composition, chamber flow path, and injection scheme on RDE performance and operability [e.g., 53, 64, 246, 288]; and 3) RDEs integrated with upstream/downstream components, such as turbomachinery, to discern the coupling between the unsteady wave behavior and external flowpath components (i.e., boundary conditions) [e.g., 87, 201, 321].

Advancements in experimental diagnostic capabilities, namely optical and laser-based measurements, have led to a substantial increase in the understanding of RDE operation. These diagnostic approaches can be classified as 1) imaging techniques for capturing the operating mode; 2) optical diagnostics to quantify the localized spatio-temporal evolution of the flow state; and 3) performance quantification through emissions, thrust, and pressure gain. In the first class, these approaches include capturing the operational and macroscopic properties of the RDE at a given operating mode, such as wave count, direction, speed, and mode shifts through imaging techniques like chemiluminescence imaging of the exit of the combustor [e.g., 20, 22]. Additionally, modified RDE combustors which incorporate a linearized section with a typical circular annulus [86] allow for enhanced optical imaging access to capture the detonation

structure and existence of secondary combustion [49, 220, 301, 313]. The second class of diagnostics specifies the equipment to capture the localized spatio-temporal evolution of state quantities, such as exit flow temperature [10, 221, 250], pressure [197], velocity [67, 72, 308], and intermediate or product species [51, 180, 295] and distribution of fuel at the combustor base [19, 73, 246], at a single point or over a plane have been used. However, access to insert experimental equipment with minimal impact on the flow field and their limited lifespan in the harsh environments of RDE combustors is one of the main challenges in their application. In the third class, RDE performance is quantified through overall combustion efficiency and exhaust emissions [77] and through a measure of pressure gain. To note, the limited NOx and O_2 emission measurements of [77] suggest that NOx emission may be low (< 30 ppm) and can be attributed to the lack of flow residence needed for NOx formation. The combustor's pressure gain performance has been evaluated through the concept of Equivalent Available Pressure (EAP) [140] defined from thrust measurements and total pressure measurements through probes at the exit of the RDE [12, 60, 152].

The harsh environments within the RDE and limited access to perform non-invasive measurements limit understanding of the non-ideal effects described in Sec. 1.2.3 and the coupling between large- and small-scale processes within the combustor. Key flow features, such as the development of turbulence and recirculation zones, which drive the mixing process at the base of the combustor need to be understood. Also, the extent and distribution of secondary combustion along with wave formation and mode transition may be difficult to capture, requiring novel approaches [39, 48]. Additionally, the extreme range of temperatures and pressures, as well as the fast timescales [e.g., 134], can increase measurement uncertainty. For instance, the high operating frequency of the DW system may prevent the pressure peak from being accurately captured by the diagnostic equipment, as the acoustic pulses are attenuated by the measurement apparatus. Numerical approaches offer the capability to investigate the

non-ideal effects within the RDE combustor.

1.4 The Impact of Numerical Approaches

RDEs contain some of the most challenging sub-physics for computational modeling. The presence of shocks and turbulence requires numerical methods that can be stable but also minimize numerical dissipation [e.g., 163]. Chemical reactions, while dominant in the near-shock region, occur over the entire flowpath. Further, the range of timescales involved can be prohibitive. Note that the smallest length scales are comparable to the induction region behind the shock wave, which can be as short as $\mathcal{O}(10\ \mu\text{m})$ for hydrogen-oxygen mixtures [230], and longer than $\mathcal{O}(100\ \mu\text{m})$ for hydrocarbon-air mixtures [175]. The wave propagation speed affects not only the total simulation time but also the small timescales. For instance, when the DW is strong, its propagation speed will be faster, but it will also increase the stiffness of the chemical kinetics due to the higher pressure and temperature conditions. In general, variations of speed are of the order of $0.5 - 0.95W$ (based on the theoretical speed for a mixture at the global equivalence ratio) but the reduction in the smallest timescale can be higher, spanning two to three orders of magnitude. Given these considerations, direct simulation of RDEs is computationally expensive [92, 213], and special procedures for handling chemical kinetics may be needed [15, 16, 168, 210, 233].

CFD computations can be divided into three types of calculations: a) canonical flows, b) 2D unwrapped simulations, and c) 3D RDE computations. Canonical flows capture component processes such as fuel injection [e.g., 96] and detonation propagation over homogeneous [144] or inhomogeneous and stratified mixtures [e.g., 75, 114, 149]. Such simulations have been routinely used in detonation science to understand the transition from deflagration ([150, 215]) or the formation of cell structures (for instance, [113, 148, 292, 345]). In the context of RDE-related physics, the effects of mixture heterogeneity on detonation propagation have been considered [e.g.,

114, 149]. These calculations typically use no subgrid models with a minimum mesh resolution on the order of $\mathcal{O}(10\ \mu\text{m})$ to resolve the reaction zone. [114] conducted detonation propagation simulations over a domain with the imposed transverse fuel concentration gradient. The flow structure inside an RDE was first established using two-dimensional unwrapped computations [126, 261]. Here, the flow in the circumferential and axial directions was simulated, along with periodic flow boundaries in the circumferential direction. While fuel and air were assumed to be premixed in these simulations, the effect of discrete injectors, plenum pressures, and other flow inputs have been studied [e.g., 261]. However, due to the two-dimensional nature of the simulations, realistic mixing effects including flow recirculation and turbulent mixing cannot be captured. Nevertheless, certain key features of the flow have been understood. For instance, [126] showed that the collision of triple points near the injector reduced detonation cell size. Since RDE flows are sensitive to the specifics of the geometry, three-dimensional simulations that take into account the details of the injection process and the flowpath have been conducted [e.g., 213, 254, 346]. Due to the computational cost, these simulations typically do not resolve the shock-detonation structure completely. Figure 1.11 shows sample calculations that capture various aspects of the three-dimensional flow in detonation-based engines.

The numerical simulations, and in particular the three-dimensional full-scale calculations, are reasonably accurate in matching experimentally-measured macroscopic quantities, such as plenum pressures and thrust. However, there can be significant differences in comparison to experiments as well. These discrepancies stem from 1) the evolution of the initial condition controlled by the numerical methods to handle wave collisions; 2) the very short flow time ($\approx 3-5$ms) of simulations compared to experiments ($\approx 100-200$ms); 3) the resolution effects on wave propagation speed and peak pressure; 4) application of chemical kinetics models formulated for deflagrative combustion; and 5) influence of the treatment of turbulence. First, the numerical sim-

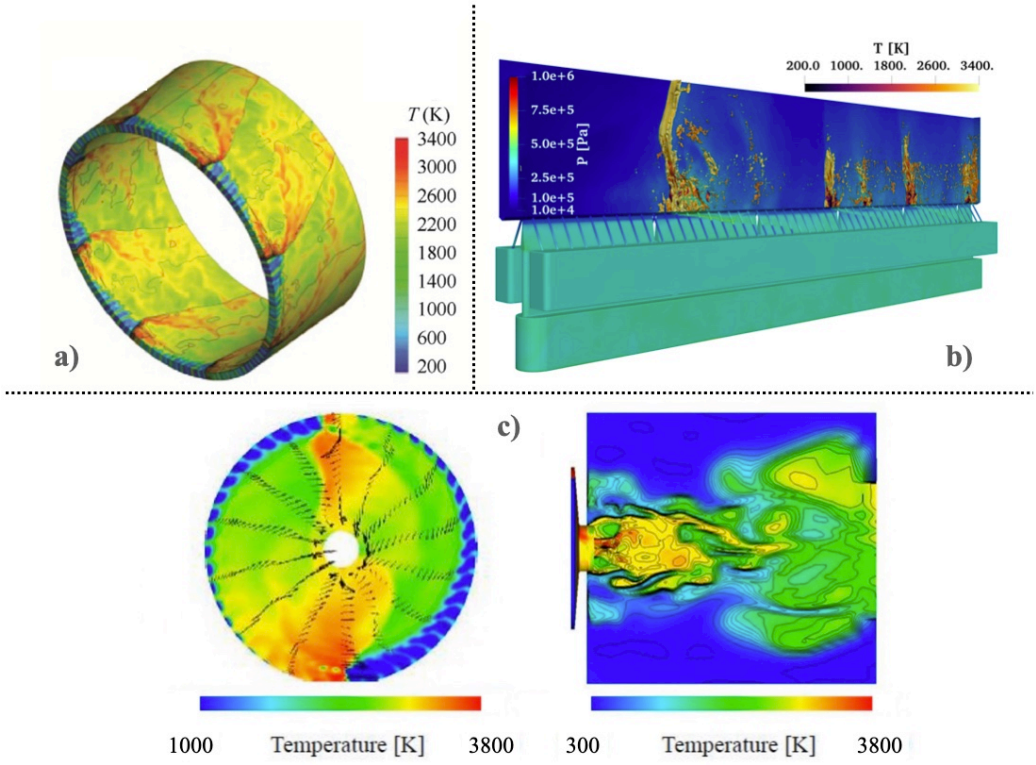

Figure 1.11: Sample numerical simulations of detonation combustor configurations: a) multi-head rotating DWs in an annular combustor (reproduced from [346]); b) multiple waves in a planar shuttling detonation combustor in a closed-open configuration; and c) radial disc-type detonation combustor with (left) two detonation heads (reproduced from [120]) and (right) external temperature flow field with detonation head (reproduced from [119]).

ulations start from a prescribed high-energy initial condition and proceed to reach a stable set of waves. This highly chaotic flow state impacts the unsteadiness in the injection process. Thus, the operating mode that emerges is controlled by the numerical methods and how they handle wave collisions. Second, highly resolved numerical calculations are computationally expensive and can typically simulate only a short flow time. Hence, it cannot be concluded that a true steady state has been reached and the operating mode may be a local steady-state solution. In experiments, sporadic changes to the wave structure may happen at certain operating conditions [28]. Third, the wave speed may become sensitive to resolution since the representation of the pressure peak reached behind the shock has a leading impact. While grid convergence studies are conducted [9, 120] to ensure convergence of macroscopic operational parameters, preliminary studies have shown that the convergence of the detonation structure can be achieved only when the reaction layer is adequately captured [14, 239]. Fourth, the chemical kinetics models used for detailed chemical kinetics (needed for non-premixed simulations) have largely been formulated for deflagrative combustion. Some of these mechanisms have been validated for use in detonating flows using macroscopic measurements (wave speed and pressure rise, for instance). But mechanisms that have been developed specifically for detonation and fully validated for these environments are not readily available. Prior studies have shown that issues such as thermal nonequilibrium could have a significant effect on predictions [273, 293, 306]. In particular, the rapid compression and expansion might cause vibrational nonequilibrium, which relaxes at timescales comparable to the flow timescales in such flows [e.g., 82, 159]. Fifth, grid-based dissipation or explicit models in the context of large eddy simulations [169, 214] are employed to model turbulence. However, the optimal treatment for RDE environments with short flow timescales is not known.

Realizing RDEs as a practical combustor requires predictions of performance met-

rics, such as thrust or upstream feed pressure needed to operate the device. As a result, fast throughput models based on thermodynamic system analysis and reduced-physics processes are commonly used [e.g., 131, 139, 140, 156, 205, 219, 272, 286, 335]. In these methods, an internal structure for the flow is assumed, and one-dimensional relations are used to estimate propulsion performance. The flow may be partitioned based on the form of combustion (detonation or deflagration) to account for injection and mixing inhomogeneities. These reduced-physics models are crucial for RDE design, given the high cost of detailed numerical simulations, but their predictive accuracy can be highly dependent on the model parameters and data used for calibration.

Nevertheless, the detailed insight offered by numerical approaches can increase understanding of the flow path within the combustor, and the effect of operating conditions and geometric variations on the formation of non-idealities. High-fidelity numerical simulations can provide insight into the formation of the detonation wave, detonation structure, the effect of the injection scheme, the injector recovery process and the development of secondary combustion, and the effect of the operating condition of the RDE. Numerical approaches also allow certain small-scale processes to be isolated and independently studied more easily than in an experimental setting. In conjunction with experimental campaigns, numerical simulations and techniques can be used to understand the complex physics inside RDEs and accelerate the design process.

1.5 Chapter Summary

This section provided motivation for an alternative combustion platform for aero-propulsion applications through the need for a step change in efficiency and emissions. Pressure gain and detonation combustion are introduced to overcome the thermodynamic cycle limitations of traditional deflagrative combustors operating on

the Brayton cycle. The rotating detonation engine is the emerging form of PGC with the capability of high thrust-to-weight, continuous operation, and interoperability with existing propulsion systems. The operation and physical flow features within an RDE are discussed. However, practical non-premixed RDEs introduce dynamics that lead to non-idealities and secondary effects that limit performance and force the combustion process to deviate from the ideal Fickett-Jacobs detonation cycle. These non-idealities need to be better understood and numerical approaches can help on this front. The effects of the non-ideal phenomena on the fundamental detonation structure and the device operation need to be better understood to guide the design of RDE devices. Further, high-fidelity simulation data that offers insight where experimental approaches are limited is crucial. The goal of this dissertation is to 1) develop an understanding of the non-idealities within RDEs and their effects on device operation, 2) contribute high-fidelity data on detonation physics and RDE operation to the community, and 3) establish a framework for assimilation of numerical and experimental data and reduced-physics models for RDE performance estimation.

1.6 Scope of the Dissertation

As background, several reviews of RDEs exist in literature [e.g., 3, 142, 143, 174, 323], which discuss basic operational principles and experimental as well as computational results. [323] discussed the different pressure gain devices and their operational characteristics. More recently, [3] compared the similarities between instabilities observed in rocket engines, which served as the driver for developing the rotating detonation concept. Further, [241] discusses the current understanding of non-idealities within RDEs and the multiscale coupling of small- and large-scale processes from numerical and experimental investigations of RDEs. The dissertation serves to outline the insight on non-idealities gained from high-fidelity numerical simulations of canonical configurations as well as practical RDEs. The underlying flow structure within

RDEs and its contribution to the development of non-idealities, such as secondary combustion, mixture inhomogeneity, and wave dynamics, is presented.

Thus, the work contained within this thesis can be segmented into three parts: I) fundamental physics of canonical detonating flows; II) simulations of full-scale, non-premixed RDEs; and III) macroscopic RDE performance estimation. Part I is explored in Chapter III, Part II is examined in Chaps. IV and V, and Part III is covered in Chap. VI. The dissertation is organized as follows:

- **Chapter II:** The next chapter will introduce the numerical tools used in the high-fidelity simulation of canonical detonating flows and non-premixed RDEs. The simulations of canonical flows utilize a high-order structured-mesh compressible flow solver, UTCOMP, with detailed chemistry allowing highly-resolved three-dimensional numerical simulations. The simulation of non-premixed RDEs mandates an unstructured-mesh compressible flow solver–UMReactingFlow–that can handle detailed chemistry, capture complex injector geometries, and balance shock-capturing and turbulent mixing for detonation environments. Additionally, the solvers need to be highly scalable to distribute the computational costs.

- **Chapter III:** In this chapter, the UTCOMP solver will be applied to simulations of canonical detonating flows. These foundational simulations isolate the effects of the small-scale processes of detonation-injector interactions, fuel/oxidizer stratification, and secondary parasitic deflagration. In particular, the propagation of a detonation wave through a linear array of injectors is simulated to study the effect of discrete injection on the detonation wave structure. The effects of fuel/oxidizer stratification and mixture preburning are studied in a confined channel with an inhomogeneous distribution of reactant gases. The outcomes of these forms of non-idealities on the strength and stability of the detonation wave are discussed.

- **Chapter IV:** With an understanding of the non-idealities of detonation in inhomogeneous flows, the UMReactingFlow solver is utilized to study the Air Force Research Laboratory (AFRL) rotating detonation rocket engine (RDRE) at multiple operating conditions. Furthermore, high-resolution representations of the geometry with a truncated feed plenum are studied to evaluate the effects of mass flow rate, numerical ignition method, and resolution. Detailed analysis of the detonation behavior, the combustion process, and the injector dynamics are presented in this chapter.

- **Chapter V:** The UMReactingFlow solver is adapted with a Lagrangian particle tracking library to perform the first set of three-dimensional numerical simulations of an RDE with liquid fuel injection. In particular, two modifications of the AFRL RDRE geometry are studied to quantify the coupling between the injection scheme on the operability of the RDE. The main purpose of the simulations within this chapter is to understand the interaction of the injection scheme and its ability to prepare a detonable mixture required to sustain detonation.

- **Chapter VI:** Realizing RDEs as a practical combustor requires predictions of performance metrics, such as thrust or upstream feed pressure needed to operate the device. In this chapter, the well-studied AFRL radial 6-inch H_2/air RDE is examined due to the availability of extensive experimental data from Ref. [244] and numerical simulation data from Ref. [258]. The reduced-physics RDE thermodynamic cycle model of Kaemming et al. [139] is exercised by performing Bayesian calibration of key model parameters to best predict macroscopic RDE performance metrics. As a supplementary approach, the method of multi-fidelity modeling is introduced to assimilate data from all three sources – experimental, numerical simulation, and reduced-physics model data – to ob-

tain performance predictions across the operating envelope with quantification of prediction uncertainty. This framework allows for increased predictive capability based on all available data.

- **Chapter VII:** In this final chapter, the outcomes of the dissertation work are summarized. Concluding remarks about the non-ideal phenomena in detonating flows and practical RDEs are presented. Further, the implications of the high-fidelity numerical simulations and data assimilation and modeling efforts are provided. Finally, suggestions for future work to address the remaining issues are discussed.

CHAPTER II

Numerical Tools for Reacting Flows

This chapter presents the numerical tools used for the high-fidelity simulations of shock-containing and reacting flows. Detonating flows, and specifically RDEs, contain some of the most challenging sub-physics for computational modeling. The presence of shocks and turbulence requires numerical methods that are stable with reduced dispersion errors, but also minimized numerical dissipation to capture the mixing accurately [163]. Chemical reactions are stiff and dominate in the near-shock region, but extend throughout the domain and across the entire flowpath. Furthermore, the range of time and length scales involved can be prohibitive. The large time scale is determined by the wave period for most designs whereas the highly unsteady flow limits time steps to the order of the flow and chemical time scales, which can be 4-5 orders of magnitude smaller. In particular, the critical length scale in detonation simulations is based on the induction region behind the shock wave, which can be as short as $\mathcal{O}(10\ \mu\text{m})$ for hydrogen-oxygen mixtures [230], and longer than $\mathcal{O}(100\ \mu\text{m})$ for hydrocarbon-air mixtures [175]. The strength of the detonation wave directly is coupled with the wave propagation speed, thereby affecting the total simulation time and the small timescales. A strong detonation wave and a highly reactive mixture will increase the wave propagation speed, but also increase the stiffness of the chemical kinetics due to the higher pressure and temperature conditions across the wave.

Similarly, the large length scale is fixed by the domain, whereas the detonation front is very thin and on the order of 1 to 100 μm. Thus, the integration of the chemical source terms can entail extreme costs, and make the direct simulation of detonating flows computationally expensive. Special procedures for handling chemical kinetics may be needed [15, 16, 168, 210, 233].

Two classes of simulations will be considered in this dissertation: 1) canonical detonating flows in a simplified geometry and 2) full-scale RDEs with complex injector schemes and flow paths. As a result, a different set of numerical tools are required for each class of problems with consideration of required capabilities and computational cost. The first class of problems will utilize an in-house compressible flow solver UTCOMP with high-order numerical methods to resolve the small-scale processes of the detonation wave (e.g., triple points, transverse waves) accurately in a structured grid configuration. The second class of problems requires a highly-scalable in-house compressible flow solver UMReactingFlow which allows for the representation of complex RDE geometries through an unstructured grid framework. Both solvers employ a direct numerical simulation (DNS) approach to the conservation equations. The solvers have been adapted for use in detonating flows and the details are described in the following sections.

2.1 UTCOMP Solver

The following section presents the fundamental details and assumptions incorporated in the in-house compressible flow solver UTCOMP. The solver has been adapted for use in detonating flows. The high-fidelity simulations of canonical detonating flows in Chap. III are performed using this solver.

2.1.1 Conservation laws and principles

In the macroscopic representation of fluid flow, the flow properties are in the continuum regime. More specifically, the mean free path – the average distance traveled by a particle before encountering a change in direction or energy due to a molecular collision with other particles – is much smaller compared to a representative physical length scale, i.e., the Knudsen number of these flows is negligible and flow is continuous. This is an assumption common to both the UTCOMP solver and the UMReactingFlow solver discussed in Sec. 2.2. The governing equations of fluid flow consist of mass, momentum, and energy conservation equations supplemented by the species conservation equations that incorporate a source term due to chemical reactions.

2.1.1.1 Conservation of mass

The first conservation principle concerns mass conservation. The mass within the thermodynamic system cannot change with time. The Eulerian formulation of the conservation principle is given as:

$$\frac{\partial \rho}{\partial t} + \frac{\partial \rho u_i}{\partial x_i} = 0, \tag{2.1}$$

where ρ is the fluid density, t is the unit of time, x_i is the spatial position in the i-th direction of three-dimensional space ($i = 1, 2, 3$), and u_i is the fluid velocity in the i-th direction.

2.1.1.2 Conservation of momentum

The second conservation principle is the momentum balance derived from Newton's second law which states that the sum of external forces on a fluid element is equal to the time rate of change of momentum. In Eulerian form, the conservation

principle is:

$$\frac{\partial \rho u_i}{\partial t} + \frac{\partial \rho u_i u_j}{\partial x_j} = -\frac{\partial P}{\partial x_i} + \frac{\partial \tau_{ij}}{\partial x_j}, \tag{2.2}$$

where x_j is the spatial position in the j-th direction of three-dimensional space ($j = 1, 2, 3$), u_j is the fluid velocity in the j-th direction, P is the fluid pressure, and τ_{ij} is the viscous stress tensor. The fluids and gases considered in these simulations are Newtonian fluids where the viscous shear stress is proportional to the strain rate. Thus, it is given by:

$$\tau_{ij} = -\frac{2}{3}\mu \frac{\partial u_k}{\partial x_k}\delta_{ij} + \mu\left(\frac{\partial u_j}{\partial x_i} + \frac{\partial u_i}{\partial x_j}\right), \tag{2.3}$$

where x_k is the spatial position in the k-th direction of three-dimensional space ($k = 1, 2, 3$) and u_k is the fluid velocity in the k-th direction. The fluid dynamic viscosity μ is evaluated using Sutherland's law and is a function of a reference temperature, fluid composition, and the local flow temperature T. The momentum balance formulation does not include body forces f_i such as gravity. The gravity-driven buoyancy force is typically neglected because the system is dominated by convective forces and its effect would be minimal on the flow solution.

2.1.1.3 Conservation of energy

The third conservation principle is the energy balance which ensures that the total energy in the thermodynamic system is constant. The total energy E is a sum of the sensible internal energy e_s and the kinetic energy K and is given as:

$$E = e_s + K = \left(\int_{T_0}^{T} c_p dT - \frac{P}{\rho}\right) + \frac{1}{2}u_i u_i, \tag{2.4}$$

where c_p is the specific heat capacity at constant pressure. The specific heat capacity, enthalpy, specific heat ratio, and transport properties are computed as a function of

temperature using NASA polynomial fits [182]. Assuming no radiation or external body forces on the fluid, the transport equation for the total energy is given in Eulerian form:

$$\frac{\partial \rho E}{\partial t} + \frac{\partial \rho u_j E}{\partial x_j} = -\frac{\partial P u_i}{\partial x_i} + \frac{\partial \tau_{ij} u_i}{\partial x_j} + \frac{\partial}{\partial x_j}\lambda\frac{\partial T}{\partial x_j} + \rho\dot{S}, \tag{2.5}$$

where λ is the thermal conductivity, T is the temperature, and $\rho\dot{S}$ is the energy source term from chemical reactions. The term $\lambda\frac{\partial T}{\partial x_j}$ represents the heat diffusion rate given by Fourier's law, where λ is evaluated from the Prandtl number $Pr = \frac{\mu c_p}{\lambda}$, a relation between heat and momentum diffusion. For the calculations performed in this dissertation, the Prandtl number is set to 0.72, a typical value for turbulent gases [315].

2.1.1.4 Conservation of species

With reacting flows, a scalar conservation equation for each fluid species α with mass fraction Y_α must be enforced. The scalar transport equation is given by:

$$\frac{\partial \rho Y_\alpha}{\partial t} + \frac{\partial \rho u_j Y_\alpha}{\partial x_j} = \frac{\partial}{\partial x_j}\rho D\frac{\partial Y_\alpha}{\partial x_j} + \rho\dot{S}_\alpha, \tag{2.6}$$

where $\alpha = 1, \ldots, N_S - 1$ is the species index for a vector of $N_S - 1$ species mass fractions $Y = [Y_1, \ldots, Y_{N_S-1}]^T$, D is the mass diffusivity, and $\rho\dot{S}_\alpha$ is species α's production source term due to chemical reactions. The non-reacting diluter, nitrogen, is the N_S-th species and its mass fraction is determined as 1- $\sum_{\alpha=1}^{N_S-1} Y_\alpha$. The Lewis number, Le, is assumed as unity. Thus, the momentum diffusion rate, a product of the density and mass diffusivity (ρD), is computed as a ratio of the dynamic viscosity, μ, to the Prandtl number, $Pr = 0.72$.

Equations 2.1, 2.2, 2.5, and 2.6 together form the Navier-Stokes (NS) governing equations of fluid flow. The system of equations is closed using the ideal gas equation of state (EoS). The gas temperature can be computed directly from the conserved

properties, and pressure is derived using the ideal gas EoS. Although this EoS is often used for detonation simulations, particularly with regard to rotating detonation engines, alternative EoS models may provide insight into real gas corrections for pressure. The ideal gas law is typically valid at sufficiently low pressures (relative to the critical pressure P_{cr}), equivalently low densities, and high temperatures (relative to the critical temperature T_{cr}). Past research has dealt with the formulation and analysis of non-ideal equations of state for gaseous products of solid propellant/explosives detonation [196, 311]. Here, the pressures of the detonation process can exceed 20 GPa for atmospheric ambient conditions, pressures significantly higher than those observed within gaseous detonation. Here, product gases are compressed to "1.5-2.5 times their normal solid densities" [311] during the reaction process. For this reason, various non-ideal equations of state have been evaluated, such as the Van der Waals EoS, Nobel-Abel (or Clausius) EoS (a variation of the Van der Waals EoS), Haar-Shenker EoS, and virial EoS [311]. Additionally, the simulations here assume a fugacity coefficient $\phi = f/P = 1$ where f is fugacity, an effective partial pressure. In real gases, a non-unity fugacity coefficient may affect calculations of chemical equilibrium. In future analyses, it may be highly beneficial to investigate the effect of the ideal gas EoS on gaseous detonation simulations, by comparing the results discussed here to those computed using a non-ideal EoS.

2.1.2 Chemical reaction treatment

The high-fidelity numerical simulation of unsteady detonations with partially-premixed reactant gases mandates the use of detailed chemistry. The detailed multi-step chemical kinetics are handled through CHEMKIN-based subroutines [146]. In the species transport equation (Eq. 2.6), the species source term is of the form

$$\rho \dot{S}_\alpha = \dot{\omega}_\alpha M_\alpha, \tag{2.7}$$

where M_α is the molecular weight of species α. For a multi-step reaction with N_S species and N_R reactions, $\dot{\omega}_\alpha$ is the molar species production rate, given by:

$$\dot{\omega}_\alpha = \sum_{l=1}^{N_R} (\nu''_{\alpha,l} - \nu'_{\alpha,l}) \left[k_{f,l} \prod_{\alpha=1}^{N_S} [A]_\alpha^{\nu'_{\alpha,l}} - k_{b,l} \prod_{\alpha=1}^{N_S} [A]_\alpha^{\nu''_{\alpha,l}} \right], \tag{2.8}$$

Here, $\nu'_{\alpha,l}$ and $\nu''_{\alpha,l}$ are the reactant and product stoichiometric coefficients, respectively, of the l-th elementary reaction in the multi-step mechanism for species α, k_f and k_b are the reaction rate constant of the forward and backward elementary reactions, respectively, and $[A]_\alpha$ is the mole fraction of each species α. The forward reaction rate constants are of the modified Arrhenius form:

$$k_{f,l} = A_l T^{\beta_l} \exp\left(- \frac{E_{a,l}}{RT} \right), \tag{2.9}$$

where A_l, β_l, and $E_{a,l}$ are the pre-exponential factors, temperature exponents, and activation energies for each elementary reaction l. Similarly, the source term for the energy transport equation (Eq. 2.5) is of the form:

$$\rho \dot{S} = \frac{\sum_{\alpha=1}^{N_S} h_\alpha \dot{\omega} M_\alpha}{c_p}, \tag{2.10}$$

where h_α is the enthalpy for species α.

In detonating flows, the chemical timescales can be significantly faster that the flow timescales where extreme pressures and temperatures are encountered. As a result, the sub-iterations are used to advance the chemical reaction system across the flow field time scale. The large rate of change of species in these environments can lead to significant errors if the sub-iterations are too generous. Thus, the source term computations for the reaction advancement are performed in one of two ways: 1) a so-called "rough" source term integration without sub-iterations and if necessary, 2) a complex source term integration using a double precision variable-coefficient ordinary

differential equation (DVODE) solver [37]. The latter method utilizes a class of general-purpose solvers for stiff ordinary differential equation (ODE) systems [125] with adjustable time-stepping to ensure error tolerances are met. In UTCOMP, the species reaction rates are computed under a constant pressure assumption, which is valid for at least one flow timestep, and for the sub-iteration of the flow timescale if DVODE is requested.

As the DVODE solver can be computationally expensive to evaluate throughout the domain, the rough source term is first computed by analytically solving Eqns. 2.7 and 2.10 across the full simulation timestep. A chemical timescale is computed from the rough solution of the energy and species source terms. In particular, the source term of a typically fast species, such as OH for hydrogen and hydrocarbon reactions, is used. The chemical timescale is defined as:

$$t_{chem} = \min\left(\frac{T}{\rho\dot{S}}, \frac{1}{\rho\dot{S_{\alpha*}}}\right), \tag{2.11}$$

where α^* is a fast representative species. If the simulation timestep is greater than 1% of t_{chem}, then the stiff ODE solver is used to advance the chemical reactions. The 1% threshold is conservatively used to ensure spurious overshoots and errors in species production rates are avoided.

In the canonical numerical simulations performed within this dissertation, the 9-species 19-reaction detailed chemical mechanism derived from Mueller et al. [192] is used to model the combustion of hydrogen H_2 and oxygen O_2 with a nitrogen N_2 diluter. The nine species consist of H_2, O_2, H_2O, H, O, OH, HO_2, H_2O_2, and N_2. The mechanism has been validated with a wide range of measurements and was generally found to agree with experimental data, such as ignition delay times in shock tubes, reaction behavior within flow reactors, and laminar flame speeds.

2.1.3 Finite volume method (FVM)

The UTCOMP solver resolves the governing equations on a discrete representation of the three-dimensional domain. Here, the flow geometry is discretized using a structured grid where each element is a rectangular cuboid and the surface normal direction of each face is aligned with one of the three Cartesian directions. The structured grid formulation allows for ease of implementation of high-order numerical methods that require expansive stencils. Each rectangular cuboid cell element represents a finite volume of flow governed by the conservation laws outlined in Sec. 2.1.1. Hence, the finite volume (FV) method is used to numerically enforce the conservation equations.

In the FV method, the flow variables are constant throughout the cell, and the integral form of the conservation equations is resolved. A cell-centered, collocated arrangement of the conserved variables $\mathcal{C}$ from the governing equations are computed: $\mathcal{C} = (\rho, \rho u, \rho v, \rho w, \rho E, \rho Y_\alpha)$. The rate of change in the conserved variables is given by the difference between the incoming and outgoing fluxes. Based on the treatment of the numerical method, strict conservation of the conserved variables is ensured and extendable to three dimensions. Further, the conservative approach permits accurately resolving the Rankine-Hugoniot condition for discontinuities – an important requirement for shock-containing flows [166].

2.1.4 Numerical schemes

The numerical fluxes of the conserved variables consist of convective and diffusive fluxes. The convective flux consists of the hyperbolic component of the Navier-Stokes equations, whereas the diffusive flux originates from the elliptic component. The convective fluxes need to be computed through numerical schemes that are shock-capturing in nature and properly resolve singularities or discontinuities within the domain. Inadequate treatment of shock waves can result in spurious oscillations

near these discontinuities which lead to non-physical flow properties and unstable simulations. On the other hand, the elliptic part of the NS equations works to stabilize the solution. Consequently, straight-forward symmetric central schemes can be used to represent the diffusive terms.

In UTCOMP, a 4^{th} order central difference scheme is used to evaluate the second derivatives and compute the diffusive flux terms. The 5^{th} order conservative weighted essentially non-oscillatory (WENO) local Lax-Friedrich (LLF) flux-splitting scheme is used for computing the non-linear convective fluxes [136]. ENO schemes adjust the local stencil by way of functional weights to compute the least oscillatory solution and switch to upwinding where necessary, such as near a shock. In this solver, the finite difference formulation (FD-WENO-LLF) is incorporated. Here, the fluxes are computed at the cell centers of the cells in the local stencil and reconstructed at the cell faces through interpolation [275]. In the finite-volume formulation (FV-WENO-LLF), the cell-averaged flow variables at the cell centers are interpolated first to the cell faces and then used to compute the fluxes. FD-WENO is less computationally expensive and suggested for use on smooth meshes (like in UTCOMP) whereas the FV-WENO approach is recommended for more complex meshes [275]. Furthermore, flux reconstruction is performed in characteristic variable space rather than in primitive or conservative space as this leads to fewer oscillations [275] and a generally less diffusive solution [78]. For further details of convective schemes within UTCOMP, and the performance of FD-WENO-LLF, the reader is referred to Ref. [78].

The non-linear scalar transport is calculated using a quadratic upstream interpolation for convective kinematics (QUICK) scheme [165]. Additional bounding of scalars is offered through the bounded QUICK (BQUICK) formulation [123] at the expense of computation cost. For the numerical simulations discussed within this dissertation, the QUICK scheme was found to be sufficient for ensuring species boundedness. Explicit forward time-stepping is performed using a 4^{th} order total-variation-diminishing

(TVD) Runge-Kutta scheme.

The solver is parallelized using message passing interface (MPI)-based domain decomposition in the first two Cartesian directions ($x_1 = x$ and $x_2 = y$ directions). Linear scalability has been demonstrated for up to 65,000 processors for similar three-dimensional problems.

2.1.5 Boundary condition treatment

In the UTCOMP solver, the boundary conditions are enforced through the treatment of so-called "ghost" cells which are padded around the domain in all three directions. The high-order WENO convective scheme requires three ghost cells beyond the domain boundary in each direction, resulting in six ghost cells in each direction. There are four classes of boundary conditions used in the simulations described in this dissertation: 1) wall, 2) periodic, 3) supersonic inflow/outflow, and 4) subsonic inflow/outflow.

For the wall boundary condition, the no-slip condition is enforced resulting in zero velocities of u, v, and w. The ghost cells are set with magnitude equal and sign opposite to the first three interior cells ("negative mirror") such that the velocity values at the location of the wall are zero. Zero-gradient density and species conditions are set by mirroring the first three cell values within the domain onto the ghost cells such that the gradient at the domain boundary is zero. The temperature of the ghost cells is also similarly set to zero-gradient for an adiabatic wall condition, or fixed to a user-defined value for an isothermal wall condition. In the canonical flow simulations, adiabatic wall conditions are used and wall heat transfer is neglected.

Periodic boundaries in computational domains with ghost cells are configured such that the thermodynamic state in the ghost cell replicates the values within the last set of cells near the opposing boundary. Thus, the transfer of information from one side of the periodic boundary to the other is handled through the ghost cells.

In the case of supersonic boundary conditions, the treatment of the ghost cells is fairly straightforward. An inflow boundary defined from an inflow file generated through prior sampling from an auxiliary simulation represents a time-varying boundary condition. If the plane-normal velocity at the inflow is supersonic, the inflow file contains the complete solution for all flow variables because all the flow characteristics (u and $u \pm c$) are positive and enter the domain. All the ghost cells replicate the solution contained within the inflow file. Similarly, if the plane-normal velocity at the outflow is supersonic, the flow characteristics all exit the domain, and the ghost cells are prescribed from the values of the last cell within the domain.

The existence of a subsonic flow-through boundary requires careful treatment because the flow characteristics are not all strictly positive and information must cross the domain boundary from either side. In the case of a subsonic inflow, the $u - c$ characteristic is negative and an upstream-running characteristic exits the domain through this inflow plane. Thus, the flow state at the inflow boundary must be partially computed by information within the domain. At a subsonic outflow, the $u - c$ characteristic enters the domain while the other two exit the domain. Here, the Navier-Stokes Characteristic Boundary Condition (NSCBC) method of Poinsot and Lele [228] is applied. The goal is to model time variations in the flow characteristics at the domain boundary. The ghost cells are set such that nonphysical flow features are not reflected back into the domain. A numerical far-field back pressure is implemented and the instantaneous thermodynamic state of the ghost cells deviates from the far-field condition to provide a partially non-reflecting boundary. High-order numerical schemes with reduced dispersion errors can encourage numerical instabilities and non-physical flow when the boundary conditions are not precisely enforced. This method allows for inflow and outflow boundary conditions where the flow is not strictly supersonic.

In UTCOMP, the numerical methods are configured for three-dimensional flow.

For one- and two-dimensional domains, the non-flow-through directions are set with periodic boundary conditions, a single cell within those directions (with associated ghost cells), and the numerical fluxes are not computed in these directions. Thus, the domain is homogeneous in the non-flow-through directions.

2.1.6 DNS and the high-fidelity approach

In the UTCOMP solver, the conservation equations (see Sec. 2.1.1) are represented exactly. For a DNS approach, the numerical representation of the domain, i.e. mesh, must be fine enough to resolve all the relevant length scales. In turbulent flows, the complete turbulence energy cascade should be captured [229], which requires that the cell size is at most twice the local turbulence length scale: the Kolmogorov length scale. In detonating flows, one aims to represent the critical length scale of the ZND detonation structure: the induction length. Powers and Paolucci [230] have shown through eigenvalue analysis of steady gas-phase detonations that the induction lengths can range from $\mathcal{O}(10\ \mu\text{m})$ for H_2-O_2 detonations to $\mathcal{O}(100\ \mu\text{m})$ for H_2-air detonations at atmospheric pressure. Furthermore, Mazaheri et al. [181] demonstrated that the flow field features continued to be refined as the computational resolution is extended into the thousands of numerical cells per induction and half-reaction zone lengths. However, these exercises are computationally feasible only with single-step chemical mechanisms and simplified geometries. Thus, even for canonical configurations, capturing the induction length with $\mathcal{O}(10^2$ cells) is not computationally tractable. The simulations of canonical flows detailed within this dissertation will lower the baseline pressure to promote a widened induction length, as induction length and half-reaction length are inversely proportional to this parameter. An operating pressure of half the atmospheric condition will be used, where flow phenomena relevant to detonative combustion continue to be present. Thus, the simulations typically do not resolve the shock-detonation structure fully and can be classified as *high-fidelity* numerical simu-

lations in the context of detonating flows. Further, the convergence of flow structures and detonation metrics (such as wave propagation speed and peak pressure rise) will be presented for validation purposes.

The UTCOMP solver with the aforementioned numerical methods has been extensively validated in the past for DNS simulations [157] and a variety of shock-containing flows, including scramjet isolators [80, 81, 158], scramjet combustors [68], nonequilibrium flows [79, 83, 159] and detonating flows [179].

2.1.7 Validation with detonation problems

The use of detailed chemical kinetics in the scope of turbulent detonations is a sparsely studied field. For this reason, this work utilizes a sequence of canonical flows to build confidence in the simulation tools and to ensure that the observed results are not determined by the choice of numerical methods. The section below thus progresses through simple flows of increasing dimension.

2.1.7.1 One-dimensional detonation

The one-dimensional configuration is modeled using a traditional shock tube configuration, using a semi-closed tube of length 0.2 m, as shown in Fig. 2.1. The shock tube is filled with premixed hydrogen and air at stoichiometric conditions at an initial pressure of 0.5 atm and temperature of 297 K. The grid used for this simulation is uniform at Δ x = 50 μm, with an analytic induction length of 398 μm at this condition. In order to drive the detonation, a region at the closed end of the tube is set to post-detonation conditions derived from the analytical solution. Following an initial transient period, the wave resembles the Zeldovich-von Neumann-Döring (ZND) detonation structure. The numerical shock front velocity, or the estimated Chapman-Jouguet velocity U_{CJ}, is calculated as 1946 m/s while the theoretical solution based on the assumption of equilibrium conditions post-detonation is 1954 m/s.

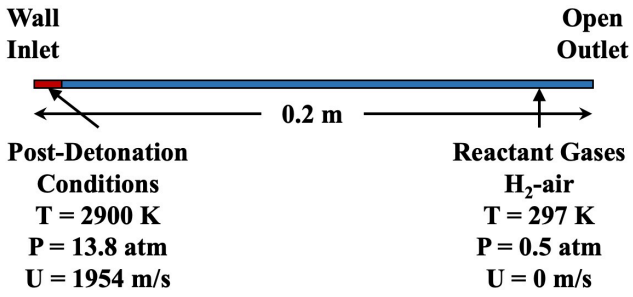

Figure 2.1: One-dimensional shock tube configuration.

Figure 2.2 shows the profile of Mach number, pressure, velocity, and temperature with respect to the shock wave location. It is seen that the pressure increases, due to compression, and accelerates the fluid, reaching a Mach number of 1.4, which is roughly the detonation speed scaled by the post-compression speed of sound. Since the detonation wave does not have back support, there is expansion leading to the reduction of pressure and speed. At the same time, chemical reactions are initiated leading to heat release and the progress of temperature toward its equilibrium value.

Figure 2.3 shows the species mass fractions in the same shock front coordinate. It is seen that past the shock, there exists a finite time before the fuel and oxidizer molecules break down to start the combustion process. After this point, there is rapid consumption of fuel molecules that pushes the mixture toward equilibrium. Note that the expansion of gases leads to a change in the local enthalpy that affects the equilibrium composition, which exhibits a gradual change after about 0.1 cm from the shock front.

The one-dimensional study shows that the compressible flow solver captures the correct post-detonation state as well as the structure of the detonation wave. Next, this approach is used with a two-dimensional flow.

2.1.7.2 Two- and three-dimensional channel detonation

Detonating flow in a confined channel is used to understand the detonability and chemistry mechanism of fuel mixtures. Here, both two-dimensional and three-

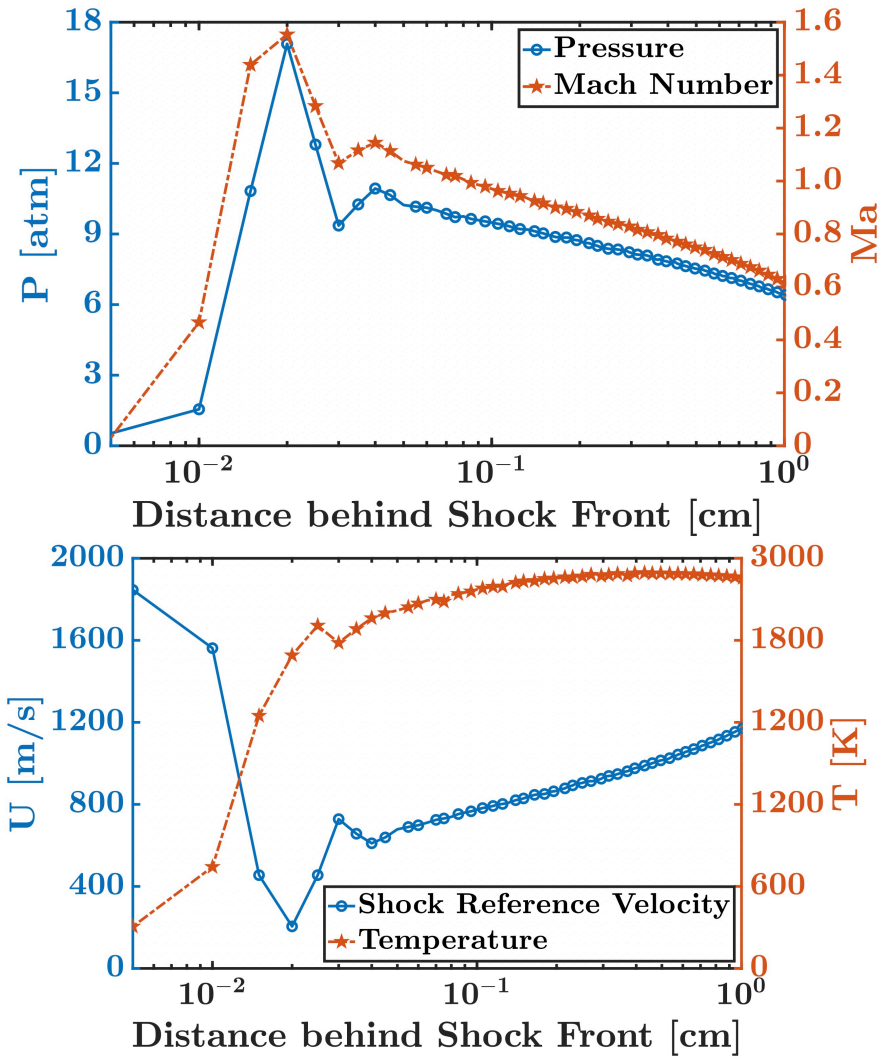

Figure 2.2: (Top) Pressure and Mach number and (bottom) temperature and velocity across the detonation front in the shock reference frame for the one-dimensional configuration.

dimensional configurations are considered. The flow domain consists of a rectangular box with walls on the top and bottom as well as in the spanwise directions. Figure 2.4 and Fig. 2.8 show the flow domains used for this study. The domain is initially split into regions, with the left region filled with a one-dimensional detonation solution obtained from the simulations described in Sec. 2.1.7.1, and the right region filled with the premixed stoichiometric fuel/oxidizer mixture at ambient conditions. For both cases, local high-temperature sparks consisting of three rectangular or cubic regions

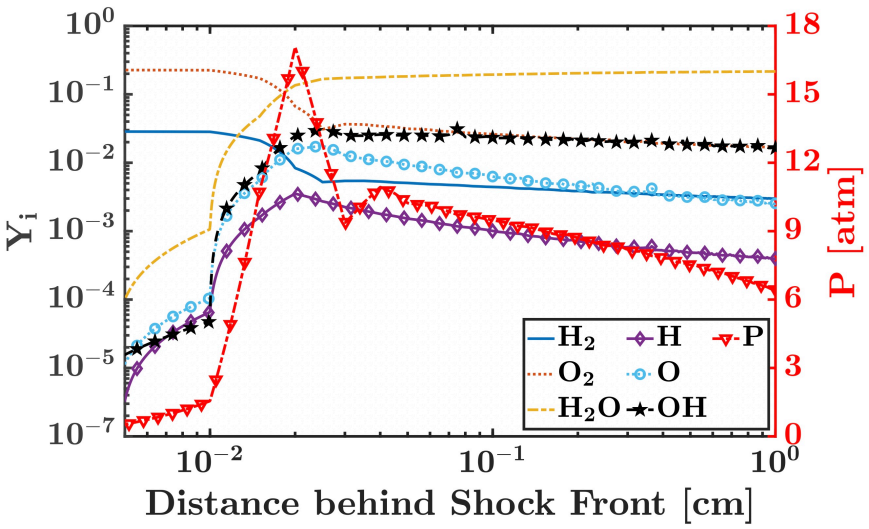

Figure 2.3: Transient response of the species and pressure behind the detonation front for the one-dimensional configuration.

are initialized to provide disturbances to the flow field. As the flow evolves, these regions trigger the formation of transverse waves, which reflect from the walls to form triple points inside the domain. These interacting waves enhance the local pressure and temperature of the fluid leading to the initiation of strong detonations.

For this study, two different cases were considered with the two-dimensional configuration: a) 0.5 atm premixed reactants, and b) 1 atm premixed reactants. The grid is uniform with $\Delta x = \Delta y = 10$ μm and $\Delta x = \Delta y = 5$ μm for the 0.5 atm and 1.0 atm cases, respectively. The induction length derived from the analytic solution for the 1 atm case is 246 μm. Figure 2.5 shows the evolution of the detonation front, with the clear presence of high-pressure concentrations that denote the existence of the triple points. Such channel detonations are often visualized using a soot foil plot [211], which is a history of peak pressure along the streamwise direction. Figure 2.5 shows the formation of regular fish-scale-like structures that visualize the evolution of the triple points. Depicted in Fig. 2.6, channel detonation at the 1 atm ambient condition was simulated using the Mueller mechanism [192] incorporated within the UTCOMP solver and is compared to the Modified Jachimowski mechanism evaluated

by Shimizu et al. [274]. The results from the present study match very well with legacy data in terms of the detonation cell size. In Fig. 2.6, a detailed view of the detonation structure at the 0.5 atm ambient condition shows the presence of four triple points across the stream-normal direction, and slight corrugation of the detonation front due to the interaction of transverse waves.

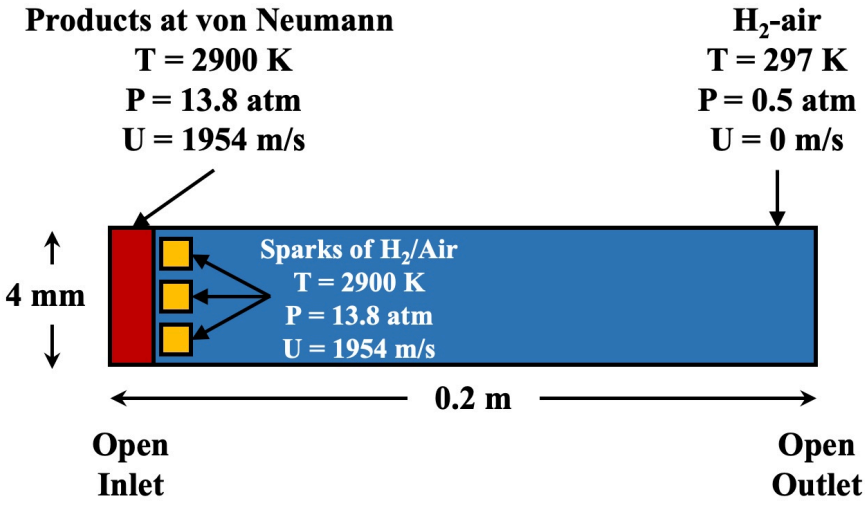

Figure 2.4: Two-dimensional channel configuration with disturbance sparks to perturb the detonation wave.

The shock front velocity and induction length profiles within the channel are of particular interest to two-dimensional channel detonations, as the existence of triple points due to shock wave reflections alter their values from the traditional ZND profile. The variation of the shock front velocity of Fig. 2.7 provides information into how the wave front is distorted due to local accelerations of the front. For this computation, the shock front is denoted by the location where pressure rapidly increases from the pre-detonation ambient condition up to a threshold value, calibrated as 130% of the ambient pressure. Ahead of the wave, the pressure is largely uniform as shown in Fig. 2.6. Thus, the location of the shock front can be systematically determined using this procedure. At every streamwise location of the shock front, the shock front velocity can be extracted as a function of wall-normal location, thereby providing a one-dimensional profile for the front velocity at each timestep.

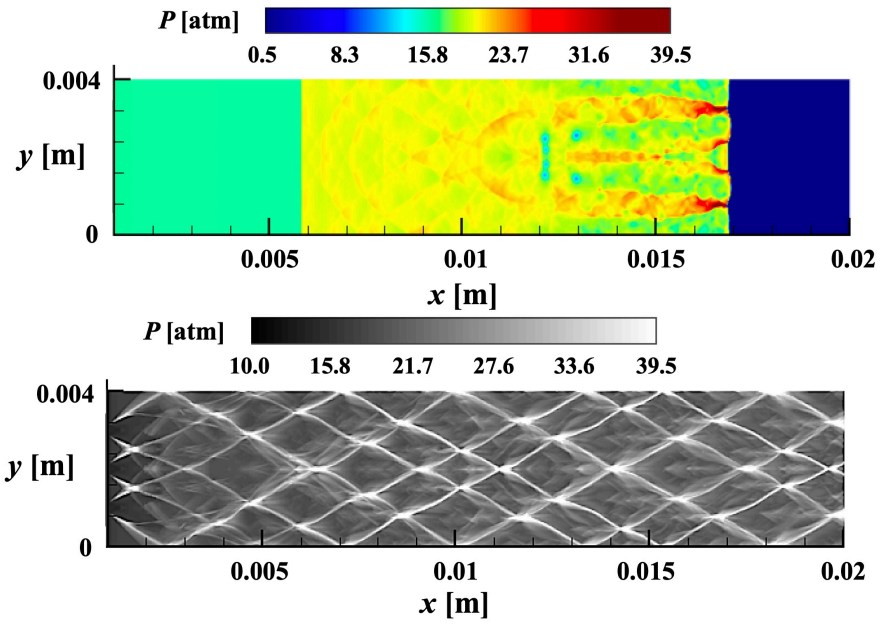

Figure 2.5: (Top) Instantaneous pressure contour and (bottom) maximum pressure history used to study the detonation cell size of H_2/air chemistry at 0.5 atm.

The induction length is defined in this work as the streamwise distance between the shock front and the reaction front. The reaction zone is characterized using a traditional definition applied by Powers et al. [230] and is defined as the location where the temperature gradient dT/dx reaches its maximum value in the streamwise direction. Alternative definitions, such as threshold values for the evolution of radicals, may be used, and similar results are obtained.

Figure 2.7 provides contour plots of the shock front velocity U_{CJ} and the induction length ℓ for a premixed two-dimensional channel, respectively, at 0.5 atm, displayed previously in Fig. 2.5. The results are in agreement with the theoretical analysis of the cellular detonation structure, as well as past numerical analysis for premixed channel detonations [179]. The shock front locally accelerates following the collision of two triple points, distorting the shock front and creating a "pinch-point" in the shock front curvature. The front velocity within the cellular structure gradually decays until subsequent triple point collisions accelerate the wave front. The triple point

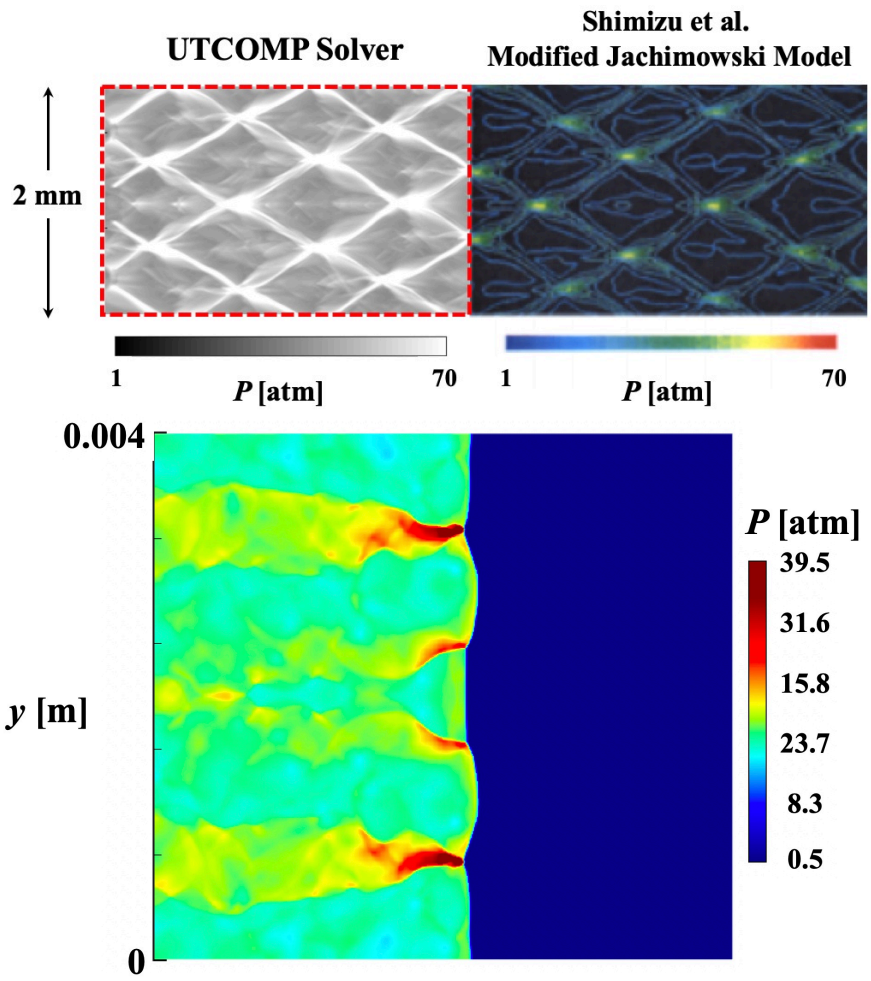

Figure 2.6: (Top) Comparison of detonation cell size using the Mueller [192] and Modified Jachimowski mechanisms [274]. (Bottom) Detailed view of the triple point structure at the detonation front.

represents a region of high pressure and temperature along the shock front, highlighted by increased wave front velocity. The induction length contour plot shows that the smallest induction lengths are located in regions immediately following the collision of two triple points, as the shock front and reaction zone reattach. Following the collision, the induction length increases by nearly an order of magnitude as the shock and reaction front locations separate in the streamwise direction. An expansion region behind the triple point collision serves to reduce the local temperature and pressure of the flow. Each collision of triple points serves to restore the detonation wave's strength, as the induction length and shock front velocity more closely resemble the

one-dimensional ZND profile in the local vicinity of a triple point collision. Thus, in two-dimensional and three-dimensional channel detonations, the shock front velocity and induction length vary in both the streamwise and wall-normal directions due to the interaction of triple points and reflected shock waves created by the initial disturbances in the flow field.

For the three-dimensional case initiated using the spark structure shown in Fig. 2.8, the wave structure shown in Fig. 2.9 provides some interesting features. The grid is uniform with $\Delta x = 10$ μm, $\Delta y = 100$ μm, and $\Delta z = 200$ μm. In the streamwise direction, there are interacting waves that form an isoline of high temperature and pressure, an extension of the triple points seen in the two-dimensional configuration. As seen in Fig. 2.9, the spatial variation of the flow features is due to the reflection of shocks and triple points from the channel walls. As a result, the additional dimension leads to a highly irregular wave front with distortion due to local flow acceleration. The three-dimensional detonation wave will be used in the simulations discussed below as an inflow condition (discussed in detail in the following section).

2.1.8 Solver summary

This section introduced and detailed the in-house compressible flow solver UTCOMP which will be used in Chap. III for the study of non-idealities in canonical configurations. The structured-grid solver enables high-order numerics; the 5^{th} order FD-WENO-LLF scheme used for computing the non-linear convective fluxes [136, 275] and the non-linear scalar terms are calculated using a QUICK scheme [165]. A 4^{th} order central scheme is used to calculate the diffusion terms and explicit time-stepping is performed using a 4^{th} order TVD Runge-Kutta scheme. The verification cases on one-, two-, and three-dimensional shows that the UTCOMP solver successfully captures the unsteady detonation process. In 1D, the von Neumann pressure and wave speed are captured well within 1% of the theoretical expectation. The two-

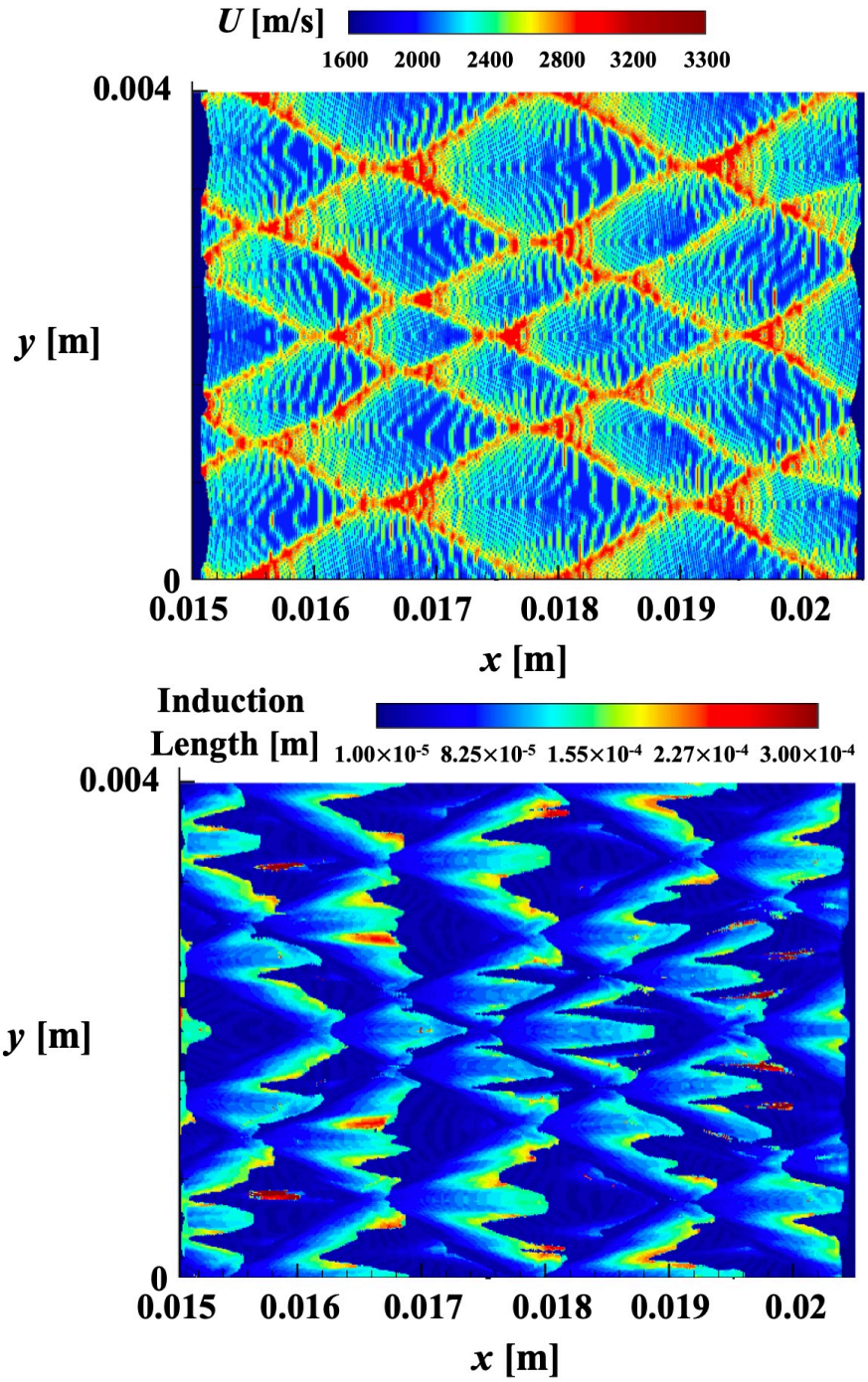

Figure 2.7: (Top) Shock velocity (U) and (bottom) induction length in the premixed two-dimensional channel.

dimensional detonation channel simulations highlight the cellular structure, which is representative of the small-scale dynamics in the induction region consisting of triple points, transverse waves, and the Mach wave. The solver successfully captures these

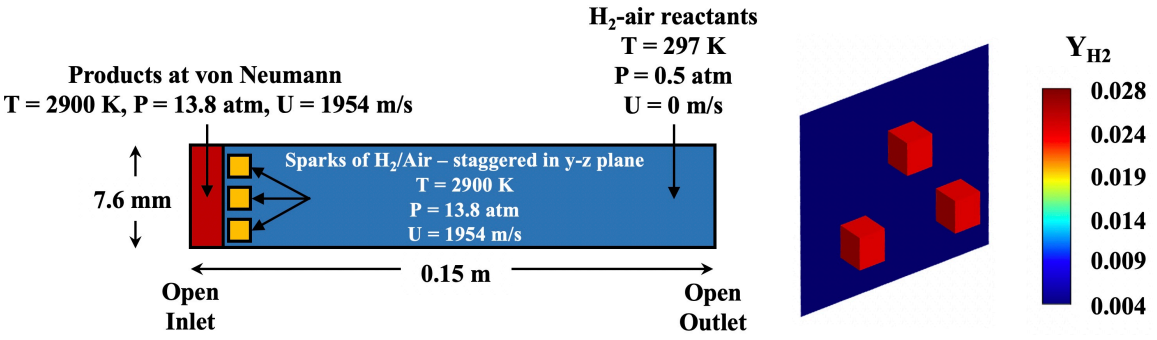

Figure 2.8: Three-dimensional channel configuration with staggered disturbance sparks to perturb the detonation wave.

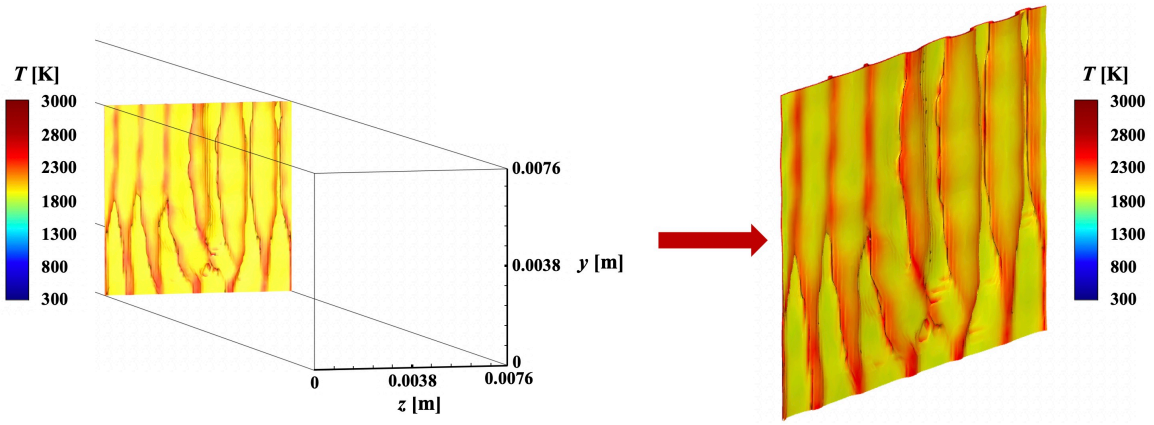

Figure 2.9: Three-dimensional channel detonation wave front as it nears the end of the pre-detonator tunnel; isocontour of $Y_H = 0.0025$, colored by temperature.

dynamics and the cell size, a measure of reaction rate at the wavefront, matches previous numerical studies with a different H_2-air mechanism thereby validating the solver performance in detonation environments. Similarly, the unsteady nature of the detonation wave is visualized by the velocity and induction length profiles, which show that the collision of the triple points serves to tighten the induction and reaction zones. The three-dimensional study shows that unsteady detonation can be established in a full-dimensioned case.

2.2 UMReactingFlow Solver

The next section presents the fundamental details and assumptions of the in-house compressible flow solver UMReactingFlow. The solver has been adapted for the simulation of full-scale RDE simulations presented in Chaps. IV and V.

2.2.1 Conservation laws and principles

Like with the UTCOMP solver, the Knudsen number of the flows of interest is assumed to be negligible and they are assumed to be in the continuum regime. The governing equations of fluid flow consist of mass, momentum, and energy conservation equations supplemented by the species conservation equations that incorporate a source term due to chemical reactions.

2.2.1.1 Conservation of mass

The first conservation principle concerns mass conservation. The mass within the thermodynamic system cannot change with time. The Eulerian formulation of the conservation principle is given as:

$$\frac{\partial \rho}{\partial t} + \frac{\partial \rho u_i}{\partial x_i} = 0, \tag{2.12}$$

where ρ is the fluid density, t is the unit of time, x_i is the spatial position in the i-th direction of three-dimensional space ($i = 1, 2, 3$), and u_i is the fluid velocity in the i-th direction.

2.2.1.2 Conservation of momentum

The second conservation principle is the momentum balance derived from Newton's second law which states that the sum of external forces on a fluid element is equal to the time rate of change of momentum. In Eulerian form, the conservation

principle is:

$$\frac{\partial \rho u_i}{\partial t} + \frac{\partial \rho u_i u_j}{\partial x_j} = -\frac{\partial P}{\partial x_i} + \frac{\partial \tau_{ij}}{\partial x_j}, \tag{2.13}$$

where x_j is the spatial position in the j-th direction of three-dimensional space ($j = 1, 2, 3$), u_j is the fluid velocity in the j-th direction, P is the fluid pressure, and τ_{ij} is the viscous stress tensor. The fluids and gases considered in these simulations are Newtonian fluids where the viscous shear stress is proportional to the strain rate. Thus, it is given by:

$$\tau_{ij} = -\frac{2}{3}\mu \frac{\partial u_k}{\partial x_k}\delta_{ij} + \mu\left(\frac{\partial u_j}{\partial x_i} + \frac{\partial u_i}{\partial x_j}\right), \tag{2.14}$$

where x_k is the spatial position in the k-th direction of three-dimensional space ($k = 1, 2, 3$) and u_k is the fluid velocity in the k-th direction. The fluid dynamic viscosity μ is the fluid viscosity evaluated from a tabulated temperature fit over the solution of collision integrals [65] using the local fluid composition and flow temperature T. The momentum balance formulation does not include body forces f_i such as gravity. The gravity-driven buoyancy force is typically neglected because the system is dominated by convective forces and its effect would be minimal on the flow solution.

2.2.1.3 Conservation of energy

The third conservation principle is the energy balance which ensures that the total energy in the thermodynamic system is constant. The conservation of energy can be expressed in multiple ways, but the total energy is used in this approach. The total energy e_t is a sum of the sensible internal energy e_s, the chemical energy due to formation, and the kinetic energy K and is given as:

$$e_t = e_s + \sum_{k=1}^{N} \Delta h_{f,k}^0 Y_k + K = \left(\int_{T_0}^{T} c_p dT - \frac{P}{\rho} \right) + \sum_{k=1}^{N} \Delta h_{f,k}^0 Y_k + \frac{1}{2} u_i u_i, \tag{2.15}$$

where c_p is the specific heat capacity at constant pressure, $h_{f,k}^0$ is the enthalpy of formation of species k, and Y_k is the mass fraction of species k. The specific heat capacity, enthalpy, specific heat ratio, and transport properties are computed as a function of temperature using NASA polynomial fits [182]. Assuming no radiation or external body forces on the fluid, the transport equation for the total energy is given in Eulerian form:

$$\frac{\partial \rho e_t}{\partial t} + \frac{\partial \rho u_j h_t}{\partial x_j} = \frac{\partial}{\partial x_j} \lambda \frac{\partial T}{\partial x_j} + \frac{\partial \tau_{ij} u_i}{\partial x_j}, \tag{2.16}$$

with the mixture total enthalpy (sensible, chemical, and kinetic) defined as $h_t = e_t + P/\rho$, thermal conductivity λ, and temperature T. The term $\lambda \frac{\partial T}{\partial x_j}$ represents the heat diffusion rate given by Fourier's law, where λ is evaluated from the Prandtl number $Pr = \frac{\mu c_p}{\lambda}$, a relation between heat and momentum diffusion. For the simulations within this dissertation, the Prandtl number is set to 0.72, a typical value for turbulent gases [315] and usually lies within the range of 0.7 to 1.0. For liquids, the Prandtl number can be an order of magnitude higher. The viscosity and thermal conductivity for each species are fit as a function of temperature and pressure to reduce computational cost.

2.2.1.4 Conservation of species

With reacting flows, a scalar conservation equation for each fluid species k with mass fraction Y_k must be enforced. The scalar transport equation is given by:

$$\frac{\partial \rho Y_k}{\partial t} + \frac{\partial \rho u_j Y_k}{\partial x_j} = \frac{\partial}{\partial x_j} \rho D \frac{\partial Y_k}{\partial x_j} + \Omega_k, \tag{2.17}$$

where D is the mass diffusivity, which is assumed to be equal for all species and taken as the mixture-averaged value weighted by species composition, and Ω_k is the production source term due to chemical reactions for the k-th species. The species production source term introduces numerical stiffness to the governing equations, due to the presence of very fast chemical timescales (in comparison to the flow timescales) in detonating flows.

Equations 2.12, 2.13, 2.16, and 2.17 together form the Navier-Stokes (NS) governing equations of fluid flow. The system of equations is closed using the ideal gas equation of state.

2.2.2 Chemical reaction treatment

The change in the species composition is driven by the production source term Ω_k. In non-premixed combustion and particularly with detonating flows, a wide range of species compositions is encountered under extreme temperature and pressure environments. Thus, capturing the combustion processes under these conditions requires the use of detailed chemical kinetics. The computation of the source term can introduce numerical stiffness due to the very fast timescales of species within detailed chemical kinetic models. In practical RDEs, the use of high-order hydrocarbons and industry-standard fuels is necessary (such as jet fuel and rocket propellants). Thus, the incorporation of detailed chemistry for these hydrocarbon mechanisms can be computationally intractable, and the algorithms used to compute the source term is critical.

In UMReactingFlow, operator splitting is utilized to compute the reaction rates and transport equation source term. The chemical timescale is assumed to be sufficiently smaller than the flow timescale (which is often the case for detonation) and the flow is "frozen" during the chemistry advancement. The fluid element is at a given thermodynamic energy state, and the chemistry locally advances toward equilibrium.

Similar to UTCOMP, sub-iterations are used to integrate the species' production rates over the flow field timescale. In each sub-iteration, the sub-timestep is selected such that the mass fraction of each species does not change by *more than* 5% from its previous state, thereby limiting the timestep even in the presence of rapidly-evolving species (such as intermediary radical species) and preventing the overshoot of species production. Further, the sub-timestep is also limited if a rapidly-evolving species is nearing complete consumption.

For a multi-step reaction with N_S species and N_R reactions, the change in the species composition due to reactions is given by:

$$\Omega_k = \sum_{l=1}^{N_R} M_k \left(\nu''_{k,l} - \nu'_{k,l}\right) \left(\Pi_{f,l} - \Pi_{b,l}\right), \tag{2.18}$$

where $\nu'_{k,l}$ and $\nu''_{k,l}$ are the stoichiometric coefficients of the reactants and products, respectively, for the l-th reaction and k-th species and $\Pi_{f,l}$ and $\Pi_{b,l}$ are the forward and backward molar production rates for the l-th reaction. These are computed as:

$$\Pi_{f,l} = k_{f,l} \prod_{k=1}^{N_S} [A]_k^{\nu'_{k,l}}, \tag{2.19}$$

$$\Pi_{b,l} = k_{b,l} \prod_{k=1}^{N_S} [A]_k^{\nu''_{k,l}}, \tag{2.20}$$

where the forward and backward reaction rate constants of the l-th elementary reaction are $k_{f,l}$ and $k_{b,l}$, respectively, and the mole fraction of species k is $[A]_k$. The forward rate constant is of the modified Arrhenius form and the reverse rate constant is computed from the forward rate constant and the equilibrium rate constant K_C.

In order to decrease the computational cost of the species production rates, a novel reformulation of the rate constant and production rate calculations into matrix form by Barwey and Raman [15] is used. By recasting the problem into a series of matrix multiplications, the computations are enabled for more efficient GPU ac-

celeration with maximized throughput. Thus, detailed chemical kinetics, consisting of the source term Ω_k evaluation, stiff time integration, and thermodynamic gas properties computations, are offloaded to the GPU using the UMChemGPU library: in-house CUDA-based modules for compatibility with heterogeneous computing platforms. The reader is referred to Refs. [13, 15, 26] for details regarding the detailed chemistry treatment. The performance increase afforded by these algorithms allows the investigation of stiff chemical mechanisms with high-order hydrocarbon fuels and $\mathcal{O}(100)$ reactions in full-scale three-dimensional systems.

2.2.2.1 Modification of NASA polynomial fits

Full-scale RDE and scramjet systems feature non-premixed injection schemes with complex flow paths. Thus, it is common for the formation of compression and expansion waves as the propellant streams traverse the system and flow through the combustion chamber. In particular, the exit flows of micronozzles and bluff body regions can result in strong expansion fans that result in a rapid reduction in flow temperature and pressure. With nominal propellant feed temperatures of 300 K, the fluid temperature in these expansion regions can fall well below this value - and below the typical 200 K minimum bound of the NASA polynomial fits (henceforth referred to as the NASA polynomials minimum temperature $T_{min,N}$) for thermodynamic properties. The typical treatment of the fluid in these regions is to clip the gas temperature at the NASA polynomials minimum temperature. However, this approach can lead to a discrepancy between the internal energy of the gas and the gas temperature, where the internal energy is typically a monotonic function of temperature. Furthermore, the flow field is artificially limited to the NASA polynomials minimum temperature while the physics dictated by the governing equations would require a lower gas temperature.

In UMReactingFlow, an alternative approach is used, where the specific heat ca-

pacity at constant pressure (c_p) of the gas is limited to the mixture-averaged value at the NASA polynomials minimum temperature, but the enthalpy is computed through a linear offset relative to a reference temperature T_{ref} (equal to $T_{min,N}$) rather than from the NASA polynomials directly. This approach is required because the specific heat capacity is computed from a quartic function which has the tendency to become unstable near the lower bound, i.e. below the NASA polynomials minimum temperature. As a result, the use of the NASA polynomial coefficients below the minimum bound can result in non-physical values for specific heat, enthalpy, and specific heat ratio. Note that the NASA polynomials provide the sum of the *sensible* and *chemical* enthalpies. In this approach, the specific heat capacity is fixed to the value at the NASA polynomials minimum temperature if the gas temperature is below this value. The specific heat capacity of the k-th species is given as:

$$\frac{Mc_{p_k}(T)}{R} = \begin{cases} a_{1,k} + a_{2,k}T + a_{3,k}T^2 + a_{4,k}T^3 + a_{5,k}T^4 & \text{if } T \geqslant T_{min,N} \\ a_{1,k} + a_{2,k}T_{min,N} + a_{3,k}T_{min,N}^2 + a_{4,k}T_{min,N}^3 + a_{5,k}T_{min,N}^4 & \text{if } T < T_{min,N} \end{cases} \tag{2.21}$$

where R is the universal gas constant, M is the molecular weight, T is the gas temperature, and the coefficients a_1 to a_5 are obtained from NASA polynomial fits [182]. Subsequently, enthalpy can be directly computed from the NASA polynomial fits if $T \geqslant T_{min,N}$:

$$\frac{Mh_k(T)}{RT} = \begin{cases} a_{1,k} + \frac{a_{2,k}}{2}T + \frac{a_{3,k}}{3}T^2 + \frac{a_{4,k}}{4}T^3 + \frac{a_{5,k}}{5}T^4 + \frac{a_{6,k}}{T} & \text{if } T \geqslant T_{min,N} \end{cases} \tag{2.22}$$

However, if $T < T_{min,N}$, the enthalpy is computed in relation to a reference enthalpy h_{ref_k} at the reference temperature $T_{ref} = T_{min,N}$ and the fixed value of specific heat $c_{p_k,fixed}$. Thus, the sensible enthalpy

$$\frac{Mh_{ref,k}(T_{ref})}{RT_{ref}} = a_{1,k} + \frac{a_{2,k}}{2}T_{ref} + \frac{a_{3,k}}{3}T_{ref}^2 + \frac{a_{4,k}}{4}T_{ref}^3 + \frac{a_{5,k}}{5}T_{ref}^4 + \frac{a_{6,k}}{T_{ref}} \tag{2.23}$$

$$h_k(T) = h_{ref,k}(T_{ref}) + \int_{T_{ref}}^{T} c_{p_k,fixed} dT \tag{2.24}$$

The internal energy $e_k(T)$ is related to the enthalpy as:

$$e_k(T) = h_k(T) - \frac{RT}{M} \tag{2.25}$$

2.2.3 Finite volume method (FVM)

The UMReactingFlow solver resolves the governing equations on a discrete representation of the three-dimensional domain. The geometry is discretized through an unstructured mesh with polyhedral cells. Thus, the mesh is formed through a tessellation of irregular patterns. The propellant flow paths, injectors, and downstream flow control devices can involve complex geometries. Thus, an unstructured grid configuration allows the mesh to capture these complex geometries most efficiently with the fewest number of cells. Consequently, the number of degrees of freedom of a geometry represented through unstructured cells is reduced compared to a structured configuration with a similar representative cell size.

For this reason, the finite volume framework of OpenFOAM [109, 135] is the basis of UMReactingFlow, as it offers open-source tools for solving partial differential equations on complex geometries. Furthermore, it is imperative that the workflow from physical geometry to numerical simulation is optimized. For an arbitrary geometry represented in a computer-aided design (CAD) document, an unstructured mesh can be generated through the use of the OpenFOAM tool snappyHexMesh. Mesh topology (i.e., the bounding surfaces of the geometry) is extracted from the CAD document

through a meshing tool, such as Ansys Mesher [8] or Gmsh [100], with polyhedral cell elements with a resolution finer than the target internal mesh resolution of the geometry. The mesh topology is presented to snappyHexMesh to generate an internal mesh with refinement regions placed throughout the geometry as needed, such as near the injectors and other intricate flow paths. The snappyHexMesh utility generates three-dimensional meshes primarily containing hexahedra automatically from triangulated surface geometries in Stereolithography (STL) format. While the mesh topology is the "ground truth" of the geometry, the mesh generated by snappyHexMesh approximately conforms to the surface by iteratively refining a starting mesh and morphing the resulting split-hex mesh to the surface. Additionally, cell layers can be added to resolve flow-surface interactions. This approach provides a relatively fast and robust mesh for use in the simulation of complex combustor systems, such as RDEs and scramjets.

Each polyhedral cell represents a finite volume of flow governed by the conservation laws outlined in Sec. 2.2.1. The conserved quantities and the thermodynamic state of each cell are attributed to the centroid of each cell. The transported conserved quantities are: $\mathcal{Q} = (\rho, \rho\mathbf{u}, \rho E, \rho Y_k)$. Special care must be taken to ensure the conservation of these quantities in an unstructured mesh configuration through the selection of numerical schemes.

2.2.4 Numerical schemes

The OpenFOAM unstructured finite volume framework is suitable for a variety of flow problems but is generally limited to lower-order methods (second-order discretization, for instance). This is because unstructured meshes can make the use of the larger stencils required by higher-order methods difficult as the irregular pattern of the cells complicates the data access of nearby cells beyond the adjacent cells that share a face.

The convective flux is computed through an approximate Riemann solution which minimizes dissipation while preserving monotonicity across the discontinuities found in the complex flowfields of shock-dominated flows, like those in RDEs. A Monotonic Upstream-centered Scheme for Conservation Laws (MUSCL)-based Harten-Lax-van Leer-Contact (HLLC) approximate Riemann solver [18, 299] is utilized due to the low computational cost and ability to model both Riemann and contact waves. A minMod interpolation limiter is utilized in the presence of shocks and discontinuities to maintain a non-oscillatory solution. Further, to reduce the errors during interpolation and flux computation at the faces, the primitive variables $\mathcal{U} = (\rho, \mathbf{u}, e, Y_k)$, rather than the conservative variables, are interpolated to the face prior to flux reconstruction. This ensures the sum of species mass at the cell face is equal to ρ and all the passive scalars travel at the same contact speed. Further, this limits dispersion errors due to discretization [298]. The convective flux method is second-order accurate for unsteady problems.

The viscous terms are computed through a Kurganov Noelle Petrova (KNP) formulation that is nominally second-order accurate. An explicit second-order Runge-Kutta time integration scheme is used to advance the governing equations. The solver is parallelized using MPI-based domain decomposition. The decomposition of complex geometries is performed through OpenFOAM tools and the Scotch library to ensure that cell distribution among MPI ranks is as even as possible. In-house CUDA-based modules are used to offload the computationally intensive subroutines for the flux and chemistry computation stages. The partition between CPU and GPU in the UMReactingFlow used for the numerical simulations presented within this dissertation is outlined in Fig. 2.10. For complete details of the solver and its development, including the numerical methods, detailed chemistry treatment, GPU acceleration, and its performance, the reader is referred to Refs. [26] and [15].

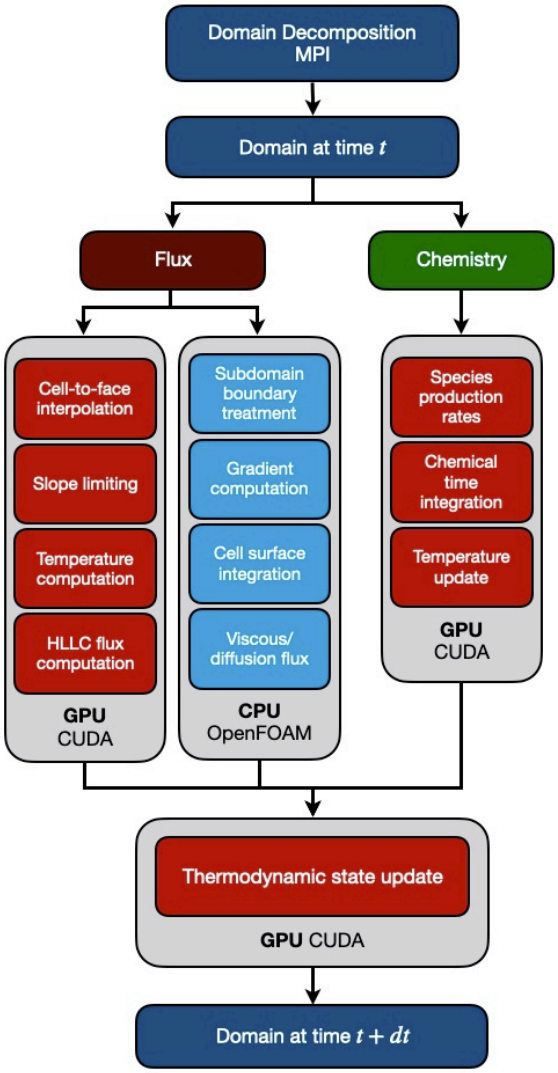

Figure 2.10: Flow chart of the major processes within UMReactingFlow and the partition between CPU and GPU subroutines used for the simulations presented within this dissertation.

2.2.5 The effect of numerics on turbulence

The numerics used in the simulation of complex reacting systems must ensure that the turbulence is captured properly. RDEs are mixing-limited and turbulent mixing is important in the quality of the fuel/oxidizer mixture prepared for combustion. Here, the system contains both high-speed shock-containing flows as well as turbulent jet mixing. With compressible fuel injection, mixing can become suppressed leading to poor device performance and combustion efficiencies [276].

To this end, the numerical scheme should balance stability in an unsteady environment through its shock-capturing ability, while preserving the turbulent kinetic energy with the flow. As a test case for the latter, DNS of compressible homogeneous isotropic turbulence (HIT) is performed for a set of numerical schemes - skew-symmetric central [128, 227], Harten-Lax-van Leer-contact (HLLC) [18], and the advection upstream splitting method flux difference and vector (AUSMDV) splitting [307] formulations.

The three-dimensional Navier-Stokes equations are solved on a cubic domain of length $x_i = 2\pi$ and periodic boundary conditions in all three directions. The decaying HIT is represented on both a uniform structured mesh and an unstructured mesh with tetrahedral elements. The structured mesh features 64^3 cells with a resolution of $\Delta x_i = 2\pi/64$ and the unstructured mesh has 32 edge elements along each direction with a mean resolution similar to that of the uniform grid ($\Delta \bar{x_i} = 0.1064$). The unstructured mesh features a maximum skewness of 0.425. Comparative visualization of the structured and unstructured meshes is given in Fig. 2.11. The unstructured mesh configuration contributes to the mesh skewness which can alter the turbulence representation, as will be demonstrated in the forthcoming examples.

The initial condition for HIT consists of a random solenoidal velocity field with an energy spectrum of the form:

$$E(k) = \frac{16}{3}\sqrt{\frac{2}{\pi}} M_{t,0}^2 c^2 \frac{k^4}{k_0^5} \exp\left(-2\left(\frac{k}{k_0}\right)^2 \right), \tag{2.26}$$

where $M_{t,0}$ is the turbulent Mach number, c is the sound speed, and k_0 is the most energetic wavenumber taken as $k_0 = 4$ here. The turbulent kinetic energy in the wave number range (k_a, k_b) is defined as:

$$K_{k_a,k_b} = \int_{k_a}^{k_b} E(k)\, dk = \frac{3u_{rms,0}^2}{2}, \tag{2.27}$$

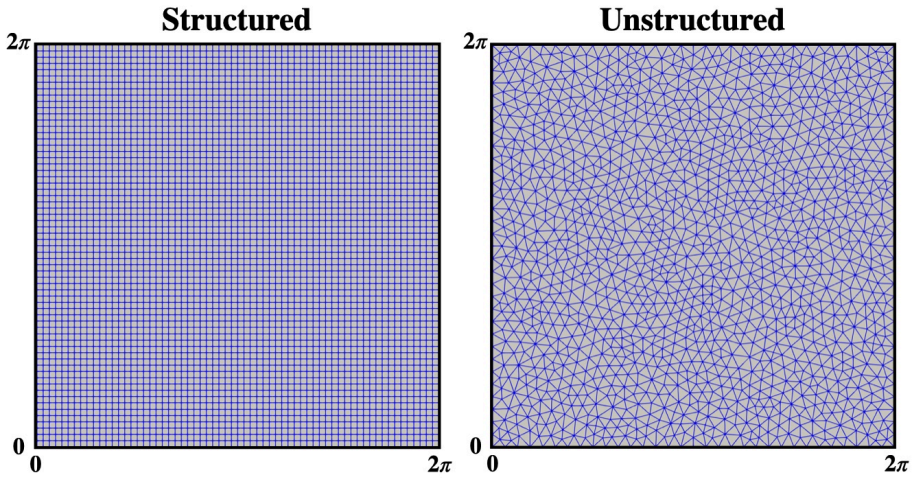

Figure 2.11: Planar slice of the three-dimensional meshes employed for the HIT simulations. These serve as a comparison of a structured mesh with 64 cells in each direction and an unstructured mesh with tetrahedral elements and 32 edge elements along each direction.

where the r.m.s. (root mean square) velocity u_{rms} is given as:

$$u_{rms} = \sqrt{\frac{\langle u_i u_i \rangle}{3}}, \tag{2.28}$$

The defining characteristics of the HIT operating condition are the turbulent Mach number - a parameter that determines compressibility - and the Taylor-scale Reynolds number Re_λ. The r.m.s. velocity can be related to the turbulent Mach number as:

$$M_{t,0} = \frac{\sqrt{3} u_{rms}}{\langle c \rangle}, \tag{2.29}$$

and the Taylor-scale Reynolds number as:

$$\mathrm{Re}_\lambda = \frac{u_{\mathrm{rms}} \lambda}{\langle \nu \rangle}, \tag{2.30}$$

where λ is the Taylor microscale, and ν is the kinematic viscosity. The Taylor microscale is computed as a function of the kinematic viscosity and the dissipation rate ε as:

$$\lambda = u_{\text{rms}}(15\nu/\varepsilon)^{1/2}, \tag{2.31}$$

The form of the energy spectrum provides an initial Taylor microscale $\lambda_0 = 2/k_0$. The dissipation rate in the wave number range (k_a, k_b) is:

$$\varepsilon_{k_a,k_b} = \int_{k_a}^{k_b} 2\nu k^2 E(k)\, dk, \tag{2.32}$$

The eddy turnover time is computed as:

$$\tau = \frac{2}{k_0 u_{\text{rms}}} = \frac{2\sqrt{3}}{k_0 M_{t,0}\langle c \rangle}, \tag{2.33}$$

Now, the energy spectrum, the turbulent Mach number, the r.m.s. velocity, the turbulent kinetic energy, the Taylor-scale Reynolds number, and the viscosity are fixed. The domain is filled with air and the initial temperature and pressure fields are taken to be constant, with $\gamma = 1.398$.

2.2.5.1 HIT with $M_{t,0} = 0.3$ and $Re_{\lambda,0} = 30$

DNS simulations of compressible isotropic turbulence is first performed with $M_{t,0} = 0.3$ and $Re_{\lambda,0} = 30$ using both the structured and unstructured grids. The UMReactingFlow solver is used with a skew-symmetric central scheme described in Refs. [128, 227], HLLC scheme [18], and AUSMDV [307]. The solutions are compared against a spectral simulation performed using a specific volume formulation, reproduced from Ref. [128]. The non-dimensional quantities of kinetic energy, pressure, temperature, and specific volume are shown in Fig. 2.12. The non-dimensional profiles reveal that the central scheme on the structured mesh captures the dynamics of the spectral scheme well. In general, the unstructured meshes result in profiles with further deviation from the spectral solution in comparison to the solutions from the structured counterpart. The profiles from the HLLC scheme capture the dynamics of the spec-

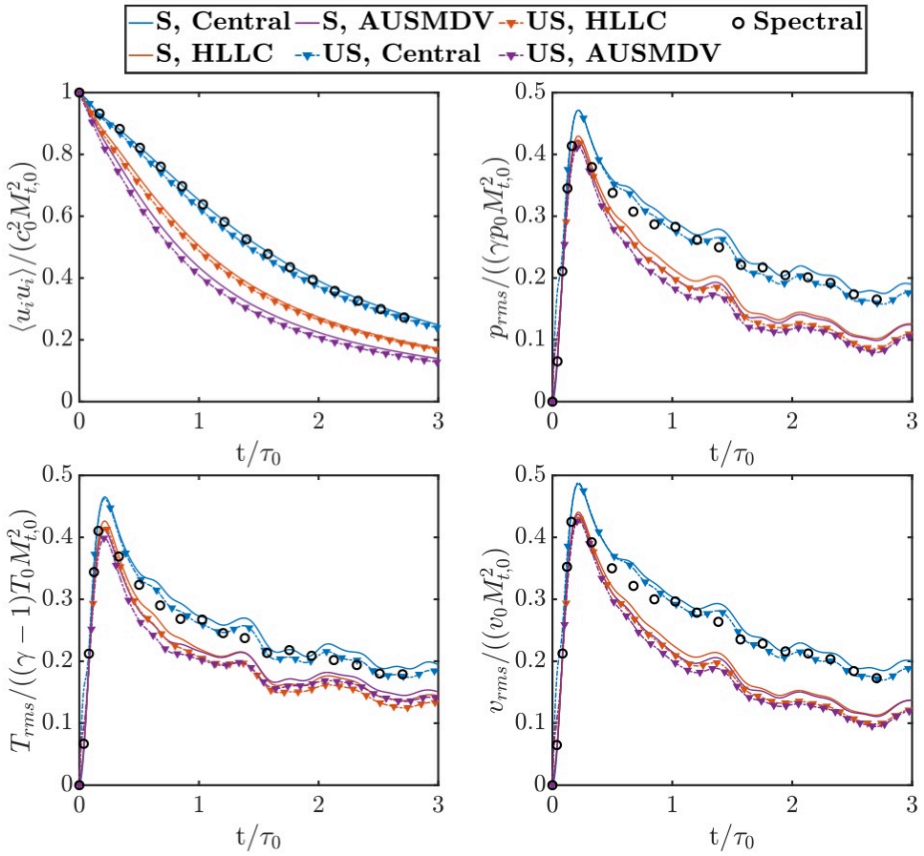

Figure 2.12: Non-dimensional kinetic energy (top left), pressure (top right), temperature (bottom left), and specific volume (bottom right) for compressible HIT at $M_{t,0} = 0.3$, $Re_{\lambda,0} = 30$, and $k_0 = 4$ for HIT simulations with skew-symmetric central, HLLC, and AUSMDV numerical schemes with both structured (S) and unstructured (US) meshes and the spectral solution of Ref. [128].

tral solution more closely compared to the AUSMDV scheme, which adds additional numerical dissipation even at the turbulent Mach number of 0.3. This is more clearly evident in the kinetic energy dissipation plot.

The energy spectrum can also be visualized as a function of time. The curves represent a statistical distribution of many velocity fields in Fourier space. The spectrum profile provides an evaluation of how well the turbulent energy cascade is captured by each numerical scheme and mesh configuration. Specifically, the overall energy preservation is identified by the area under the curve and the amount of small-scale (high wavenumber) energy pileup. The energy cascade at time $3t/\tau_0$ is shown in

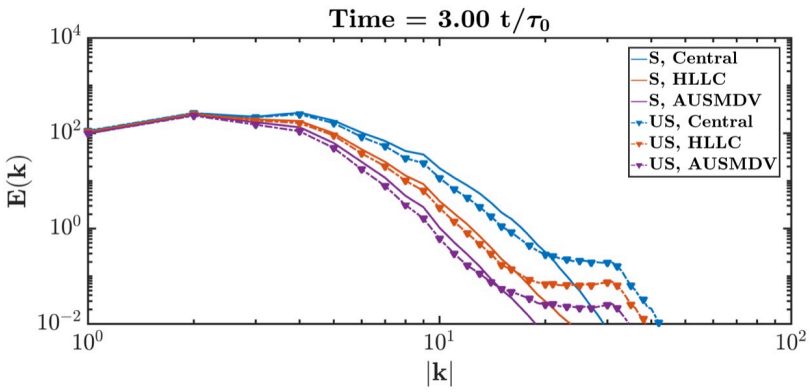

Figure 2.13: Energy spectrum for compressible HIT at $M_{t,0} = 0.3$, $Re_{\lambda,0} = 30$, and $k_0 = 4$ for HIT simulations with skew-symmetric central, HLLC, and AUSMDV numerical schemes with both structured (S) and unstructured (US) meshes.

Fig. 2.13. As expected, the central scheme leads to the greatest energy preservation. The HLLC scheme performs closer to the central method than the AUSMDV scheme. Further, the unstructured meshes result in small-scale energy pileup compared to the structured mesh counterparts. In particular, the region of constant energy at high wavenumber is wider in wavenumber space for the energy cascade of the AUSMDV scheme than the HLLC scheme. Interestingly, the unstructured mesh simulation with the central scheme is very similar in energy distribution to the simulation with the structured mesh counterpart.

2.2.5.2 HIT with $M_{t,0} = 0.6$ and $Re_{\lambda,0} = 100$

The second compressible HIT operating condition is at a sufficiently high turbulent Mach number, $M_{t,0} = 0.6$, such that weak shock waves, termed eddy shocklets by Ref. [138], are induced by the turbulent dynamics. This high turbulent Mach number condition evaluates the shock-capturing capability of the numerical schemes when the location of the shocks is not known *a priori* and their accuracy in representing the turbulent dynamics. The prescribed initial condition is selected due to the large acoustic and entropy modes which allow for better evaluation of the performance of

the numerical methods. Figure 2.14 shows the temporal evolution of non-dimensional kinetic energy and enstrophy along with the variance of non-dimensional temperature and dilatation for the central, HLLC, and AUSMDV numerical schemes with both structured and unstructured meshes with a comparison to the spectral results of Ref. [138]. Similar to before, the central numerical scheme captures the kinetic energy dissipation profile of the spectral scheme well, with HLLC performing better than AUSMDV. It must be noted that the difference between the two shock-capturing schemes is diminished, and the solution is notably more dissipative than the central scheme solution. The temperature fluctuations (and the pressure and specific volume fluctuations which are not shown here) exhibit a similar outcome. In the enstrophy dynamics and dilatational fluctuations, the shock-capturing schemes are significantly more dissipative across all wavenumbers and damp out small-scale variations. In particular, the shock-capturing schemes damp out dilatational motions very quickly. Consequently, they underpredict the spectral and the central scheme solutions. In general, the influence of structured versus unstructured skewed meshes are minimal in comparison to the dissipation encompassed by the numerical scheme itself. While HLLC performs better than AUSMDV for the non-dimensional kinetic energy and enstrophy dynamics, the difference becomes minimal for the temperature and dilatational fluctuation. From these results, it can be postulated that a hybrid scheme that incorporates the central scheme along with the shock-capturing capability of HLLC would be beneficial.

The energy cascade for the high turbulent Mach number condition at time $3t/\tau_0$ is shown in Fig. 2.13. The distribution of energy is similar to that observed at $M_{t,0} = 0.3$, with the HLLC numerical scheme preserving the total energy better than the AUSMDV scheme. The unstructured mesh features less small-scale energy pileup than at the lower turbulent Mach number due to the higher compressibility of this case. Interestingly, the central scheme with the unstructured mesh is more dissipative,

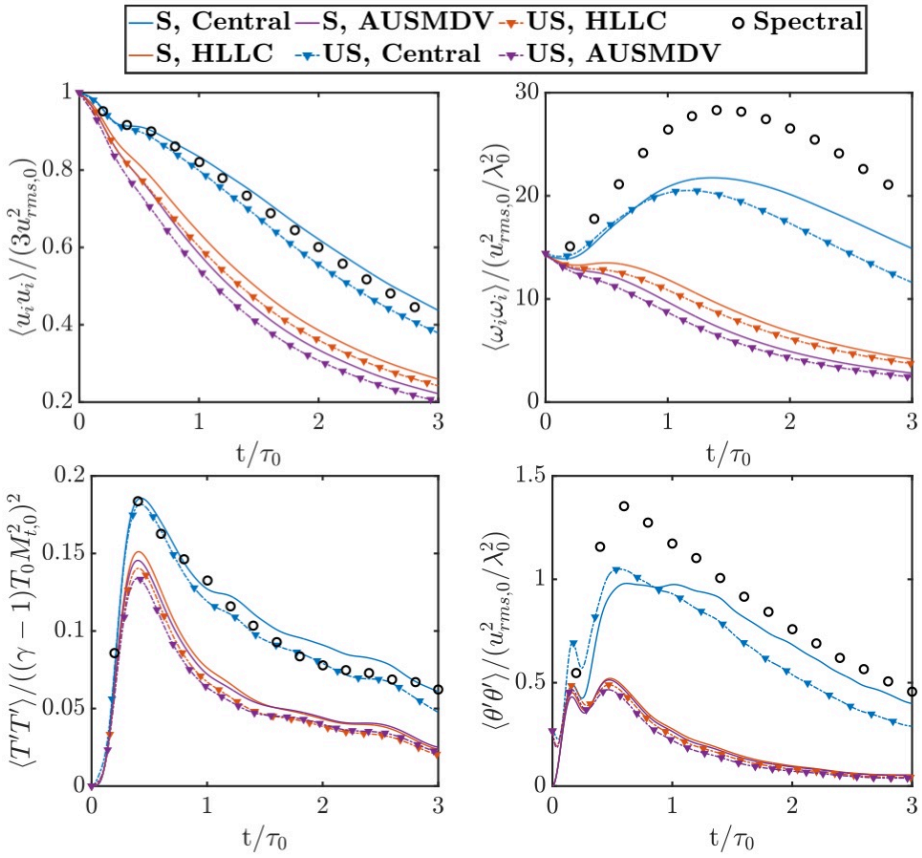

Figure 2.14: Non-dimensional kinetic energy (top left) and enstrophy (top right), and variance of non-dimensional temperature (bottom left) and dilatation (bottom right) for compressible HIT at $M_{t,0} = 0.6$, $Re_{\lambda,0} = 100$, and $k_0 = 4$ for HIT simulations with skew-symmetric central, HLLC, and AUSMDV numerical schemes with both structured (S) and unstructured (US) meshes and the spectral solution of Ref. [138].

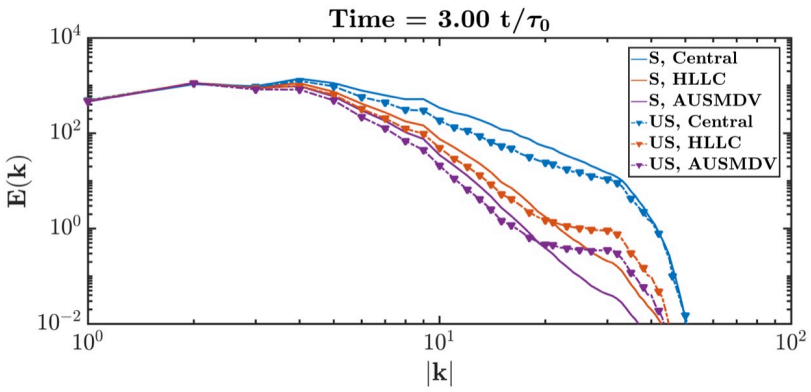

Figure 2.15: Energy spectrum for compressible HIT at $M_{t,0} = 0.6$, $Re_{\lambda,0} = 100$, and $k_0 = 4$ for HIT simulations with skew-symmetric central, HLLC, and AUSMDV numerical schemes with both structured (S) and unstructured (US) meshes.

but the high wavenumber energy cascade is nearly identical to the structured mesh solution. The energy cascade plots show that the unstructured mesh configurations (with nominal cell skewness) are more dissipative than the structured mesh solutions.

2.2.5.3 Hybrid numerical schemes

Hybrid schemes provide a compromise between the diffusive nature of shock-capturing schemes and unstable central schemes. The variable scheme consists of a local shock sensor that is used to determine a linear combination of both schemes to ensure a continuous spatial transition between the schemes. For instance, Ducros et al [71] suggests a dilatation-based parameter that identifies regions of sharp velocity gradient:

$$\Phi = \frac{(\nabla \cdot \mathbf{u})^2}{(\nabla \cdot \mathbf{u})^2 + (\omega)^2 + \epsilon}, \tag{2.34}$$

Similar formulations by Johnsen et al. [138]:

$$\Phi = \frac{-\nabla \cdot \mathbf{u}}{|\nabla \cdot \mathbf{u}| + \omega + \epsilon}, \tag{2.35}$$

and Modesti and Pirozzoli [191]:

$$\Phi = \max\left(\frac{-\nabla \cdot \mathbf{u}}{\sqrt{(\nabla \cdot \mathbf{u})^2 + (\omega)^2 + \epsilon}}, 0\right), \tag{2.36}$$

have been presented. Here, $\mathbf{u}$ is the flow velocity vector, ω is the vorticity magnitude, and ϵ is a small value to prevent numerical divergence in regions where both the dilatation and vorticity magnitude are zero. These forms of shock sensor-based hybrid schemes have been shown to perform better than the shock-capturing schemes alone with reduced numerical dissipation when discontinuities are not present. However, the application of a universal sensor in unstructured meshes is the focus of ongoing research. While hybrid schemes are not used in the present work, they would be a valuable addition to the capabilities of UMReactingFlow.

2.2.6 Boundary condition treatment

In the UMReactingFlow solver, the boundary conditions are enforced at the boundary faces of the polyhedral cells at the edge of the domain. There are three types of boundary conditions used in the full-scale simulations presented within this dissertation: 1) wall, 2) mass flow rate inflow, and 3) outflow.

For the wall-type boundary condition, a no-slip condition is enforced such that all three Cartesian velocity components are set to 0. Furthermore, zero-gradient conditions for pressure, temperature, and species mass fractions are used by using a zero gradient value in the computation of the boundary face value. Near-wall refinement of the mesh is not provided for the simulations discussed here. Furthermore, adiabatic walls are used as wall heat transfer is not considered. This is of future research interest and will require the wall thermal boundary layer to be refined. To note, the unsteady, predominantly supersonic flow within an RDE limits the formation of boundary layers as diffusion effects are limited [256], and additional near-wall refinement was not

found to impact the macroscopic processes within the device [252].

For the subsonic inflows to the propellant feed plenums, a mass flow rate boundary condition is typically used. The inflow surface normal flow velocity is computed such that the mass flow rate through the surface based on the gas density immediately adjacent to the inflow boundary matches the mass flow rate of the requested operating condition. The composition of the propellant is prescribed and the pressure is set with a zero-gradient boundary condition, while the temperature is fixed to the propellant feed temperature adjusted for the low subsonic flow velocity (typically $\mathcal{O}$(1-10 m/s)). A total pressure boundary condition is an alternative approach where the total pressure and temperature at the inflow surface are set from prior knowledge of the system (such as from experimental campaigns) and a flow rate is induced through the plenum. However, this approach can result in greater deviation from the requested mass flow rate [252] and require additional simulation time for the pressures within the plenum to stabilize and establish steady flow. For these reasons, the mass flow rate boundary condition for the inflows is used here.

For the outflow, zero-gradient boundary conditions for the temperature, pressure, and species are employed. If the surface normal velocity at the outflow is supersonic, this treatment does not pose numerical problems. However, in a full-scale RDE simulation, the outflow surfaces are not typically aligned with the primary supersonic flow within the combustor. Consequently, an exhaust plenum downstream of the combustor and any flow control device is used as a "sponge" to dissipate strong pressure waves and prevent wave reflections from the boundary in subsonic conditions. This exhaust plenum is typically much larger than the combustor and the mesh resolution is progressively coarsened towards the outflow. The mesh coarsening is configured such that each step results in *at most* a factor of two increase in cell size and the mesh resolution near the outflow is more than an order of magnitude greater than the resolution within the combustion chamber and injector (regions

of interest). Special care must be taken in the generation of the exhaust plenum to avoid these reflections. However, in certain configurations, acoustic waves with sufficient energy can reach the plenum outflow boundary and cause unwanted wave reflections. Case-specific solutions include the use of a low-velocity air co-flow at the base of the exhaust plenum to turn and straighten the exhaust flow towards the exit, and fixed atmospheric back pressure boundary conditions to prevent weak acoustic wave reflections. Often, a multitude of solutions may be required based on the encountered wave dynamics [236, 237, 300]. NSCBC [228] treatment in an unstructured mesh is more difficult to incorporate due to the irregular polyhedral cells and data access limitations. Future research interest lies in the incorporation and verification of NSCBC for unstructured FV frameworks. However, the approach would require precise tuning to ensure the choice of boundary condition treatment does not influence the solution within the combustion chamber. At present, the dissipation of strong waves through a "sponge" region ensures that the flow dynamics (or lack thereof) in the exhaust plenum do not influence the results within the RDE combustion chamber. In an RDE, wave reflections and instabilities can lead to a vastly different solution because the device is a sensitive, high-dimensional system [268, 300] and precise treatment of the chamber exit is requisite.

An additional type of boundary condition used in simple verification cases of UMReactingFlow is the periodic or cyclic boundary. Here, the face at the periodic boundary is treated as a shared surface between the two cells adjacent to the boundary, similar to a boundary between MPI rank sub-domains during parallelized simulations, and cell gradients are computed between these adjacent cells. In the OpenFOAM framework, simulations are nominally three-dimensional. Similar to the treatment in UTCOMP, one- and two-dimensional simulations are configured such that the non-flow-through directions are set with periodic boundary conditions with a single cell within these directions and the numerical fluxes in these directions are

set to zero.

2.2.7 The high-fidelity approach

In the UMReactingFlow solver, the conservation equations (see Sec. 2.2.1) are represented exactly without subgrid-scale turbulence models. The simulations do not comprehensively handle turbulence and for the selection of simulations presented within this dissertation, grid-based dissipation is used to model the turbulence. While some simulations in the literature contain explicit models in the context of large eddy simulations [169, 214], the models must be tuned for use in the RDE environment. The RDE is characterized by mixing-limited operation, and the mixing process and the development of turbulence are not complete within the flow-through timescales of the device.

Unstructured meshes allow optimal mesh sizes for a given cell resolution. However, due to the computational cost of representing full-scale systems, these simulations typically do not resolve the shock-detonation structure completely. For instance, the simulations of [214] employs adaptive mesh refinement (AMR) with grid sizes of 125-250 μm for hydrogen/air detonations while cell sizes of similar order have been used by the fixed-mesh simulations of Ref. [61]. The numerical simulations with Chaps. IV and V employ fixed meshes with relatively-fine resolutions afforded by the GPU acceleration of key solver subroutines, thereby increasing numerical capability and reducing simulation turn-around time. The massively-parallel GPU-based simulations of RDEs discussed in this dissertation were performed on the Oak Ridge Leadership Computing Facility's (OLCF) Summit supercomputer [216].

To conclude, the solver and its low-Mach number adaptation have been previously validated on a number of turbulent, reacting flows [57, 58, 116, 290] and in particular, detonating flows [252–257].

2.2.8 Validation with detonation problems

The section below will serve to demonstrate and verify the UMReactingFlow solver on simple detonating flow problems. For these studies, hydrocarbon combustion will be the focus. Practical RDEs, like the rocket-type RDE that will be studied in Chap.IV, require the use of non-premixed propellant streams with stable hydrocarbon-based fuels (with or without hydrogen blending [254]). Here, the detonative combustion of methane and oxygen is simulated using the skeletal mechanism FFCMy-12 of Xu et al. [277, 326]. The use of detailed chemical kinetics is needed in the study of non-premixed detonation as the remnants of partially-deflagrated gas drive many of the non-idealities observed RDEs. The skeletal mechanism tracks the reaction pathways of these crucial intermediary species (which one- or two-step mechanisms [305] may limit) while reducing the number of transported species and the associated computation cost of the full mechanism. Based on the Foundational Fuel Chemistry Model 1.0 [277], this mechanism employs 38 reaction steps with 12 species to model the combustion of methane/oxygen mixtures. However, the model must be validated for detonation simulations through a series of one- and two-dimensional numerical simulations to evaluate the Chapman-Jouguet (CJ) velocity, von Neumann pressure, and detonation cell size. To ensure that the choice of chemical mechanism does not unduly affect the outcomes of this study, several canonical flow configurations are considered.

2.2.8.1 One-dimensional detonation

The first case is the one-dimensional detonation tube. The purpose of this study is to validate the transient behavior of the species at the detonation front, the CJ velocity, and the von Neumann pressure. Here, methane and oxygen at a rich equivalence ratio of 1.15 at 300 K are filled in a 30 cm tube, as depicted in Fig. 2.16. In order to initiate the detonation wave, an overdriven post-detonation region of width 3 mm at

a high pressure of 5.84 MPa, a high temperature of 3750 K, and at the CJ velocity of 2462 m/s is prescribed. The post-detonation state is determined through analytical calculations. The detonation wave propagates towards the outlet by processing the fuel/oxidizer mixture in the domain. Detailed species behavior is shown in the right plot of Fig. 2.16. Methane and oxygen are consumed and intermediate species, such as CH_2O and OH, rise to a peak value at the detonation front, and post-detonation products are created after a finite distance behind the front.

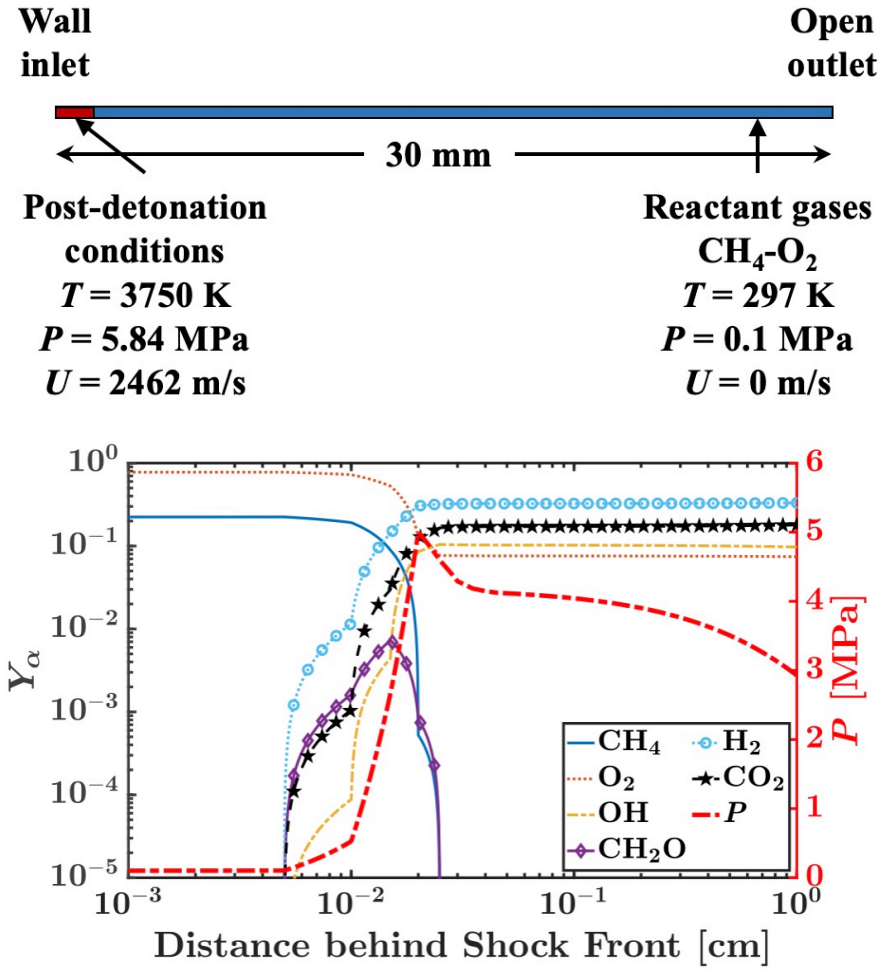

Figure 2.16: (Top) Configuration for the one-dimensional shock tube configuration and (bottom) transient response of the species and pressure behind the detonation front for the one-dimensional configuration.

Based on analytical calculations, the induction length for the methane-oxygen mixture of equivalence ratio 1.15 is on the order of 0.17 mm, similar to that of a

stoichiometric hydrogen/air mixture at 0.24 mm. With a grid resolution of 50 μm, a tractable resolution for full-scale RDE simulations, the percent error in CJ velocity and von Neumann pressure are 0.24 and 15.8 percent, respectively. A wave speed and peak pressure of 2469 m/s and 4.81 MPa are observed. This resolution is extended to the two-dimensional channel detonation cases.

Furthermore, Fig. 2.17 shows near-linear convergence of peak pressure to the CJ pressure with grid resolution and demonstrates that the one-dimensional wave speeds are nearly identical (within 1%) to the CJ speed for all resolutions studied. Additional validation of this mechanism developed specifically for high-pressure combustion is being conducted by Prof. Wang (Stanford University) (author of the mechanism).

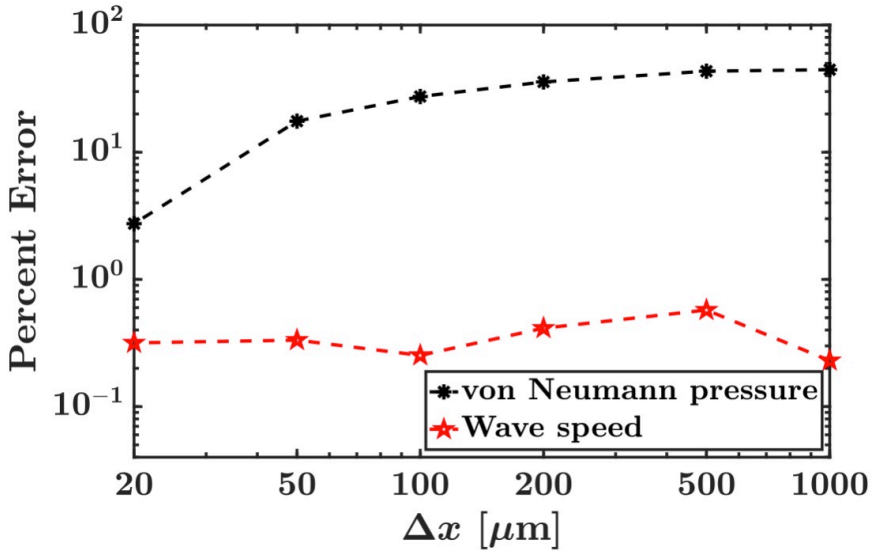

Figure 2.17: Convergence of von Neumann pressure and wave speed for one-dimensional detonation tube simulations using the FFCMy-12 skeletal mechanism.

2.2.8.2 Two-dimensional channel detonation

Detonating flow in a confined channel is used to understand the detonability and chemistry mechanism of fuel mixtures. Here, a channel detonation is initialized at 0.1 MPa and 300 K ambient conditions within a channel of length 30 mm and width

1 mm. Past numerical work by Schwer et al.[266] has primarily focused on methane combustion with hydrogen diluent and air as the oxidizer. In contrast, the cell size of methane-pure oxygen mixtures is smaller. In the channel, a region of overdriven post-detonation conditions is patched on the left, similar to the one-dimensional case. However, a pair of sparks of reactant mixture at high temperature and pressure are placed to perturb the detonation wave, creating transverse waves. The interaction of these transverse waves forms triple points along the detonation front. The channel configuration is given in Fig. 2.18, reflecting past channel detonation simulations of Sec. 2.1.7.2. Streamwise and stream normal grid resolutions of 1-50 μm with a range of channel widths were studied. With the skeletal mechanism, a channel narrower than the experimental cell width was required to induce the formation of triple points due to confinement effects. As a result, a grid resolution of 2 μm with a 1 mm channel was required to resolve the complex "fish scale"-like cell structure. The trace of triple points is shown in the soot foil diagram in Fig. 2.18. The cell structure contains 1 longitudinal track and 2 transverse tracks, with cell sizes similar to that of past simulations with hydrogen/air mixtures at similar conditions. This provides verification of the FFCMy-12 chemical mechanism for detonation applications and the capability of the UMReactingFlow solver in modeling unsteady detonations.

2.2.9 Solver summary

This section introduced and detailed the in-house compressible flow solver UMReactingFlow which will be used in Chaps. IV and V for the study of non-premixed full-scale RDEs. The unstructured mesh solver allows for the simulation of complex geometries with practical, high-order detailed chemical mechanisms. The solver employs a high-fidelity simulation approach with no sub-grid scale turbulence models to solve the governing equations of mass, momentum, and energy along with species conservation equations to incorporate the chemical reactions. The Navier-

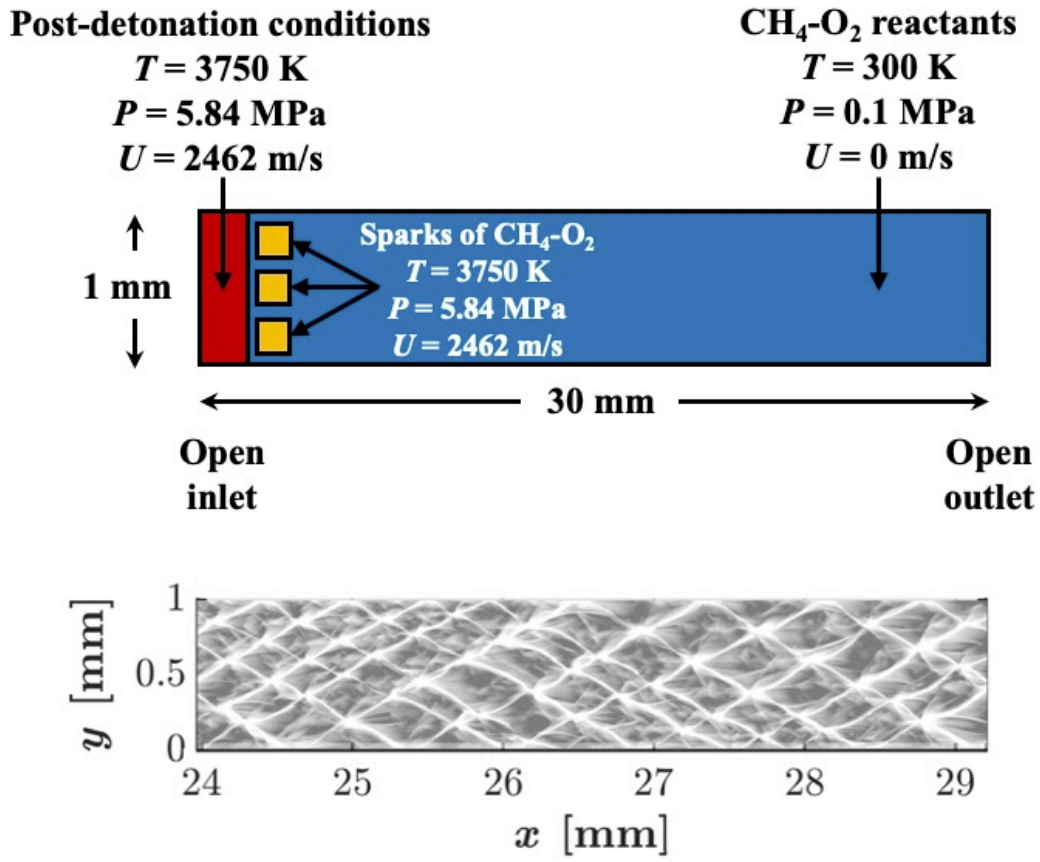

Figure 2.18: (Top) Two-dimensional channel detonation configuration with sparks to induce an unsteady detonation wave and (bottom) soot foil plot for methane-oxygen detonation with a detailed view of complex cell structure.

Stokes equations are closed using an ideal gas equation of state. A MUSCL-based HLLC approximate Riemann scheme [18, 299] is utilized due to the low computational cost and ability to model both Riemann and contact waves. The viscous terms are computed through a Kurganov Noelle Petrova (KNP) formulation that is nominally second-order accurate. An explicit second-order Runge-Kutta time integration scheme is used to advance the governing equations.

Computationally intensive subroutines for convective and reaction stages are offloaded to the GPU using in-house CUDA-based modules for compatibility with heterogeneous computing platforms. The computing architecture used in this dissertation is outlined in Fig. 2.10. For GPU-based reaction treatment, detailed chemical

kinetics (chemical source term evaluation and stiff time integration), as well as thermodynamic gas properties, are evaluated in a matrix-based formulation that maximizes throughput. Complete details of the solver and its development are provided in Refs. [26] and [15].

The UMReactingFlow solver has been used to simulate one- and two-dimensional detonations in shock tubes. Here, near-linear convergence of peak pressure to the CJ pressure with grid resolution was achieved and one-dimensional wave speeds are nearly identical (within 1%) to the CJ speed for all resolutions studied. The peak pressure within 5% was obtained at a cell resolution of 20 μm. Furthermore, the cellular structure of unsteady detonation in a two-dimensional channel was captured. The solver's numerical methods have been successfully demonstrated on detonating flows with a range of fuels and validated with experimental data [254, 256, 257].

CHAPTER III

Simulations of Canonical Detonating Flows

The next chapter investigates the characteristics of non-idealities in detonative combustion and their impact on the detonation wave structure, as well as implications on RDE operation and performance. Through simulation of canonical configurations, such as a linear array of injectors and confined channels, the effects of discrete injection, mixture stratification, and deflagrative preburning of the reactant mixture. Performed using the UTCOMP solver exclusively (see Sec. 2.1), these simulations study the non-idealities in simplified geometries where detonation behavior and statistics of combustion can be interrogated. Section 3.1 presents the structure of a detonation propagating through an array of partially-premixed fuel and air injectors and depicts the effects of Section 3.2 introduces a stratified mixture of fuel and air arranged as irregular patches inside a confined channel, while Sec. 3.3 adds preburning to this stratified propellant mixture to introduce partially-deflagrated combustion products ahead of the detonation wave.

3.1 Detonation Propagation through Discrete Injectors

3.1.1 Motivation

In an RDE, the propagation of the detonation wave is a largely two-dimensional phenomenon, where the wave propagates continuously through an annular chamber in

the azimuthal direction of the RDE cylinder. The development of turbulence is vastly different from the fully three-dimensional turbulence found in gas turbine combustors. The physics of the wave propagation is a function of the chemical composition of the fuel/oxidizer mixture and the geometric configuration of the combustor annulus and injector system [38, 42, 43, 85]. Thus, alterations in the fuel/oxidizer mixture and the local chemical composition near the injectors will affect the stability and periodicity of the detonation wave as well as the structure of the detonation wave and its subsequent reaction zone [40].

One of the fundamental challenges in the successful operation of RDEs is the design of a robust fuel/oxidizer injection system. To minimize pressure losses while ensuring efficient mixing that promotes stable detonation, the injection has to satisfy many different constraints. In this work, the impact of discrete injection on wave propagation is studied in an effort to understand the impact of fuel stratification on detonation stability. This involves a characterization of the detonation structures and an understanding of the interaction of post-detonation turbulence with the fuel/oxidizer injectors. Following the passage of the detonation wave, the pressure gain initially suppresses the injector and the transient pressure gradient allows for the injector to re-develop prior to the passage of the next wave. The fuel/oxidizer mixture is injected from the base of the annular chamber before the next passage of the detonation wave. Thus, based on the size of the RDE and the detonation wave propagation velocity, there may not be a sufficient amount of time to fully develop an ideal mixture of fuel and air inside the chamber. This can lead to a periodically-varying chemical composition at the base of the annulus [40]. In non-premixed configurations, the actual wave velocity may not reflect the theoretical wave velocity for the mixture, the Chapman-Jouguet (CJ) velocity. The CJ velocity for a given mixture is determined under the assumption of fully premixed reactants. While non-premixed fuel/oxidizer injection is the main design challenge, the study here focuses on the

discrete injection of premixed fuel/oxidizer mixture into ambient air. The passage of the detonation wave is still subject to fuel/oxidizer stratification due to the partial-premixing of the injection mixture with the ambient fluid. The research stems from the experimental work of Burr and Yu [40], where a linearized model detonation engine (LMDE), an unwrapped model of an RDE combustor featuring a simplified geometry, is used to visualize a detonation wave propagating through a narrow channel. The LMDE primarily simulates the interaction between the fuel/oxidizer mixture injected transversely into the channel and the detonation wave while removing the effects of curvature [40]. The experimental objectives were to identify the key flow features in this canonical configuration and better understand the complex interactions between the injectors, the detonation wave, and the various waves in the wake of the DW.

The numerical simulation of the LMDE system will allow for the visualization of small-scale turbulence structures and the induction region, which is very thin compared to other length scales in the combustor. For most chemical compositions and flow conditions, the ideal one-dimensional detonation wave, which consists of the pressure/shock wave followed by a reaction zone, is on the order of a few micrometers in length [230]. In comparison, the three-dimensional detonation structure consists of multiple pressure waves and a broad reaction zone. Furthermore, the spatial distribution of the fuel/oxidizer mixture within the chamber is highly variable. Thus, the detonation wave itself is spatially-varying and leads to local acceleration and deceleration of the wave front [179]. The interaction of the fuel/oxidizer mixture and the detonation wave is driven by multiscale turbulence, which requires that the gradients are properly resolved in the flow. Thus, the combustion processes require a direct numerical simulation approach with multistep chemical mechanisms to study detonation wave propagation accurately.

3.1.2 Numerical representation

To replicate the wave structure in a practical RDE, the linearized model detonation engine (LMDE) configuration of Burr et al. [40] is simulated. The experimental LMDE contains an array of transverse (wall-normal) reactant jets in a linear open channel of width 7.6 mm. The detonation wave propagates streamwisely through this channel. Fuel/oxidizer injectors of diameter 2.5 mm with 6.4 mm center-to-center spacing are placed within the LMDE. The injector diameter d_{inj} is a characteristic length scale in this study. In the numerical analysis, the primary region of interest is the interaction of the detonation wave structure with the transversely-injected fuel/oxidizer jets. Thus, the fuel/oxidizer mixture is fully-premixed at a given equivalence ratio ϕ, and the individual fuel and oxidizer streams and mixing plenums are not modeled. The channel is open to the surrounding on the top and the far end of the channel. The channel is initially pre-filled with air as the background gas at ambient conditions. The velocity and height of the transverse reactant jets are calibrated such that the jets are choked at the inflow and establish a stable fill height into the LMDE. A pre-detonator is used to initiate a detonation wave from the inlet end of the channel through a square tunnel of size 7.6 mm by 7.6 mm. In the experimental configuration, the pre-detonator is operated using a stoichiometric hydrogen/oxygen mixture. Similarly, the pre-detonator tunnel is closed after all the post-detonation gases have exited the tunnel into the LMDE channel. The numerical simulation replicates this fuel/oxidizer composition and a time-dependent inflow boundary condition is used; a wall inlet boundary condition is used after 50 μs, roughly the time required for the detonation wave to process all 15 injectors. As the detonation wave expands through the channel, the lower pressure on the outflow of the LMDE leads to a radial expansion of the detonation wave as it passes through the channel [40]. The schematics of the LMDE setup reproduced from Burr et al. [40] are given in Fig. 3.1.

The numerical simulation geometry replicates the experimental setup but is sim-

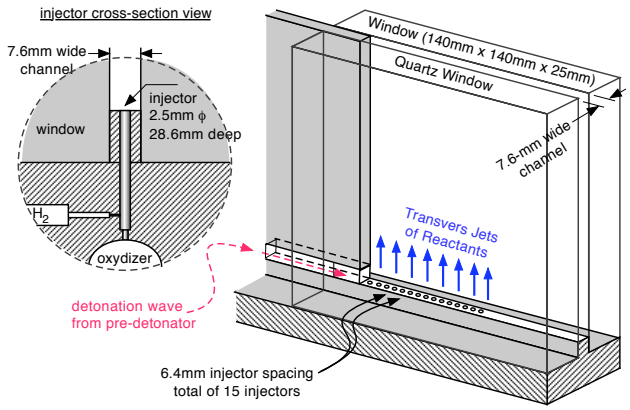

Figure 3.1: LMDE schematic with injector orientation and channel configuration reproduced from [40].

plified to analyze only the interaction of the premixed injection jets with the passing detonation wave. To this end, the narrow channel of width 7.6 mm has been represented with the full length of 14 cm, and the height has been truncated to 6.25 cm, equivalent to 25 injector diameters. The region beyond this height is not of interest with regard to the scope of this study. This results in a three-dimensional rectangular region of dimensions 14 cm $\times$ 6.25 cm $\times$ 7.6 mm, filled with an ambient mixture of air (O_2-N_2) at 297 K and 0.5 atm for the H_2/air cases and 1.0 atm for the H_2/O_2 case. The operating pressure of the LMDE was reduced from the experimental configuration of 1 atm due to numerical considerations. The 1 atm ambient pressure condition poses a numerical limitation as the post-detonation pressure of hydrogen/oxygen combustion is approximately 33 atm and the induction length, established as the length scale of interest, is on the order of 53 μm [230]. Thus, fully resolving the detonation structure and flow field with a sufficient amount of cells across the induction region can become computationally intractable. However, due to the limited detonability of the H_2/air at the lowered operating pressure, a high-energy release mixture - H_2/O_2 - with an ambient pressure of 1 atm was included to validate fuel detonability. This configuration is one of the experimental test cases.

The grid resolution for the three-dimensional geometry is uniform with a core

region in the streamwise and wall-normal directions. A hyperbolic tangent function is used to blend the core and outer regions of the mesh. The LMDE is largely two-dimensional in nature; the resolution in the spanwise direction is double that of the wall-normal directions. These modifications allow for manageable computational costs while calibrating the simulation configurations and boundary conditions. Grid convergence on the two-dimensional and three-dimensional channel detonation waves was completed to ensure that a resolution in the wall-normal direction of 100 μm and depthwise direction of 200 μm captures the detonation cell size, wave behavior, and detailed chemistry of finer resolution cases. In order to ensure that the streamwise evolution of the triple points is not suppressed through numerical errors, the following resolution is selected. The core region is defined as the domain up to roughly 3.5 injector diameters beyond the final injector in the streamwise direction and 419 y^+ for the H_2/air cases and 1656 y^+ for the H_2/O_2 case in the wall-normal direction. For the H_2/air cases, the core grid consists of Δx = 10 μm and Δy = 3-99 μm. Outside the core region, Δx = 100 μm and Δy = 100 μm. Δz = 200 μm throughout the domain. Similarly, for the H_2/O_2 case, the core grid consists of Δx = 25 μm and Δy = 0.8-49 μm. Outside the core region, Δx = 250 μm and Δy = 50 μm. Δz = 100 μm throughout the channel.

The top and right boundaries are set as outflows, while the spanwise boundaries are treated as walls. Two different inflow conditions are considered. For this discussion, the list of test cases and associated operating parameters are shown in Tab. 3.1. In cases 1a, 2, 3, and 4, the inlet boundary is prescribed through a sampled inflow in a region corresponding to the pre-detonator tunnel, with a wall boundary condition spanning the remainder of the inlet plane. In case 1b, the boundary condition of the complete inlet plane is prescribed by the sampled inflow condition. The sampled inflow condition in all cases is used to introduce a right-running, well-developed, three-dimensional detonation wave into the domain. This is generated using the

Table 3.1: Injector jet conditions for different cases

	Case 1a	**Case 1b**	**Case 2**	**Case 3**	**Case 4**
Reactant composition	H_2/air	H_2/air	H_2/air	H_2/air	H_2/O_2
Inflow condition	Pre-detonator tunnel	Full inlet	Pre-detonator tunnel	Pre-detonator tunnel	Pre-detonator tunnel
Equivalence ratio [ϕ]	$\phi_{\text{inject}} = 1.0$	$\phi_{\text{inject}} = 1.0$	$\phi_{\text{inject}} = 1.2$	$\phi_{\text{inject}} = 0.8$	$\phi_{\text{inject}} = 1.0$
Initial pressure [atm]	0.5	0.5	0.5	0.5	1.0
Jet total pressure [atm]	0.948	0.949	0.948	0.948	1.899
Jet total temperature [K]	297	297	297	297	297
Jet injection velocity u_{inject} [m/s]	372	381	361	372	491
Injection fill height h_{inject} [mm]	20-25	20-25	20-25	20-25	20-25

outflow of the three-dimensional channel detonation wave in the premixed channel simulation described in Sec. 2.1.7.2. The background gas condition is similar to the experimental configuration, with the ratio of O_2 and N_2 identical to the premixed two- and three-dimensional channels. Premixed H_2/air for cases 1a, 1b, 2, and 3, and premixed H_2/O_2 for case 4 is supplied from the bottom wall through an array of 15 circular injectors with geometry identical to the experimental configuration, with a stagnation temperature and pressure set such that the jets are choked when there is no detonation in the channel. The injector boundary condition is calculated from the static pressure within the channel, using the method prescribed by Schwer and Kailasanath [260].

For all five test cases, the detonation wave is not initially present within the LMDE, and the jets are allowed to develop, which supports the turbulent mixing of

the fuel/oxidizer jets with the ambient air. This is consistently performed for a time of $t = 200$ μs in all cases. At the end of the initialization time, the jets are developed to a height of roughly $20 - 25$ mm (8-10 injector diameters) above the base of the channel. Thus, the lower region of the channel is partially filled with the fuel/oxidizer mixture, as displayed in Fig. 3.2. At this time, the detonation wave is introduced from the inlet plane.

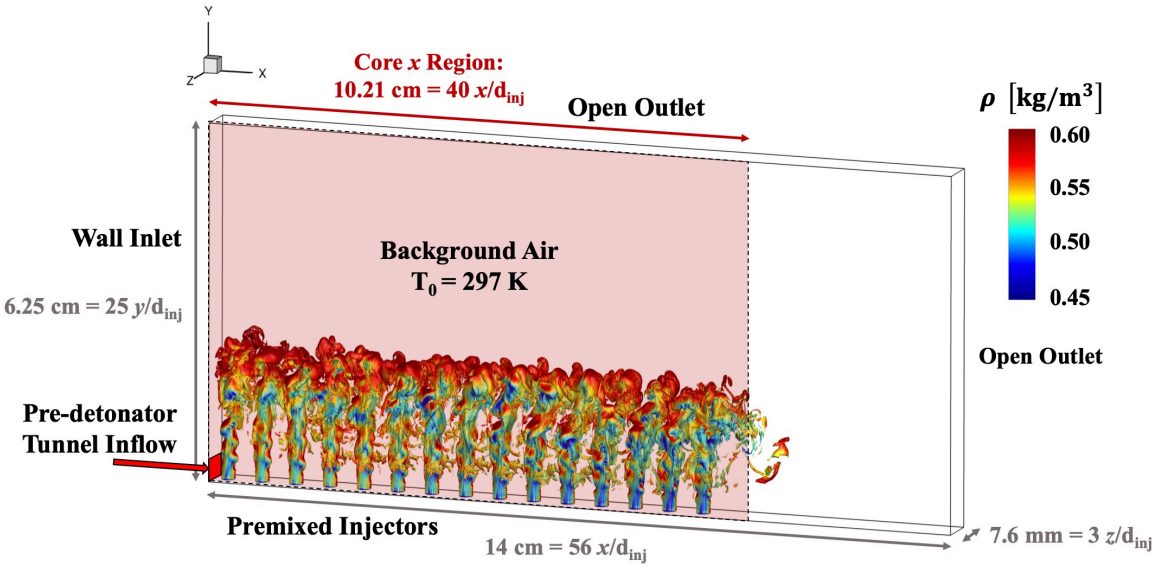

Figure 3.2: Fully developed injector jets in LMDE; isosurface of $Y_{H_2} = 0.016$, colored by density.

3.1.3 H_2/air case with detonation tube inflow

In cases 1a, 2, 3, and 4, the detonation wave is introduced into the LMDE from a small square region corresponding to the connection between the pre-detonator tunnel and the injection channel. Similar to the experiment, the detonation wave is generated in the pre-detonator tunnel using a stoichiometric mixture of H_2/air and H_2/O_2 for cases 1a, 1b, 2, and 3, and case 4, respectively. A hydrogen fuel/oxidizer mixture is supplied from the injector jets and pure air is the background gas. Figure 3.3 displays a sequence of numerical Schlieren images of the detonation wave entering the channel.

Figure 3.3a displays the wave as it enters the channel, with the first injector base one-half of an injector diameter away. In Fig. 3.3b, the wave begins to expand and diffract into the surrounding gas as the kinetic energy component, initially largely in the streamwise direction, is divided into streamwise and wall-normal components. Furthermore, as the wave enters a region of pure air, there is a lack of hydrogen fuel to sustain the wave. Subsequently, the wave rapidly separates into a lead pressure wave followed by a trailing reaction zone. In general, this separation between the shock front and the reaction front increases with time. Similar to the experiment, the material interface between the pre-detonator reaction products and the channel gas is visible trailing behind the reaction front in Fig. 3.3d. The wave travels faster near the base of the domain due to the lower density of the fuel/air mixture. As a result, the detonation wave accelerates as it passes through the injectors, and slows down in the gap between the injectors.

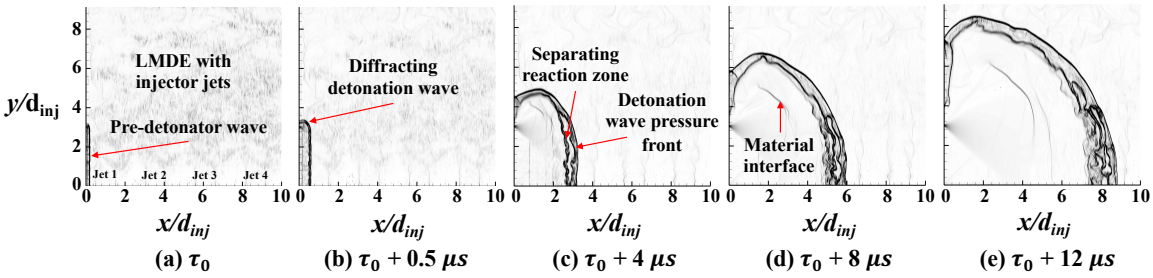

Figure 3.3: Detonation wave from the pre-detonator inflow entering the LMDE with injector jets at $\phi_{\text{inject}} = 1.0$.

In the numerical simulation of cases 1a, 2, and 3 with the pre-detonator tunnel inflow, the detonation wave fails to sustain detonation as the wave progresses through the channel. The initial diffraction of the wave from a confined three-dimensional channel into the open geometry allows the wave to expand radially. While the detonation sustains itself over a few injectors (the number depends on the equivalence ratio), the shock wave and the reaction front separate causing the detonation to quench as it traverses the domain.

The fuel/air injection enters the channel with a laminar flow profile and the flow transitions to turbulence through the onset of vortices at a jet-streamwise distance of approximately 1/2 injector diameter. The turbulent jet profile increases the mixing and dissipation of the fuel/air mixture into the background gas. To this end, the behavior of the detonation wave as it passes through these two regions is analyzed in Figs. 3.4, 3.5, 3.6. The averaging procedure of the shock-normal profiles is detailed in Sec. A.2. For all three cases, turbulent mixing leads to fluctuations in the pressure and Mach number profiles. In the laminar profiles, the pressure and Mach number follow a similar trend. The profiles feature an initial peak at the shock front and decay to a post-detonation equilibrium value. In contrast, in the turbulent region, the peak pressures are significantly higher. From the one-dimensional simulation shown in Fig. 2.2, it was seen that the stable von Neumann pressure for the ZND detonation is roughly 17 atm. However, in the turbulent region, peak pressures reach nearly three times this value due to the triple points. Following the peak pressure location, the increase in the free radical concentration up to a local maximum corresponds to the ignition of the fuel/oxidizer mixture. The distance between the peak pressure location and the local maxima of the free radicals, such as O and OH, is roughly the induction length.

Relating pressure and density behind the detonation wave front at various heights above the base of the channel can provide insight into deflagration and detonation processes. Figure 3.7 displays the pressure versus specific volume (Rankine-Hugoniot) relation for cases 1a, 2, and 3 at the same time as above. Here, the top row plots the Rankine-Hugoniot relation for heights up to 6 injector diameters from the base of the channel. The values at each height are populated from a region within 1 cm normal to the detonation front at each height. In the Rankine-Hugoniot curve, the fluid particles traverse the shock Hugoniot up to the von Neumann spike condition (15-17 atm pressure) at regions near the base of the channel. However, additional increases

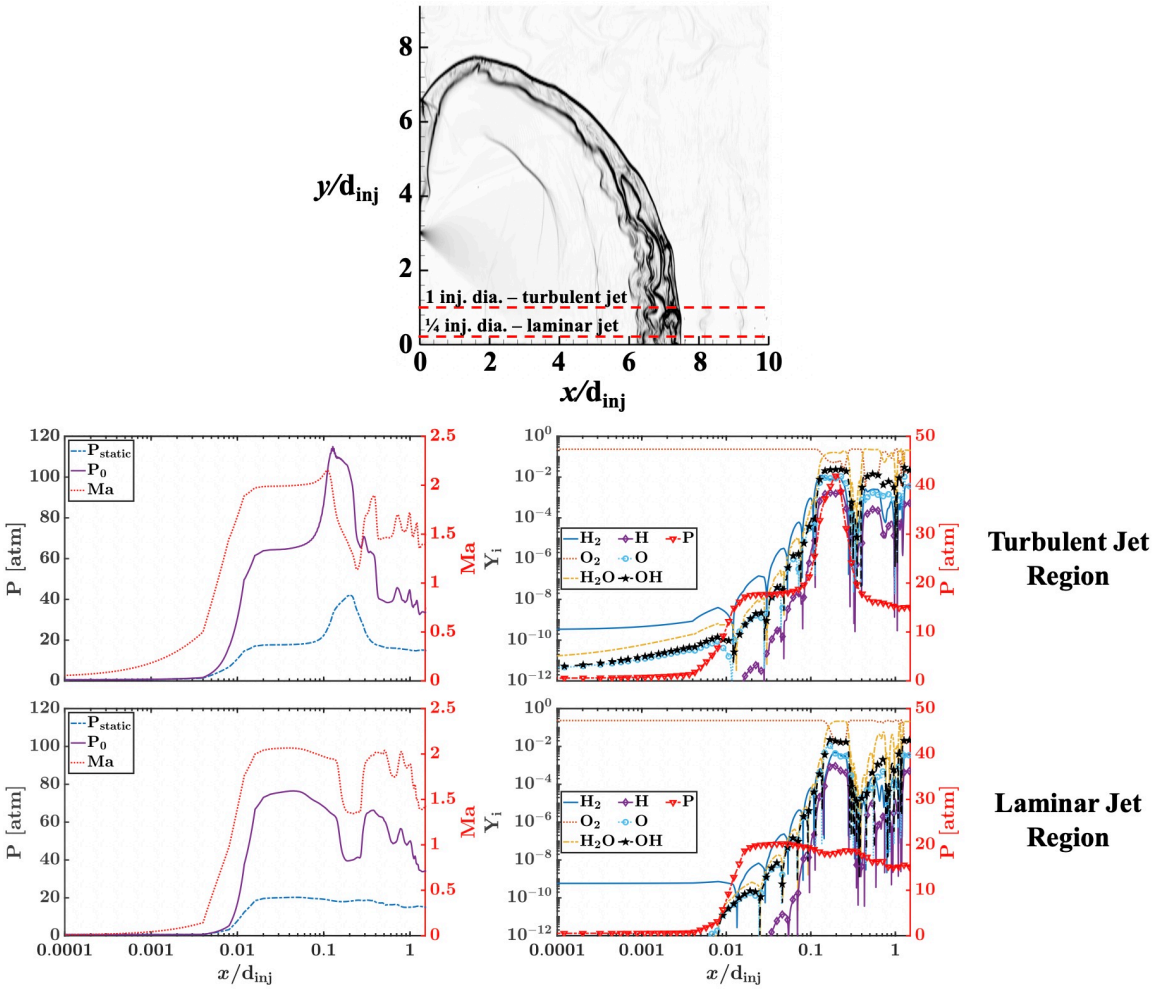

Figure 3.4: Case 1a; detailed pressure, Mach number, and species mass fraction behavior normal to the shock front as the wave passes the 3rd injector.

in pressure correspond to triple-point collisions and the effects of three-dimensional detonation. Thus, confined three-dimensional detonation results in higher compression than the previously-simulated one-dimensional ZND wave. Across all three cases, the region approximately 1 injector diameter from the base of the channel results in strong detonation, with peak pressures corresponding to that of the triple points. Indeed, as viewed in the numerical Schlieren images, the curved detonation wave front can be characterized by the existence of visible triple points. Furthermore, it must be noted that with increasing equivalence ratio, the peak pressure in the region 1 injector

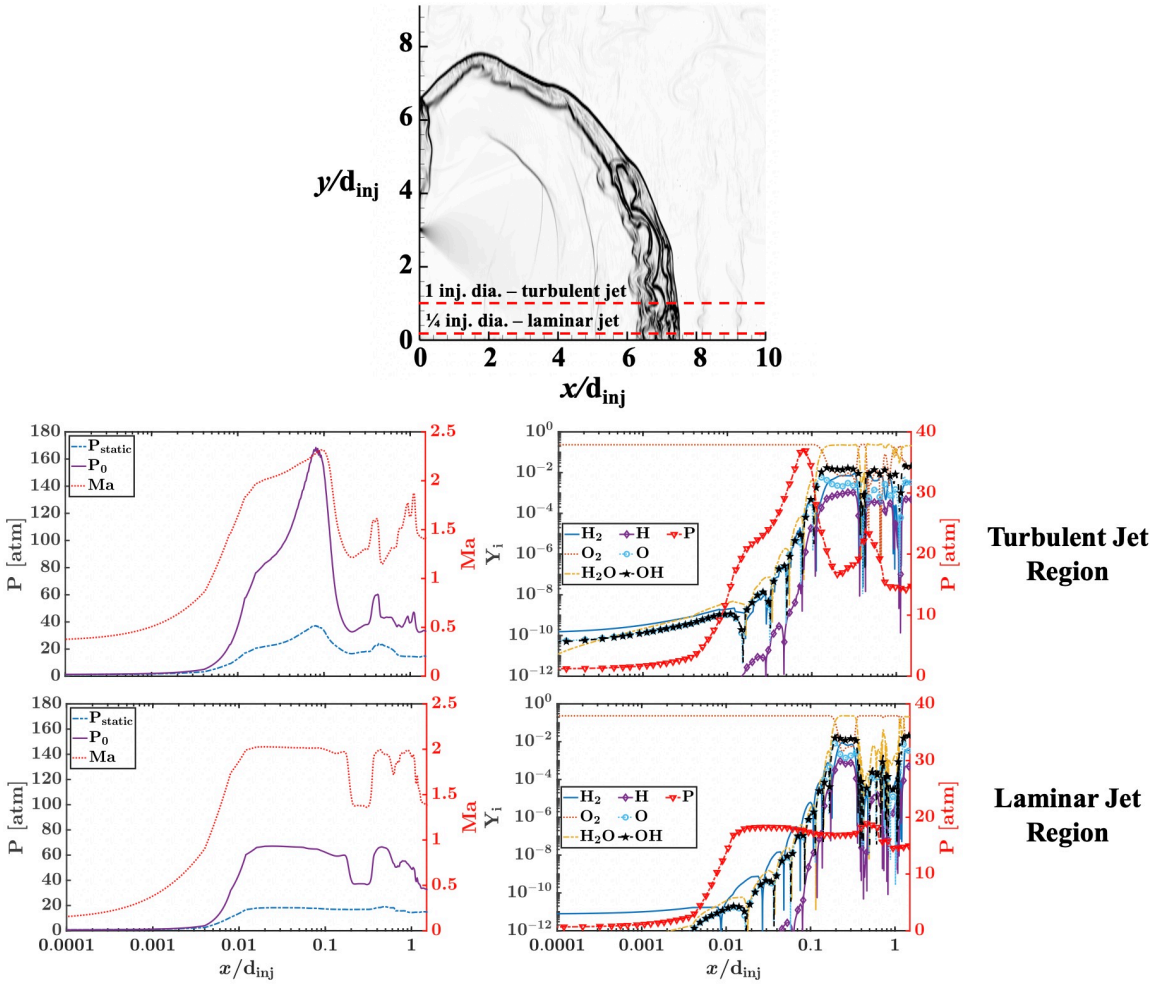

Figure 3.5: Case 2; detailed pressure, Mach number, and species mass fraction behavior normal to the shock front as the wave passes the 3rd injector.

diameter above the base of the channel increases. There is a marked transition to deflagration above roughly 4 injector diameters from the base of the channel. This is as expected as the local equivalence ratio is higher near the base of the injector, and the increased mixing from the turbulence at the 1 injector diameter height aids in the interaction of the fuel/air mixture with the reaction zone. The heat release rate per unit volume relations for the three cases reflect the peak pressures observed in the Rankine-Hugoniot curves. For all three cases, there exists a primary peak (highlighted by the dotted red line) at the post-detonation pressure of approximately

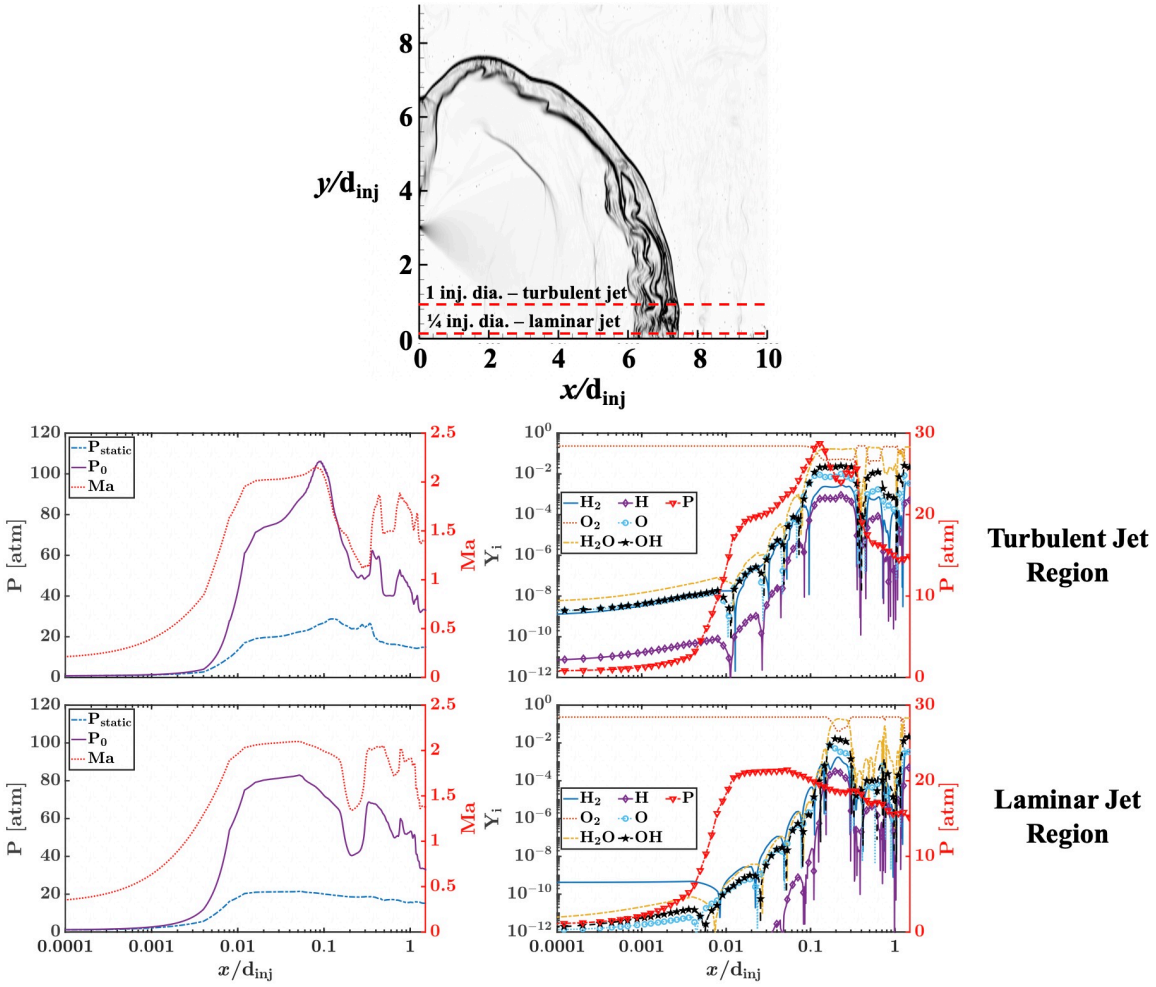

Figure 3.6: Case 3; detailed pressure, Mach number, and species mass fraction behavior normal to the shock front as the wave passes the 3rd injector.

15-17 atm and a secondary peak at the deflagration pressure of approximately 10-11 atm (highlighted by the dotted green line) in the heat release rate per unit volume relation of Fig. 3.7. Thus, the highest heat release occurs in the detonation mode, with a secondary heat release in the deflagration mode. Additionally, high heat releases at peak pressures above post-detonation conditions correspond to triple points and three-dimensional effects along the detonation front.

The time history of static pressure along the path of the detonation wave is displayed in Fig. 3.8, at streamwise locations similar to the experimental results of Burr

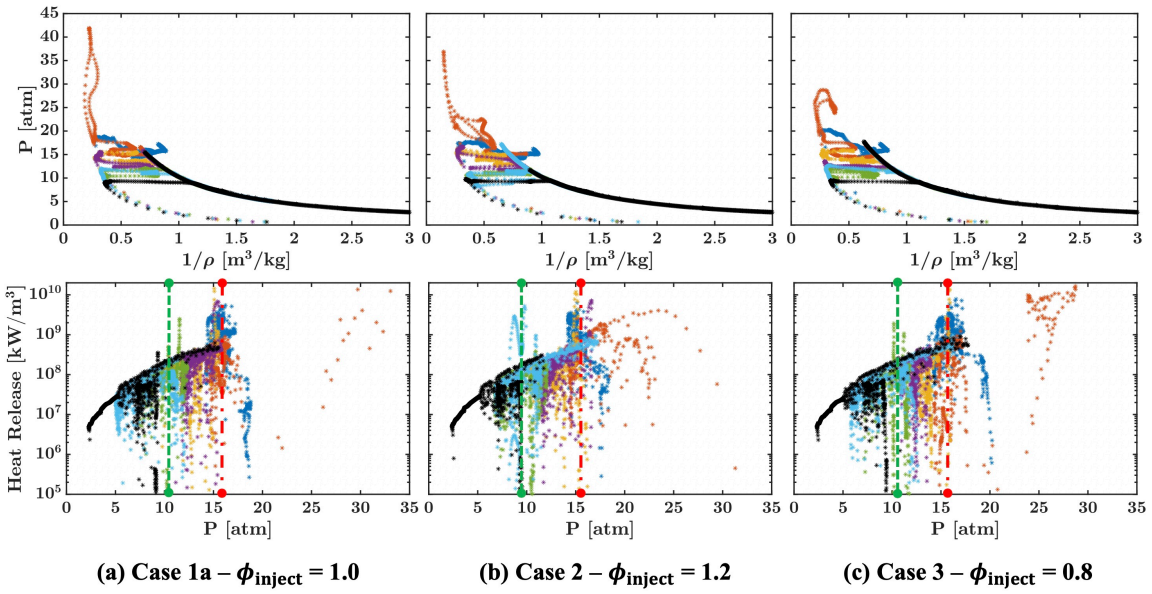

Figure 3.7: (Top) Pressure versus specific volume (Rankine-Hugoniot) and (bottom) heat release rate per unit volume relations as the detonation wave passes the 3rd injector. Legend: * : Injector Base; * : 1.0 x/d_{inj}; * : 2.0 x/d_{inj}; * : 3.0 x/d_{inj}; * : 4.0 x/d_{inj}; * : 5.0 x/d_{inj}; * : 6.0 x/d_{inj}; – – – : deflagration pressure; – · – · – : detonation pressure.

et al. [40]. The pressure traces are obtained at two locations: (1) within the laminar region, 1/4 of an injector diameter from the base of the channel, and (2) within the turbulent flow region, 1 injector diameter from the base of the channel. The pressure trace results begin from the inlet plane of the LMDE, at $x = 0$ mm. For all three cases, as the detonation wave moves further downstream, the peak pressure at subsequent pressure "probe" locations decay in value. Similar to the experimental results, the change in amplitude of the pressure trace at points downstream suggests that the shock front loses strength due to the separation of the pressure front and reaction zone as the wave diffracts in the LMDE. However, unlike the experimental results, the wave amplitude continues to diminish, until the peak pressure is below the von Neumann pressure derived from the one-dimensional and analytical results. Beyond this point, the wave pressure does not recover, suggesting that the shock wave front and the reaction zone are decoupled, and the detonation wave dissipates in time. For

the leanest case of $\phi_{\text{inject}} = 0.8$, the peak pressure value is seen to decay gradually further downstream in the channel, approaching a stable blast wave configuration. However, Y_{OH} profiles reveal that the production of radicals across the detonation wave front diminishes and the wave does not reignite, as observed in the experimental results. This may be attributed to the increased ignition delay time at the lower ambient pressure of 0.5 atm. Thus, with the current LMDE geometry, the detonation wave may traverse the fuel/air injector at a time scale faster than the ignition delay time for complete combustion. The peak pressure at a given streamwise location decreases with the equivalence ratio. Furthermore, for all cases, the detonation wave front pressure is highest at a height 1 injector diameter above the base of the channel, suggesting that the strongest detonation occurs at a location where the flow is turbulent yet the local equivalence ratio more closely resembles the injection equivalence ratio.

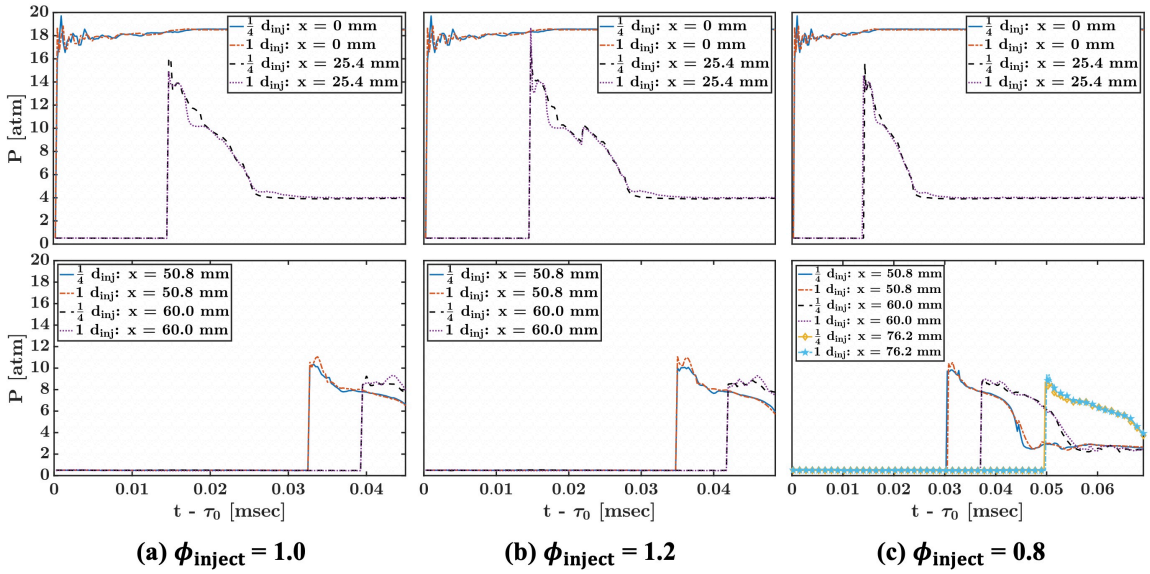

Figure 3.8: Pressure traces at the base of the LMDE channel for (a) case 1a; (b) case 2; and (c) case 3, at the prescribed locations.

3.1.4 H_2/air behavior with full channel inflow

In cases 1a, 2, and 3, the diffraction of the detonation wave as it enters the LMDE is a definitive mechanism leading to the separation of the shock front and reaction zone. Thus, the loss of wave energy causes the wave to dissipate further downstream of the channel. An additional investigation was performed into the effect of an inflow with a largely planar detonation wave with momentum primarily oriented along the streamwise direction. Here, the three-dimensional detonation wave inflow is sampled repeatedly along the inflow plane by patching the right-running detonation wave across the full cross-section of the LMDE channel. This inflow creates a detonation wave with a corrugated wave front with motion orthogonal to the jet-streamwise direction. This eliminates the pre-detonator tunnel, removing the influence of wave diffraction on the behavior and stability of the wave.

Figure 3.9 contains a numerical Schlieren image of the detonation wave as it passes the 3rd injector, observed in the mid-plane of the spanwise direction. Here, the complex reaction zone is closely attached to the detonation wave front. The region of the wave crossing the hydrogen fuel locally accelerates, creating a curved detonation wave front as opposed to the flat wave front above the extent of the jets, corresponding to the region with pure air as the background gas. The interaction between the flat wave front and curved zone of reaction creates a shear layer, allowing unburnt hydrogen/air mixture to enter the region behind the detonation wave front through turbulent mixing processes. The base of the detonation wave exhibits the existence of triple points due to the reflection of the transverse waves with the walls in the spanwise direction, and the base of the channel. The shock front is curved in the lower portion of the domain where the lower density from the presence of hydrogen allows the front to accelerate. In comparison to cases 1a, 2, and 3, the shock front and reaction zone are coupled for a greater wall-normal distance from the base of the channel, with the two regions separating only where no fuel is present. Here, an oblique

shock stems from the detonation wave front below. The shock front is fairly flat where no detonation occurs, with the post-detonation species from the inflow simply being convected through the domain, lagging behind the pressure front. Within the region of fuel and air mixture, there is a complex reaction zone with partially-burnt product gas, similar to the structure observed in the experimental results. Within the turbulent flow region, the variation of scalars across the detonation wave front is similar to cases 1a, 2, and 3, where bands of post-detonation products from previous injectors are compressed behind the detonation front.

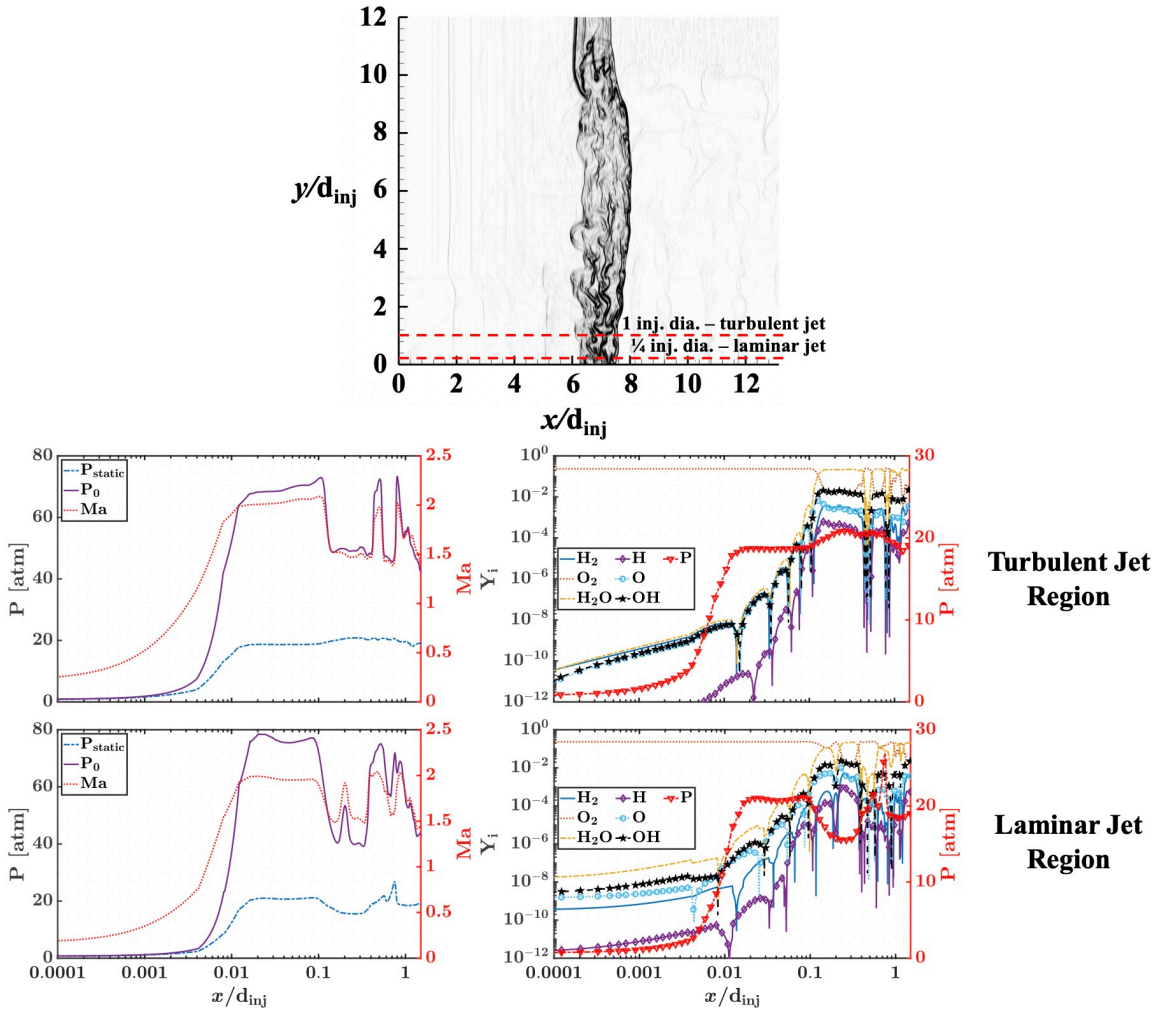

Figure 3.9: Case 1b; detailed pressure, Mach number, and species mass fraction behavior normal to the shock front as the wave passes the 3rd injector.

The pressure versus specific volume plot for case 1b is shown in Fig. 3.10. The region of strong detonation is equally distributed along the wave front, due to the planar nature of the wave front. The strongest detonations are observed near the base of the injector within a height of a few injector diameters from the base of the channel. However, due to the mixing of excess hydrogen/air throughout the channel fill region, detonations of increased strength are observed up to the height of 10 injector diameters above the base of the channel. The heat release rate per unit volume plot features a lower bound at the hydrogen/air detonation pressure as the majority of the wave front is in the detonation mode, as given by the Rankine-Hugoniot curve. The peaks above the post-detonation pressure correspond to triple points and shock interactions. The peak pressure observed in this inflow configuration is lower than that of case 1a, although detonation is sustained for the full length of the injector array. This is confirmed by observing the pressure-time traces of the channel at a height of 1/4 injector diameter and 1 injector diameter, outlined in Fig 3.11. The initial pressure trace is very similar to case 1a. However, at a streamwise location between the 4^{th} and 5^{th} injectors, the pressure peak increases from the initial condition, due to the ignition at the wave front. Further downstream, the pressure peaks exhibit spurious values due to the lack of pressure loss from the radial expansion of the detonation wave. The wave front pressures at locations downstream are largely stable, varying between 16-18 atm. This value is higher than the one-dimensional result due to the existence of flow non-uniformities such as triple points. However, peak pressure does not diminish as observed in cases 1a, 2, and 3.

The shock front velocity contour and average value as a function of streamwise location are displayed in Fig. 3.12, computed in the mid-plane along the spanwise direction. The shock speed is computed through the method described in Sec. A.3. It is noteworthy that the shock front velocity is highly correlated to the injector locations. These local accelerations of the shock front occur in the region following

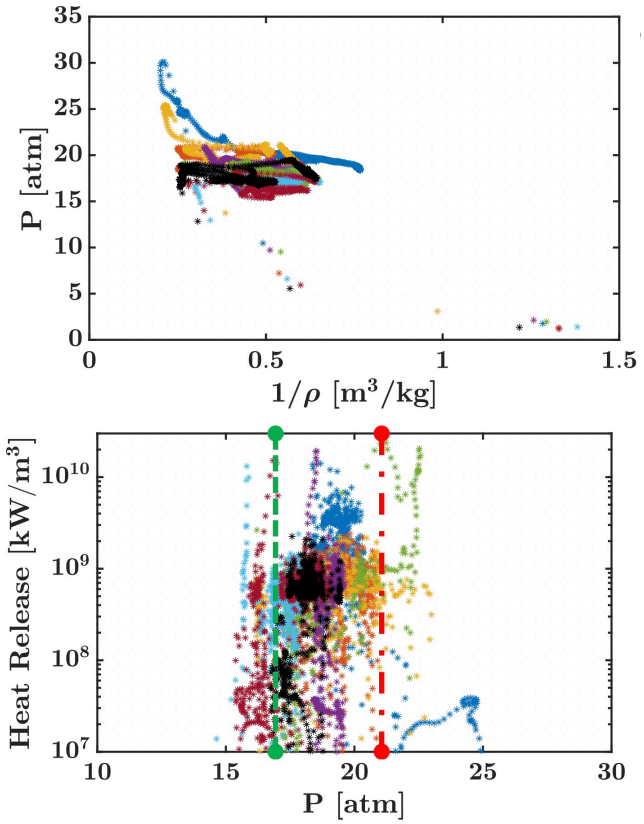

Figure 3.10: Case 1b; (top) pressure versus specific volume (Rankine-Hugoniot) and (bottom) heat release rate per unit volume relations as the detonation wave passes the 3rd injector. Legend: * : Injector Base; * : 1.0 x/d_{inj}; * : 2.6 x/d_{inj}; * : 4.0 x/d_{inj}; * : 5.5 x/d_{inj}; * : 7.0 x/d_{inj}; * : 8.5 x/d_{inj}; * : 10.0 x/d_{inj}; - - - : deflagration pressure; - · - · - : detonation pressure.

the injector centerline. This is due to the lower-density background medium resulting from the presence of hydrogen gas above the injectors. Furthermore, the ignition of hydrogen also accelerates the wave front as the pressure front and reaction zone reattach following each subsequent ignition process. Due to the ignition delay time of hydrogen/air combustion, the wave front travels beyond the injector centerline prior to fuel ignition. Thus, the high velocities are offset to the jet centerline locations but are clearly correlated. Within the array of injectors, the highest accelerations are observed near the base of the channel. In the turbulent region further away from the channel base, the velocity is more uniform as the density stratification is less apparent. The induced shock front velocity is generally much higher than the one-dimensional

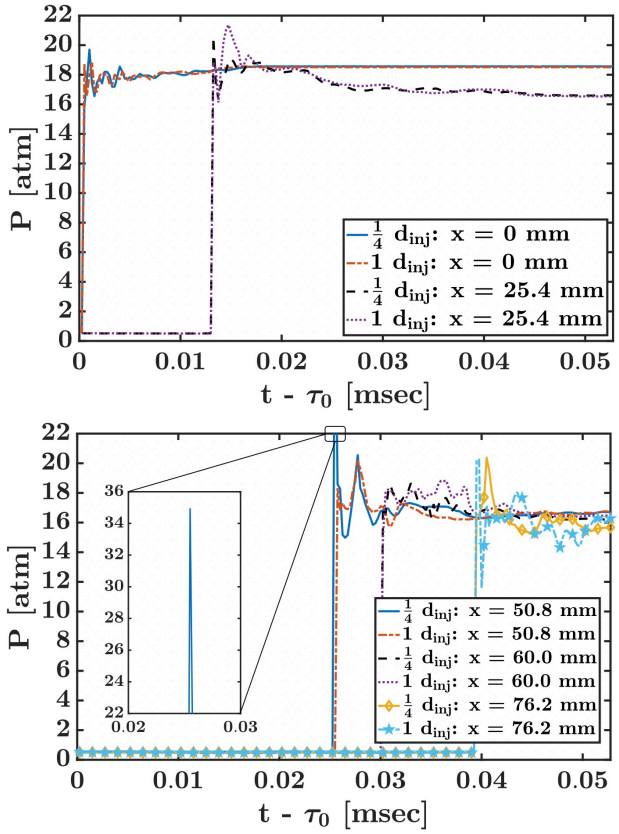

Figure 3.11: Case 1b; pressure traces at various streamwise locations at the base of the LMDE channel.

solution for the stoichiometric equivalence ratio. Thus, the partially-premixed nature of the fuel/air mixture further away from the base of the channel induces flow property variations in comparison to the ZND detonation wave. The average shock velocity figure shows a steady decline in the induced shock front velocity with streamwise location. However, the decay becomes more gradual further downstream, resembling the experimental behavior observed in the pressure-time traces at locations more downstream of the LMDE. Thus, the detonation wave tends to adapt to the flow conditions and approaches a stable configuration.

3.1.5 H_2/O_2 case with detonation tube inflow

The limited detonability of the H_2/air cases 1a, 2, and 3 resulted in a detonation wave behavior different from that of the experimental trials. As a result, an

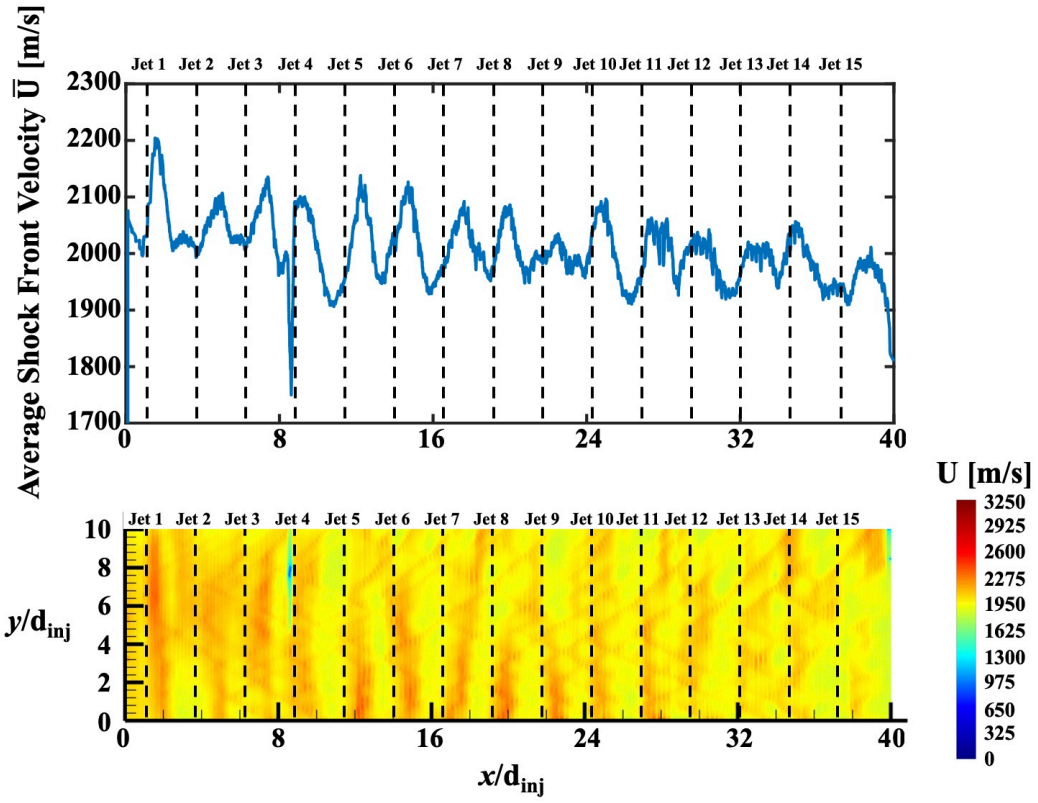

Figure 3.12: Shock U velocity history in the LMDE for Case 1b, with jet centerline locations of the 15 injectors outlined with black markings.

additional case with pre-detonator inflow and a H_2/O_2 fuel/oxidizer mixture was examined to validate the detonability of the injection mixture in the LMDE. The ambient pressure was additionally increased to 1 atm to replicate the experimental conditions. Hydrogen-oxygen combustion is characterized by high heat release and a small induction length of 53 μm [230]. The lower ignition delay time allows the mixture to more readily detonate in the presence of a detonation wave. For this case, a three-dimensional detonation wave was developed in a homogeneous stoichiometric mixture of H_2/O_2 through the method described in Sec. 2.1.7.2. The inlet boundary condition is prescribed as the detonation wave from the pre-detonator.

A detailed time history of the detonation wave as it enters the LMDE for the hydrogen/oxygen case is provided in Fig. 3.13. The numerical Schlieren image sequence shows the wave diffracting into the surrounding gas. In comparison to the

H_2/air case, the detonation wave initially maintains a narrower reaction zone, characterized by sharper density gradients at the shock front. Furthermore, the shock and the detonation front are closely attached, with inflection points along the shock front corresponding to the triple point locations. As the reaction zone broadens, it is characterized by multiple pressure and shock waves, and vortices mixing the post-detonation and intermediary gases. The processed detonation gases exit the reaction zone at injection height. Further away from the base of the channel, the shock and pressure fronts separate. However, the interface between the attached and separated wave front serves as confinement to support detonation below the injection height. At the base of the channel, the reaction zone widens due to viscous effects near the wall, leading to an increase in boundary layer thickness δ with detonation wave streamwise distance. The boundary layer-induced drag and reflected pressure waves from the wall increase pressure locally near the wall. Thus, residual post-detonation gases within and trailing behind the detonation reaction zone reignite under ideal detonable conditions as the wave is midway through the LMDE. The shock and detonation wave stemming from the reignition kernel accelerate into the primary reaction zone, acting to broaden the overall detonation wave. The detonation wave base accelerates due to the low-density hydrogen/oxygen mixture offering reduced resistance to the wave front. The confinement effects induced by the wall and the fuel-background air interface at the injection fill height provide the support required to sustain the detonation wave. This behavior is also observed in case 1b as the upper confinement interface is clearly defined.

Figure 3.14 depicts a numerical Schlieren image of the detonation wave as it passes the 3$^{\text{rd}}$ injector, observed in the mid-plane of the spanwise direction. The detailed species behavior is similar to prior cases, with previously-processed post-detonation and intermediary gases entrained within the reaction zone. The partially-burnt gases from preceding jets are continuously reacting. Specifically, there are 3 distinct maxima

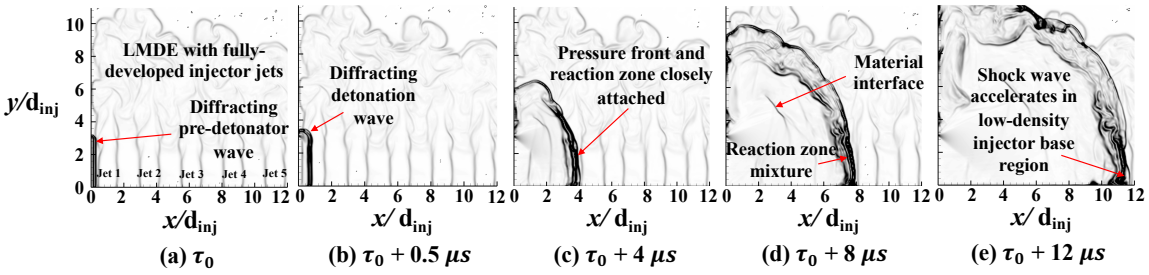

Figure 3.13: Detonation wave from the pre-detonator inflow entering the LMDE with H_2/O_2 injector jets.

in the free radical concentration, corresponding to the ignition of gases from the current injector and the 2 previously-processed injectors. For example, as the wave is passing the 3rd injector, there exist three distinct regions of ignition until the species concentrations stabilize to the post-detonation condition. Similarly, the pressure and Mach number profiles exhibit oscillations within the reaction zone prior to reaching the post-detonation condition.

Figure 3.15 features the pressure versus specific volume relation and heat release rate per unit volume up to a height of 6 injector diameters from the base of the channel for case 4. In comparison to the H_2/air cases, the pressure and heat release rate peak at a height of 1-2 injector diameters from the base of the channel. This is due to a change in the wall-normal distance at which the injector jet transitions to turbulence; in the H_2/air cases, the injector jet transitions to turbulence at 1 injector diameter whereas in the H_2/O_2 case, the jet remains laminar until 2 injector diameters due to a change in the Reynolds number. The Reynolds number of the H_2/O_2 case at 47,000 is roughly 50% higher than that of the H_2/air case at 30,000. Thus, detonation strength is a balance between the local equivalence ratio of the injector jet and the amount of turbulent mixing further downstream of the injector jet. The local equivalence ratio of the injector jet decreases with wall-normal distance within the turbulent mixing region. Therefore, at the location of jet transition to turbulence, the local equivalence ratio is maximized within the turbulent region. Turbulence aids the mixing process of

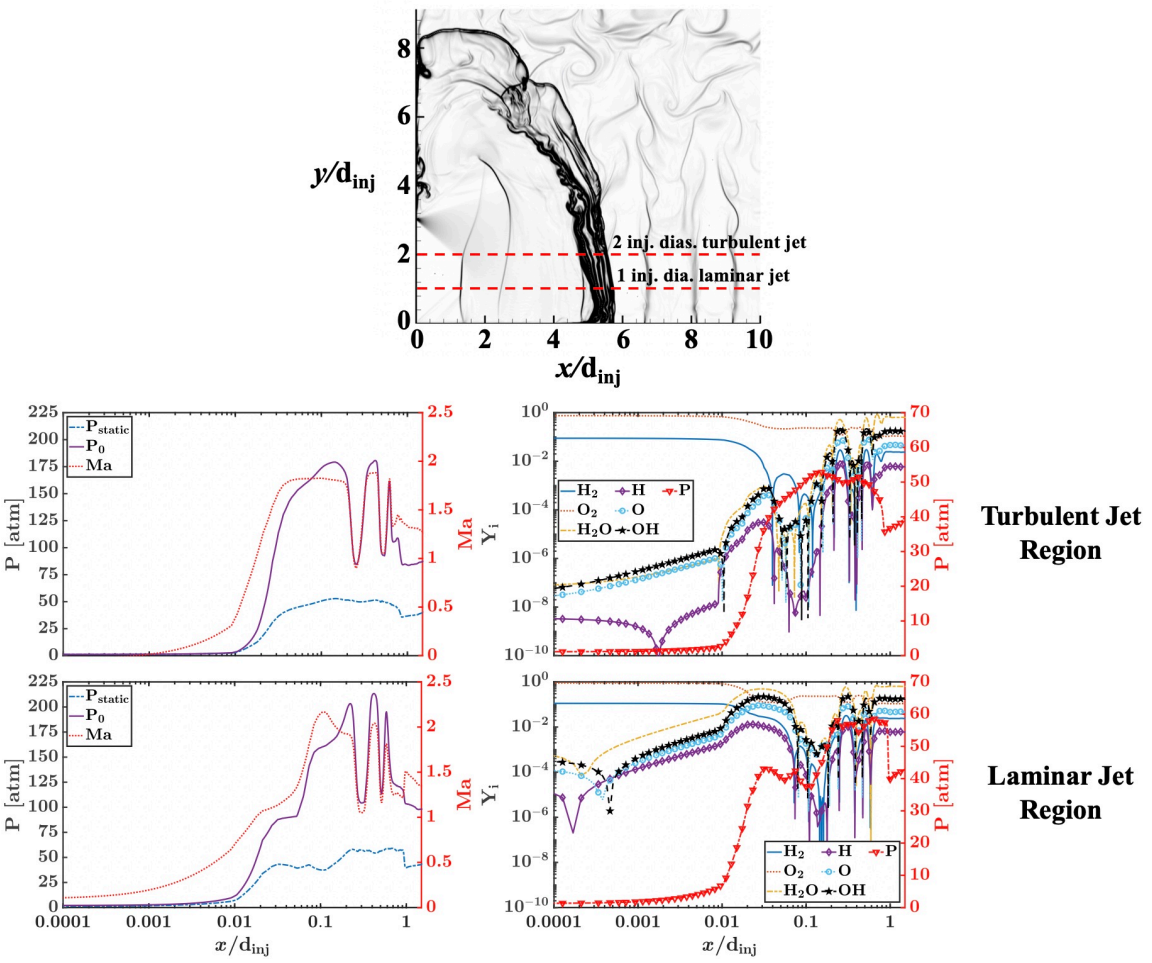

Figure 3.14: Case 4; detailed pressure, Mach number, and species mass fraction behavior normal to the shock front as the wave passes the 3rd injector.

the fuel/oxidizer mixture with the detonation wave, lending to stronger detonations. Further along in the jet-streamwise direction, combustion transitions from strong detonation to deflagration. In the Rankine-Hugoniot relation, fluid particles processed by the detonation wave are compressed and transition to Rankine-Hugoniot curves of higher heat release, up to the Chapman-Jouguet condition. Similarly, in the heat release rate per unit volume relation, a peak is observed at a post-detonation pressure of roughly 33 atm, with additional peaks in the 50-70 atm range. These peaks occur at heights of 1-2 injector diameters from the base of the channel. The secondary mode in the heat release rate per unit volume plot corresponding to deflagration

would become more prominent with additional passes of a detonation wave through the residual gases.

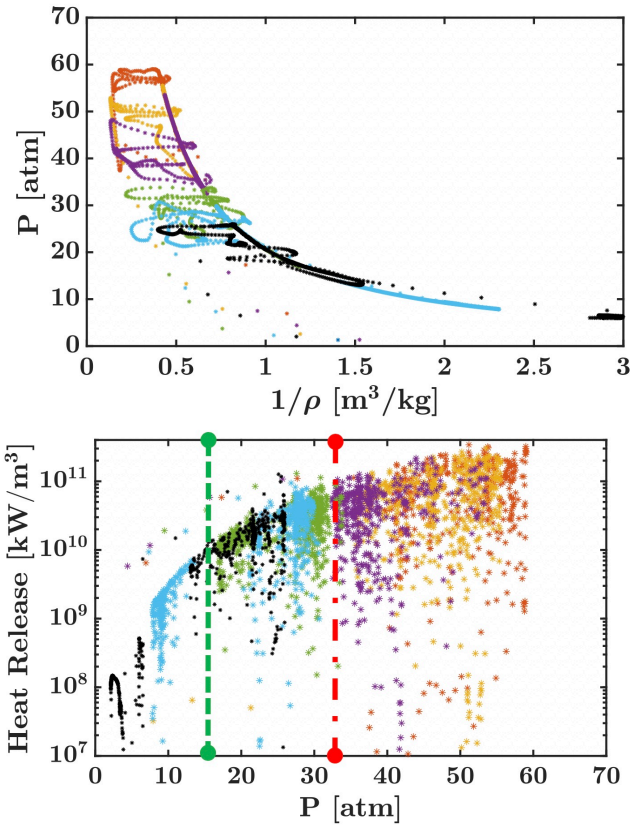

Figure 3.15: Case 4; (top) pressure versus specific volume (Rankine-Hugoniot) and (bottom) heat release rate per unit volume relations as the detonation wave passes the 3rd injector. Legend: * : Injector Base; * : 1.0 x/d_{inj}; * : 2.0 x/d_{inj}; * : 3.0 x/d_{inj}; * : 4.0 x/d_{inj}; * : 5.0 x/d_{inj}; * : 6.0 x/d_{inj}; - - - : deflagration pressure; - · - · - : detonation pressure.

The pressure trace of the channel for the H_2/O_2 case is given in Fig. 3.16. The pressure at the inflow plane corresponds to the post-detonation pressure of the channel detonation wave. Further downstream in the LMDE, the detonation wave is self-sustained by the ignition of the injected fuel/oxidizer mixture. The pressure at this location is similar to the inflow pressure. However, beyond the 8th injector, the detonation wave pressure has decayed to a stable condition corresponding to the post-detonation pressure for hydrogen/oxygen combustion of approximately 33 atm. The detonation wave has relinquished memory of its initially over-driven state and

has stabilized to a self-sustained condition. Thus, the detonation wave in case 4 does not dissipate as in cases 1a, 2, and 3.

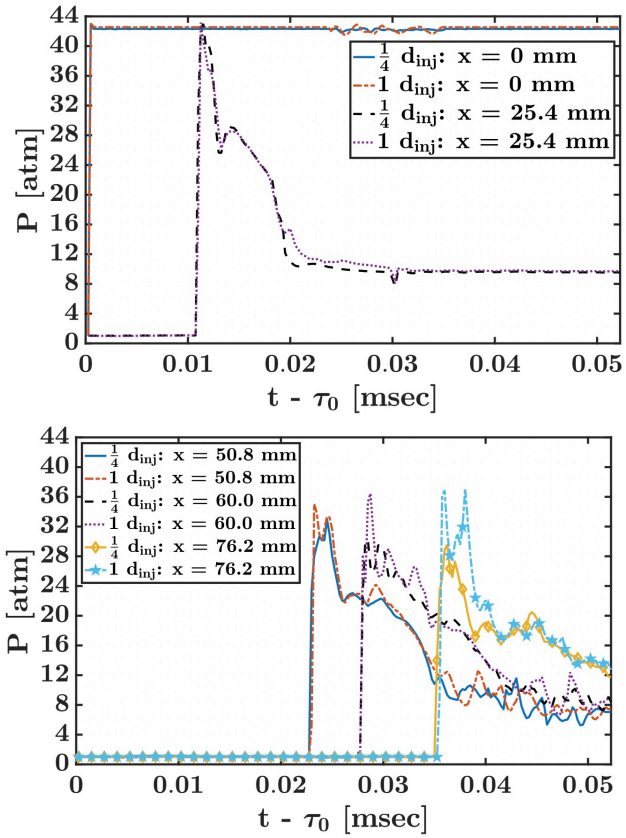

Figure 3.16: Case 4; pressure traces at various streamwise locations at the base of the LMDE channel.

3.1.6 Study conclusions

The detonation wave structure of hydrogen and air chemistry has been analyzed using three-dimensional simulations of the detonation wave. The confined channel detonation cases provide a fundamental understanding of the ZND profile, detonation cell structure, and the evolution of triple points in multiple dimensions. The canonical LMDE is used to understand the dynamics of an unwrapped RDE configuration with partially-premixed injectors at equivalence ratios of 1.0, 1.2, and 0.8 for H_2/air cases and 1.0 for H_2/O_2 cases. The results are compared to the experimental observations of Burr et al. [40]. The detonation wave structures and complex

reaction zones observed in the numerical simulation are similar to those seen in the experiment. The structures along the detonation front are multi-dimensional in nature. The region of detonation is characterized by a coupled high-pressure front and reaction zone. A detonation wave passing through non-detonable mixtures purely convects the initial species, causing them to lag behind the shock front. This shear layer between the detonable and inert regions lends to the increased mixing of the partially-burnt hydrogen and air within the reaction zone.

The use of the detonation tube to introduce a detonation wave of height smaller than the LMDE channel causes the wave to immediately diffract when entering the channel, and therefore lose energy due to the separation of the detonation front and reaction zone. In the H_2/air cases, the detonation wave dissipates midway through the LMDE. However, in the H_2/O_2 case at increased initial pressure, the detonation wave stabilizes halfway through the LMDE and sustains detonation due to differences in ignition delay time. For the H_2/air case, a detonation wave that spans the full height of the channel is able to sustain detonation throughout the array of injectors, exhibiting local accelerations of the wave front as it passes through mixtures of low-density hydrogen and consequently detonating. Thus, the present results show that the diffracting detonation wave in H_2/air cases with the pre-detonator inflow condition, incomplete mixing between the fuel and oxidizer, and the gap between successive injectors consisting of the non-detonable background gas affect the sustainability of the detonation wave. It should be emphasized that the initial pressure of 0.5 atm for cases 1a, 2, and 3, below the experimental value of 1 atm, may contribute to the unsustained detonation within the prescribed LMDE geometry. The confinement effects induced by the wall and the fuel-background air interface at the injection fill height provide the support required to sustain the detonation wave, as observed in the full inflow H_2/air and H_2/O_2 cases. Richer equivalence ratios sustain detonation for a greater streamwise distance, as the local equivalence ratio following

turbulent mixing with the background gas is closer to or above stoichiometric conditions. Furthermore, for the H_2/air cases, the highest peak pressures and strongest detonations are generally observed within one injector diameter from the base of the channel, where the injector flow is turbulent. Similarly, for the H_2/O_2 case, the highest peak pressures are observed within one to two injector diameters from the base of the channel, where the hydrogen/oxygen injector jets transition to turbulence. However, the largest magnitude of wave front local acceleration is observed near the base of the channel where the local density is the lowest. Thus, the detonation wave characteristics differ from the one-dimensional condition, as the wave adapts to local variations in the flow properties.

The canonical linearized configuration is a simple geometry that allows for significant analysis of the stability of the detonation wave. The results provide insight into the detonation wave structure, the flow features that lend to wave stability, and the effect of equivalence ratio and density fluctuations in the flow field. The LMDE configuration provides details of the evolution of the detonation wave as it propagates downstream. Further analysis of detonation wave stability through a stratified, partially-burnt mixture of fuel, air, and post-detonation products will provide knowledge of the flow features observed within a periodic RDE.

3.2 Detonation Propagation through a Stratified Mixture

3.2.1 Motivation

In practical designs being considered now [50, 52, 76, 316], the fuel and oxidizer streams are injected separately, where they enter the annulus region and mix. The annulus within an RDE features a complex distribution of fuel/oxidizer due to the turbulent mixing of the fuel and oxidizer streams, with regions of varying equivalence ratios. This stratification is driven by the recirculation zones and free shear/jet

interactions within the injector plenums and RDE annulus. Prior studies [44] have shown that the mixing process directly determines the detonation wave characteristics. In particular, poorly-mixed gases have an effect similar to that of inert diluents on mixture detonability [189]. Since the RDE is a continuously operating device, post-detonation gases interact with incoming fresh fuel and oxidizer streams, which may lead to premature ignition. Such residual gases have a substantial effect on detonation wave propagation velocity in the non-premixed operation mode [95]. Understanding the impact of such mixing processes on RDE performance is crucial for realizing the potential of pressure gain combustion.

In the past, several studies have explored the role of such inhomogeneities on detonation wave propagation in canonical flows. In a three-dimensional detonation wave, transverse shock waves stemming off the triple points of the primary detonation front periodically interact [97, 162]. The collision of these waves creates regions of high temperature and pressure. The triple points serve to reattach the shock and reaction fronts of the detonation wave [235]. The shock front is accelerated at the triple-point collision point. The subsequent expansion zone serves to decelerate and weaken the shock front [235, 251]. The periodic triple-point collision process creates a series of detonation cells, often visualized using a soot foil [226, 271]. Fuel concentration gradients have been shown to induce curvature of the detonation front, leading to irregular detonation cell sizes [133]. The mixture inhomogeneity forces the leading detonation wave front to decouple from the reaction zone, activating a turbulent deflagration mode [149]. Additionally, the peak detonation pressure and the overall detonability of mixtures are altered [251]. The concentration gradients in the reactant mixture affect the detonation cell shape, wave stability, and pressure distribution [75]. Boulal et al. experimentally studied the effect of mixture composition gradients parallel to the direction of detonation propagation, stating that quenching is controlled by the magnitude of the composition gradient and its characteristic length [32]. Further-

more, transverse concentration gradients have been extensively studied by Boeck et al., where steep composition gradients do not quench detonation but rather diminish wave propagation velocities in comparison to those of homogeneous mixtures [30]. However, sharp concentration gradients result in single-headed, unstable detonation waves with "galloping" wave front behavior.

Numerical simulations of transverse concentration gradients in a confined channel showed that instabilities promote flame acceleration and strong detonation-to-deflagration transition (DDT) in unobstructed channels [150], similar to the geometry studied here. Thus, overall detonation stability is affected due to the fuel concentration gradient, and rapid changes in the composition narrow the detonability envelope. Spatial inhomogeneity has been previously studied through one- and two-dimensional numerical simulations with single-step Arrhenius chemical kinetics by introducing a detonation wave to discrete reactive layers and squares, respectively [187]. Here, the fuel sources are spaced regularly within the domain. With sufficiently inhomogeneous mixtures, where the spacing between successive reactive zones is greater than the reaction zone length, a "super-CJ" (Chapman Jouguet) wave behavior is observed, with propagation speeds 15 percent higher than the CJ speed of a homogeneous mixture [188]. Thus, discretely-placed fuel sources act as concentrated pockets of energy release and enforce a non-equilibrium state for the detonation wave. Levin et al. showed that the presence of non-reacting pockets of gas alters the local propagation speed of the detonation wave [167], leading to the complex wave structures seen in the experiments. Similarly, numerical simulations of detonations in pulse detonation engines (PDEs) show that the wave speed fell drastically when propagating through lean fuel/air mixtures [224]. In a linear RDE configuration [40, 235], similar behavior of local wave acceleration/deceleration was observed when passing between discrete sets of injectors. Hence, given the total fuel mass, the detonation structure depends on the distribution of this fuel within the system. The current study extends past work

by imposing discrete fuel sources distributed in irregularly-shaped patches within a confined channel; concentration gradients are not solely aligned parallel or transverse to the direction of detonation propagation.

Within an RDE, there is variation in the local equivalence ratio, leading to differing heat release profiles in the fuel-rich and fuel-lean regions. To understand the propagation of a detonation wave through a stratified reactant mixture, channel detonation with irregular fuel/air patches is modeled. However, as the inhomogeneity is highly uncertain, the influence of the fuel/air stratification length scale is characterized. The interaction of the fuel/air mixture and the detonation wave is driven by multi-scale turbulence, which requires that flow gradients be properly resolved. Thus, a direct numerical simulation approach with detailed chemical kinetic mechanisms is required to model the detonation wave behavior accurately. The study will evaluate the effect of fuel/air stratification at various length scales on detonation wave behavior and the subsequent turbulent mixing mechanisms. An initial scalar field is generated using a scalar energy spectrum function where the integral length scale of the scalar distribution can be systematically altered, similar to the method of Eswaran et al. [74]. Section 3.2.2 explains the simulation configuration with the generation of the initial fuel/air stratification and inflow detonation wave detailed in Sec. 3.2.2.1 and Sec. 3.2.2.2, respectively. The results and discussion with a statistical approach and relevance to RDE performance are provided in Sec. 3.2.3. Finally, concluding remarks are outlined in Sec. 3.2.5.

3.2.2 Numerical representation

The annulus of the rotating detonation engine features a complex flow field and mixture distribution of fuel and oxidizer. The turbulent mixing of the fuel and oxidizer streams within an RDE creates reactant stratification, with regions of varying equivalence ratio arranged in irregular patches within the domain. This stratifica-

tion is driven by the recirculation zones and free shear/jet interactions within the injector plenums and the post-detonation mixing. The effect of fuel stratification on detonation wave propagation is studied using DNS with a detailed chemical mechanism. To replicate the wave structure in a practical RDE geometry, the linearized model detonation engine (LMDE) channel configuration of Burr et al. [40] and past wave structure analyses [235] is used. To this end, a narrow channel of length 14 cm, width 7.6 mm, and height 6.25 cm is modeled. The channel is filled with a background mixture of air (O_2-N_2) at 297 K and 0.5 atm. The fuel/oxidizer stratification is represented by hydrogen/air (H_2/air) and the generation of the scalar distribution is discussed in the following section (Sec. 3.2.2.1). As an extension of past studies of Prakash et al. [235], the operating pressure of the channel is lowered to 0.5 atm to increase detonation thickness such that the detonation wave can be adequately captured for a given numerical resolution. The ZND induction length ℓ_{ind}, established as the length scale of interest, for hydrogen/air combustion at 0.5 atm is analytically computed as 338 μm. At lowered pressure, the detonation structure is resolved by roughly 12 cells across the half-reaction length $\ell_{1/2}$ in the axial direction, while managing computational costs. Note that numerical simulations [235, 254, 257] and experiments [50] have shown that the incomplete mixing process and stratification reduce shock strength and increases the thickness of the reaction zone behind the shock in practical systems. The past analyses [235] contained grid convergence studies on one-, two-, and three-dimensional channel detonations with premixed stoichiometric hydrogen/air to verify that the macroscopic results are not sensitive to the range of grid resolutions considered. Additionally, the numerical results of Ref. [235] captured the experimental detonation wave structure, reaction-zone thickening, wave extinction behavior, and wave speed in partially-premixed configurations.

The present simulations only aim to resolve the larger scales through a macroscopic view of the detonation structure. As with past multi-dimensional simulations of

unsteady detonations [240], the numerical configuration does not resolve the fine-scale turbulent dissipation nor the diffusive mechanisms on the molecular scale. Thus, the simulations limit the range of scales that are represented and cut off the finer scales which would affect the flow field for computational tractability. Further, the choice of resolution introduces artificial dissipation at the larger scales that are captured. The high-fidelity simulations in the present study are performed with the aim of capturing the macroscopic detonation structure and characterizing wave propagation differences due to variations in the stratification length scale.

The channel is confined with walls in the stream normal and spanwise directions, and the right boundary is set as an outflow. The inflow boundary condition is prescribed by a sampled right-running, well-developed, three-dimensional detonation wave as a time-varying field. This inflow is generated using the outflow of an auxiliary three-dimensional premixed channel simulation detailed in Sec. 3.2.2.2. The grid resolution for the three-dimensional main geometry is uniform with a core region in the stream normal and spanwise directions, with clustered cells near the wall to properly resolve the boundary layer. Note that the near-wall regions are not included in the analysis, but the higher resolution is maintained to ensure that non-physical flow is not developed. In past studies, it was discovered that the boundary layer region is critical in entraining post-detonation gases and accurately representing the wall reflection of the triple points and pressure waves [235]. This results in a total of 303 million control volumes, with $2800 \times 858 \times 126$ points in x, y, and z directions, respectively. The clustered grid regions in the stream normal and spanwise directions extend up to 435 y^+ from the wall, where one y^+ is 0.6 μm. The clustered grid region is characterized by $\Delta y = \Delta z =$ 3.2-74.7 μm. Outside the near-wall region, $\Delta y = \Delta z = 75$ μm, corresponding to 8.3 cells per $\ell_{1/2}$. $\Delta x = 50$ μm throughout the domain, corresponding to 12.4 cells per $\ell_{1/2}$. The length scale of the fuel/air stratification within the domain is varied using the method described in the following section.

3.2.2.1 Fuel/air stratification

The fuel/air distribution within the domain is altered to investigate the interaction between stratification length scale and detonation wave propagation. The channel is prescribed with stratification of fuel and air using post-detonation turbulence to further drive the mixing of fuel and air. Using a method similar to Eswaran and Pope [74] and Hassanaly [115], a three-dimensional scalar field corresponding to fuel mixture fraction and equivalence ratio is generated within the channel. The initial scalar field, $\psi(\mathbf{x}, 0)$, is generated such that the PDF of the scalar values resembles a double-delta function, with either a value of 0 or 1, while keeping the field smooth enough to be well-resolved in the numerical simulation. The initial scalar field is created in three steps:

1. The Fourier amplitudes of the scalar field are assigned random values such that the resulting scalar-energy spectrum function is defined by a double-delta function. This is defined by:

$$\boldsymbol{\Psi(\mathbf{k}, 0)} = \left[\frac{f_\psi(k)}{4\pi k^2}\right]^{1/2} e^{2\pi i \theta(\mathbf{k})} \tag{3.1}$$

   where k is the magnitude of wavenumber vector $\mathbf{k}$, $\theta(\mathbf{k})$ is the uniformly-distributed random number between 0 and 1 (independently chosen at each point), and $f_\psi(k)$ is the scalar-energy spectrum function.

2. The scalar field is transformed into physical space using an inverse-Fourier operation. Here, the scalar value at each location in physical space is reset to 0 if negative, and 1 if positive.

3. The scalar field is retransformed into spectral space using the Fourier transform operation. In order to correct for large changes across adjacent cells, the Fourier amplitudes of the scalar field are scaled by a filtering function, $F(\mathrm{k})$, to remove

the high wavenumber components of the scalar field:

$$F(\mathrm{k}) = \begin{cases} 1, & \text{if } k < k_\mathrm{c} \\ (k_\mathrm{c}/k)^2, & \text{if } k > k_\mathrm{c} \end{cases} \tag{3.2}$$

where k_c is a cutoff wavenumber. The specified cutoff wavenumber is calculated as:

$$k_\mathrm{c} = (k_\mathrm{c}/k_\mathrm{s})_\mathrm{ratio} * k_\mathrm{s} \tag{3.3}$$

where k_s is a selected integer wavenumber, defined as:

$$k_\mathrm{s} = (k_\mathrm{s}/dk)_\mathrm{ratio} * dk \tag{3.4}$$

where dk is the width of the scalar-energy spectrum function. Thus, the parameters $(k_\mathrm{c}/k_\mathrm{s})_\mathrm{ratio}$ and
$(k_\mathrm{s}/dk)_\mathrm{ratio}$ are characteristic parameters.

To observe the effect of the fuel/air stratification, the length scale of the initial scalar field must be precisely altered. Thus, the scalar-energy spectrum function must be changed systematically. Applying the method of Eswaran and Pope [74], the scalar-energy spectrum function is calculated as:

$$f_\psi(k) = \begin{cases} 1, & \text{if } k_\mathrm{s} - dk/2 \leqslant k \leqslant k_\mathrm{s} + dk/2 \\ 0, & \text{if } k \leqslant k_\mathrm{s} - dk/2 \text{ or } k \geqslant k_\mathrm{s} + dk/2 \end{cases} \tag{3.5}$$

The width of the top-hat portion of the scalar-energy spectrum function, dk, is defined as:

$$dk = \frac{2\pi}{L_{\text{char}}} \tag{3.6}$$

where L_{char} is a characteristic large length scale within the domain. In this study, since the channel is of non-uniform length in the streamwise, stream normal, and spanwise directions, the stream normal length scale (height of the channel) is selected as L_{char}. This selection provides an adequate patch size and scalar distribution for the physical size of the channel domain. The characteristic parameters $(k_{\text{c}}/k_{\text{s}})_{\text{ratio}}$ and $(k_{\text{s}}/dk)_{\text{ratio}}$ determine the high-wavenumber cutoff and the integral length scale of the scalar distribution, respectively. The former is proportional to the high-wavenumber scalar energy of the scalar distribution and the latter is inversely proportional to the integral length scale of the scalar distribution. For the purposes of this study, a value of $(k_{\text{c}}/k_{\text{s}})_{\text{ratio}} = 2$ is selected as it provides a well-resolved initial scalar field. This parameter is held constant in all cases. Statistical information on the spatial structure of the initial scalar field is given by the two-point correlation:

$$R_{ij}(\mathbf{r}, \mathbf{x}, 0) = \langle \psi_i'(\mathbf{x}, 0)\psi_j'(\mathbf{x} + \mathbf{r}, 0)\rangle \tag{3.7}$$

where $\mathbf{r}$ is the vector between points i and j, $\mathbf{x}$ is the location at which the two-point correlation is evaluated, and $\psi'(\mathbf{x}, 0)$ is the fluctuation of the initial scalar field in the domain. Thus, the streamwise integral length scale is determined as:

$$L_{11}(\mathbf{x}, 0) = \frac{1}{R_{11}(0, \mathbf{x}, 0)} \int_0^\infty R_{11}(\mathbf{e_1} r, \mathbf{x}, 0)\text{dr} \tag{3.8}$$

where $\mathbf{e_1}$ is the unit vector in the streamwise-coordinate direction and r is the distance between points i and j.

The scalar distribution field is rescaled to be representative of the mixture fraction, Z_{mix}, such that the minimum and maximum equivalence ratios are 0.0 and 1.3, respectively. For hydrogen/air combustion, the minimum and maximum mixture

Table 3.2: Fuel/air stratification parameters for different cases

	Case 1	Case 2	Case 3
$(k_\mathrm{s}/dk)_\mathrm{ratio}$	30	20	10
$(k_\mathrm{c}/k_\mathrm{s})_\mathrm{ratio}$	2	2	2
L_{11} [mm]	0.581	0.894	1.854
ϕ_min	0	0	0
ϕ_max	1.309	1.300	1.304
$\langle \phi'^2 \rangle$	0.187	0.187	0.187
$\sqrt{\langle \phi'^2 \rangle}$	0.433	0.433	0.433
m_fuel [mg]	0.4869	0.4869	0.4869
P_amb [atm]	0.5	0.5	0.5
T_amb [K]	297	297	297

fractions corresponding to the aforementioned equivalence ratios are 0 and 0.0368, respectively. The fuel and oxidizer mass fractions are computed accordingly and the local density is computed using the ideal gas law. Thus, the initial scalar field $\psi(\mathbf{x}, 0)$ is rescaled to the initial equivalence ratio field $\phi(\mathbf{x}, 0)$.

In this study, a fuel/oxidizer mixture consisting of hydrogen and air is considered. In each case, only the scalar field length scale is varied. The fuel/air patches are at ambient conditions of 297 K and 0.5 atm. Thus, the conditions do not allow the fuel patches to prematurely react before being processed by the detonation wave. For this discussion, the test cases, their stratification length scales, and associated parameters are outlined in Table 3.2. Based on numerical simulations of rotating detonation engines [254, 257], the detonation thickness has been found to be on the order of a few millimeters length. Thus, the stratification length scales studied here are within the range of practical detonation length scales, ranging from just below the observed detonation thickness for Case 1 to the same order as the observed detonation thickness for Case 3. The fuel/air distributions within the channel for cases 1, 2, and 3 are displayed in Figs. 3.17, 3.18, and 3.19.

The medium stratification length scale is used as the baseline case. The random numbers as a function of wavenumber are stored, such that $\theta(\mathbf{k})$ is preserved among

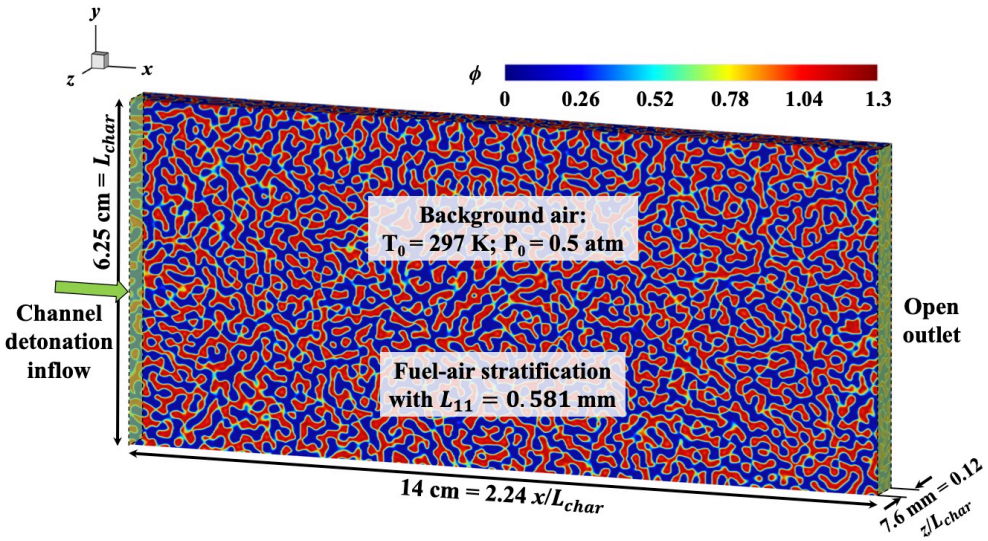

Figure 3.17: Fuel/air stratification within the channel domain, displayed as equivalence ratio contour, for case 1.

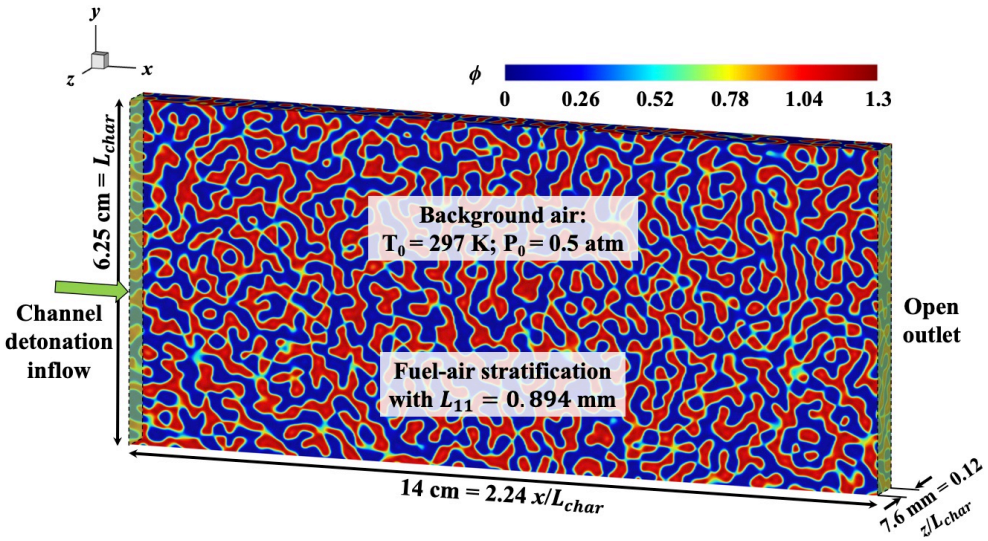

Figure 3.18: Fuel/air stratification within the channel domain, displayed as equivalence ratio contour, for case 2.

all cases. Thus, the difference between the cases is in the scalar-energy spectrum function, due to the choice of characteristic parameters and their influence on the rectangular top-hat function defined by Eq. 3.5. The parameter $(k_s/dk)_{\text{ratio}}$ is varied to change the stratification length scale. The primary aim is to conserve exactly the total fuel mass within the channel domain in all three cases. As a result, the mixture fraction distribution is scaled by a constant value to obtain the total fuel

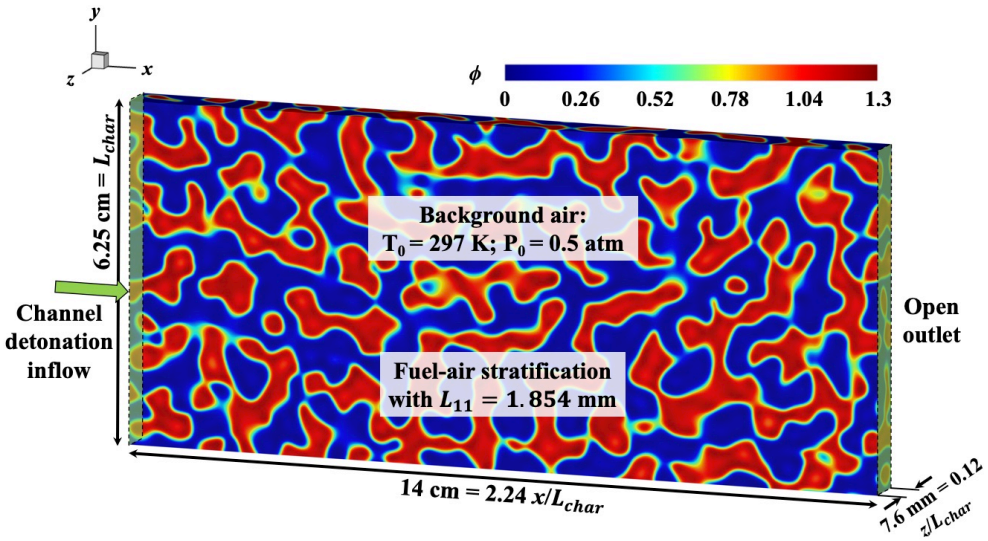

Figure 3.19: Fuel/air stratification within the channel domain, displayed as equivalence ratio contour, for case 3.

mass of the baseline case. As a result, the maximum equivalence ratio across all three cases is within 0.1% of 1.3. The mean, variance, and subsequently, the standard deviation, of the equivalence ratio are also conserved to within 0.1% across all three cases. The initial fuel/air distribution is at a homogeneous temperature and pressure, as described in Tab. 3.2, with quiescent flow. A well-developed three-dimensional detonation wave (as described in the following section) is then introduced into the channel containing the fuel/air stratification.

3.2.2.2 Three-dimensional channel detonation

Confined channel detonation characterizes the detonability and cell structure of fuel mixtures. A three-dimensional configuration, as shown in Fig. 3.20, is used to initialize a stable detonation wave within a closed channel. This serves as an auxiliary calculation to the main set of simulations. The channel detonation features a uniform grid of 304 million cells with $\Delta x = \Delta y = \Delta z = 50$ μm, corresponding to 12.4 cells per $\ell_{1/2}$. The channel is of length 8 cm, width 7.6 mm, and height 6.25 cm. The stream normal and spanwise boundaries are walls to provide the confinement

required to sustain detonation. The channel domain is initially divided into two regions: a stoichiometric hydrogen/air mixture at ambient temperature and pressure on the right, and a hydrogen/air analytic detonation solution on the left. Cubic sparks of high-temperature and pressure stoichiometric hydrogen/air mixture are placed 500 μm ahead of the standing detonation wave to serve as perturbations to the passing detonation wave. The upper schematic in Fig. 3.20 shows the series of stacked sparks of reactants ahead of the standing detonation wave in the channel.

The flow field disturbances distort the wave front and trigger the formation of stream normal and spanwise waves, which reflect from the channel walls and form triple points within the domain. In a three-dimensional configuration, the triple points are allowed to travel across the wave front, and subsequently, shock waves emanate radially from the collision of triple points. The collision of triple points enhances detonation strength by locally creating high-temperature and pressure regions, where the reaction front of detonation is closely attached to the leading pressure wave. The interaction of the reflected pressure waves forms a corrugated wave front where the trace of triple points across the stream normal plane form isolines of high temperature and pressure, as depicted in Fig. 3.21. The addition of the third dimension of spatial variation enhances the highly irregular wave front with distortion due to local flow acceleration. To ensure that the cellular structures are regular after an initial transition period, the detonation wave front is shifted left to the entrance of the channel, and the wave is allowed to travel through the channel once again. This method creates an essentially infinite-length channel. As the detonation wave approaches the end of the channel, the triple points propagate at a constant frequency and the detonation wave is stable and well-developed. The wave speed converges to the equilibrium Chapman-Jouguet (CJ) wave speed at "steady-state" propagation. The steady-state wave speed is generally within 5% of the theoretical value of 1954 m/s (derived from analytical computations of hydrogen/air detonation), indicative of stable detonation.

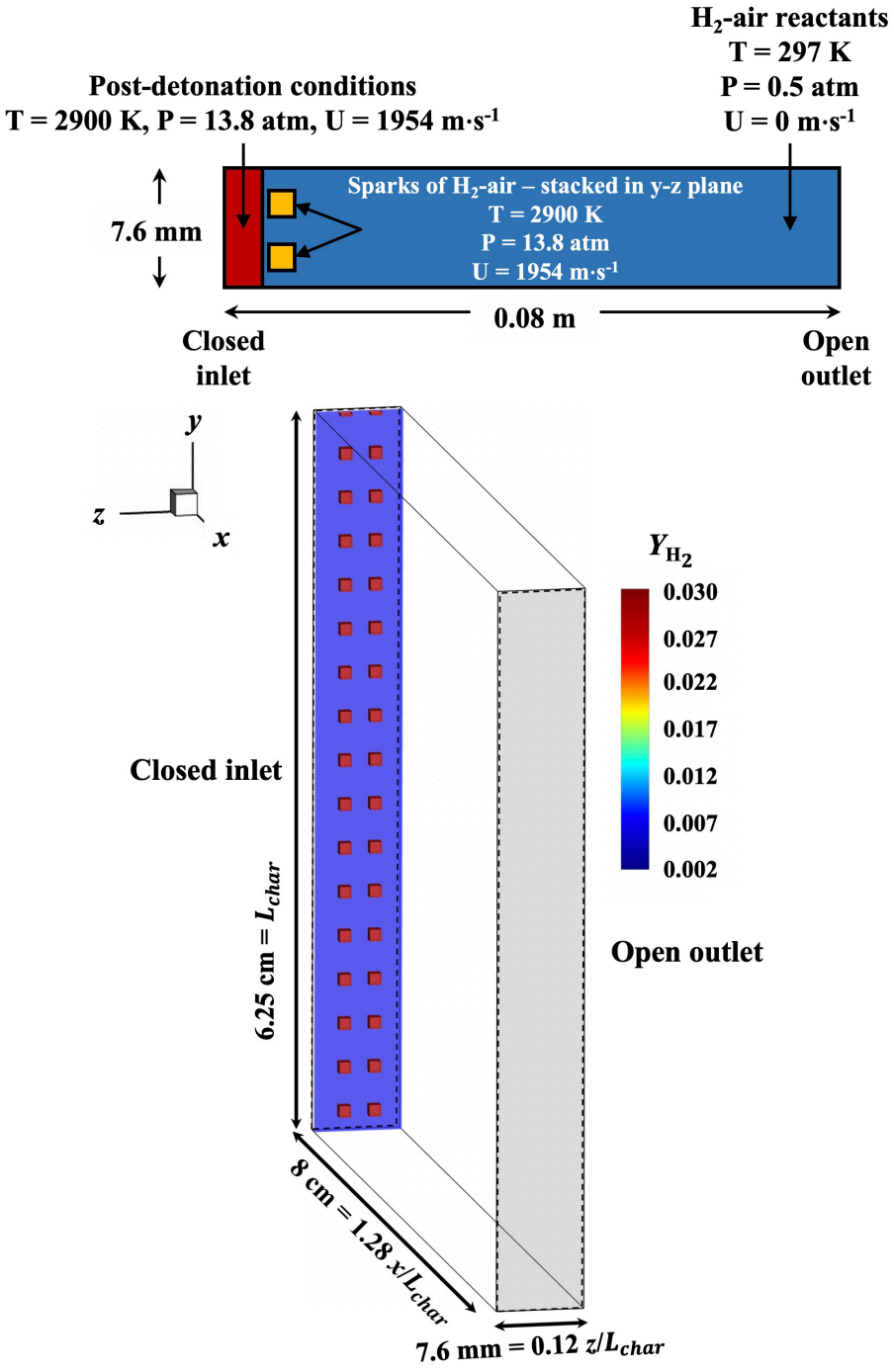

Figure 3.20: (Top) Channel configuration for the three-dimensional channel with disturbance sparks to perturb the detonation wave and (bottom) three-dimensional channel detonation initial configuration with high-temperature and pressure sparks of reactant gas ahead of a standing detonation wave.

The detonation wave is sampled as a high-frequency (100,000,000 Hz) time-varying field at the outflow plane to be applied as an inflow boundary condition through the fuel/air stratification (discussed in Sec. 3.2.2.2).

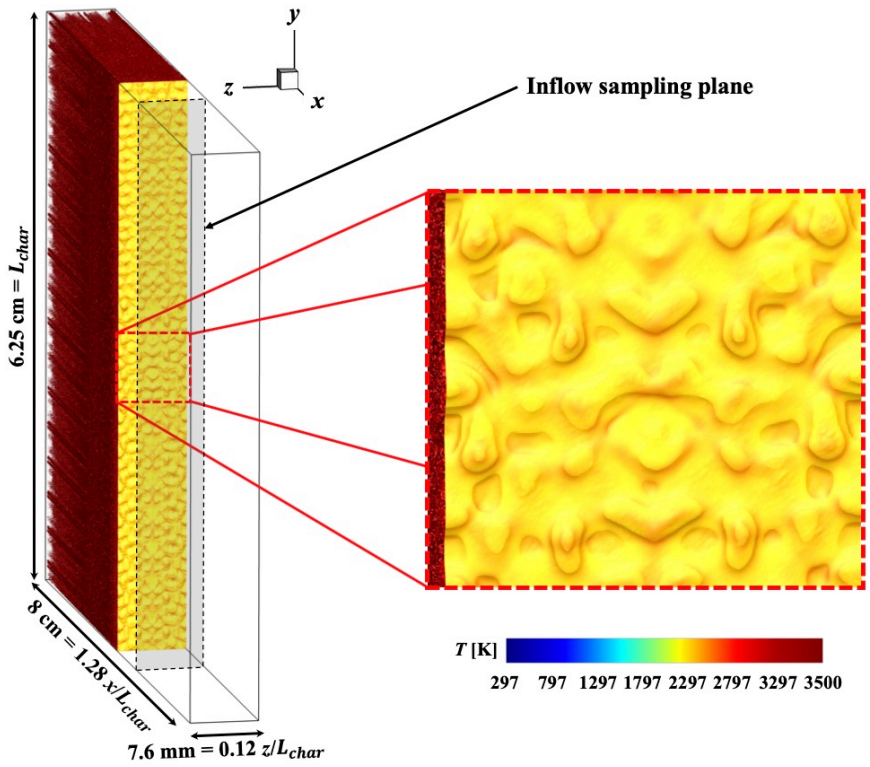

Figure 3.21: Three-dimensional channel detonation wave front in a stable configuration; isocontour of $Y_{\mathrm{OH}} = 0.025$, colored by temperature. Local acceleration of the wave due to shock interactions creates a corrugated wave front.

3.2.3 Detonation wave structure

3.2.3.1 General behavior

The fully-developed hydrogen/air detonation wave is introduced into the channel with the fuel/air stratification of cases 1, 2, and 3, and the behavior of the detonation wave through the stratified fuel mixture is observed. The detonation wave is allowed to travel through the length of the channel, and exit through the open outlet. The simulations are run for roughly 75 μs until the trailing reaction zone and the residual

gas region also completely exit the domain. Due to the length scale of the fuel/oxidizer stratification, the development of turbulence and the eddy structures behind the detonation wave differ amongst the cases. Figure 3.22 displays numerical Schlieren images of the detonation wave as it nears the end of the channel.

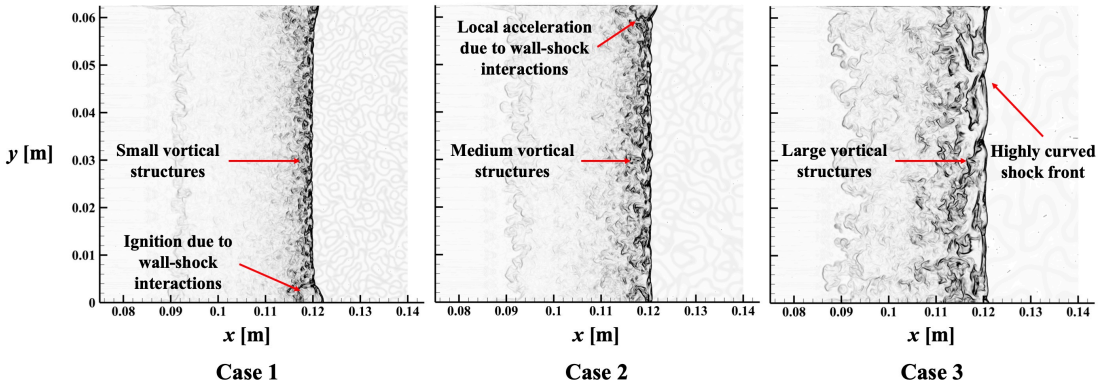

Figure 3.22: Numerical Schlieren images of the detonation wave as it nears the end of the channel domain, comparing the onset of turbulent mixing and eddy structures for cases 1, 2, and 3.

The detonation wave evolves very differently among the three cases. The stratification length scale has a direct effect on the wave front, the reaction zone, and the turbulent mixing of post-detonation and residual gases. The local sound speed and acoustic impedance (product of sound speed and density) of the gas affect wave transmission. Consequently, the passing detonation wave experiences local acceleration, due to regions of either largely pure air or detonable hydrogen mixture. Generally, the wave accelerates through hydrogen/air fuel mixture patches, reinforced by the heat release behind the wave. On the other hand, regions with predominantly air result in a reduction of instantaneous wave speed. Additionally, as the wave front passes a region of fuel, the mixture reacts exothermically following a finite ignition delay time. The irregular boundary of the fuel patch in the stream normal and depthwise directions impose disturbances in the form of composition gradients in the flow field, resulting in a distortion or wrinkling of the wave front due to the density changes. As the wave moves through relatively-small gaps of detonable mixture, the shock and

reaction fronts can decouple, but the propagation of triple points persists. However, the interplay between the density and pressure gradients and mixture detonability results in a spatial and temporal variation of triple-point (and three-shock) strength. Detonable mixtures reattach the shock and reaction fronts, helping sustain detonation with locally very high temperature, pressure, and energy release at the triple points. A node is denoted as the wave front segment between consecutive triple points. In the three-dimensional wave, the triple-point collisions lead to a corrugated wave front, with the size of each node corresponding to the distance between subsequent triple-point collisions. The node length is also representative of the stratification length scale, as triple points form at this length scale. The decoupling of the shock and reaction fronts is most prominently seen in some nodes along the wave front of case 3. This is due to the lack of fuel required to sustain detonation strength. The smallest scale stratification leads to a fairly flat wave front, where the curvature of the nodes does not manifest completely. With increasing stratification length scale, the wave front in each node is characterized by increasing curvature. This is explained by the increased distance between triple-point collisions, allowing the onset of reaction following each fuel patch to accelerate and further distort the wave front.

Vortical structures form behind the primary detonation front due to an interaction of the three-shock configuration of unsteady detonation waves: the leading shock, the Mach shock, and the transverse waves [240]. These eddies serve to mix the residual and post-detonation gases, allowing for more efficient fuel consumption. However, the discrete fuel/air mixture patches in the domain impose density and pressure gradients in the flow field. Additional vorticity generated by stratification due to composition gradients, particularly in directions transverse to wave propagation, result in a complex interaction with the vortices introduced at the triple points. In the numerical Schlieren images, the detonation reaction zones are characterized by sharp pressure gradients near the wave front. The width of the reaction zone and the size of the

eddies are directly proportional to the stratification length scale. The interaction of vorticity due to triple points and the composition gradients results in an altered eddy size compared to the homogeneous case, where the smallest vortical structures are observed in case 1. Beyond the complex reaction zone, there is a transition to the deflagration mode. Deflagration comprises a large region behind the primary wave front, up to the dissipation of secondary vortical structures observed near $x = 0.09$ m in each image of Fig. 3.22. The reaction zone entrains partially-burnt gases in pockets which are shed off of the primary detonation wave front.

The confinement effects of the wall reflect triple points and pressure waves within the reaction zone. Interestingly, the boundary-layer effects near the wall lead to a relatively-low pressure/high-temperature region with a highly arced wave front. The complex interaction of a turbulent boundary layer with the passing detonation wave results in a near-wall region where the deflagration mode dominates. This is observed most prominently in cases 1 and 2. In this region, there is high-temperature burning of residual gases as evidenced by the lack of a sharp pressure gradient. The near-wall weak detonation wave gains strength by the end of the channel as triple points are observed along the wave front and the curvature of the wave front is less pronounced. The shock-boundary layer interaction is not a focus of this study and the mechanisms leading to this behavior are not explored further.

The soot foil plot in Fig. 3.23 highlights that the detonation cell size is a function of the stratification length scale. Similar to premixed channel detonations, the triple-point collision point is identified by the highest pressure within the domain and is followed by an expansion region. The detonation cell size ℓ_{d} for hydrogen/air combustion at 1 atm and 300 K is experimentally measured at 8 mm [59]. The cell size is generally inversely proportional to pressure, with larger cell sizes expected at 0.5 atm. However, the narrow channel width and the stratification length scale in the present configuration control the detonation cell size since the distance between triple-point

collisions is limited by the geometry and the size of the fuel/oxidizer patch. In case 1, the closer spacing of the triple points along the shock front corresponds to smaller detonation cell structures. The soot foil visualizations for cases 1-3 feature an inset image of the observed cell structure for detonation through a homogeneous mixture (from the auxiliary calculation described in Sec. 3.2.2.2). Here, the cell structure from a stable detonation wave is fairly regular, with a cell size of approximately 5 mm. Thus, the finer stratification of case 1 results in cell sizes smaller than the homogeneous case, whereas case 3's cell sizes are larger. In fact, the cell size of case 2 closely resembles that of homogeneous hydrogen/air detonation at 0.5 atm although the structure is more irregular. Concerning RDE design, the stratification of fuel and oxidizer within the annulus can modify the effective cell size, causing it to vary vastly from the homogeneous values typically used for annulus sizing.

The detonation wave features a "fish-scale"-like cell structure as it traverses the channel. However, the fuel patch and subsequent density irregularities cause the cells to be staggered within the domain. In case 3, the maximum pressure trace follows an unconventional path as triple points weaken in regions with very lean composition, and reinvigorate within regions of rich fuel. Thus, the cell boundaries are not clearly defined at times, with discontinuities in the cell boundary shape as triple points transition to trace a new cell. The detonation cell pattern becomes more regular with decreasing fuel stratification length scale. The dependency of detonation cell size on the distribution of fuel is related to how the boundaries of these patches represent discrete composition gradients in this configuration. Hence, they serve as confinement to the detonation wave by reflecting transverse shocks and triple points. Similar behavior has been observed in a linear array of injectors [235] as well as practical RDE systems [237] where the composition gradient at the mixture fill height is crucial to sustaining detonation wave propagation.

The effect of the fuel-stratification on the spatial history of the shock front velocity

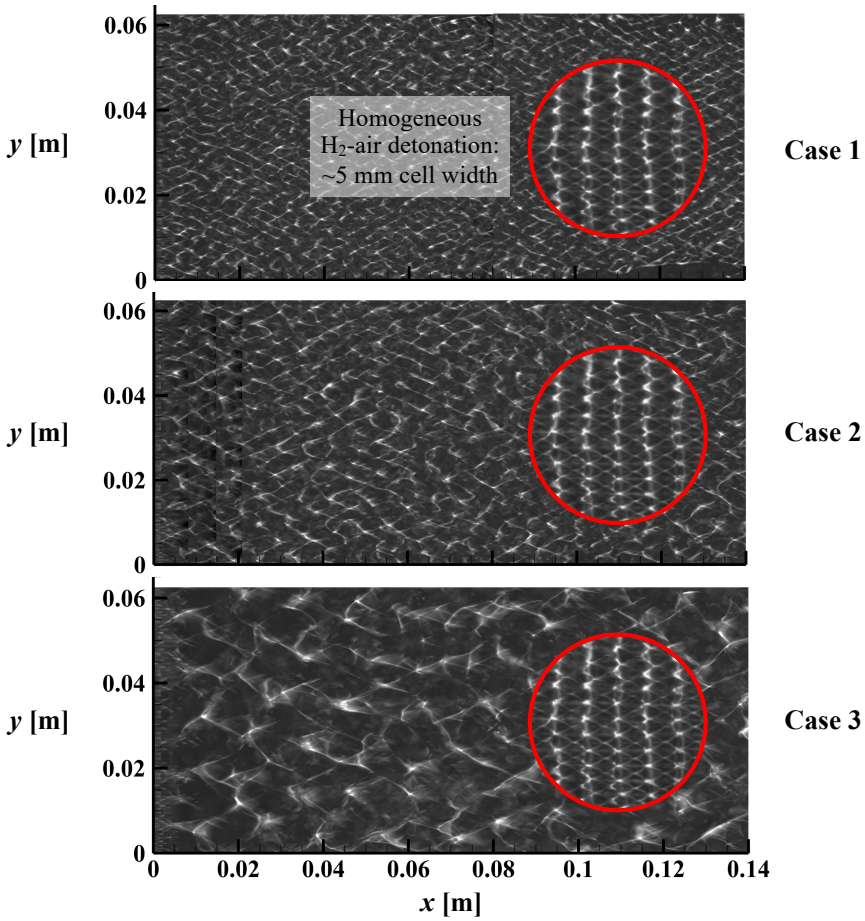

Figure 3.23: The soot foil plot visualizes the maximum pressure history within the channel and the detonation cell size for each case. The inset image compares the soot foil structure of a detonation wave through a homogeneous stoichiometric hydrogen/air mixture, from the auxiliary calculation of Sec. 3.2.2.2.

is shown in Fig. 3.24. The detonation wave velocity contour is computed in the depthwise midplane by tracking the evolution of the shock front with time. The shock front is denoted by a rapid increase in pressure from the pre-detonation ambient condition to a threshold value, calibrated as 140% of the ambient pressure. Ahead of the wave, the pressure is largely uniform. Thus, the location of the shock front can be systematically determined using this procedure. At every streamwise location of the shock front (corresponding to different time steps in the evolution of the wave), the shock front velocity can be extracted as a function of stream normal location through

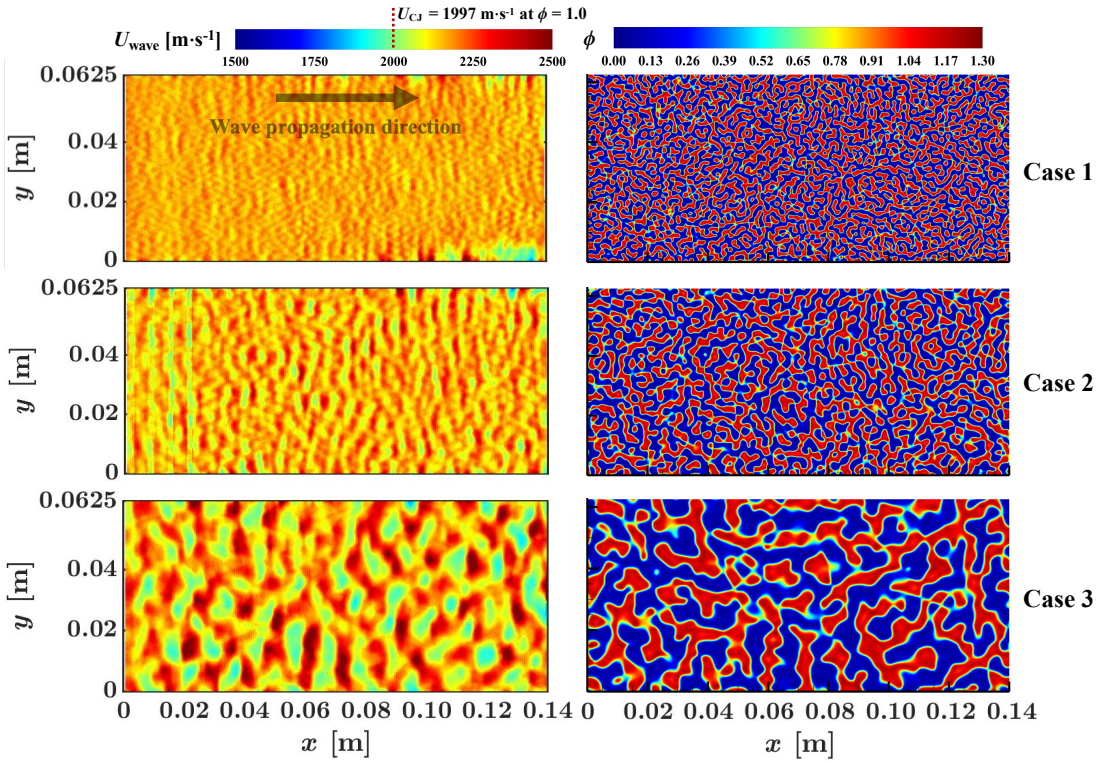

Figure 3.24: Detonation wave front velocity contour plots compared to the stratification of fuel and oxidizer in the depthwise midplane for each case.

the method described in Sec. A.3.

As seen in the numerical Schlieren images, the magnitude of local wave acceleration and its distortion effect on the wave front is a function of the fuel/oxidizer stratification length scale. In the finest stratification case, the shock velocity is largely homogeneous within the channel. With increasing stratification length scale, the front is allowed to slow down significantly in regions of very lean mixtures or those largely composed of air. In these regions, the shock front velocity drops below that of the CJ velocity for stoichiometric hydrogen/oxygen detonation. In case 3 with the largest stratification length scale, the regions of acceleration and wave momentum loss are most pronounced. The wave front accelerates shortly after passing a fuel/oxidizer patch due to a finite reaction initiation delay. The locations of high shock front velocity are correlated directly to the locations of fuel-rich patches. In case 3, the wave appears to propagate with a wider band of velocities than in cases 1 and 2;

the fuel-rich regions accelerate the wave well above the CJ velocity due to a lower acoustic impedance reinforced by detonative heat release, while slowing down in air or very lean mixtures. Overall, the shock velocity contour mirrors the equivalence ratio distribution of the channel. The wave velocity is at or above the CJ velocity through the regions of fuel as the wave is still slightly over-driven from the sampled channel detonation with a homogeneous fuel/oxidizer mixture. Furthermore, the "super-CJ" behavior highlighted by Mi et al. [187, 188], is observed in case 3, with wave velocities nearly 25% greater than the theoretical expectation. The magnitude of "super-CJ" behavior diminishes with a smaller stratification length scale. The discrete fuel patches act as concentrated energy sources as the distance between them is increased, resulting in high wave acceleration due to detonation. The wave velocity is largely regular for the length of the channel, suggesting that the wave is operating in a stable mode.

3.2.3.2 Conditional statistics

The conditional average of temperature, heat release rate, and the H_2O and OH species mass fractions in mixture fraction space in a region around the detonation wave front (wave front to 1.5 cm behind) are computed over the duration of the simulation and shown in Fig. 3.25. These conditional averages are computed using a volume-weighted approach utilizing data constrained by the shock front surface to 1.5 cm behind the front. Additional details of the computation procedure are given in Sec. A.1. In all cases, the temperature and heat release rate are largely proportional to the mixture fraction up to the stoichiometric mixture fraction $Z_{\mathrm{st}} = 0.0285$. The standard deviation of temperature narrows at intermediate lean mixture fractions, corresponding to the dip in the heat release rate curves, suggesting that the combustion mode in this mixture fraction regime is consistent. At very lean and near-stoichiometric conditions, the heat release rate increases due to a distributed en-

ergy release process. As expected, the highest heat release occurs at a richer mixture fraction, with the heat release rate dropping off beyond this point. In general, higher heat release rates result in higher temperature variability, where combustion modes of detonation and deflagration are competing. Interestingly, at the stoichiometric mixture fraction, the temperature peaks whereas the averaged heat release rate features a local minimum. This may be attributed to the induction processes occurring at stoichiometric conditions resulting in negative heat release at this local mixture fraction condition. Further, the narrower temperature variability at this point suggests that combustion is more stable, with lower heat release due to a relatively uniform mode of combustion. Case 1 features the highest heat release value at richer mixture fractions, whereas the larger stratification length scale seems to have diminished heat release at richer conditions. Similarly, the temperature and its standard deviation in these rich conditions are lower as well. It appears that the mixture homogenization of case 1 leads to increased deflagrative heat release which increases the average temperature at fuel-rich and fuel-lean mixture fractions in comparison to cases 2 and 3. As detonation and deflagration compete, the standard deviation of temperature also increases. The species profiles resemble the one-dimensional Zeldovich-von Neumann-Döring (ZND) profile. As expected, the H_2O and OH mass fractions increase linearly up to the stoichiometric mixture fraction of $Z_{\text{mix}} = 0.0285$ and continue to increase at a reduced rate for richer mixture fractions. Similar to the temperature profile, there is increased OH production up to the stoichiometric condition. However, this value begins to drop off at richer mixture fractions. On the other hand, H_2O mass fraction continues to increase at rich conditions, although a local maximum is observed at the stoichiometric condition. Beyond the mixture fraction of 0.0368, corresponding to the maximum imposed equivalence ratio of 1.3, the variance in species and temperature is greatly reduced. There is a notable increase in low mixture fraction heat release (deflagration) with decreasing fuel/oxidizer stratification length scale. Thus,

the smaller stratification length scale allows for more complete combustion of residual gases within the reaction zone, as evidenced by the increased heat release in the deflagration mode.

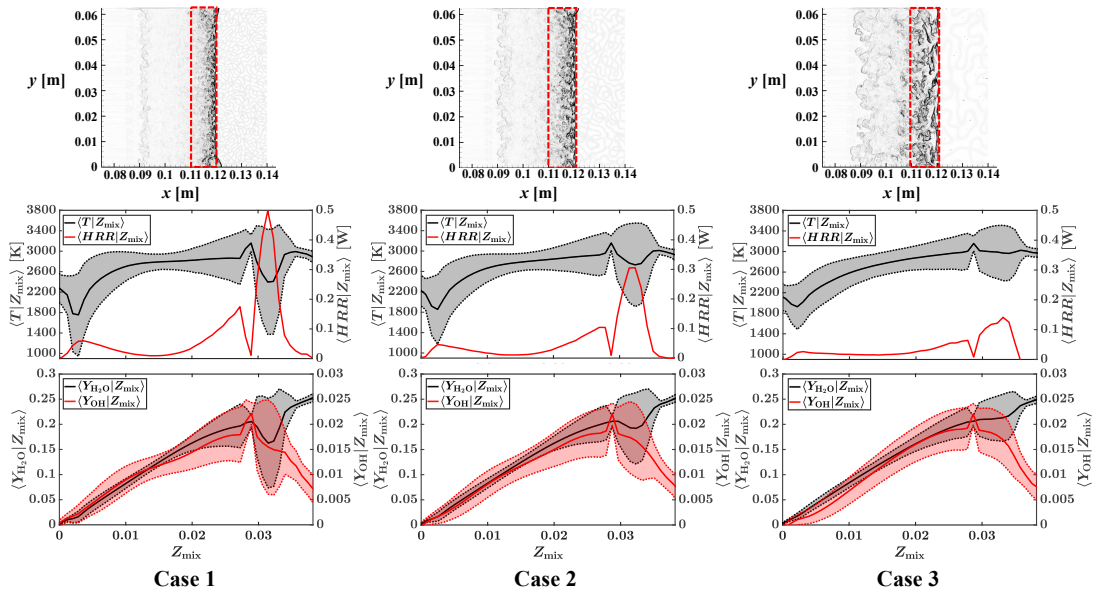

Figure 3.25: The conditional average of temperature, heat release rate, and H_2O and OH mass fraction conditioned on mixture fraction in a region around the detonation wave outlined by dashed red line (from wave front to 1.5 cm behind the front) for cases 1, 2, and 3. The shaded region denotes $\mu \pm \sigma$.

Relating the heat release rate and pressure across the detonation wave's reaction zone can provide insight into deflagration and detonation processes. Figure 3.26 displays the volume-weighted average heat release rate conditioned on pressure in a region around the detonation wave front as in Fig. 3.25, exhibiting a complex relationship. There are two primary modes of heat release with respect to pressure. At lower pressures, heat release peaks due to deflagration, with heat release ordered by the stratification length scale; case 3 exhibits a slightly higher average heat release here. On the other hand, at even higher pressures, the heat release rate continues to increase due to detonation. The conditional average does not contain a sufficient number of samples at very high pressures due to their relatively sparse occurrence

within the domain (such as at triple points). Here, high-pressure heat release is higher for case 1, where mixture homogenization behind the detonation wave may lend to the increased values. However, the pressure range extends to higher values with increasing stratification length scale, suggesting that large fuel patch size aids initial shock wave strength as seen in the "super-CJ" wave behavior. The high-pressure data is more contiguous for case 3, allowing for a smoother conditional average of heat release rate. There exists a notable reduction in the heat release at a pressure of approximately 18 atm, corresponding to a transition between high-pressure detonative heat release and lower-pressure burning. At the von Neumann pressure, which represents the ZND peak pressure of the wave front primarily due to shock compression, heat release due to combustion is limited. At pressures below this inflection in the conditional heat release, the detonative energy release is augmented by ongoing heat release due to deflagration, lending to the higher energy release rates. The significantly higher heat release rates at pressures above the von Neumann condition are due to the triple points - regions of concentrated energy release and high pressure - and three-dimensional effects of detonation. Preburning of the fuel/oxidizer patches can further limit the strength of detonation at high pressures [232].

3.2.3.3 Unconditional statistics

The normalized standard deviations of pressure, temperature, and fuel mass fraction are computed as a function of distance from the shock front to identify the effect of the fuel/air stratification length scale on the fluctuation of gas properties across the shock. The normalized standard deviation is obtained from the surface-averaged one-dimensional shock-normal ($y - z$ plane-averaged) variance within 1.5 cm of the detonation wave front at each time step. This temporally-changing variance is then time-averaged to obtain the result in Fig. 3.27. The normalized standard deviation of pressure and temperature are initially identical immediately behind the detonation

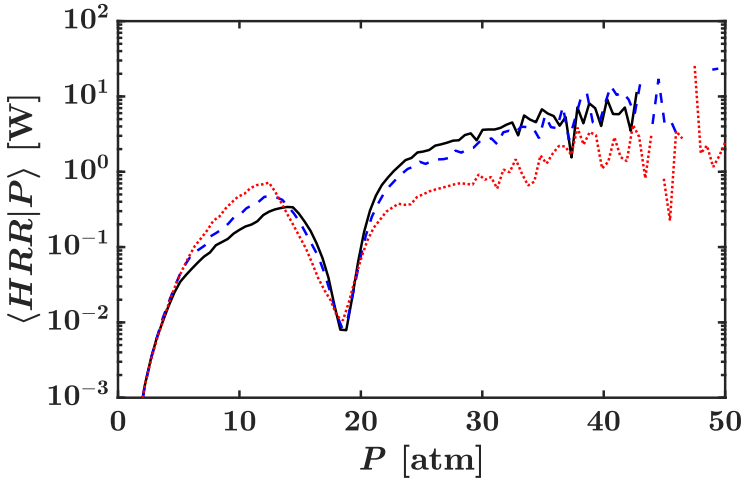

Figure 3.26: The conditional average of heat release rate conditioned on pressure in a region around the detonation wave front (from wave front to 1.5 cm behind the front) for cases 1, 2, and 3. Legend: —— Case 1; - - - Case 2; ..... Case 3;

wave front and during the shock-compression and induction processes. The effect of the fuel/oxidizer stratification length scale is observed at approximately 0.5 mm behind the shock front. As expected, the finer stratification case features a smaller variation than that of the large stratification case. Indeed, the profiles feature a transient response across the detonation wave, ordered by decreasing the stratification length scale. High variability in the temperature and pressure is sustained farther behind the wave front, up to 5 mm for case 3. This separation in variability due to the stratification length scale extends through the post-detonation mixing region. The onset of this mixing region is distinctly observed at 1 mm behind the wave front, where the variability in the fuel mass fraction features an inflection point, and the profiles for all three cases overlap. Ahead of this inflection point, the amount of variability increases with the stratification length scale, and the peak in variability occurs farther away from the wave front, which can be described as the reaction front where the spatial gradient of temperature is maximized. The differences in this local maximum are proportional to the stratification length scale, as the larger length scale results in greater variation along all locations from the wave front. To the right of

this inflection point, the ordering of fuel mass fraction variability reverses, and an interesting response is observed. The variability profiles plateau at a peak value during the mixing region, with a plateau wider for smaller length scales and occurring closer to the inflection point. With increasing stratification length scale, the plateau occurs further away, and the variability in mass fraction first decreases (almost down to pre-detonation values) before rising up to the plateau. It appears that with smaller length scales of stratification, the mixing region is wider and occurs closer to the detonation front. Variability drops off at nearly 1 cm behind the wave front and the value of this parameter is ordered by stratification length scale, with case 1 featuring the lowest variability. Further, case 1 features a more rapid decay in variability in comparison to that of case 3. Thus, case 1 is more effective in the post-detonation homogenization process.

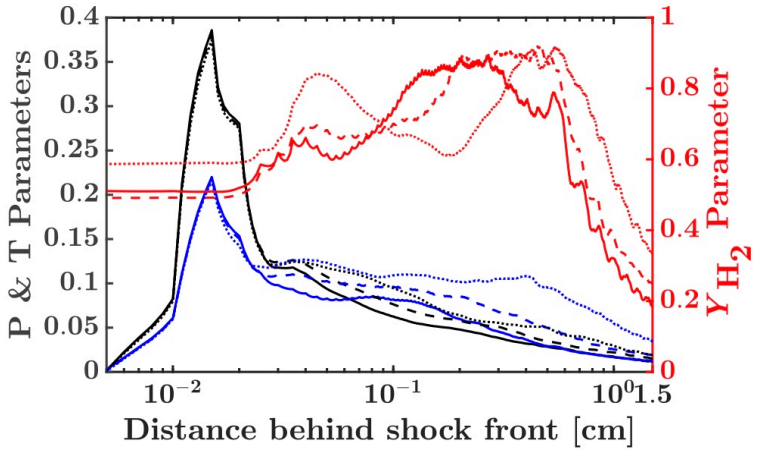

Figure 3.27: The streamwise-normal plane-averaged normalized standard deviation of pressure, temperature, and fuel mass fraction behind the detonation wave front for cases 1, 2, and 3. Legend: —— Case 1 - $\sqrt{\langle P'^2\rangle}/\langle P\rangle$; —— Case 1 - $\sqrt{\langle T'^2\rangle}/\langle T\rangle$; —— Case 1 - $\sqrt{\langle Y'^2_{H_2}\rangle}/\langle Y_{H_2}\rangle$; - - - Case 2 - $\sqrt{\langle P'^2\rangle}/\langle P\rangle$; - - - Case 2 - $\sqrt{\langle T'^2\rangle}/\langle T\rangle$; - - - Case 2 - $\sqrt{\langle Y'^2_{H_2}\rangle}/\langle Y_{H_2}\rangle$; ····· Case 3 - $\sqrt{\langle P'^2\rangle}/\langle P\rangle$; ····· Case 3 - $\sqrt{\langle T'^2\rangle}/\langle T\rangle$; ····· Case 3 - $\sqrt{\langle Y'^2_{H_2}\rangle}/\langle Y_{H_2}\rangle$.

Figure 3.28 contains shock-normal profiles of static and stagnation pressure, Mach number, the normalized species mass fractions, temperature, and heat release rate

per unit volume across the detonation wave. These profiles represent surface-averaged one-dimensional shock-normal profiles and details of the computational procedure are provided in Sec. A.2. The static and total pressures increase to a peak value 0.5 mm from the detonation wave front. Behind this peak location, the gas is traveling at a local Mach number of approximately 1.5 in the fixed laboratory reference frame. The expansion behind the detonation wave is more gradual with increasing stratification length scale, as the post-shock Mach number settles further away from the shock front. The peak pressure and Mach locations occur at a similar location. However, the peak pressure is slightly higher with increasing stratification length scale, suggesting increased detonation strength due to a more concentrated energy release process. This phenomenon is evidenced by the larger acceleration in wave front velocity observed in case 3 in comparison to that of case 1. The static pressure decays more rapidly with smaller length scales, suggesting a more compact reaction zone. The local pressure in all three cases continues to increase further into the post-detonation region, as deflagrative combustion simultaneously increases the local temperature due to a slow, distributed heat release process, as seen in the lower row of curves in Fig. 3.28. The peak temperature occurs in line with the location of peak H_2O production and O_2 consumption, and this location occurs further away from the wave front with increasing stratification length scale. Peak heat release occurs at similar distances from the shock front for the three cases (0.3 mm), but post-detonation energy release profiles are unique. Deflagrative heat release at 1 mm from the wave front is nearly an order of magnitude lower for case 3 than for case 1.

The species profiles exhibit some reversal and undergo relaxation due to post-detonation mixing. The minimum fuel mass fraction is observed within this region in all three cases, and this region is situated closer to the wave front for case 1 as opposed to case 3. While the half-reaction length $\ell_{1/2}$, defined as the distance from the shock front where half the reactant is consumed, occurs at a distance of 0.25

mm from the shock front for all three cases, the minimum fuel mass fraction point, signifying the complete consumption of reactant, is distinguishable. This location is at 3.8 mm for case 1, 5.5 mm for case 2, and 8.1 mm for case 3, highlighting the compactness of reaction for the smallest stratification length scale. Similarly, the consumption of oxidizer reaches a minimum farther from the shock front with increasing stratification length scale. Thus, it is evident that larger fuel/air distributions lead to a more distributed reaction process. Interestingly, the completion of the detonation process can be bounded by the local minimum in the temperature profile prior to an increase due to deflagrative heat release. This local minimum occurs at roughly 1.1 mm behind the wave front for case 1 and is extended to nearly 7-8 mm behind the front for case 3. The heat release rate profiles are similar among all three cases during the detonation process, with peak heat release appearing near the wave front but case 3's value is slightly lower than that of case 1. In the deflagrative heat release region, the profile decays consistently for case 1 whereas a plateau is observed between 1.5 mm and 7-8 mm in the profile for case 3. The heat release rate features significant oscillations far away from the shock front, corresponding to where the vortical structures are dissipated due to viscous forces as seen in Fig. 3.22, and the deflagrative homogenization process is reduced. The dissipation of the rotational eddies occurs closer to the shock front for smaller stratification length scale as the size of these structures is proportional. The smaller eddies generated in part due to finer fuel/air stratification lead to a more homogeneous mixture behind the detonation wave, and increased combustion efficiency (discussed in Sec. 3.2.3.4.

3.2.3.4 Combustion performance

The distribution of detonable mixture in RDE can greatly influence the macroscopic performance of the propulsive system as its combustion efficiency is often mixing-limited. The influence of fuel/air mixture stratification length scale on the

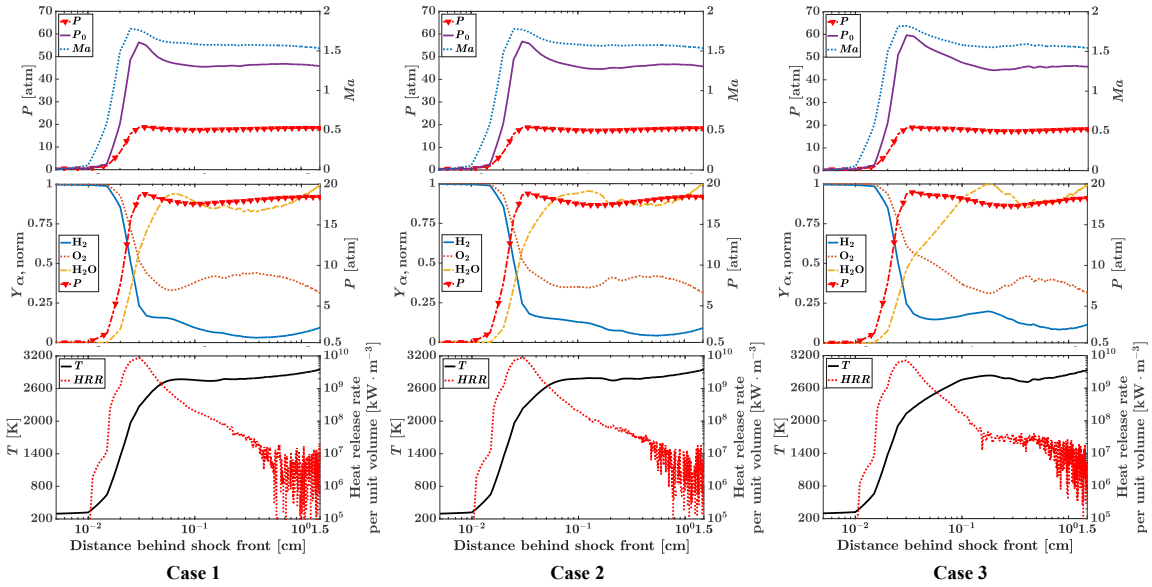

Figure 3.28: Surface-averaged one-dimensional shock-normal profile of static and stagnation pressure, Mach number, detailed species behavior, temperature, and heat release rate per unit volume as a function of distance from shock front.

combustion capability of the detonation wave can be assessed through the overall energy release due to detonation. Outlined in Fig. 3.28, the heat release rate per unit volume diminishes within a shock-normal distance of 5 mm from the front, transitioning to higher frequency noise well into the post-detonation region. Thus, the heat release is integrated over the course of the detonation wave's path through the stratified mixture, locally constrained to a distance of 5 mm from the shock front surface. The shock front is made "planar," as described in Secs. A.1 and A.2, and the heat release due to combustion is integrated over this volume. Provided in Tab. 3.3, the overall heat release markedly decreases with increasing stratification length scale. Case 1 represents an approximate 2.1% increase in energy release due to combustion over case 3, supported by the higher heat release observed across all mixture fractions (Fig. 3.25) and at the higher pressures (Fig. 3.26) within the reaction zone.

The average pressure and heat release profiles within the shock front-constrained distance of 5 mm are depicted in Fig. 3.29. Here, the pressure is temporally-averaged

Table 3.3: Heat release performance

	Case 1	Case 2	Case 3
m_{fuel} [mg]	0.4869	0.4869	0.4869
HR [J] wave constrained	52.91	52.03	48.70
η_{c} [%]	96.7	95.5	91.6
$\left\langle \frac{p_2}{p_1} \right\rangle$	37.6	37.7	38.0
$\left\langle \frac{p_{0,2}}{p_{0,1}} \right\rangle$	112.5	113.4	119.2

on a volume-weighted basis within a volume defined by a region within 5 mm of the local shock-front surface. The average heat release is integrated in the depthwise (out-of-plane) direction and averaged in time (on a volume-weighted basis), providing a contour profile of heat release as a function of location in the x-y plane. Here, it is evident that for case 1, the energy release near the detonation wave front is nearly a factor of two greater than that of case 3. The heat release is more concentrated for case 1 as reactions extend farther behind the wave front for case 3. In all three cases, energy release is diminished at the near wall region, likely due to deflagration-dominated combustion resulting from complex detonation wave-boundary layer interactions. Similarly, the average pressure profile shows a more compact shock compression process for case 1. It must be noted that the smoothness in the near-front pressure profile of case 3 is due to the larger fluctuation in front curvature described in Sec. 3.2.3.1. Similarly, high-pressure regions can extend further behind the wave front for case 3 due to heat release driven by larger patches of detonable mixture.

Ultimately, the combustion efficiency for each case can be defined utilizing the average shock-normal mass fraction of fuel, integrated over the shock-front surface described in Sec. A.1. The combustion efficiency, η_c, for the present configuration is computed based on the mass flow rate of fuel at two positions across the shock

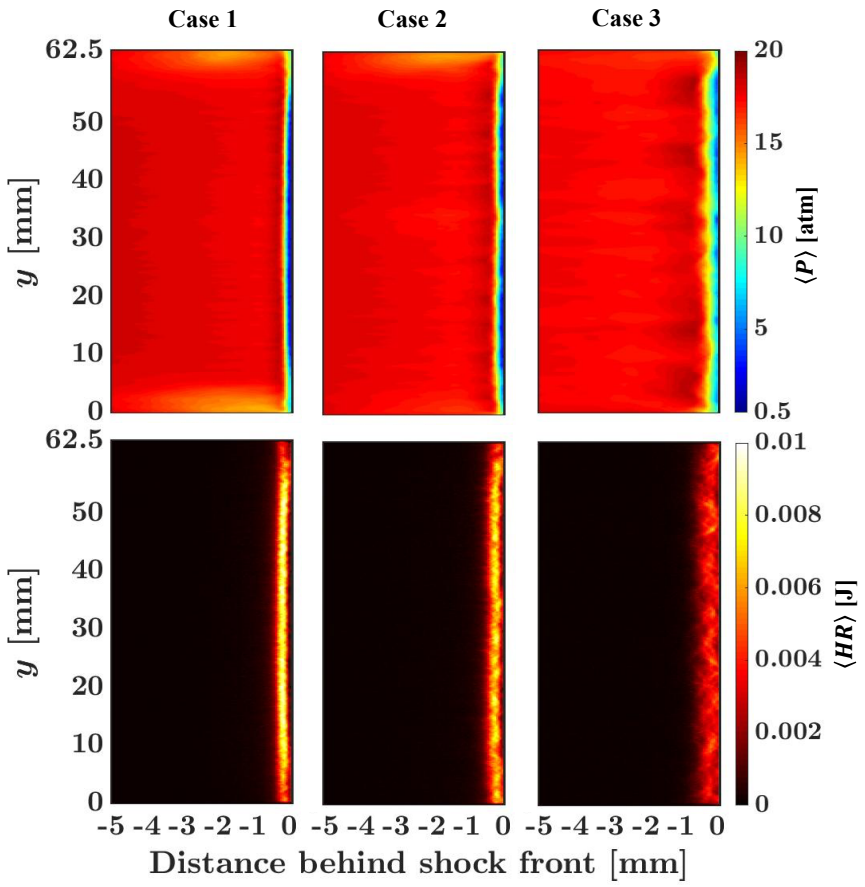

Figure 3.29: Mean pressure and heat release profiles within a region 5 mm from the wave front, averaged in time and in the depthwise direction, tracking the wave location.

wave: (1) initial state ahead of the shock front and (2) post-detonation state at the location of minimum H_2 mass fraction. In the *wave-fixed* reference frame, the shock surface is reconstructed as a planar front based on the one-dimensional profiles at each transverse location in the channel (y/z directions). This procedure is detailed in Sec. A.2. The combustion efficiency is computed based on the surface-averaged one-dimensional shock-normal profile as follows:

$$\eta_c = 1 - \frac{\int (\rho \cdot U)_{\text{fuel,min}} \mathrm{dS}_{\text{fuel,min}}}{\int (\rho \cdot U)_{\text{inlet}} \mathrm{dS}_{\text{inlet}}} \tag{3.9}$$

where the subscript fuel, min signifies the post-detonation state where residual H_2 is at a minimum, subscript inlet signifies the pre-detonative state, and $\mathrm{dS}_{\text{inlet}}$ and

$dS_{fuel,min}$ are the inlet and exit surface areas of the control volume (equivalent in this formulation). The control volume is fixed about the shock front surface, with the inlet situated 1 cm ahead of the shock front, and the exit placed at the distance of minimum H_2 mass fraction from the shock front, outlined in Sec. 3.2.3.3. The control volume in the *wave-fixed* reference frame, along with the inlet and exit surface areas, is depicted in Fig. A.3.

The computed combustion efficiencies are outlined in Tab. 3.3. Case 1 features the highest efficiency in terms of fuel consumption, followed closely by case 2. Case 3 features a notably lower efficiency, supported by the overall heat release specification for this fuel/air distribution. On the other hand, overall pressure rise exhibits the inverse trend, with case 1 featuring a 1.1% greater volume-averaged pressure jump and a 6% higher volume-averaged total pressure rise than case 1. Thus, this offers further support that initial detonation strength is greater with case 3 whereas overall combustion efficiency is greater with case 1.

3.2.4 Comments on grid convergence

The simulations performed within this study solve the full set of compressible Navier-Stokes equations augmented by detailed chemical kinetics. Thus, there are no models used in the resolution of turbulence. In the context of unsteady detonation with turbulence, a fully-resolved representation of the dynamics with detailed chemical kinetics within the present geometry is beyond the state-of-the-art simulation capability at this time. Previous analyses [181, 240] have demonstrated that the diffusive scales in gas detonations would require order 10^4 points per induction length scale to capture the underlying dynamics. Furthermore, at least two orders of magnitude decrease in grid size may be required to resolve the finest scales estimated by eigenvalue analysis [230]. However, for the geometry of interest, computation cost would be exceedingly high. Approximately 10^2 cells per induction length may be

possible for simpler configurations and/or with fewer dimensions.

The current study nears the limit for computational tractability, resulting in the selected resolution. As with past multi-dimensional simulations of unsteady detonations, the numerical configuration does not resolve the fine-scale turbulent dissipation (K-H instabilities, etc.) nor the diffusive mechanisms on the molecular scale. Thus, the simulations limit the range of scales that are represented and cut off the finer scales which would affect the flow field. Further, the choice of resolution introduces artificial dissipation at the larger scales that are captured. However, as the study aims to comparatively investigate the effect of stratification length scale, these are accepted limitations of the current set of simulations.

With regards to grid independence, a grid refinement calculation was performed using case 1 where the resolution within a subdomain (2 cm in length with the original height of 6.25 cm and width of 7.6 mm) was refined by a factor of two in the axial direction, and a factor of three in the stream normal and spanwise directions. Thus, within the core region of the domain $\Delta x = \Delta y = \Delta z = 25$ μm, corresponding to 24.8 cells per half-reaction length $\ell_{1/2}$. This resolution approaches the lower resolution tested in Ref. [181]. The near-wall region is characterized by $\Delta y = \Delta z =$ 1.3-24.9 μm, where one y^+ is 0.6 μm. Thus, this truncated domain contains approximately 671 million cells with $800 \times 2528 \times 332$ points in x, y, and z directions respectively. The fuel/air distribution in the truncated domain is obtained from the latter half of the channel geometry. The detonation wave from the original simulation is sampled (at intervals on the order of the simulation time step - $\mathcal{O}(10^{-9})$s) ahead of this truncated domain and fed in as an inflow. The detonation wave is allowed to evolve through this truncated geometry in two different configurations: (1) original mesh and (2) refined mesh, and the macroscopic results are compared.

The numerical Schlieren images of the detonation wave in the mid-channel plane for both the original and refined mesh as the wave is mid-way through the truncated

geometry are given in Fig. 3.30. Here, the wave position and wave front surface curvature are nearly identical between the two solutions. However, the ability of the refined mesh in capturing the turbulent mixing structures is higher, with increased vortical structures and a greater range of eddy length scales observed in the post-detonation region. The decay of vorticity stemming from the triple points is better defined with the finer mesh. While the large-scale eddy structures are similar well into the post-detonation region, the smaller vortical structures are captured whereas numerical diffusion suppresses the formation of these vortices with the original mesh. The large-scale structures in both meshes extend to approximately 3-4 mm behind the primary wave front, and the gas mixture becomes more homogeneous beyond this point. Furthermore, additional vortical structures and shear layers are captured in the near wall region, where a factor of three wall-normal mesh size reduction aids in resolving the boundary layer.

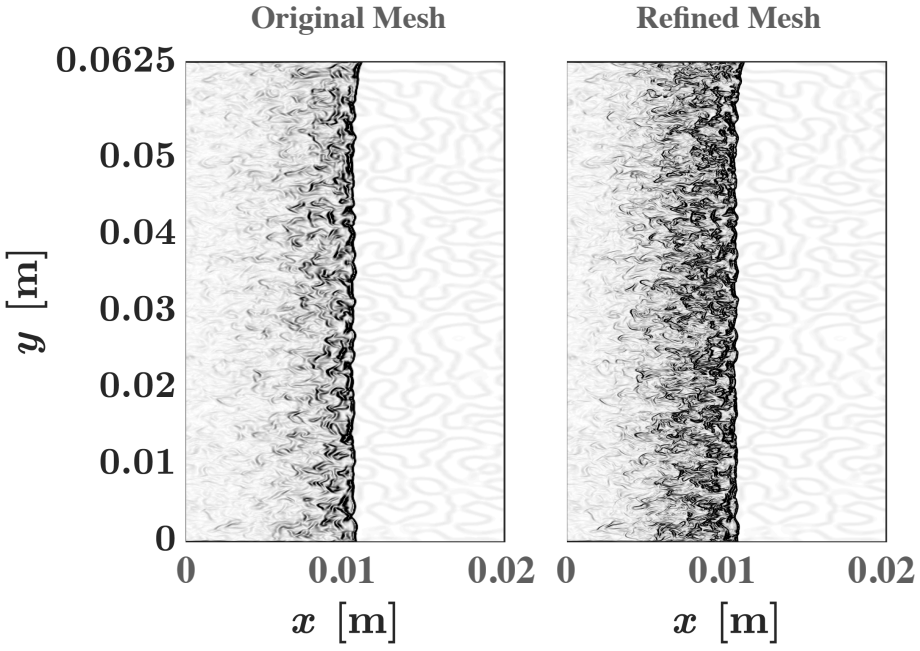

Figure 3.30: Numerical Schlieren images of the detonation wave in spanwise center plane for the (left) original mesh resolution and (right) the refined mesh resolution.

Figure 3.31 depicts the wave velocity history for both the original and refined

meshes. The velocity history contour of the original mesh is smoother than that of the refined mesh, as discrete regions of local acceleration due to variations in acoustic impedance and heat release are not as defined. However, the structure in local wave speed is cohesive, coinciding with the distribution of fuel. The volume-weighted average wave velocity is 2203 m/s for the original mesh, and 2232 m/s for the refined mesh, representing a 1.3% error. However, the PDF of wave velocity is narrower for the original mesh, as the extreme velocities due to local accelerations span a greater range for the refined mesh.

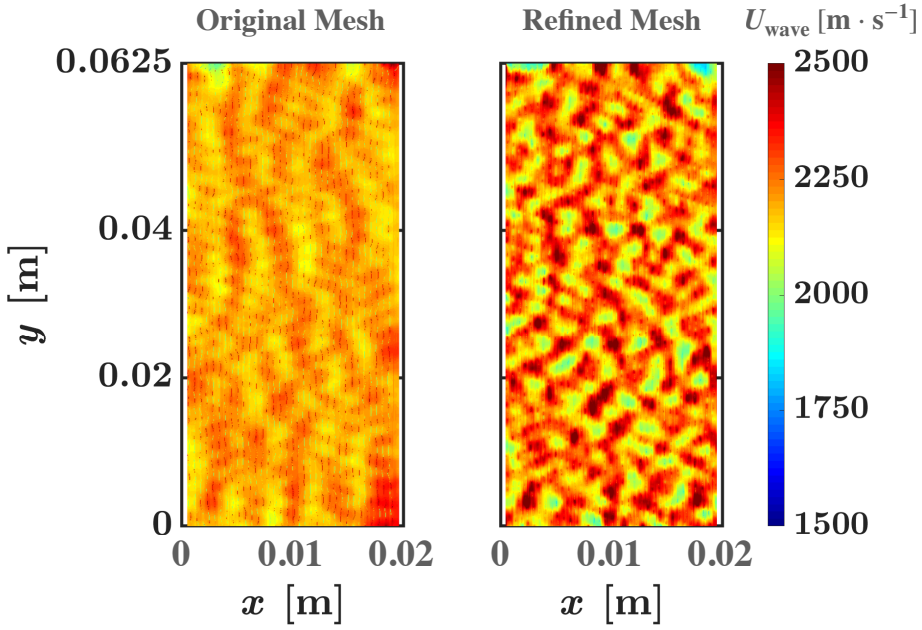

Figure 3.31: Wave velocity contour at the spanwise center plane for the (left) original mesh resolution and (right) the refined mesh resolution.

In a manner similar to Figs. 12 and 13 in the manuscript, average one-dimensional profiles of properties as a function of distance from the shock front are provided in Fig. 3.32. The surface-averaged one-dimensional shock-normal profiles are very similar between the original and refined meshes. As expected, due to the finer resolution, shock compression and the onset of reaction occur closer to the shock front by approximately 50 μm for most parameters. However, pressure, temperature, and species evolution stabilize at very similar values. The greatest difference is observed with the

mean total pressure and heat release rate per unit volume profiles. Due to the higher peak velocity observed in Figure 3.31, the kinetic energy component biases the mean total pressure profile, with a 7.7% difference between peak values. Similarly, the peak heat release at the wave front is greater by nearly 18.1% for the refined mesh. However, these profiles converge by 0.5 mm from the shock front and become nearly indistinguishable. The percent difference in peak pressure, temperature, and Mach number is notably more similar, with values of 0.30%, 0.25%, and 4.8%, respectively.

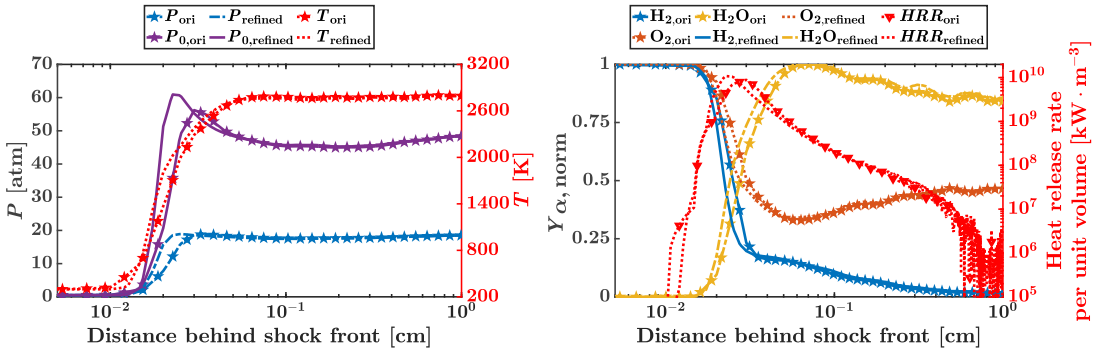

Figure 3.32: Surface-averaged one-dimensional shock-normal profiles of static and stagnation pressure, temperature, detailed species behavior, and heat release rate per unit volume as a function of distance from shock front.

While greater fluctuation in wave velocity and peak heat release as a function of local composition is observed with the refined mesh, the heat release within this truncated geometry provides insight into the overall detonative combustion behavior. The combustion heat release constrained to a region from the wave front to 5 mm behind it is 7.44 J for the original mesh, and 7.59 J for the refined mesh, representing a percent difference of 2.1%. Thus, although greater instantaneous heat release may be observed with the refined mesh, a measure of overall combustion performance is significantly more similar. The increased heat release in the refined mesh is due to a combination of higher heat release near the wave front, and more complete combustion in the post-detonation region due to greater mixture homogenization driven by the complex interaction between triple-point vortices and composition gradients.

While the small-scale diffusion is better captured by the refined mesh and the influence of mesh-induced numerical diffusion is reduced, the resolution of the refined mesh would be intractable for the full geometry. The results observed with the current grid refinement study are expected, and changes will continue to be observed as the resolution approaches the standards given by past studies on unsteady detonations. However, these resolutions are not achievable without exascale computations and a geometry smaller than the present configuration. With regard to macroscopic detonation structure and characterizing wave propagation differences due to variation in stratification length scale, the original mesh is capable of providing this information.

3.2.5 Study conclusions

The effect of fuel/oxidizer stratification length scale on the detonation wave structure has been studied through the high-fidelity numerical simulation of confined channel detonation. In an RDE, the fuel/oxidizer injection dynamics result in a complex fuel stratification. Thus, a traveling detonation wave passes through regions of fuel and oxidizer mixture of varying distribution and equivalence ratio which thereby distort the detonation wave front. A detonation wave passing through non-detonable mixtures purely convects the reaction zone species, causing them to lag behind the shock front. In a stratified mixture, shearing forces generated as the detonation passes through the fuel-rich and fuel-lean regions augment the vortical structures generated at the triple points and mix the partially-burnt reactants within the reaction zone and post-detonation region. Through a DNS approach, three different length scales of fuel/air stratification were simulated. The initial fuel/oxidizer stratification is generated such that the PDF of the scalar values closely conforms to a double-delta function. The integral length scale of the fuel/air distribution is changed by altering the scalar energy spectrum function. The three cases, with streamwise integral length scales of 0.581, 0.894, and 1.854 mm, preserve the total fuel mass within the domain

and isolate the effect of the stratification length scale on the detonation wave behavior. These length scales are comparable to the detonation wave thickness observed in practical RDE simulations [254, 257].

The fuel/air stratification length scale directly affects the size of the vortical structures that are formed by the interaction of triple points and transverse waves along the detonation wave front. The small eddy size in the finest stratification case results in a fairly planar wave front, where the curved nodes along the wave front are more closely spaced. With increasing stratification length scale, the vortical structures increase in size, and the reaction zone (characterized by mixing structures and sharp pressure gradients) broadens. However, the large eddies are less efficient at allowing the residual and post-detonation gases to thoroughly mix within the reaction zone. This is evidenced by the increased variability of fuel mass fraction across the detonation wave in cases with increased stratification length scale. Similarly, the detonation cell size scales with the stratification length scale. The soot foil patterns for the three studied cases show that the distribution of fuel and oxidizer can alter the effective detonation cell size for the mixture. As the wave passes through large regions of lean composition dominated by air, the shock and reaction fronts separate and the wave slows down. Thus, in the shock front velocity contours, the wave passing through the smaller fuel/oxidizer stratification is able to maintain a more homogeneous wave speed, whereas there is greater variance in wave velocity, with a maximum wave speed of nearly 25% above the CJ speed, in the large stratification case due to a concentrated energy release process enforced by the increased distance between discrete fuel sources.

Additionally, the small stratification length scale encourages more complete combustion and deflagration within the reaction zone, as there exists a region of increased heat release and high temperature at leaner mixture fractions. The eddies stemming from the smaller stratification length scales lend to greater homogeneity in the reac-

tion zone, with lower temperature, pressure, and fuel species variances. Further, the relaxation of temperature and species to their post-detonation values occurs closer to the shock front for a small stratification length scale, highlighting a more compact reaction zone due to the complex interaction between composition gradients and the eddies formed at the triple points. With larger stratification, the heat release due to both detonation and subsequent deflagration is distributed with a slow energy release process. However, due to the concentrated energy release with larger, more discrete stratification, detonation strength can temporarily be higher. Ultimately, the smaller stratification length scale leads to a higher combustion efficiency by nearly 5% over case 3. On the other hand, the larger stratification scale is beneficial for increased total pressure rise - nearly 6% greater than that of case 1. Heat release in a wave front-constrained region for case 1 is approximately 2.1% higher than in case 3. As a result, detonation strength and combustion efficiency compete with variations in fuel/air stratification. Overall, the physical structure of the detonation wave front is highly dependent upon the distribution of the fuel and oxidizer.

3.3 The Effects of Mixture Preburning on Detonation Wave Propagation

3.3.1 Motivation

In RDEs, the aerodynamically-driven turbulent mixing is always imperfect, leading to a stratified fuel/air mixture that is processed by the detonation wave. In practical systems, this variability in the level of mixing can critically affect the detonation wave. For instance, typical wave velocities are considerably lower than the Chapman-Jouguet (CJ) speed [3, 247, 316], which is partially caused by reduced heat release behind the shock wave. While different mechanisms for this reduction have been postulated [41, 50, 283], one main cause is so-called parasitic combustion

[50, 218, 255]. In this regime, in addition to incomplete mixing, interaction with product gases from the previous cycle can lead to premature deflagration and heat release. For instance, Chacon et al. [51] found two distinct regions of deflagration: 1) recirculation of product gases trapped near the inlet due to injector design, and 2) a contact burning region caused by mixing between product gases and incoming fresh gases (preburning effect). The former flameholding feature is not universal but depends on the injector configuration used [237]. The latter preburning mechanism is the focus of the present study.

Numerical studies of full-scale RDE systems have suggested that up to 35-50% preburning of the fuel/oxidizer mixture is prevalent within the combustor [61, 255]. Detonation waves in RDEs are structurally different from ideal premixed waves [235]. Due to incomplete mixing, flow property variations can lead to a weaker shock wave, which in turn lengthens the induction zone. A delayed heat release profile moves the thermal choke further behind the wave front, leading to reduced wave speeds. In discrete injection systems, such wave structure may occupy the entire inter-injector distance [41] with multiple compression-expansion waves present in the induction zone. If deflagrated products are present ahead of the wave, this further weakens the shock and may even cause the reaction layer to detach. For instance, Fig. 3.33 shows an instantaneous image from a full system calculation for a hydrogen/air system [257]. Here, it is seen that although the detonation wave is followed by a temperature change, there are regions ahead of the wave (especially near the bottom of the domain) where the temperature is rising despite not yet being processed by the shock wave. In practical RDEs, this weakening results in a higher fraction of heat release in the deflagration mode (lower pressure, volumetrically distributed) rather than the detonation mode (higher pressure, compact region). Since detonation combustors are not optimized for deflagrative heat release, even with complete fuel consumption, the net efficiency may become lower than conventional deflagrative combustors.

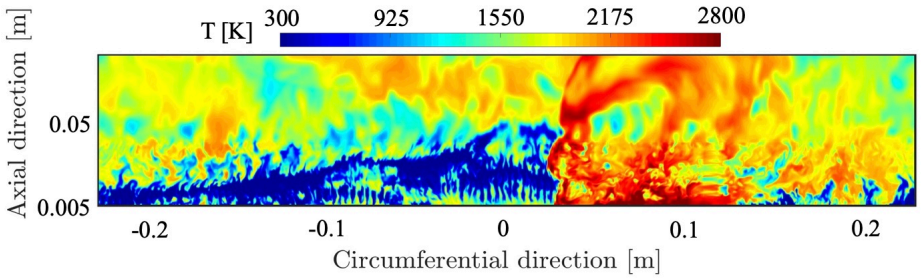

Figure 3.33: Snapshot of temperature profile from a three-dimensional full-system simulation shown as an unwrapped image at the mid-channel location. Reproduced from [257].

With this background, the focus of this study is to isolate the effect of preburning on detonation propagation. For this purpose, a canonical flow configuration with a quiescent initial condition with stratification of fuel/air mixture is considered. Based on the previous section (see Sec. 3.2) that considers only the role of stratification, this study introduces the effect of preburning by imposing deflagration ahead of the wave. Specific operating parameters are obtained from full-scale RDE calculations [255, 257].

3.3.2 Numerical representation

To replicate the wave structure in a practical RDE geometry, a canonical channel geometry of length 14 cm, width 7.6 mm, and height 6.25 cm is modeled as shown in Fig. 3.34. The height of the channel corresponds to the characteristic large length scale, L_{char}, within the domain. As an extension of past studies of Prakash et al. [235], the operating pressure of half the atmospheric condition with background air is used. The channel is confined with walls in the stream normal and spanwise direction, and the right boundary is set as an outflow. The inflow boundary condition is prescribed by a sampled right-running, well-developed, three-dimensional detonation wave. The grid for the three-dimensional geometry consists of 1) a uniform resolution core region and 2) a near-wall region. A near-wall region in the stream normal and spanwise directions contain clustered cells to properly resolve the boundary layer. Note that

the near-wall regions are not included in the analysis, but the higher resolution is maintained to ensure that non-physical flow is not developed. This results in a total of 303 million cells, with $2800 \times 858 \times 126$ points in the x, y, and z directions, respectively. Within the uniform core region, $\Delta y = \Delta z = 75$ μm, and $\Delta x = 50$ μm. The near-wall region is characterized by $\Delta y = \Delta z = 3.2$-$74.7$ μm. The clustered grid near the wall extends up to 435 y^+, or 0.261 mm, from the wall, where one y^+ is 0.6 μm. The length scale of interest is the induction length ℓ, which, for stoichiometric hydrogen/air detonation at these operating conditions, is analytically given by 398 μm. Thus, approximately 6-8 grid points are used to resolve the induction length.

The range of equivalence ratios is set to be between 0.75 and 1.5, which is based on full-system RDE calculations [255]. Fuel/air stratification is introduced in the form of patches of varying equivalence ratios sampled from a model energy spectrum as per the methods of Ref. [74, 115]. An integral length scale is used as an input to create a corresponding homogeneous isotropic distribution with no mean gradient present. In this sense, this study is different from prior detonation studies with concentration gradients [30, 32]. In the selection of conditions for this study, a study of a full-scale hydrogen/air RDE with axial air inlet is utilized [257]. An integral length scale of 4.3 mm, extracted from the full-scale RDE data, is applied to the scalar energy spectrum function. Note that this length scale is roughly 10 times the induction length of an ideal detonation under these conditions. The resulting fuel/air distribution in terms of equivalence ratio is shown in Fig. 3.34.

From the three-dimensional RDE data, a one-dimensional profile along an azimuthal path at the mid-channel location and 2 cm height from the injectors is obtained. The profile is temporally-averaged about the wave front location. Data was collected at a height identified from mixing analysis performed by Sato et al. [257] as a location strongly affected by parasitic combustion due to recirculation zones and injector dynamics. Thus, the region was characterized by reduced detonation strength

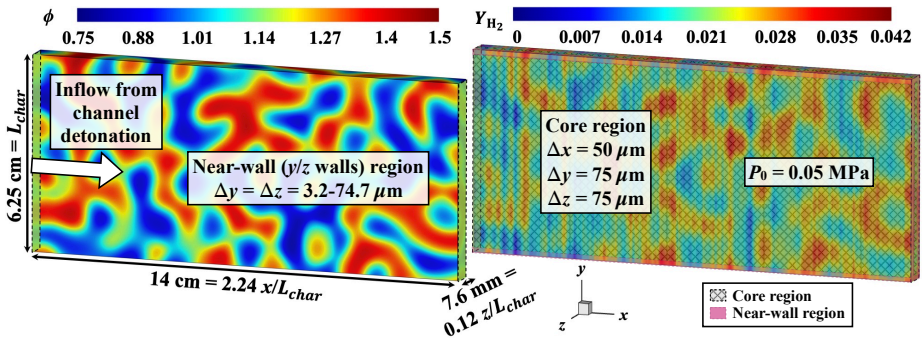

Figure 3.34: (Left) Contour of local equivalence ratio and (right) H_2 mass fraction along with a description of the three-dimensional channel domain for a preburnt mixture with an integral length scale of 4.3 mm. The uniform core and near-wall (y/z walls) grid regions are denoted in the right image.

due to mixture inhomogeneity and preburning. Figure 3.35 shows this nominal profile along the azimuthal or circumferential direction. It is seen that the peak in pressure is reached close to $\bar{x} = 0$, which defines the location of the detonation wave. The temperature profile progressively decreases, which indicates that fresh gases at a lower temperature are entering this region. However, at $\overline{x} > 0.7$, the temperature begins to increase even though the pressure profile observes either nearly constant or slightly decaying behavior. This is the region of deflagration, where the autoignition of pockets of fuel and air mixed with product gases from the previous cycle has initiated. The parameters for the current study are extracted from the region $\bar{x} = 0.7 - 1$.

To introduce the preburning effect, the following procedure is used. Based on the local equivalence ratio shown in Fig. 3.34, a corresponding equilibrium solution based on deflagration at constant pressure is obtained. The species composition at each point in the computational domain is then updated toward this equilibrium:

$$Y_{pb}(\boldsymbol{x}, 0) = Y(\boldsymbol{x}, 0) + f\left(Y_{eq}(\boldsymbol{x}) - Y(\boldsymbol{x}, 0)\right), \tag{3.10}$$

where Y_{eq} and Y_{pb} denote the equilibrium and partially-burnt compositions, respectively, corresponding to the initial fuel mass fractions $Y(\boldsymbol{x}, 0)$ at a particular spatial

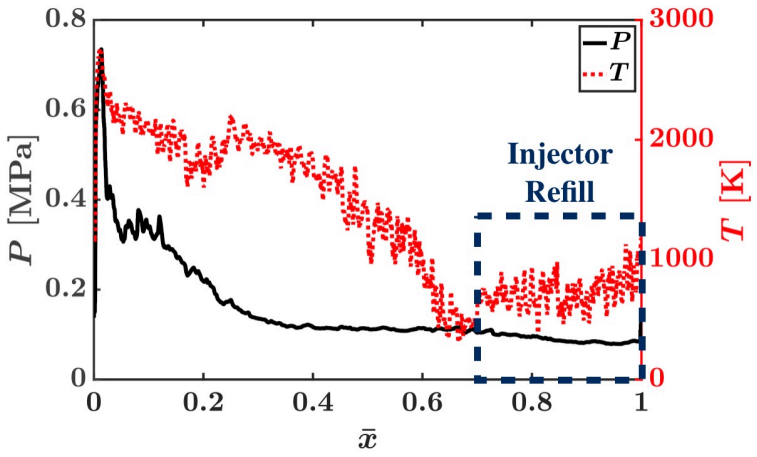

Figure 3.35: Temporally-averaged (about the wave front location) pressure and temperature profiles from the axial air inlet full-scale RDE simulations unwrapped into a one-dimensional profile as a function of normalized azimuthal distance, reproduced from [257].

location. Here. f is the preburning ratio, a fractional measure of deflagration.

In order to associate f to the local composition, the preburning ratio is defined using a progress variable $c = Y_{H_2O} + Y_{OH}$. Thus, it follows that f can be defined as a ratio of the local progress variable to its value at equilibrium:

$$f = \frac{Y_{H_2O} + Y_{OH}}{\left[Y_{H_2O} + Y_{OH}\right]_{eq}} = \frac{c}{c_{eq}} \tag{3.11}$$

From the full-scale RDE data described in Fig. 3.35, the distribution of f is shown in Fig.3.36. It is seen that f has a high degree of linear correlation with the normalized temperature. This linear relation shows that data in this region is dominated by constant pressure deflagration. From the RDE data of a small number of detonation cycles, a short-time averaged profile of f along the direction of wave propagation is obtained. The short-time average is used to ensure that significant fluctuations in the equivalence ratio are not present, in order to preserve the homogeneous initial conditions. The region from $\bar{x} = 0.7 - 1$ from the full-scale RDE (Fig. 3.35) represents a length equal to 0.14 cm.

This directional profile of f from $\bar{x} = 0.7 - 1$ is flipped and then imposed in the

streamwise direction on the initial condition given in Fig. 3.34, along with Eq. 3.10, to obtain the preburning-based initial condition that is also shown in Fig. 3.34. As a result, the profile of f at $\bar{x} = 1.0$ is applied at the entrance to the channel, and the profile at $\bar{x} = 0.7$ location is at the exit of the channel. The preburning ratio varies in the streamwise direction and is homogeneous in the stream normal directions. Note that the wall confinement and three-dimensionality of the flow are necessary to ensure the propagation of triple points along the detonation front. Furthermore, the mixture within the channel geometry is allowed to burn as the detonation wave inflow travels through the domain. Consequently, the mixture near the exit of the channel (with a preburning ratio corresponding to $\bar{x} = 0.7$) continues to burn until the detonation wave arrives at this location in the channel, thereby increasing the local level of burning with time. Because the detonation wave travels at a finite speed similar to the RDE system, the time for deflagration is roughly constant at each streamwise location. No diffusion-based flames are established during the burning process as the time-scale of their development will be much longer than the time taken for the shock to pass through the domain.

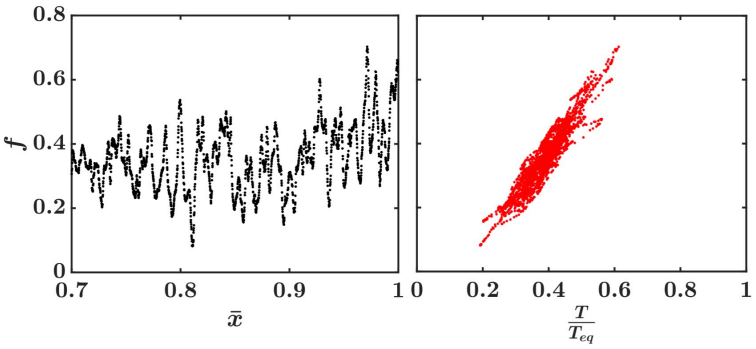

Figure 3.36: (Left) Preburning ratio f from the injector refill region and (right) correlation of preburning ratio with local temperature to equilibrium temperature for the local composition.

In a confined channel of equivalent cross-section filled with a homogeneous stoichiometric hydrogen/air mixture, a fully-developed detonation wave is created and sampled as a three-dimensional time-varying field to be used as the inflow. Molecular

transport is not included within these simulations as the primary scope of this work is detonation propagation through an inhomogeneous mixture.

3.3.3 Results and discussion

3.3.3.1 General behavior

As the detonation wave travels through the stratified mixture from left to right, it exhibits a nearly steady behavior shown in Fig. 3.37. The wave front is marked by a thin shock region with a trailing reaction zone. Behind this reaction layer, the expansion waves originating from the triple points lead to the creation of both vortical structures and a mixing region. The mixing region is sustained over significant lengths and is finally dissipated by viscous forces. Ahead of the wave, density variations caused by the imposed f profile are seen manifesting as striations due to the streamwise-only variation of this quantity. The simulations in Sec. 3.2 have shown that the size of these vortices is related to the stratification length scale. Further, the generation of vortices is consistent with the complex shock structure seen in detonation waves passing over discrete injectors [40, 235].

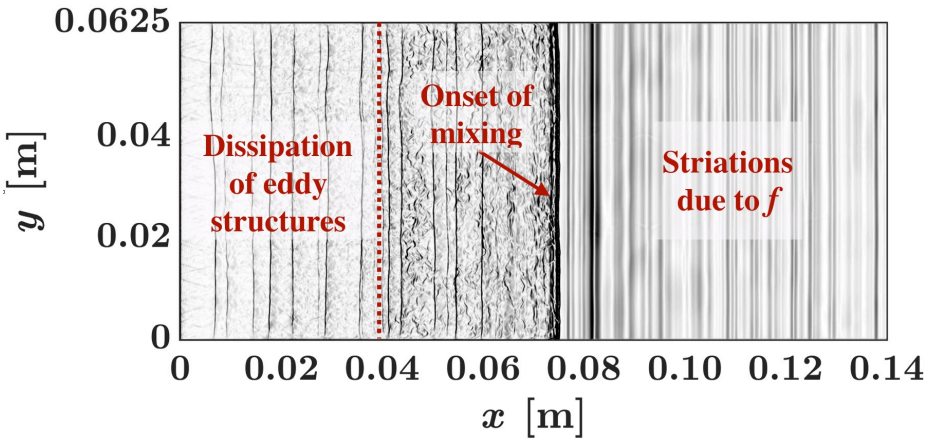

Figure 3.37: Contour of density gradient at the depth-wise mid-channel plane as the wave is midway through the channel, highlighting the reaction zone and turbulent mixing imposed by the detonation wave.

Figure 3.38 shows the pressure contour at an intermediate time, with an inset

view of the triple points along the wave front. The peak pressure observed is roughly 0.8 MPa, which is less than half the ideal peak pressure of 1.7 MPa for an average equivalence ratio of 1.12 at the ambient conditions of 0.05 MPa and 300 K. More importantly, these peak pressures are observed only at triple points, with much lower values across the detonation front. Note that even after the detonation wave has passed through the region, the pressure variations still persist. This is due to the fact that the wave is traveling at supersonic speeds, while the pressure waves are relaxing at acoustic speed in the post-detonation gases. It is also seen that a small amount of hydrogen remains behind the wave, denoting some reduction in combustion efficiency even for this canonical case. In practical RDEs, this residual fuel/air mixture is found to deflagrate as it convects downstream.

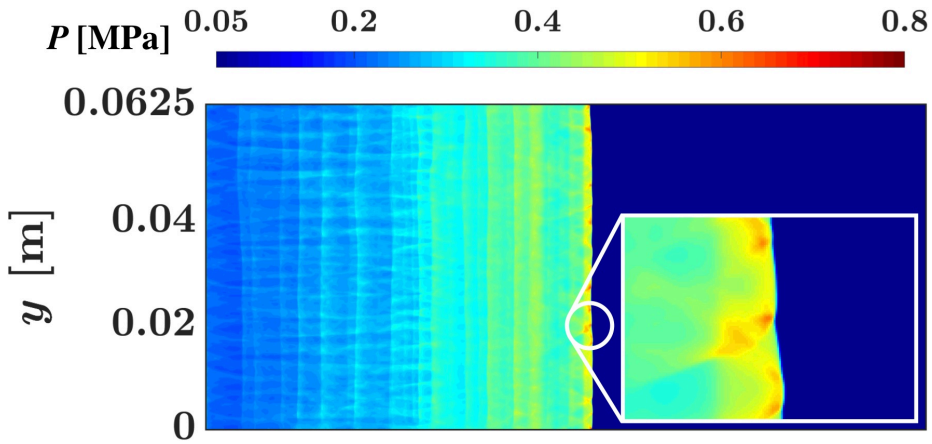

Figure 3.38: Contour of pressure at the depth-wise mid-channel plane as the wave is midway through the channel. A microscopic view of the triple point structure along the wave front is provided.

A key quantitative measure of shock strength is its propagation velocity. Figure 3.39 illustrates the variation in wave speed measured locally across the entire simulation. The simulation domain is set up such that the strong homogeneous detonation wave enters from the left and progresses through the stratified mixture. It is seen that the wave velocity exhibits very large fluctuations with variations of up to nearly 500 m/s about the average over short segments of the domain. The in-

stantaneous oscillations in wave velocity are due to changes in local composition and density. This "galloping" feature has been observed in most practical RDEs [3, 51]. The pressure profiles show that the shock front is nearly normal to the propagation direction, and is not as corrugated as seen in practical RDEs [247] given the lack of large-scale turbulence found in full-scale systems.

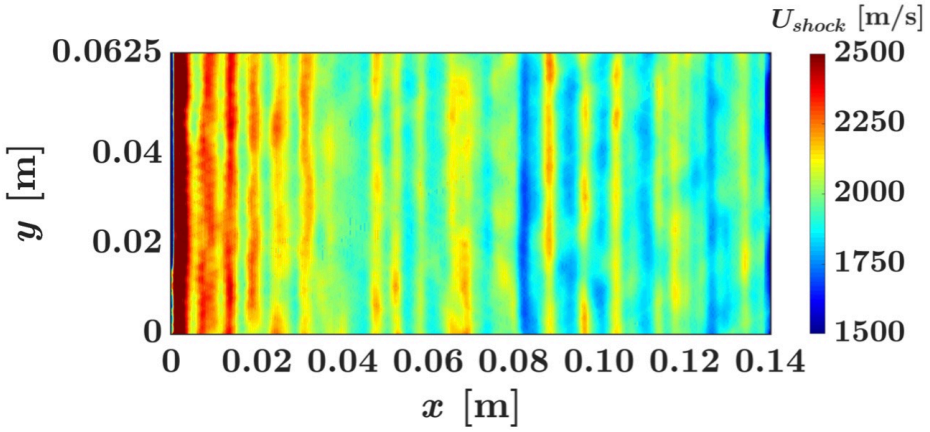

Figure 3.39: Contour of wave velocity at the depthwise mid-channel plane.

Figure 3.40 shows the streamnormal-averaged wave velocity as a function of axial position and the PDF of wave velocity within different regions of the domain. As seen in Fig. 3.39, there is a slow decay in propagation speed with streamwise distance. Regardless, the full computational domain PDF of wave velocity shows a large spread, with the most probable velocity close to the CJ speed of 1960 m/s for this operating condition. The PDFs of velocity sampled in 2 cm wide sub-domains within the full domain highlight that the spread of velocities remains approximately unchanged over the different sub-domains at locations downstream. While there is considerable statistical variation, there is no clear trend in the peak of the PDF moving towards lower velocity values. Thus, the wave velocity exhibits sustained fluctuations but the average propagation speed converges in the latter part of the domain ($x > 0.08$ m). Note that while stratification can lead to a slight increase in speeds due to discrete energy source effects as noted by [187], the high observed wave speeds for the available

reduced energy may be a consequence of the finite domain length. In other words, a quasi-steady state might not have been reached by the end of the computational domain. However, these results indicate that even in the absence of turbulence-induced wrinkling of the detonation front, the wave behavior in this canonical system is similar to that of practical RDEs.

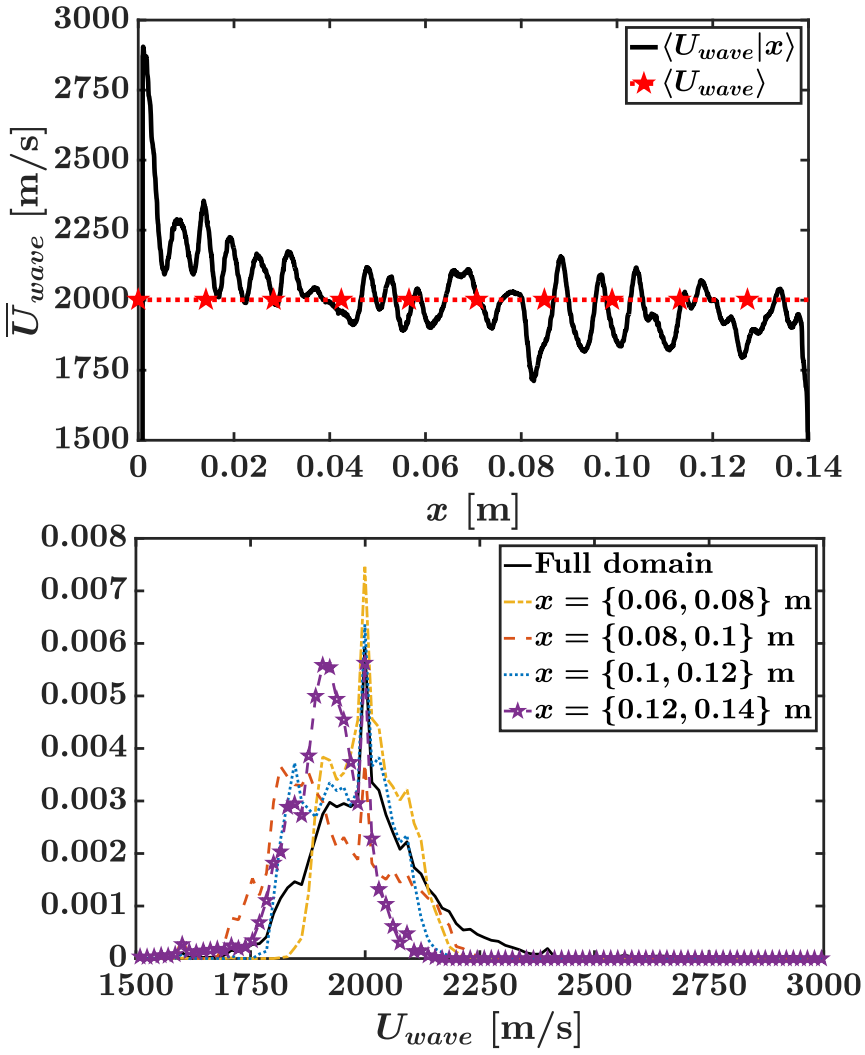

Figure 3.40: (Top) Wave velocity averaged in stream normal direction and (bottom) PDF of wave velocity within 2 cm sectors of the latter half of the domain compared to the PDF sampled from the entire domain.

3.3.4 Detonation structure

In order to gain insight into the detonation process across the wave, spatially and temporally-averaged one-dimensional profiles of properties across the wave front are provided in Fig. 3.41. The wave front location is tracked and a normal vector at every $\{y, z\}$ location on the wave front surface is determined. Thus, the shock front location is assumed to be the same for each surface-normal vector. The one-dimensional profile extracted along this vector at each location across the front surface is then temporally averaged to obtain a representative one-dimensional profile of properties across the detonation wave. The pressure profile shows interesting features. First, the pressure jump across the wave is much smaller than the theoretical expectation of ∼34x (from 0.05 MPa to 1.7 MPa), with an observed pressure jump of only ∼8x to 0.5 MPa. The initial shock wave is roughly 200 μm in thickness, which provides compression to raise the fluid temperature by nearly 1000 K. Denoted by position A, the increase in temperature occurs simultaneously with shock compression. However, the subsequent heat release increases the temperature only by 600-700 K, indicating reduced heat release due to preburning. This effect is seen in the heat release plot, with a small positive heat release in the pre-shock region and a large negative heat release in the induction region followed by the combustion process leading to high energy release. Further, the heat release process, highlighted by position B, continues further away from the compression wave, with a slow expansion of the gases, with the release rate still higher than the pre-shock preburning values. This delayed heat release is another source of efficiency loss, resulting in the so-called commensal combustion or leakage process [51], whereby the energy release does not directly support the wave propagation process.

The statistical properties of the detonation front show a complex process (Fig. 3.42). First, it is seen that the normalized pressure and temperature fluctuations peak in the compression region associated with the shock. This indicates that as the wave

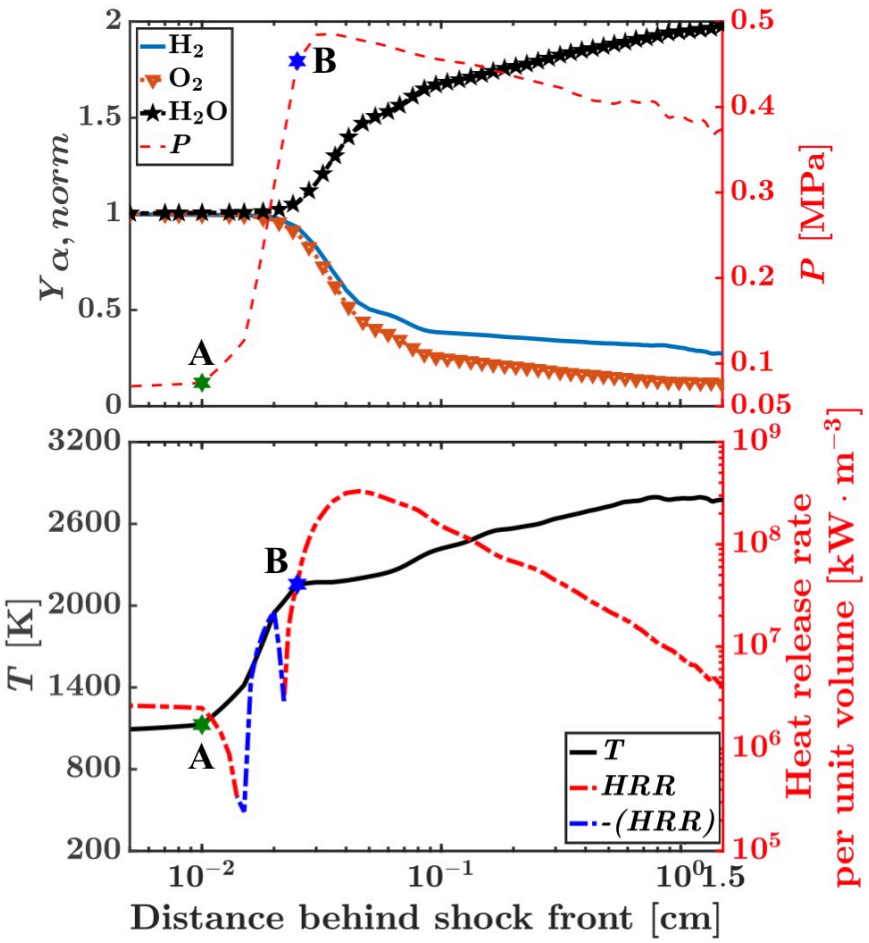

Figure 3.41: Spatially and temporally averaged one-dimensional profiles of properties across the detonation wave front. Similar positions behind the shock front between both profiles are marked by positions A and B.

propagates through the domain, there are large variations in the structure of the shock wave. This fluctuation is caused by the transverse motion of the triple points (Fig. 3.38) as well as the variations in the preburning ratio. The fluctuations for hydrogen mass fraction appear downstream of this region, in the post-combustion zone. This variation is merely caused by the changes in post-shock temperature and pressure that lead to reduced consumption of fuel. As seen in the average species mass fraction plot (Fig. 3.41), hydrogen is depleted near the induction zone, but an appreciable fraction is still present far downstream. For comparison, the equilibrium mass fraction at the stoichiometric condition for H_2 and 1000 K preburning temper-

ature is approximately 0.0033, while nearly 3 times this mass fraction is found at distances of up to 1 cm behind the wave.

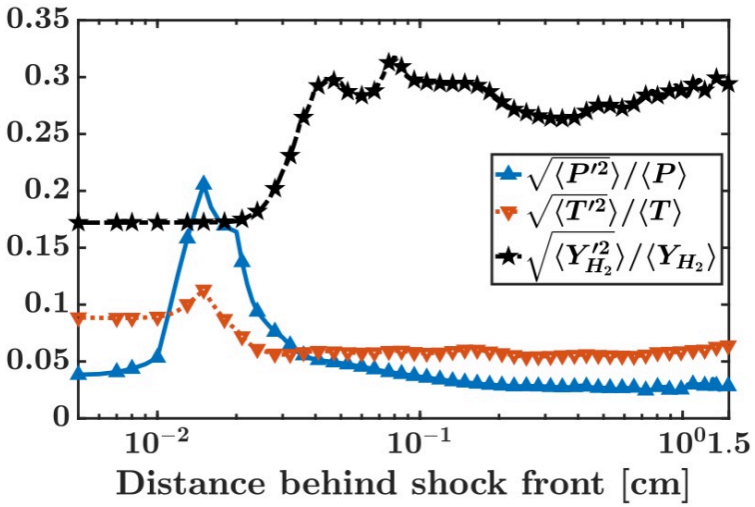

Figure 3.42: Normalized standard deviation of temperature, pressure, and hydrogen mass fraction across the detonation wave front.

Finally, the heat release rate per unit volume conditioned on pressure is shown in Fig. 3.43. The first notable feature is that high heat release rate is directly associated with higher pressure. Although lower heat release rate is possible at all pressures, shock-based compression is necessary to increase the compactness of the combustion process. However, the peak heat release does not occur at the highest pressure, which is also seen in Fig. 3.41. Furthermore, appreciable heat release continues to occur at a distance of 1 cm behind the wave (as noted above).

3.3.5 Study conclusions

Practical RDEs exhibit combustion inefficiencies due to a number of factors including turbulence-induced wave front wrinkling, incomplete mixing, and premature deflagration or preburning. In this study, the preburning process is isolated by using a canonical system, where a prescribed preburning profile is used. A near-ideal detonation wave formed in a homogeneous and stoichiometric mixture is introduced into the domain with this stratified mixture and fixed preburning profile. Analysis of the

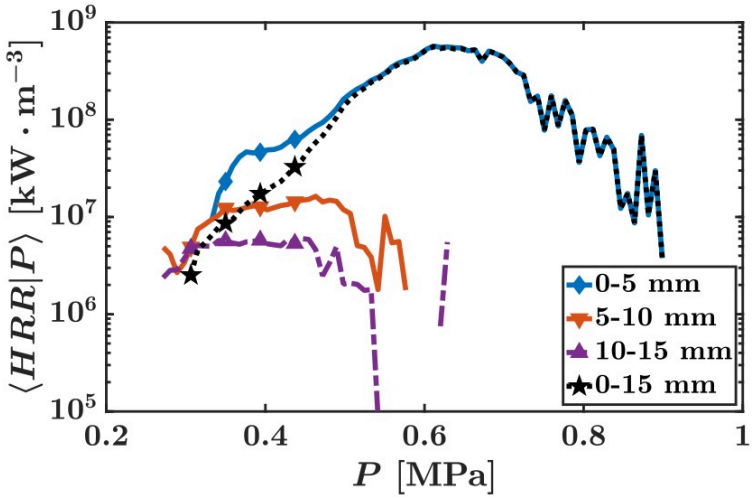

Figure 3.43: Conditional average of heat release rate per unit volume conditioned on pressure at different distance ranges behind the detonation wave front.

wave propagation and detonation structure was conducted.

The detonation wave was found to propagate with a spread of speeds, indicating that the preburning of the mixture significantly affects the strength of the leading shock. The most probable speed was close to the CJ speed, but the standard deviation was $\pm 15\%$, even for equivalence ratio variations that are small compared to practical RDEs. The detonation wave exhibited a complex structure, with a mixing region behind the propagating front where vortical structures with a length scale comparable to the stratification length scale were created. Overall, the detonation structure was weaker, with even the triple points exhibiting lower peak pressures compared to expected theoretical values.

The shock weakening was directly related to the preburning of the fuel/air mixture. The initial compression was smaller than theoretical values, with an average pressure increase of approximately 8 times the pre-shock pressure. As a result, the induction zone was much longer, leading to slower heat release extending far behind the shock front, where vortex-driven mixing enforced the homogenization of fuel/air mixtures.

These results indicate an important connection between pre-shock deflagration and loss of efficiency. In general, to have a compact heat release zone, it is necessary

to have a strong compression wave. Any reduction in peak pressure can adversely affect the heat release profile. The premature deflagration process directly weakens this shock front, leading to a slow and distributed heat release. There is considerable unburnt fuel downstream of the shock front. In other words, so-called parasitic combustion (deflagration ahead of the wave) directly leads to commensal combustion (heat release far downstream of the wave), indicating that parasitic combustion is the root cause of loss of combustion efficiency. The fact that these features could be reproduced without significant turbulence in the system indicates that turbulence is more critical to the fuel/air mixing ahead of the shock rather than shock propagation itself.

3.4 Chapter Summary

A series of simulations of detonating flow in canonical configurations have been carried out to study the impact of non-idealities on the detonation wave structure along with their implications on RDE operation and performance. Exclusively using the UTCOMP solver (described in Sec. 2.1), a high-fidelity direct numerical simulation approach at a computationally-tractable resolution was used to identify the small-scale processes at the detonation wave scale. The first set of simulations utilized a linear array of injectors (denoted the linear model detonation engine (LMDE)) with partially-premixed reactants to observe detonation wave propagation. The detonation structures are multi-dimensional in nature. The region of detonation is characterized by a coupled high-pressure front and reaction zone. As the wave moves through the columns of injectors, through regions of varying equivalence ratios, the reaction zone broadens as the region of post-detonation deflagration grows in time. The pressure and reaction fronts are closely attached when passing through the injector jets due to lower acoustic impedance reinforced by detonative heat release and become decoupled in very lean regions between injector columns. A cyclical process occurs over the

course of the injector region. The complex reaction zone consists of multiple pressure waves and density gradients. The initial wave does not completely consume the available fuel/oxidizer mixture, and turbulent mixing driven by vortices stemming from the triple points and three-shock region serves to mix the intermediary gases and ensure more complete combustion. In turn, the reaction zone is thicker and the detonation wave is of lower strength than the ideal ZND solution through a homogeneous mixture. The results are compared to the experimental observations of Burr et al. [40]. The detonation wave structures and complex reaction zones observed in the numerical simulation are similar to those seen in the experiment.

The second set of calculations evaluated detonation propagation through a stratified mixture of fuel and oxidizer arranged in irregular patches throughout a confined three-dimensional channel. Additionally, mixture preburning was added to the propellant mixture to simulate the effects of secondary combustion and premature deflagration observed in practical RDEs. These simulations highlight the importance of numerical simulations in their ability to interrogate configurations that may not be controllable through experiments. A detonation wave passing through non-detonable mixtures purely convects the reaction zone species, causing them to lag behind the shock front. In a stratified mixture, shearing forces generated as the detonation passes through the fuel-rich and fuel-lean regions augment the vortical structures generated at the triple points and mix the partially-burnt reactants within the reaction zone and post-detonation region. Through a DNS approach, three different length scales (0.581, 0.894, and 1.854 mm) of fuel/air stratification were simulated. The fuel/air stratification length scale directly affects the size of the vortical structures that are formed by the interaction of triple points and transverse waves along the detonation wave front. The small eddy size in the finest stratification case results in a fairly planar wave front, where the curved nodes along the wave front are more closely spaced. With increasing stratification length scale, the vortical structures increase in size,

and the reaction zone (characterized by mixing structures and sharp pressure gradients) broadens. There is greater variance in wave velocity, with a maximum wave speed nearly 25% above the CJ speed, in the large stratification case due to a concentrated energy release process enforced by the increased distance between discrete fuel sources. However, the large eddies are less efficient at allowing the residual and post-detonation gases to thoroughly mix within the reaction zone. This is evidenced by the increased variability of fuel mass fraction across the detonation wave in cases with increased stratification length scale.

Similarly, the detonation cell size – a product of the small-scale triple point and transverse/Mach wave interactions – scales with the stratification length scale. The soot foil patterns for the three studied cases show that the distribution of fuel and oxidizer can alter the effective detonation cell size for the mixture. Ultimately, the smaller stratification length scale leads to a higher combustion efficiency by nearly 5% over case 3. On the other hand, the larger stratification scale is beneficial for increased total pressure rise - nearly 6% greater than that of case 1. Heat release in a wave front-constrained region for case 1 is approximately 2.1% higher than in case 3. As a result, detonation strength and combustion efficiency compete with variations in fuel/air stratification. Overall, the physical structure of the detonation wave front is highly dependent upon the distribution of the fuel and oxidizer.

In the final simulation, premature deflagration is isolated by using a canonical channel system, where a prescribed preburning profile is used. The detonation wave was found to propagate with a spread of speeds, indicating that the preburning of the mixture significantly affects the strength of the leading shock. The most probable speed was close to the CJ speed, but the standard deviation was $\pm 15\%$, even for equivalence ratio variations that are small compared to practical RDEs. The detonation wave exhibited a complex structure, with a mixing region behind the propagating front where vortical structures with a length scale comparable to the stratification

length scale were created. The shock weakening was directly related to the preburning of the fuel/air mixture. The initial compression was smaller than theoretical values, with an average pressure increase of approximately 8 times the pre-shock pressure. Overall, the detonation structure was weaker, with even the triple points exhibiting lower peak pressures compared to expected theoretical values. These results indicate an important connection between pre-shock deflagration and loss of efficiency. In general, to have a compact heat release zone, it is necessary to have a strong compression wave. Any reduction in peak pressure can adversely affect the heat release profile. The premature deflagration process directly weakens this shock front, leading to a slow and distributed heat release. There is considerable unburnt fuel downstream of the shock front. In other words, so-called parasitic combustion (deflagration ahead of the wave) directly leads to commensal combustion (heat release far downstream of the wave), indicating that parasitic combustion is the root cause of loss of combustion efficiency. The fact that these features could be reproduced without significant turbulence in the system indicates that turbulence is more critical to the fuel/air mixing ahead of the shock rather than shock propagation itself. These simulations provide critical insight into how critical secondary effects influence detonation structure and performance. The non-ideal processes and their implications will influence the modeling choices and the analysis procedures of the full-scale simulations in Chaps. IV and V.

CHAPTER IV

Non-idealities in Non-premixed RDEs

The next chapter marks a shift in the dissertation towards the simulation of full-scale RDEs with non-premixed operation and a complex injection scheme. The numerical simulation of full-scale systems allows the analysis of secondary effects at the system level: unsteady mixing process, injector dynamics, multiple detonation waves with secondary competing waves, and the combustion process. To this end, the rotating detonation rocket engine (RDRE) designed and operated by Air Force Research Laboratory (AFRL) [21] and collaborators [132, 154, 278] is numerically represented and studied. Here, gaseous methane and oxygen are used as propellants and the detonation behavior under different operating conditions is evaluated. Furthermore, through Model Validation for Propulsion effort at the 2021 AIAA Scitech Forum, different aspects of the numerical simulation of non-premixed detonation engines are interrogated, using the RDRE as a representative design. The first section, Sec. 4.1, will describe the background for the application of RDEs in rocket applications. There are two numerical representations of the RDRE that will be studied: revision A and revision B. The numerical representation of the revision A RDRE geometry is described in Sec. 4.2.1. Section 4.2.2 presents the detonation behavior at three operating conditions. Additionally, the modifications to the numerical RDRE geometry developed during the MVP effort (revision B) are provided in Sec. 4.3.1.

The results with the revision B RDRE, along with various studies performed on resolution and ignition effects, are outlined in Sec. 4.3.2. The current understanding of the AFRL RDRE gleaned through numerical simulations of the revision A and revision B representations are summarized in Secs. 4.2.3 and 4.3.3.

4.1 Motivation

Rotating detonation engines have shown considerable promise for use in rocket propulsion applications. For instance, it has been theoretically shown that a 6-8% increase in specific impulse is feasible with the rotating detonation rocket engine (RDRE) [282, 317]. Rocket-type impinging injector designs have been studied numerically [96] and experimentally [44]. Kasahara et al. [106] have demonstrated the RDRE design for a sounding rocket system.

Realizing the advantages of an RDE is entirely dependent on an efficient design that can reduce losses due to incomplete or non-ideal detonation [316]. Due to the non-premixed injection, mixing the reactants sufficiently such that the detonation wave is sustained is critical. At the same time, the shock wave creates a high-pressure blockage of the inlets, and can temporarily inhibit or reduce reactant inflow during a detonation cycle, altering the mixing performance for the next cycle. Moreover, if the incoming flow is compressible (i.e, Mach number greater than 0.6), mixing is further suppressed [276]. In fact, the lack of complete mixing can lead to premature deflagration [255], weaker detonation waves [40], and slower heat release that does not support the detonation wave [50].

RDEs are closely linked to acoustic instabilities found in rocket combustors [3, 4]. In particular, multiple waves and weaker secondary waves that interact with the primary detonation are possible. At the same time, the detonation wave speed may not be stable, with variations due to turbulent mixing-induced stratification. Consequently, regular failure/re-ignition of detonations is possible. It has been consistently

observed that turbulence leads to enlarged reaction zones in RDEs [40, 226, 235]. Prakash et al. [235] found that discrete injection led to thicker detonation structures with a leading shock wave followed by a complex set of pressure waves created by a distributed reaction zone. Moreover, this structure creates vortical flow and lends to mixture homogenization behind the shock wave. The wave itself is weaker than ideal premixed detonations, with a reduced pressure increase [61, 247]. Discrete injection of methane/oxygen in a linearized system has demonstrated that the wave propagation velocity ranges from over 90% of the theoretical Chapman Jouguet (CJ) velocity to as low as 81% based on the phasing of the oxidizer injection in comparison to that of the fuel [41]. In the development of a stable and efficient RDE, it is important to understand the relationship between the injection and detonation processes.

While a number of different mixing configurations have been studied [45, 91, 96, 122], the impinging jet design is preferred due to its use in conventional rocket combustors [302]. Understanding the impact of mixing in compressible conditions (which deters turbulent mixing) on the detonation process is critical for designing robust RDREs. Here, the fuel and oxidizer are introduced at an angle, which creates a shear layer where the jets meet and convect downstream. The onset of mixing and the breakdown of the shear layer are influenced by the relative composition of the fuel and oxidizer streams. Hence, a region of non-mixed or poorly mixed reactants exists near the base of the detonation chamber, which may serve to diminish detonation strength near the base of the channel. In past numerical studies, the detonation wave is found to be situated at some standoff distance from the injector plane, as peak heat release occurs within well-mixed regions [61]. This wave positioning may be beneficial in suppressing the heat flux into the injector plenums and erosion of the injector surface [174]. However, if the mixing is incomplete or if there is sufficient time for autoignition prior to wave arrival, the detonations will be weaker [95].

Further, methane and natural gas are favorable fuels for use in RDREs due to their

high specific impulse and lower coking propensity compared to some RP fuels [287]. These fuels are readily available and workable low-cost energy sources [33]. Methane-fueled RDEs have been extensively studied both experimentally and numerically [94, 151, 283, 312]. With this background, the focus of this study is on understanding the interaction between mixing and detonations in an RDRE designed for operation with methane and oxygen, a configuration studied experimentally at the Air Force Research Laboratory (AFRL) [21]. In particular, the role of the transient mixing process in stabilizing the detonation wave is extracted from detailed simulations. The injector dynamics and the combustion process are also interrogated.

4.2 Revision A AFRL RDRE

4.2.1 Numerical configuration and approach

The AFRL RDRE geometry consists of 72 pairs of impinging discrete fuel and oxidizer injectors arranged within an annular combustion chamber, as shown in Fig. 4.1, with inner and outer diameters of 66.2 mm and 76.2 mm, respectively, resulting in an annulus width of 5 mm. Due to the similar detonability of methane/oxygen mixtures in comparison to hydrogen-air mixtures, the annulus width is similar to that of hydrogen-air RDCs used in past studies [247]. Figure 4.2 provides a cross-sectional schematic of this geometry. The fuel and oxidizer injector diameters are 0.787 mm and 1.245 mm, respectively. The area ratio between the oxidizer injectors and the detonation annulus is 0.099.

An unstructured mesh resolution of 200 μm is provided throughout the injector and the lower detonation channel region, relaxed to 400 μm within the upstream plenum and aft region of the detonation channel and outflow plenum. The resolution of 200 μm is equivalent to the order of the induction length for methane/oxygen detonation at atmospheric pressure. The full-scale resolution resolves 1-2 points

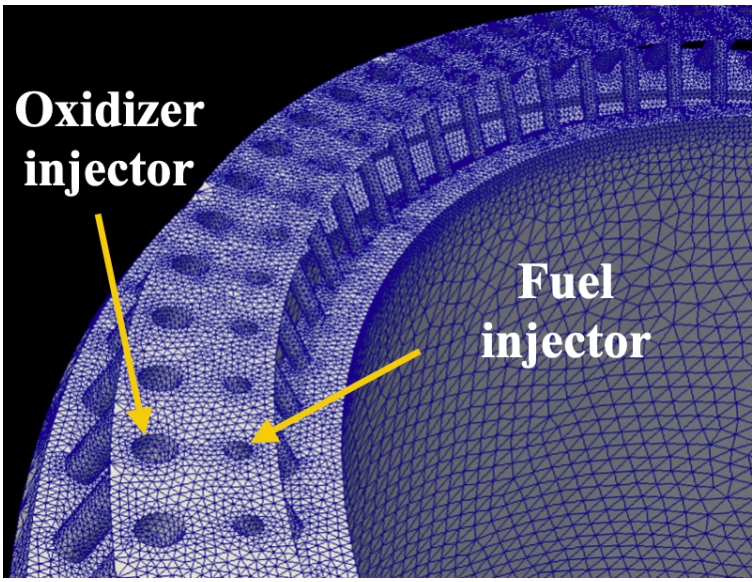

Figure 4.1: Cut-away view of the RDRE combustion chamber with impinging fuel and oxidizer injectors.

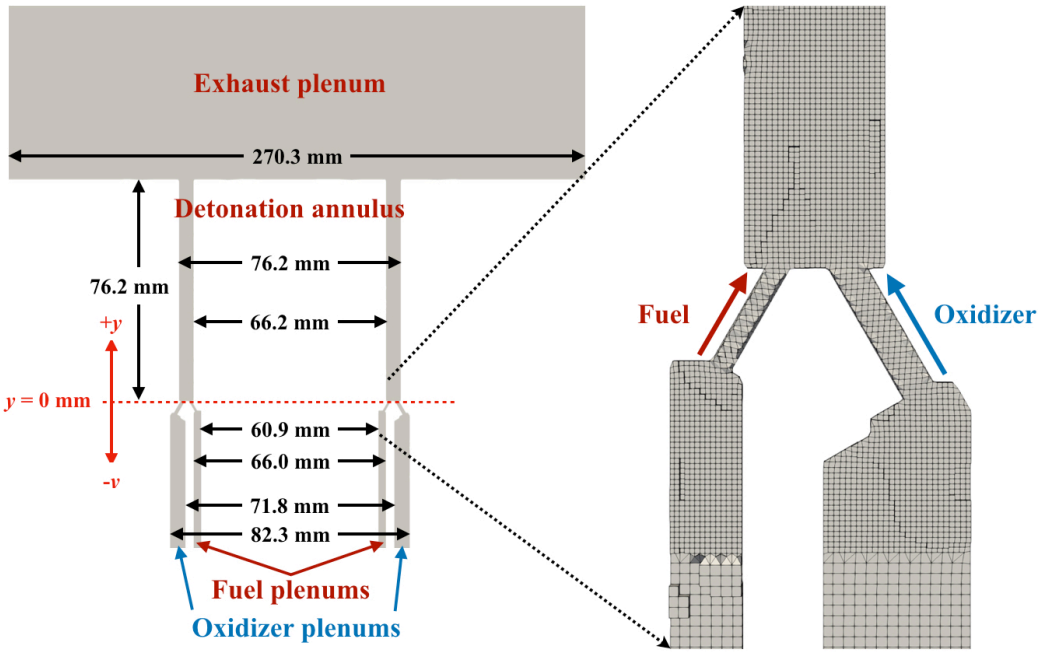

Figure 4.2: Cross-sectional schematic with primary dimensions of the AFRL methane/oxygen RDRE with a detailed view of the computational mesh near the injector scheme and detonation annulus.

across the one-dimensional induction length. However, in three-dimensional detonation with non-premixed injection, the detonation process is highly non-ideal, leading to broad reaction zones and induction lengths that are significantly longer than the

one-dimensional relation [40, 231, 234, 235]. The selected grid resolution resulted in at least 10 cells across the broadened induction length, approximately an order of magnitude larger than that of the ideal detonation case. Consequently, the selection of refinement sufficiently captures the detonation process, and note that a similar refinement for numerical simulations is used in both full system RDC studies and two-dimensional unwrapped RDC analysis [212, 263]. As a result, there are 29.2 computational control volumes within the domain. The walls are modeled with a no-slip, adiabatic boundary condition. At this time, additional resolution is not provided near the walls to resolve boundary layer effects.

A range of flow rates is considered to isolate the effect of plenum pressures on wave behavior. A list of the simulations is provided in Tab. 4.1. The back pressure is set to 0.1 MPa for all cases. The macroscopic design parameters of the RDRE are obtained as follows. The mass flow rate is computed by:

$$\dot{m} = \int_{inlet} \rho u dA_{inj}, \tag{4.1}$$

where $\dot{m}$ is the target mass flow rate, ρ is the gas density, u indicates the axial flow velocity, and A is the cross-sectional area. The net thrust reaction force is obtained as:

$$T = \int_{exit} \rho u^2 + (p - p_{back}) dA_{exit}, \tag{4.2}$$

where p is the gas pressure and p_{back} is the imposed back pressure.

The specific impulse is given by:

$$I_{sp} = \frac{F}{\dot{m}_{fuel} g}, \tag{4.3}$$

where g is the gravitational acceleration and $\dot{m}_{fuel}$ is the mass flow rate of fuel.

The numerical procedure is as follows. The detonation annulus is initialized with

Table 4.1: RDRE case parameters for three different operating conditions.

	Nominal	**High ϕ**	**High $\dot{m}$**
$\dot{\boldsymbol{m}}_{\boldsymbol{fuel}}$ **[g/s]**	5.97	7.95	7.58
$\dot{\boldsymbol{m}}_{\boldsymbol{oxidizer}}$ **[kg/s]**	0.207	0.185	0.277
$\dot{\boldsymbol{m}}_{\boldsymbol{total}}$ **[kg/s]**	0.267	0.265	0.353
$\boldsymbol{\phi}$	1.15	1.71	1.09
$\mathbf{P}_{\boldsymbol{f,plen}}$ **[MPa]**	1.21	1.49	1.39
$\mathbf{P}_{\boldsymbol{o,plen}}$ **[MPa]**	1.10	0.94	1.34
$\mathbf{T_0}$ **[K]**	300	300	300
$\mathbf{P}_{\boldsymbol{back}}$ **[MPa]**	0.1	0.1	0.1

a quiescent flow field. Fuel and oxidizer issue from the upstream plenums which are pressurized with a uniform velocity. Further, a mass flow rate boundary condition is employed at the plenum axial inflow boundary surface to ensure that the desired feed mass flow rate is achieved. The injectors are developed in the absence of combustion for 0.5 ms and the flow is choked at the injector throat. A shear layer forms at the mid-channel location, parallel to the channel walls. Due to the highly turbulent flow, the fuel and oxidizer mix as the jet shear layer breaks down. The temperature and pressure within the domain do not support the onset of combustion. A one-dimensional Zeldovich-von Neumann-Döring (ZND) profile is patched within the base of the annulus to drive the formation of a detonation wave. The patched region occupies the full width of the detonation annulus and has a height similar to the injector fill height. The highly unsteady flow is allowed to evolve for 1.0 ms until statistically-stationary detonation behavior with a stable number of waves is established. Under steady-state operation, the simulation is executed for an additional 1.0 ms, corresponding to roughly 6-8 system cycles (depending on the wave speed). At this point, a detailed analysis of the system is performed.

4.2.1.1 Chemical kinetics mechanism

The skeletal mechanism, FFCMy-12, of Xu et al. [277, 326] is utilized to reduce the number of transported species and decrease the computational cost. Based on the Foundational Fuel Chemistry Model 1.0 [277], this mechanism employs 38 reaction steps with 12 species to model the combustion of methane/oxygen mixtures. This model has been developed for use in detonative flow problems. The mechanism has been validated through a series of one- and two-dimensional numerical simulations to evaluate the Chapman-Jouguet (CJ) velocity, von Neumann pressure, and detonation cell size. To ensure that the choice of chemical mechanism does not unduly affect the outcomes of this study, several canonical flow configurations are considered in Sec. 2.2.8.

4.2.2 Simulation results and discussion

4.2.2.1 General behavior

The AFRL RDRE is numerically evaluated at the three different operating conditions outlined in Tab. 4.1. The baseline, high equivalence ratio, and high mass flow rate cases primarily differ in the global equivalence ratio of the fuel-oxidizer mixture. The pressure and temperature contours at the midchannel location of the three-dimensional geometry, unwrapped and projected onto two dimensions, are provided in Fig. 4.3. In the baseline and high mass flow rate cases, two co-rotating waves are observed. While weak counter-rotating secondary waves are shed from the primary wave system, these structures do not manifest completely and are suppressed during the collision with the primary waves. It must be noted that the secondary waves are of slightly higher strength in the high mass flow rate case. The primary wave system is largely planar and stands vertically in the detonation chamber, whereas the oblique shock wave stemming above the fill height of the injectors is at a greater

angle with the vertical in the high mass flow rate case, arcing away from the direction of wave propagation. Here, the peak pressures observed along the wave front are significantly stronger, and the triple point structure enforces greater corrugation of the wave front. Due to the higher pressures observed at the wave front, the expansion zone extends further behind the wave. The oblique shock wave stemming from the detonation front imposes higher compression of the gases in this high mass flow case. On the other hand, the high equivalence ratio case is distinguished by the existence of four waves, consisting of two counter-rotating wave pairs, within the detonation chamber. Both waves in each counter-rotating pair are of similar strength, and as a result, are sustained at a steady-state mode of operation. The detonation waves are significantly weaker than the high mass flow rate and baseline cases, with a reduced amount of triple points along the front. Consequently, the wave front is noticeably arced towards the direction of propagation, as it seems the shock front is leading the detonation front. Due to the lower peak pressures observed here, the expansion to atmosphere conditions occurs more compactly.

In the temperature contours of Fig. 4.3, the effect of the detonation wave system on the injector recovery process is discernible. In comparison to the baseline case, the high mass flow rate case features a greater fill height of the fuel-oxidizer mixture. While preburning of the reactant mixture imposes a contact surface and a parabolic injector profile between detonation waves in both cases, the effect of preburning is noticeably lower in the high mass flow case. The preburning (in the baseline case, for instance) is visualized through the contours of OH and the normalized product of HCHO and OH in Fig. 4.4. Here, the wave in the azimuthal plane is projected onto two dimensions, replicating a viewing window from experimental optical imaging. OH residual ahead of the detonation wave front is seen, and the normalized product of formaldehyde and hydroxide increases just ahead of the wave and continues through the reaction zone. In the baseline case, the injector height reaches a peak value at

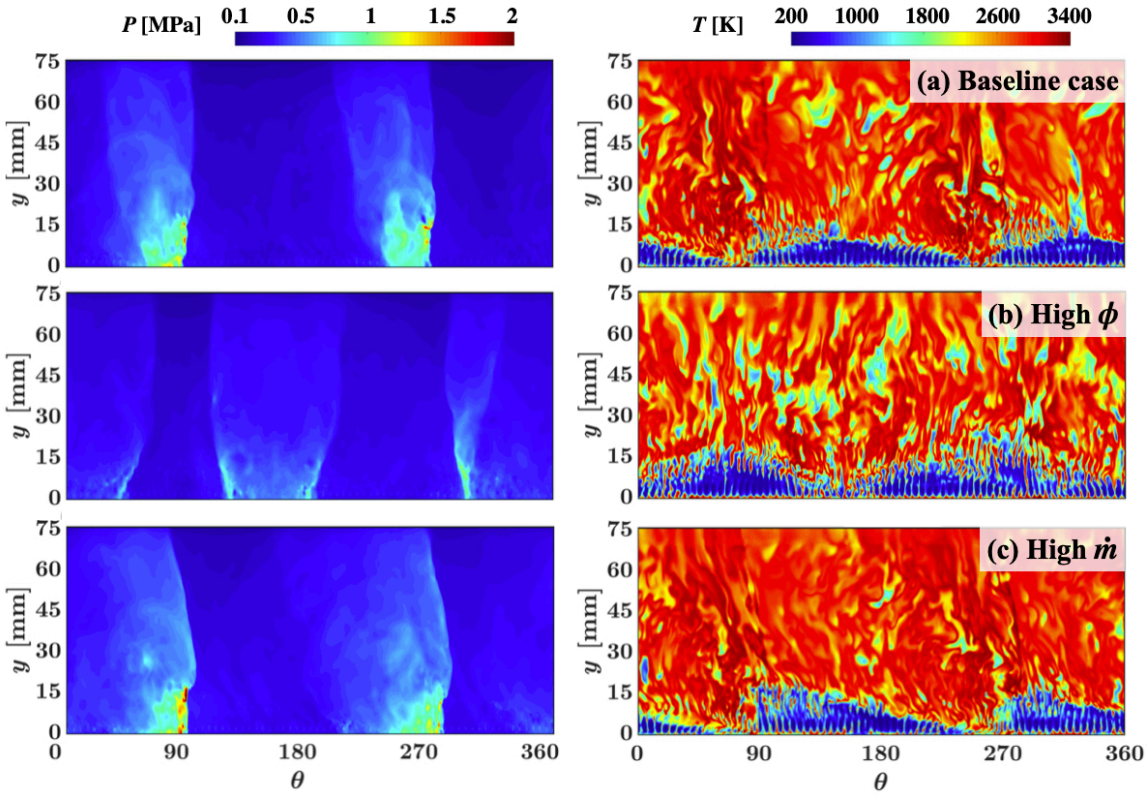

Figure 4.3: Two-dimensional projection of pressure and temperature contours for a) the baseline (top row), b) high ϕ (middle row), and c) high $\dot{m}$ (bottom row) cases.

the midpoint between the two detonation waves whereas, in the high mass flow rate case, the fill height continues to grow prior to the arrival of the second wave. Contact surface burning of the injectors starts to narrow the injector column width beyond this intermediate location but the column remains attached. This is primarily due to the high plenum pressures and increased stiffness of the fuel and oxidizer injectors in this configuration. The low-temperature region near the base corresponds to the cold fuel and oxidizer jets issuing from the injectors. This region is separated from the high-temperature fluid by a contact surface, which is similar to the structure seen in two-dimensional simulations [264]. When the detonation wave passes over a pair of injectors, it introduces high-temperature post-detonation gases to the base of the channel. However, as will be shown below (Sec. 4.2.2.2), the high plenum pressures

prevent complete blockage of the reactant flow. As a result, the jets quickly recover behind the detonation wave. Further, jet impingement appears to prevent much of the post-reaction gases from entering the region between the injectors near the base of the channel, which can cause premature deflagration and loss of efficiency. As a result, only limited deflagration ahead of the wave is observed close to the base as much of the high-temperature gas is evacuated from the injector region.

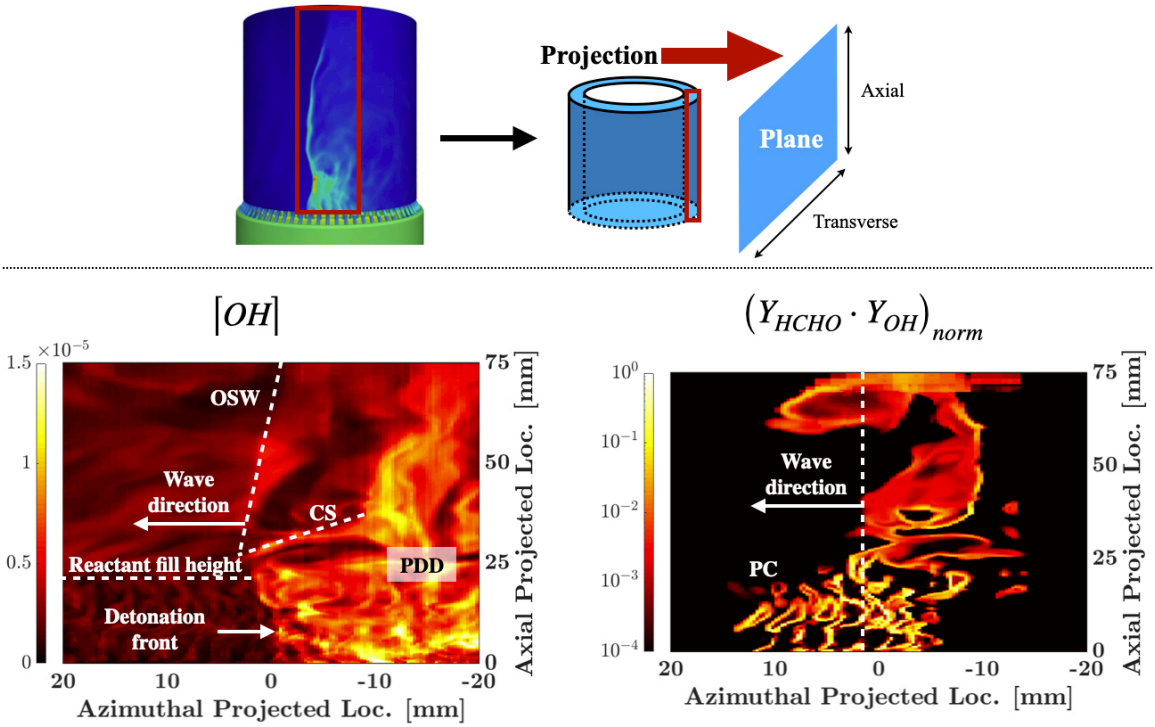

Figure 4.4: (Top row) projection method for two-dimensional optical window visualization and (bottom) two-dimensional projection of OH molar concentration and normalized product of HCHO and OH as a detonation wave passes the "optical window."

On the other hand, contact with the post-detonation gases at the top of the jet fill height seems to introduce significant deflagration ahead of the wave, reflected in the parabolic shape of the jet height of the baseline case. The jet recovery following wave passage reaches a maximum injection height midway between the detonation waves, followed by deflagration of the contact layer and a reduction of the unreacted fluid

height. Figure 4.3 also shows the pressure contour highlighting the two detonation waves. Unlike ideal two-dimensional flows, the pressure waves display a spatially-distributed structure. In discrete injection-based systems, it has been observed that the detonation wave can become thicker, primarily due to the variations in the mixture properties between injectors [41, 95, 235]. However, shock-weakening is considerably more severe in discrete injection-based hydrogen-air systems [50, 247, 255]. In these systems, it was found that parasitic combustion, in the form of premature ignition of the fuel-oxidizer mixture led to a weakening of the detonation structure. In contrast, the temperature contour here does not show significant deflagration close to the injection plane.

In the high equivalence ratio case, a curved injector profile is also visualized, but greater column heights are enforced due to the higher relative mass flux of the fuel stream. Further, the prevalence of lower temperature gas in the detonation chamber in this configuration results in slightly diminished preburning of the reactant mixture at the fill height contact surface. The additional waves observed here result in a more chaotic injector profile. However, even at the location of the detonation wave, the injector stream is not suppressed to the extent observed in the baseline and high mass flow cases due to the lower ratio between the detonation pressure and reactant plenum pressures. Further, higher temperature gas is observed throughout the detonation channel in the high mass flow rate case, and the amount of low-temperature gas increases with the baseline case, and even more low-temperature gas is observed in the high equivalence ratio case. Thus, the detonation efficiency appears to decrease with the baseline and high equivalence ratio case as a more partially burnt and low-temperature gas mixture is prevalent. In the high equivalence ratio case, large pockets of cold gas exist at locations downstream of the detonation chamber and are convected towards the exit.

To understand the source of the efficiency loss, the mixing structure close to any

given pair of injectors is considered for the baseline case (Fig. 4.5). It is seen that right when the wave arrives, the jet is fully developed. However, a region of very high fuel concentration is formed near the wall, which leads to reduced detonation strength. As the wave passes over the injectors, the jets become suppressed and recover to full height as the second wave arrives. It is important to note that no large-scale circulation is observed here. The region of detonable mixture is near the center of the annulus. In order to understand the flow structure, it is useful to plot the Takeno flame index [330]: $\xi = \nabla Y_F \cdot \nabla Y_O / |\nabla Y_F||Y_O|$. A value of -1 indicates a diffusion-flame-like behavior, while 1 indicates a premixed deflagration. In the present context, this quantity could be used to deduce the local mixing structure. Figure 4.5 shows that the interface between the rich fuel and the oxidizer stream is predominantly diffusion-like, while regions closer to the wall are more characteristic of premixed-like mixtures. Closer to the walls, the premixed structure would indicate that fuel entrainment into the oxidizer stream is nearly complete. In spite of the large variations in fuel composition throughout the cross-section and as a function of time, the indicator function is nearly randomly distributed, with lamellar-like structures.

Figure 4.6 provides the mean axial pressure distribution at the outer wall for the three different cases, in comparison to experimental continuous tube attenuated pressure (CTAP) measurements. Note that the numerical measurements represent temporally-averaged pressure values at the outer wall location and do not model the CTAP dynamics. All three cases provide a gradual decay in pressure with axial distance, however, the high mass flow rate case results in the highest pressure for the length of the detonation channel as expected. The baseline and high equivalence ratio cases feature similar profiles, with a peak pressure observed between 5-10 mm downstream of the channel. Between 20 and 70 mm, a near-linear decay in average pressure is observed. Similar behavior is observed in the pressure contour of Fig. 4.11. In the baseline case, the numerical pressure measurements overpredict the pressure in

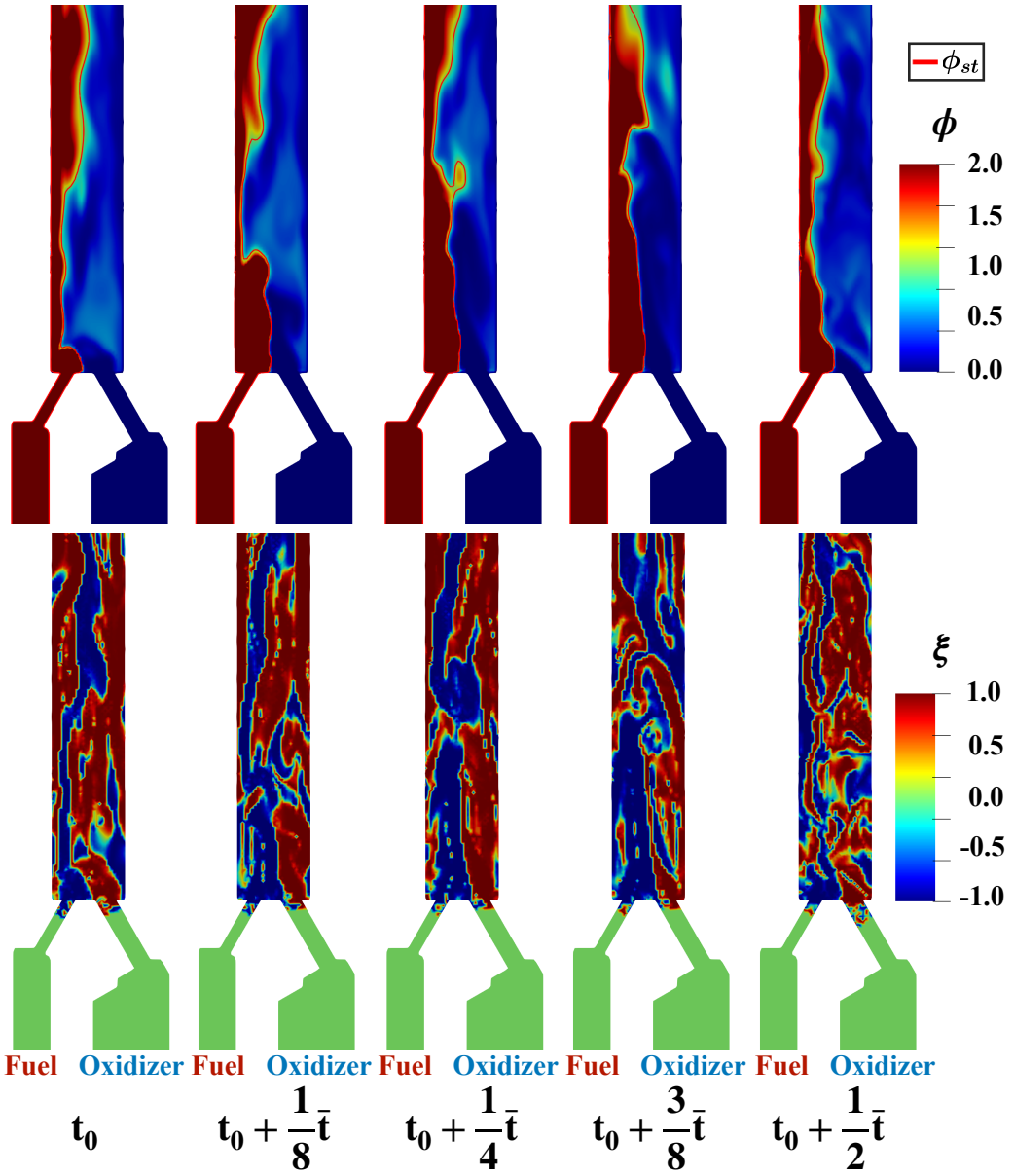

Figure 4.5: (Top row) Equivalence ratio and (bottom row) Takeno flame index contour time history during the passage of a detonation wave in a cutting plane normal to the injector system, where $\bar{t}$ is the period of the detonation wave pair. An initial wave has passed t_0 and a second wave has swept the injector at $t_0 + \frac{1}{2}\bar{t}$.

the detonation annulus for the length of the combustor. The pressure peaks transpire over a very short duration (roughly 1μs), which may not be measurable even using high-frequency dynamic pressure equipment. Other studies [49] have shown that peak pressure measurements in experiments are consistently lower than expected values ei-

ther from theory or from simulations [255]. It is also seen that the peak pressures along the wave front vary with time, indicating unsteady and variable detonation behavior. In the high equivalence ratio case, the numerical measurements are similar to the experimental measurements, with lower mean pressures than the baseline case, indicating that a weaker detonation wave (lower pressure jump and gradient) may contain a broader pressure front that may be captured by CTAP equipment more accurately. However, in the high mass flow case, the numerical measurements undershoot the experimental values but are roughly 20% higher than the baseline and high equivalence ratio cases. Further, the numerical pressure profile is distinguished from that of the other cases by a plateau until about 10 mm channel height. Beyond, this point the decay in pressure with axial distance occurs more rapidly with downstream distance until approximately 30 mm channel height, with an increased presence of oscillations in the pressure profile. The plateau highlights that a strong detonation wave exists throughout the first 10 mm of the detonation chamber. Subsequently, a stronger expansion region exists from 10 to 20 mm, resulting in a more rapid reduction in pressure. By the end of the detonation channel, the mean pressure is still higher than the baseline and high equivalence ratio cases.

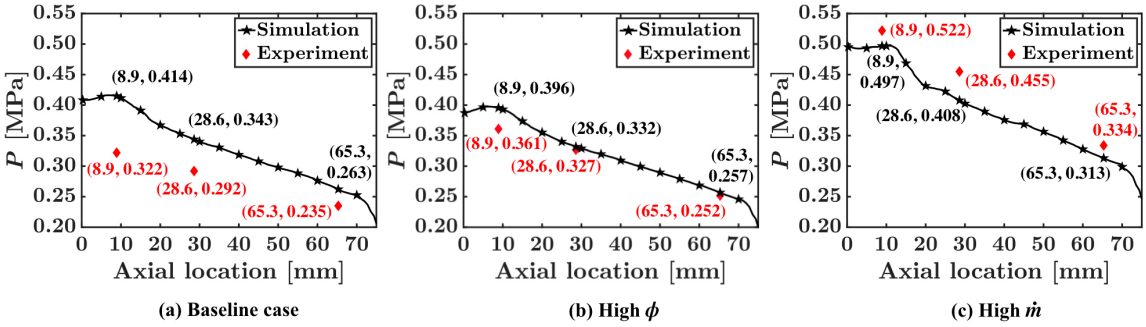

Figure 4.6: Comparison of average axial pressure at the outer wall with experimental results for (a) the baseline, (b) high ϕ, and (c) high $\dot{m}$ cases.

To understand the differences in the axial pressure profiles, the transient pressure signal sampled from simulations at 2,000,000 Hz is plotted on the right in Fig. 4.7.

It is seen that the pressure peaks transpire over very short durations (roughly 1μs), which may not be measurable even using high-frequency pressure sensors. Other studies [49] have shown that peak pressure measurements in experiments are consistently lower than expected values, either from theory or from simulations [255]. In the capillary tube average pressure (CTAP) measurement, viscous dissipation within the tube results in a temporal average of the pressure measurement. Viscous effects attenuate the pressure perturbations and may dampen the unsteady pressure fluctuations observed within the chaotic RDE flow environment. Further, the numerical measurements do not model the CTAP dynamics. It is also seen that the peak pressures significantly vary between cycles, indicating a highly unsteady and variable detonation front. Further, it was found that the wave speed can be as high as 50% over this baseline value, and could also quench/re-ignite during the run.

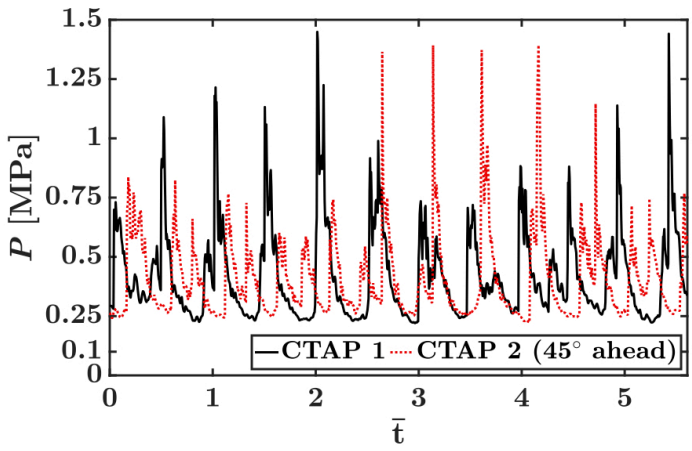

Figure 4.7: The pressure trace at two locations azimuthally 45° apart and at 8.9 mm axial height from the injection plane, for the baseline case. Sampled at 2,000,000 Hz, the pressure trace highlights the cycle-to-cycle variation in peak pressure and the narrow duration of the passing detonation front tracked by the pressure measurement.

Table 4.2 outlines the wave speeds observed among the three cases for both the numerical simulations and the experiment. Due to the weaker detonation in the high equivalence ratio case, wave speeds 7% lower than the baseline condition were computed. The decay in wave speed between the baseline and the high equivalence

Table 4.2: Wave speed for the three different operating conditions.

	Baseline	**High ϕ**	**High $\dot{m}$**
$\boldsymbol{U_{wave,sim}}$ **[m/s]**	1279	1202	1405
$\boldsymbol{U_{wave,exp}}$ **[m/s]**	1563	1179	870

ratio case observed in the experiment is captured here. However, while the experiment observed largely diminished wave speeds at the high mass flow rate condition, the simulation predicts 10% higher wave speeds, supported by the increased detonation strength and higher average chamber pressure (Fig. 4.6) of the high mass flow rate case.

4.2.2.2 Unconditional features

To quantify the behavior of the injection system to the passing detonation wave, temporally-averaged axial flow velocity (U_y) and static pressure is presented in Fig. 4.8. The profile is sampled at the middle of the fuel and oxidizer throat cross-section at $y = 0$ mm, the base of the detonation chamber. Note that this profile is also spatially averaged over multiple injectors at an equidistant spacing from one another. $\bar{t}$ represents the mean cycle period of the detonation wave system. In all three cases, a single cycle of the RDRE features two passes of the detonation wave system at a given point in the domain. In the high equivalence ratio case, a pair of counter-rotating detonation waves arrive at a given injector at roughly the same time. Consequently, each injector recovers within half the mean cycle period. In the response of both the fuel and oxidizer streams, the high mass flow rate imposes the greatest suppression due to the highest observed detonation pressure. For the high mass flow rate case, the fuel stream diminishes to nearly 20% of the full flow rate due to wave passage, while a reduction to approximately 25% is observed for the baseline case. The baseline case exhibits slightly lower decay whereas the fuel stream is minimally affected by the

passing detonation wave in the high equivalence ratio case, as expected. Further, the stiffness of the injector is demonstrated in the initial response to the detonation wave: in the baseline and high equivalence ratio cases, the injector flow velocity is affected by the increased pressure ahead of the detonation wave due to mixture preburning and the flow responds more gradually to the passing detonation wave than in the high mass flow rate case. Here, the fuel mass flow rate is stable at the fully-choked condition until it decays abruptly due to the spike in the chamber pressure. Similar behavior is observed in the oxidizer stream.

Due to the asymmetry in the fuel distribution seen in Fig. 4.10, the detonation wave is stronger near the inner wall for the baseline and high mass flow rate cases, and hence the fuel injector. Consequently, the detonation wave arrives earlier at the fuel injector than the oxidizer injector. The formation of triple points and detonation wave ignition near the inner wall of the chamber results in greater acoustic fluctuations in the response of the fuel injector. Interestingly, in the oxidizer stream, the baseline and high equivalence ratio cases respond similarly. As seen in Fig. 4.10, the detonation process shifts towards the outer wall in the high equivalence ratio case, resulting in pressures near the oxidizer injector similar to that of the baseline case (as seen in the pressure profiles). The benefit of the high feed pressures of RDRE injector schemes manifests in the lack of reverse flow observed in both the fuel and oxidizer injector streams, even in the high mass flow case. For the baseline and high mass flow rate cases, both the fuel and oxidizer injector recover completely before the arrival of the next detonation wave. In the pressure profiles of the fuel and oxidizer streams, the flow pressure momentarily exceeds the plenum pressure in the high mass flow rate case. However, this does not lead to flow reversal due to the short duration of the high pressure. With increasing detonation strength, the injectors are more affected by the passing detonation wave, but the recovery to the choked condition occurs more rapidly. Even though flow reversal is not observed, pressure waves from

the detonation front do enter the feed plenums but are quickly dissipated by viscous forces. An increased detonation pressure (due to a mass flow rate higher than those tested here) may result in a momentary flow reversal for this injection scheme.

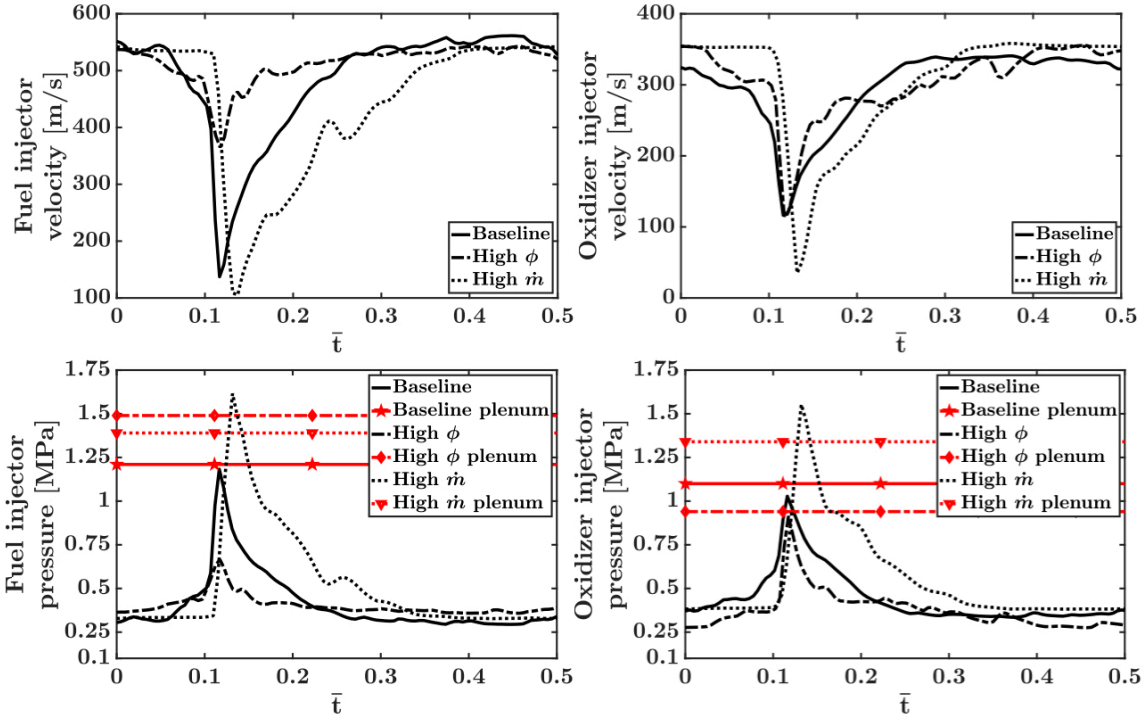

Figure 4.8: Comparison of temporally and spatially-averaged axial flow velocity ($\boldsymbol{U_y}$) and pressure for the fuel and oxidizer injector among the baseline, high ϕ, and high $\dot{m}$ cases. $\bar{\boldsymbol{t}}$ is the mean cycle period of the detonation wave system, where a cycle is composed of two detonation wave passes in all three cases.

In order to understand the combustion processes among the three different cases, Fig. 4.10 shows time-averaged mixture fraction and heat release contours within the lower detonation chamber. The mixture fraction is defined (through Bilger's method [29]) with the elemental mass fractions of carbon (C), hydrogen (H), and oxygen (O) as:

$$Z_{mix} = \frac{\frac{Z_C}{mW_C} + \frac{Z_H}{nW_C} + \frac{2(Y_{O_2,2} - Z_O)}{\nu'_{O_2} W_{O_2}}}{\frac{Z_{C,1}}{mW_C} + \frac{Z_{H,1}}{nW_C} + \frac{2Y_{O_2,2}}{\nu'_{O_2} W_{O_2}}} \tag{4.4}$$

where Z_l is the elemental mass fraction of the l-th element, Y_k is the species mass

fraction of the k-th species, W_k is the molecular weight of the k-th species, the subscripts 1 and 2 denote the fuel and oxidizer streams, respectively, the subscripts C, H, O and O_2 refer to the parameters for carbon, hydrogen, oxygen, and oxygen gas, respectively, the values of m and n are the number of carbon and hydrogen atoms, respectively, in the representative hydrocarbon fuel C_mH_n, and ν_{O_2} is the stoichiometric coefficient for O_2 in the representative chemical reaction.

In the baseline and high mass flow rate cases, the higher mass flux of the oxidizer in comparison to that of the fuel biases the stoichiometric line towards the inner wall. The heat release profiles for the baseline and high mass flow rate cases are similar in structure, but a greater fraction of heat release occurs around the 10 mm channel height in the high mass flow case. This is supported by the increased detonation strength, as the primary front is established at some standoff distance from the base of the channel. As seen in Fig. 4.6, the peak pressure in all three cases occurs at this axial distance. It appears that the heat release is more spatially distributed in the baseline case. The heat release profile follows the stoichiometric isoline in both cases, which signifies the shear layer between the fuel and oxidizer streams. The high equivalence ratio case exhibits interesting behavior, with a near-vertical stoichiometric isoline near the base of the channel. Further downstream, the stoichiometric line shifts very near to the outer wall. Near the injection plane, the stoichiometric isoline shifts toward the fuel stream rather than toward the oxidizer stream as observed in the other two cases. Thus, it seems that in the baseline and high mass flow cases, the fuel is entrained in a recirculation zone due to the impingement of the oxidizer stream at a higher relative mass flow rate than in the high equivalence ratio case. In the high equivalence ratio case, the heat release is highly concentrated in a region ranging from 7.5 to 12.5 mm injection height, near the mid-channel location. Due to the high local equivalence ratio, the majority of heat release occurs further downstream than the other two cases; the local equivalence relaxes more slowly than the baseline and high

mass flow cases as a higher mixture fraction is observed at distances downstream of the channel. The heat release also features two distinct pathways near the base of the channel, separated by a region of diminished heat release between 2.5 to 5 mm axial location. The mixture fraction contour shows lower mixture fraction near the inner wall at this height than in the baseline and high mass flow rate cases, lending to a lower heat release fraction. Overall, the heat release occurs across a broader radial region than in the baseline and high mass flow conditions. In all three cases, the heat release fraction drops off beyond the 20 mm axial location.

Since detonations occur at slightly richer mixtures, wave propagation occurs preferentially closer to the inner wall where a well-mixed layer exists. Following reignition, the high-pressure region spans the full width of the channel. On the other hand, the wave is slanted forward in the azimuthal sense (as seen through an axial cross-section view of Fig. 4.9), with the shock leading near the outer wall. This is attributed to the expansion effects of a detonation through a curved channel. However, due to the well-mixed layer near the inner wall, wave strength near the outer wall cannot be sustained. Consequently, an oscillatory wave strength phenomenon in time, due in part to the competition between the fuel distribution and curvature effects, is observed in this configuration. While heat release is oriented towards the inner wall as well, it is more uniformly distributed across the cross-section. Interestingly, the peak heat release occurs close to the injection plane, where deflagration is observed (Fig. 4.3). This is mainly because the deflagration process is stably-observed throughout the cycle, while detonation-based heat release occurs only during wave passage over the injectors.

Additionally, an unmixedness factor, defined as $\chi = \langle Z''^2 \rangle / (\langle Z \rangle (1 - \langle Z \rangle))$, which is a measure of the variation in the local mixture fraction, shows that the high mass flow rate case features slightly greater variation in the local composition along the jet mixing layer than in the baseline case, but a similar trend is observed. However,

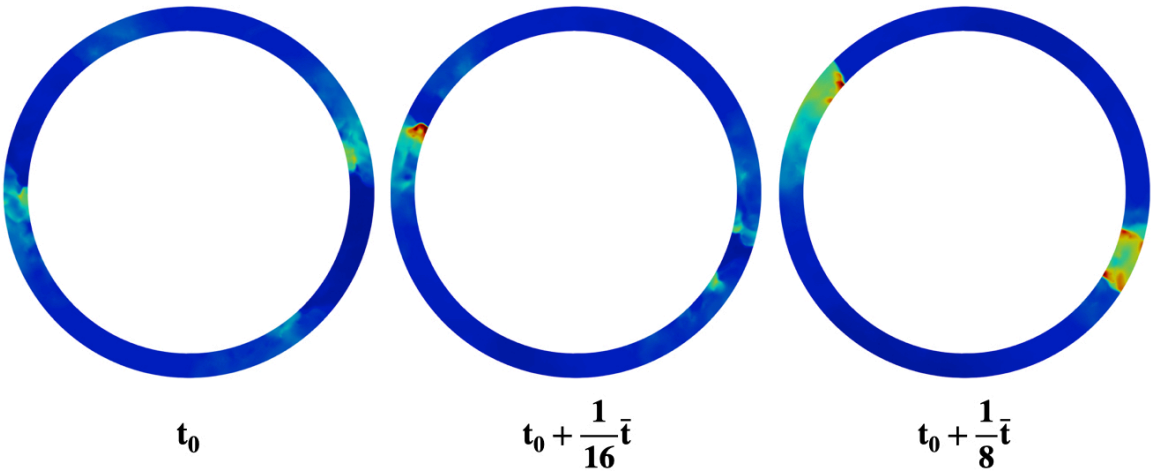

Figure 4.9: Baseline case pressure profile time sequence in the axial cross-section at a height of 8.9 mm from the base of the detonation chamber, separated by approximately 0.01 ms.

near the stoichiometric line for the high equivalence ratio case, a very large χ value is observed, reminiscent of jet flapping behavior, indicating that the local composition is highly susceptible to the passing detonation wave. Further, the high local equivalence ratio supports the large level of unmixedness observed in this case. Compared to the other cases, the unmixedness parameter of not insignificant values exists beyond 10 mm in a broader radial region. Similarly, due to the slightly higher global equivalence ratio of the baseline case in comparison to that of the high mass flow case, the flow remains unmixed for a slightly longer downstream distance here, and higher unmixedness levels are observed near the base of the chamber. The high equivalence ratio case results in the least mixing, supported by the weaker detonation and more chaotic flow behavior observed in this configuration. For all the cases, χ is quite high (at least 0.4), which shows jet unsteadiness similar to flapping. Further, the flow remains unmixed for a significant distance downstream, indicating that fuel-oxidizer mixing is not high in this configuration. This further validates the lower wave speeds observed in the simulation and experiment in comparison to theoretical values.

Figure 4.11 provides the temporally-averaged mixture fraction [29], temperature,

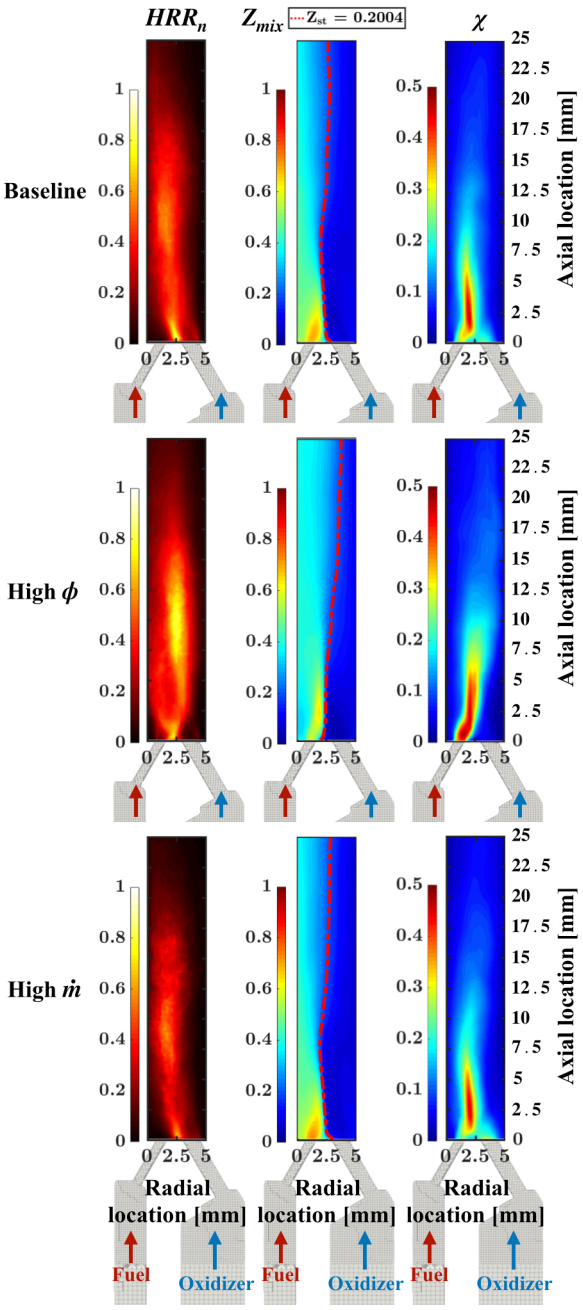

Figure 4.10: Normalized heat release rate (left column), mixture fraction (middle column), and unmixedness factor $\chi = \langle Z''^2 \rangle / (\langle Z \rangle (1 - \langle Z \rangle))$ (right column) for (top row) the baseline, (middle row) high ϕ, and (bottom row) high $\dot{m}$ cases in the lower detonation channel averaged over multiple cycles during steady-state operation. The isoline of mixture fraction (middle column) highlights the stoichiometric region within the detonation channel.

and pressure in the complete detonation channel for the three cases. While the baseline and high mass flow rate cases result in similar profiles for all three parameters, the high mass flow results in stronger detonation with higher pressures in the lower detonation channel. Further, high pressure is biased towards the outer wall and the highest temperature occurs in the midchannel location beyond the 20 mm axial location. On the other hand, in the high equivalence ratio case, the region of higher mixture fraction is interestingly shifted away from the inner wall; the low temperature associated with the fuel stream is located near the mid-channel location and a high-temperature pocket of gas exists at the inner wall location, a behavior not observed in the other two cases. Furthermore, the isoline of rich mixture fraction of $Z_{mix} = 0.40$ shows that the composition contains less fuel near the inner wall as a region of rich mixture fraction is bounded at the midchannel location. Further downstream, the mixture becomes more homogeneous with a higher mixture fraction throughout the inner half of the annulus. Thus, the higher momentum flux of the fuel in comparison to the oxidizer creates a stiffer column of fuel that is able to penetrate the oxidizer jet more effectively, resulting in higher mixture fractions at locations downstream. Similarly, this biases the mixing layer towards the outer wall, and the fuel stream is not constrained near the lower inner wall due to recirculation zones. Due to the increased fuel mass fraction at locations downstream, the inner wall is coated by a layer of cooler gas than in the baseline and high mass flow cases. Interestingly, the layer of cooler gas along the inner wall extends further downstream the channel in the high mass flow rate case than in the baseline case. For the high equivalence ratio condition, the pressure profile in the radial direction is more homogeneous compared to the other two cases.

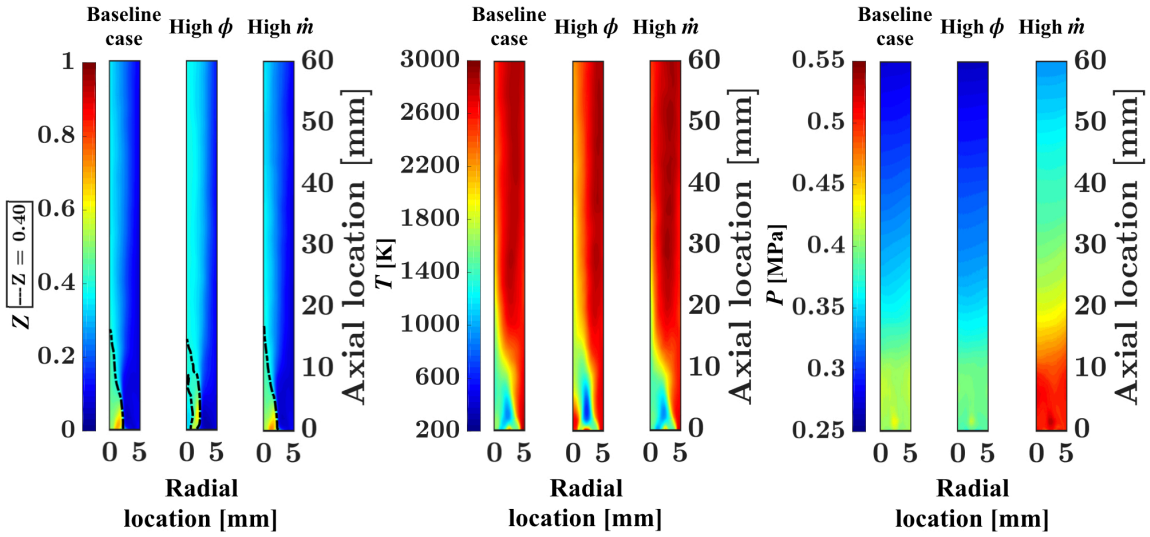

Figure 4.11: Mixture fraction, temperature, and pressure for the baseline, high ϕ, and high $\dot{m}$ cases throughout the detonation channel averaged over multiple cycles during steady-state operation. The black isoline (left) highlights the rich mixture fraction of $Z_{mix} = 0.4$ within the detonation channel.

4.2.2.3 Conditional statistics

Figure 4.12 displays the conditional averages of temperature, heat release rate, and fuel and oxidizer mass fraction in mixture fraction space, computed at different heights in the channel. The conditional averages provide insight into the reactivity of the mixture. The conditional temperature profile is parabolic with a peak near the stoichiometric mixture fraction of $Z_{mix} = 0.2004$, rather than the Burke-Schumann-type profile expected for this nominally-fast chemistry. Thus, the detonation reaction process in three-dimensional systems is significantly slower than the theoretical expectation. In all three cases, similar peak temperatures are reached at distances downstream of the jet impingement location at a 5 mm axial distance. Note that a lower temperature is observed at the 8.9 mm axial location, with the peak temperature occurring at a lean mixture fraction. With a higher mass flow rate (and lower global equivalence ratio), the peak at the lean condition is less pronounced. In the high equivalence ratio case, the temperature at locations downstream of 10 mm is

lower than the other cases, whereas the conditional temperature is higher at the base of the channel. This occurs due to a broad region of deflagrative heat release in the lower channel, supported by the heat release profile of Fig. 4.10. For an ideal detonation of stoichiometric CH_4-O_2 mixture, the post-detonation temperature is roughly 3700 K, which is nearly 700 K higher than the values reached here.

The conditional heat release rate (HRR) per unit volume curves (Fig. 4.12) show that a broad region in mixture fraction space contributes to the overall exothermicity of the system. While heat release appears to be higher near the stoichiometric value, similar to the conditional temperature plot, richer mixtures also contribute to this process. Heat release in lean mixtures is lower than the values observed in the other two cases. Further, high heat release at rich conditions is observed throughout the full detonation channel. The heat release profiles for the baseline and high mass flow rate cases are similar, but heat release extends to richer mixtures at the 8.9 mm axial location for the high mass flow case. Contrary to the conditional temperature plot, peak heat release occurs both at the base of the channel and roughly 9 mm. At the base, deflagration and the passage of the shock wave contribute to this value, while detonation is strongest in the 5-15 mm height range. With downstream distance, the heat release rate drops in magnitude. It should be noted the consumption of O_2 occurs over a considerable axial distance. As a result, even though the temperature increases with downstream distance, this increase is driven by a weaker and spatially-distributed deflagration process. However, the heat release due to detonation in the high mass flow rate case is greater than in the other two cases.

The fuel species profiles are similar for the three cases, but greater fuel mass fraction at distances downstream is observed in the high equivalence ratio case as expected. The oxidizer mass fraction profiles exhibit interesting behavior. In typical diffusion flames, the conditional average of fuel and oxidizer should diminish to zero at leaner/richer than stoichiometric conditions. Here, however, it is observed that while

the oxygen mass fraction approaches zero at Z_{st}, the value increases further at richer conditions. Near the base of the channel, the oxygen consumption is higher than at distances downstream, corresponding to the temperatures and high heat release rates observed at this location in richer conditions. The consumption of oxygen is also greater at this height than at the baseline and high mass flow rate conditions. At the 8.9 mm axial location, there is reduced consumption of oxygen compared to the other two cases. This interesting reversal is due to the large deflagrative heat release near the base of the channel. However, near the 10 mm height, reduced detonation strength results in the partial consumption of fuel and oxidizer that is purely convected towards the exit while undergoing a slow heat release process, as observed in the pockets of low-temperature gas in Fig. 4.3. At distances far downstream, 50 and 70 mm, oxygen is more completely consumed in the baseline and high mass flow rate cases. However, in the high equivalence ratio case, increased amounts of oxidizer exist in rich mixtures even at these downstream distances. Near the stoichiometric condition, the oxidizer is more completely consumed. Thus, partially-burnt mixtures with a rich composition of fuel are entrained in the post-detonation gas.

This delayed consumption of oxygen provides insight into the heat release structure. As seen in Fig. 4.6, the detonation-induced pressure rise decays axially, but the highest pressures are observed below 20 mm. While all of the primary heat release occurs in this region, there is still unburnt fuel and oxidizer that escape the detonation region. In other words, the detonation wave is unable to process all the fuel-oxidizer mixture available. This is mainly due to the weak detonation wave. As a result, partially oxidized fuel is carried downstream in a relatively high-temperature gas, where subsequent oxidation to CO_2 occurs. This delayed processing of the fuel is reflected in the conditional oxidizer relation. It is also seen that downstream, the conditional temperature on the rich side increases, which is due to the completion of the combustion process through deflagration or homogeneous reactions.

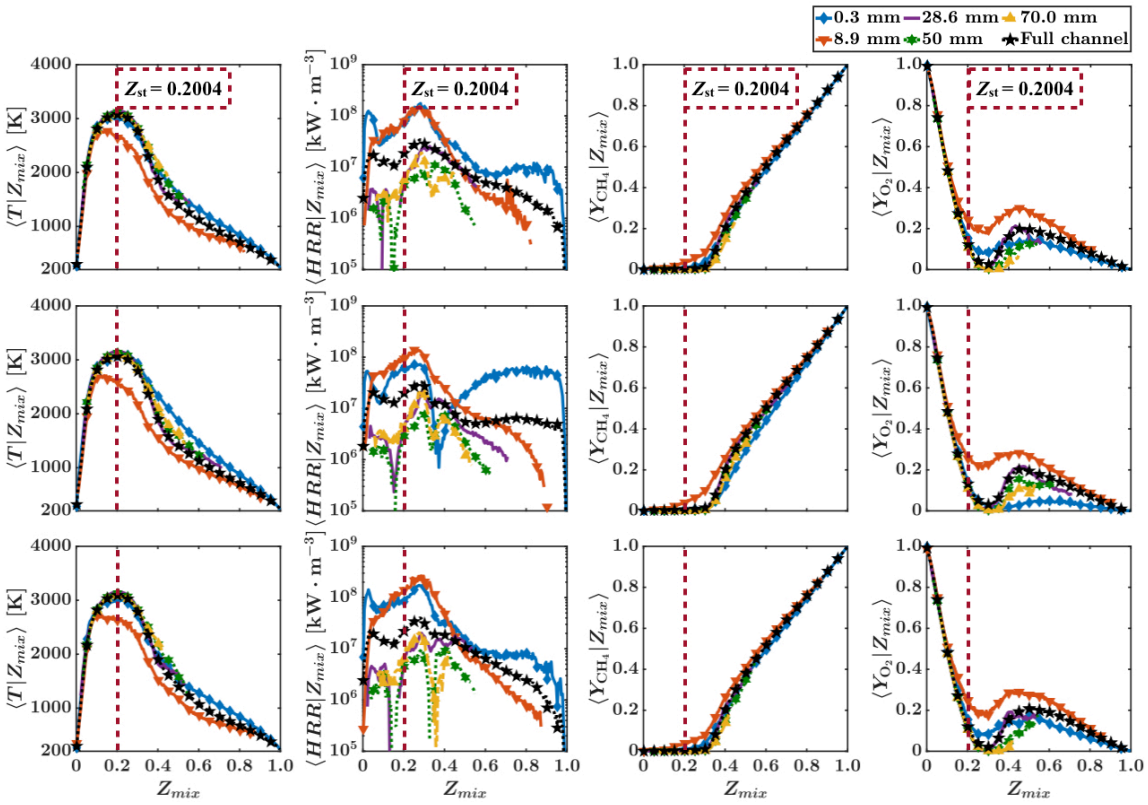

Figure 4.12: Conditional average in mixture fraction space at different heights from the injection plane within the detonation channel averaged over multiple cycles of the system for (top row) the baseline, (middle row) high ϕ, and (bottom row) high $\dot{m}$ cases.

The average heat release rate per unit volume conditioned on pressure is displayed in Fig. 4.13. Here, the high mass flow rate case features the highest pressure at the 8.9 mm axial location, followed by the baseline case, and the high equivalence ratio case. Hence, the strongest detonation is observed here. Within the full detonation channel, peak pressures due to triple points and three-dimensional effects are nearly double that of the baseline case. The profiles for the baseline and high equivalence ratio cases are interestingly similar, with heat release at similar pressures near the base of the channel, corresponding to deflagration. In the high mass flow rate case, the heat release near the chamber base is almost an order of magnitude higher than the high equivalence ratio case, occurring at pressures nearly 80% higher; the detonation wave

front in the high mass flow rate case spans a larger range of axial distances. At the base of the channel, the heat release begins to drop off at higher pressures. At very high pressures, the heat release due to detonation is nearly an order of magnitude greater than the baseline and high equivalence ratio, signifying high detonation efficiency in this configuration. In all three cases, high heat release is generally associated with high pressure throughout the domain. More importantly, at downstream distances, the heat release rate is substantially lower and also occurs at lower pressures, consistent with a spatially-distributed deflagration-driven combustion process.

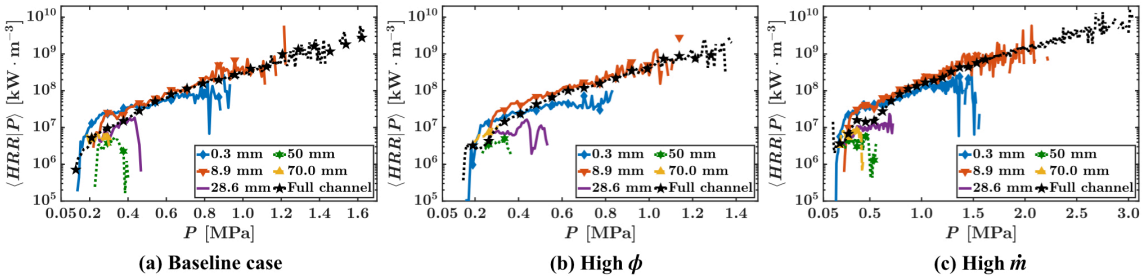

Figure 4.13: Conditional average of heat release rate per unit volume conditioned on pressure at different heights from the injection plane within the detonation channel averaged over multiple cycles of the system for the (a) baseline, (b) high ϕ, and (c) high $\dot{m}$ cases.

4.2.3 Study conclusions

High-fidelity numerical simulations of the methane/oxygen RDRE were performed at the different operating conditions that vary the global equivalence ratio and the system mass flow rate: 1) baseline configuration, 2) high equivalence ratio, and 3) high mass flow rate. These conditions provide insight into the operating envelope of the RDRE and highlight the merit of numerical studies in investigating the combustion processes and injector dynamics within such complex combustion systems. In particular, an initial revision of the AFRL RDRE geometry, denoted here as revision A, was studied. The baseline and the high system mass flow rate cases behave simi-

larly, with stronger detonation and higher peak pressures observed in the high mass flow rate condition. Here, detonation dominates the combustion process with heat release nearly an order of magnitude greater than the baseline and high equivalence ratio cases. Further, the peak and average pressures in the lower detonation channel are significantly higher. The increase in detonation pressure at the base of the channel due to the higher mass flow rate is greater than the increase in plenum pressures used to feed this configuration. However, the higher detonation pressures un-choke the injectors to a greater extent, with lower injector velocities during wave passage than in the other two cases.

The high equivalence ratio case results in chaotic behavior with two pairs of counter-rotating detonation waves. However, the increased relative mass flux of the fuel in this configuration allows for greater penetration of the fuel jet into the oxidizer flow, resulting in higher local mixture fraction throughout the width of the channel and at distances far downstream of the jet impingement point. The high mass flow rate case results in increased detonation wave strength whereas the high equivalence ratio case results in increased deflagrative heat release near the base of the channel and in locally-rich regions of the domain.

The high plenum pressures in all three cases ensure that no flow reversal is observed. In the baseline and high mass flow cases, no large-scale circulation in the reactant mixture. The fuel-oxidizer distribution is asymmetric with a rich mixture attached to the inner wall of the annulus. The detonation waves are stronger near the inner wall in this configuration, and heat release peaks in this region as well. For the high equivalence ratio case, the fuel stream exhibits a large level of unmixedness near the base of the channel and becomes more well-mixed further downstream of the channel. However, the mixture fraction throughout the width of the detonation channel is higher in this case, and the mixing layer between the fuel and oxidizer streams is shifted toward the outer wall. The wave speeds and peak pressures ob-

served are significantly lower than the CJ conditions, at approximately 57% and 62% of the CJ expectation, respectively, for the high mass flow rate case. Significantly lower pressures were recorded for the baseline and high equivalence ratio cases.

The high plenum pressures and injector geometry result in fairly stiff injectors that are minimally affected by the passing detonation wave. This is evidenced by a lack of detonation products and reverse flow through the injector during a detonation wave passage. There is no large-scale circulation observed in the reactant mixing region, and the fuel distribution is asymmetric with a rich mixture attached to the inner wall of the annulus. The interface between the rich fuel and the oxidizer stream is predominantly diffusion-like, while regions closer to the wall exhibit more premixed-like behavior. Parasitic combustion of the reactant mixture ahead of the detonation wave diminishes its strength, and the wave energies spatially fluctuate, with large variations in local wave speed and flow compression. The high mass flow rate condition assists in limiting the amount of parasitic combustion at the injector fill height, contributing to the higher detonation strength observed here. Thus, high-fidelity numerical studies provide valuable information on the detailed detonation physics and anomalous behavior within the system.

4.3 Revision B AFRL RDRE

4.3.1 Numerical configuration and approach

The revision B numerical representation of the AFRL RDRE differs from the revision A configuration in the upstream feed plenums and exhaust plenum volumes. As shown in Fig. 4.14, the fuel and oxidizer plenums are truncated with shorter plenum flow paths. The fuel radially enters the fuel plenum from the inner side wall, rather than axially at the base of the extended plenum in revision A. Additionally, the exhaust plenum has been enlarged, with a diameter approximately 3.5 times that

of the annulus outer wall and a length nearly 6.5 times the chamber height. The feed plenum modifications were performed to 1) more precisely control the mass flow rate through the injectors and 2) closely replicate the feed plenum dynamics of the experimental configuration. The high plenum pressures of the RDRE and micro-nozzle injectors limit the feedback of pressure waves into the feed plenums through viscous forces, and issues arising from wave-inflow boundary interactions within the time simulated numerically are not a concern based on the simulations with the revision A representation. The exhaust plenum with progressive mesh coarsening dissipates pressure waves and isolates the dynamics within the RDRE combustion chamber from the outflow boundary condition treatment. The revision B geometry incorporates the standardization set forth by the Model Validation for Propulsion effort outlined by AFRL.

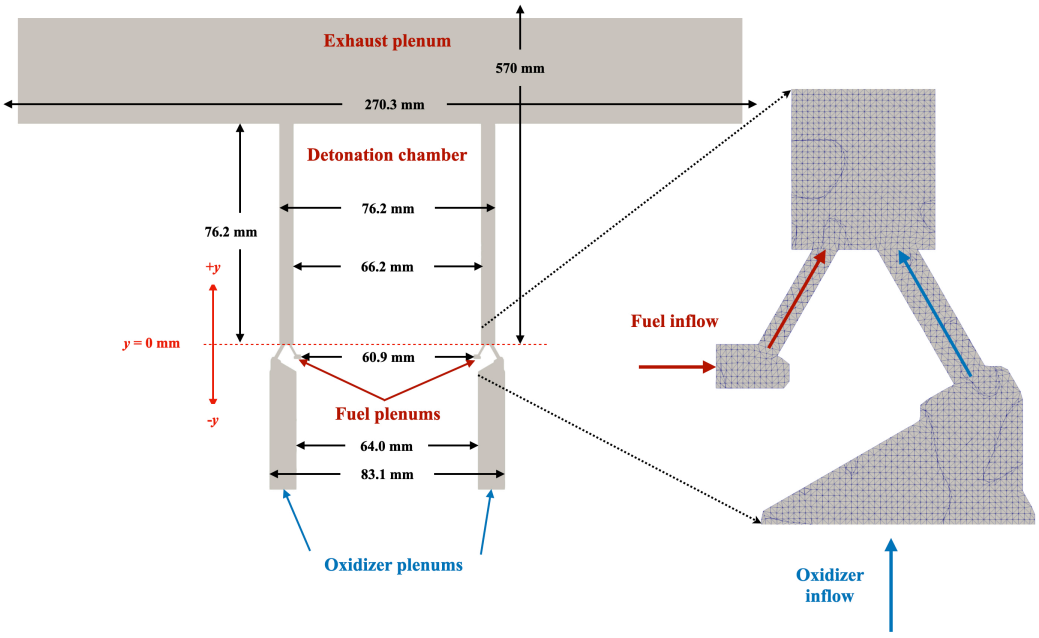

Figure 4.14: Cross-sectional schematic with primary dimensions of the AFRL methane/oxygen RDRE with the revision B modifications and a detailed view of the finer computational mesh within the RDRE.

Two different mesh resolutions with primarily hexahedral cells will be discussed here: 1) coarse mesh with 21.9 million control volumes and 2) fine mesh with 118.3

million control volumes. In the coarse mesh, a cell resolution of 200 μm was employed throughout the feed plenums, injectors, and combustion chamber. On the other hand, the cell resolution for the fine mesh was refined to 100 μm throughout the area of interest. In both meshes, the cell resolution is progressively coarsened beginning in the lower exhaust plenum to dissipate adverse pressure waves. Similar to the revision A studies, a mass flow-rate boundary condition is applied on the plenum inflow surfaces to enforce the operating condition, and adiabatic, no-slip wall boundary conditions are used. In the fine mesh, there are approximately 8 cells across the fuel injector and 13 cells across the oxidizer injector. A cross-sectional visualization of the RDRE combustion chamber and injection scheme is shown in Fig. 4.15. The fine mesh serves as the baseline mesh for the studies in this section, while the coarse mesh is used to evaluate mesh resolution effects. The solver speed-up enabled by the GPU-accelerated chemistry and flux routines (partition outlined in Fig. 2.10) allows simulation of these larger meshes with hydrocarbon-based detailed chemistry.

In order to standardize the RDRE initialization procedure, a homogeneous ignition kernel is used to perturb the system as follows. The combustion chamber and exhaust plenums are filled with air at ambient quiescent conditions. The fuel and oxidizer plenums are pressurized with initial estimates from experimental solutions or analytical calculations, and a mass flow rate boundary condition is prescribed at the inflow surfaces of the plenums to define the operating condition. The injector jet columns develop and the combustion chamber fills with a fuel/oxidizer mixture up to a nominal fill height of 0.5 ms. At this point, a homogeneous ignition kernel consisting of methane and oxygen (with mass fractions of $Y_{CH_4} = 0.2$ and $Y_{O_2} = 0.8$) at a high temperature (3000 K) and pressure (4 MPa) is placed within the combustion chamber. This kernel spans the full width of the combustion chamber, covers 2° in the azimuthal direction, and extends up to a height of 5 mm. The ignition kernel expands and induces a chaotic flow field within the combustion chamber. This

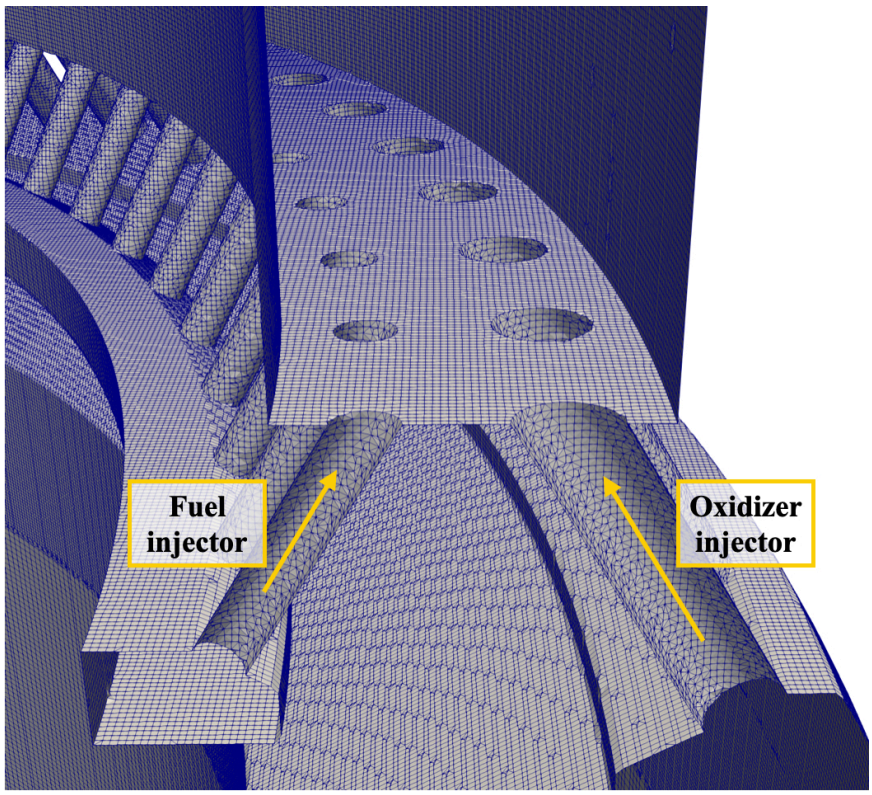

Figure 4.15: Visualization of the fine mesh in the injector and combustion chamber cross-section with a cell resolution of 100 μm.

method perturbs the chamber with a high energy impulse and does not provide a directional preference for the detonation waves that emerge. The chaotic combustion period evolves for approximately 1-1.5 ms before an operating mode with co- or counter-rotating waves becomes established. After this point, an additional 0.5 ms of the system is simulated under a quasi-steady state mode of operation, under which the operational statistics are extracted and analysis is performed.

4.3.2 Simulation results and discussion

Employing the fine mesh revision B representation, two operating conditions are studied: 1) the nominal and 2) the high mass flow rate conditions. These are similar to the set points studied in Sec. 4.3.2, but the experimental geometry and numerical representation are more closely matched. A summary of the experimental properties

Table 4.3: RDRE operational parameters for the nominal and high $\dot{m}$ operating conditions.

	Nominal		**High $\dot{m}$**	
	Exp.	**Sim.**	**Exp.**	**Sim.**
$\dot{m}_{fuel}$ [g/s]	6.0	5.96	7.9	7.9
$\dot{m}_{oxidizer}$ [kg/s]	0.207	0.215	0.273	0.268
$\dot{m}_{total}$ [kg/s]	0.267	0.275	0.352	0.347
ϕ	1.16	1.11	1.16	1.18
$P_{f,plen}$ [MPa]	1.31	1.22	1.49	1.60
$P_{o,plen}$ [MPa]	1.20	1.23	1.44	1.49
$P_{CTAP,1}$ [MPa]	0.380±0.014	0.475	0.497±0.014	0.590
$P_{CTAP,2}$ [MPa]	0.296±0.014	0.373	0.431±0.014	0.472
Wave speed [m/s]	1809.8±11.4	1357	1668.3±12.9	1189
No. Waves	2	2 (co-rotating)	3	4 (2 counter-rotating pairs)
Thrust [N]	357.6±2.2	469.3	585.4±2.7	620.5
I_{sp} [s]	139±1	177	164±1	185

along with the numerical results is shown in Tab. 4.3.

The evolution of the operating condition for both cases can be visualized in a so-called "detonation surface plot." Here, the azimuthal pressure trace at a given height in the combustion chamber is plotted as a function of time from the point of ignition to steady-state operation. In this study, the 8.9 mm combustion chamber height is used to coincide with experimental pressure equipment at this axial position. The surface plot visualization method allows for clear identification of the operating mode, the number and direction of the waves, and the wave speeds. The detonation surface plots for the nominal and high mass flow rate cases are shown in Fig. 4.16. The nominal case establishes two co-rotating waves with a mean wave speed during

steady-state operation of 1357 m/s. On the other hand, the high mass flow rate case appears to result in wave splitting: at the higher mass flow rate, rather than faster waves of increased strength or an increased number of co-rotating waves, two counter-rotating wave pairs are established with a mean wave speed of 1189 m/s. The wave speeds follow expectations and the trends observed in the experiment: as the number of waves in the system is increased, the wave speed is reduced to support this operation. While counter-propagating waves shed of the primary system are often seen in RDEs, the counter-propagating wave mode in the high mass flow rate is of equal strength in either azimuthal direction. The wave strength is reinforced through the collisions but the operation does not have a preferential direction.

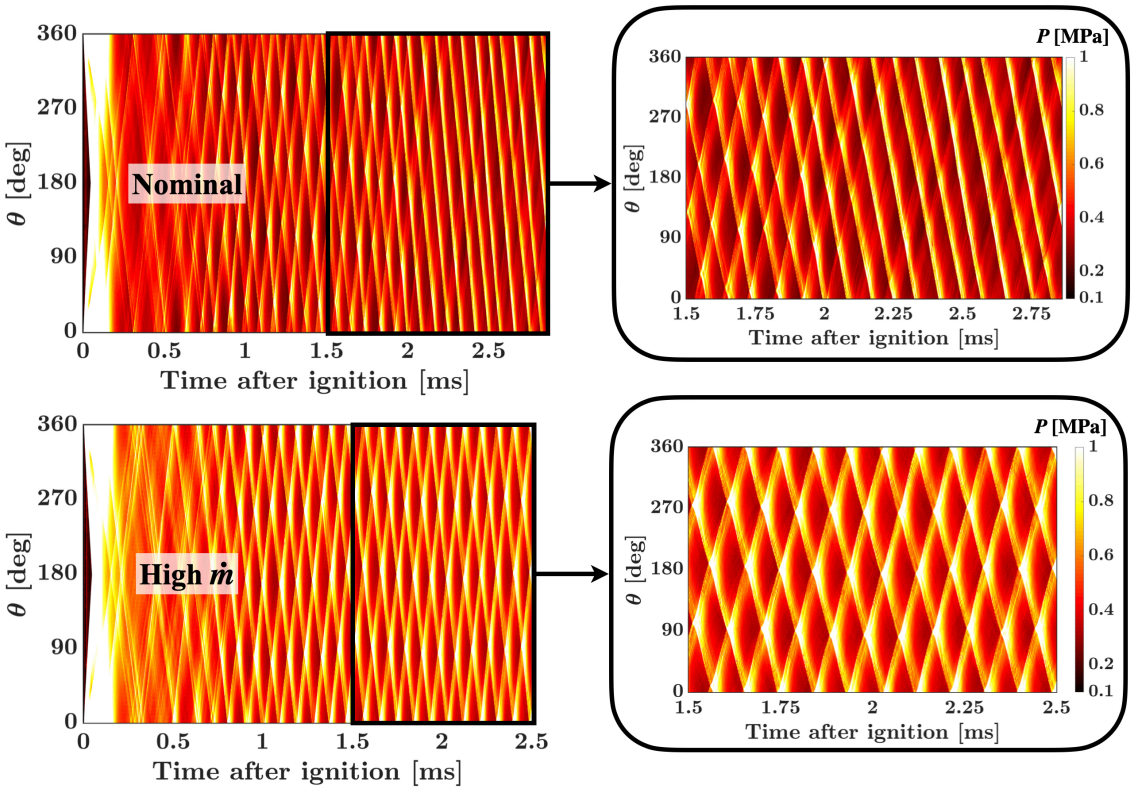

Figure 4.16: The detonation surface plots for the nominal and high mass flow rate cases show the evolution of the operating mode from ignition to steady-state operation, with inset images highlighting the wave structure during the steady-state period exclusively. The surface plots are constructed using the azimuthal pressure trace at the 8.9 mm chamber height.

The unwrapped profile of Mach number in the laboratory reference frame is displayed in Fig. 4.17. The product gases from the detonation waves are expanded and accelerated towards the exit of the combustor. In both cases, the exit remains choked throughout the wave cycle, although the exit flow is more uniformly sonic in the nominal mass flow rate case, with an increased number of supersonic flow regions. This choked outlet boundary contributes to the operating mode of the RDE through acoustic wave reflections which feedback to the injection plane.

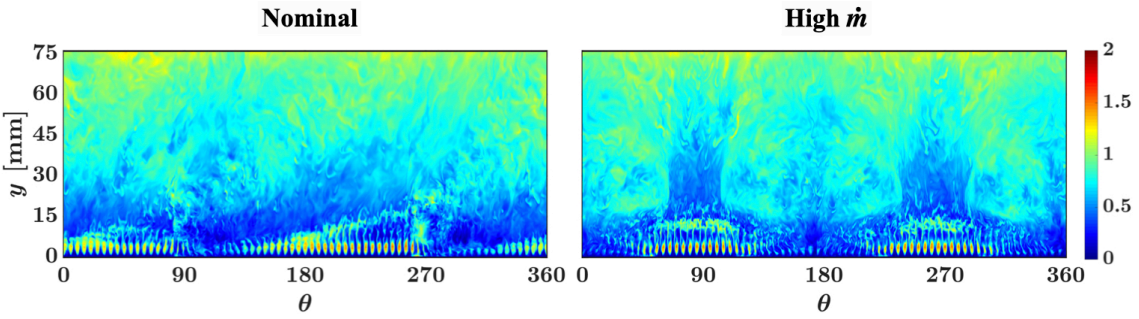

Figure 4.17: Instantaneous profile of Mach number in the laboratory reference frame for the (left) nominal and (right) high mass flow rate cases. The profiles along the RDRE combustion chamber mid-channel plane are unwrapped and projected onto two dimensions.

The axial pressure profile along the outer wall is shown in Fig. 4.18. The experimental trends are captured in the axial pressure decay, although the absolute pressure values are over-predicted in both cases by approximately 25% for the nominal case and 10% for the high mass flow rate case. The discrepancies in the averaged pressure profiles may be subject to pressure peak attenuation in the experimental data, as explained in Sec. 4.2.2, and numerical effects. In the detonation plot, it is clear that while a homogeneous ignition kernel is used, the operating mode of the RDRE is established from the propagation of minor instabilities in the flow field, reinforced by the numerical effects. Thus, a symmetric perturbation results in an asymmetric operating mode. The selection of the numerical scheme affects the unsteady dynamics within these systems.

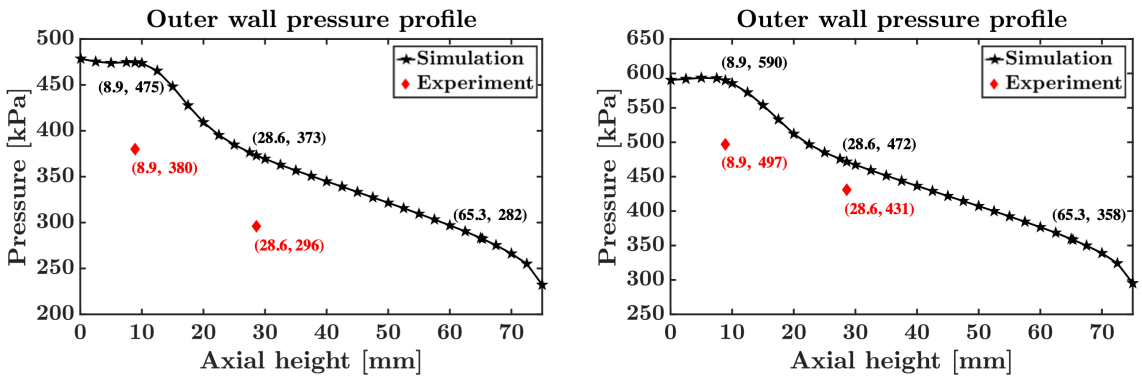

Figure 4.18: The axial pressure profile comparison between the numerical simulation (during steady-state operation) and the experiment extracted along the outer wall position for (left) the nominal case and (right) the high mass flow rate case.

Table 4.3, the feed plenums stabilize at slightly different values from the experimental expectation. For instance, in the nominal case, the fuel plenum decreases in pressure while the oxidizer plenum increases in pressure, resulting in steady-state plenum pressures that are of similar value. In the high mass flow rate case, both the fuel and oxidizer plenum pressures increase to support the target mass flow rates. The time history of pressure fluctuations during steady-state operation is provided in Fig. 4.19. The pressure variations in the fuel plenum are of higher frequency and the pressure impulses echo the pressure jumps due to the passing detonation wave. The oxidizer plenum features lower-frequency variations with a period encompassing a few wave cycles. The pressure variations in the nominal case are greater, with amplitudes of approximately 4.5% and 7.7% of the baseline values of the fuel and oxidizer pressures, respectively. On the other hand, the amplitudes of the pressure variations in the high mass flow rate case are 2.8% and 4.1% of the baseline steady-state values for the fuel and oxidizer plenums, respectively. Thus, the higher feed pressures and the weaker individual waves in the high mass flow rate case lead to dampened pressure effects in the plenums.

The chamber-averaged profiles of temperature, normalized heat release rate, mix-

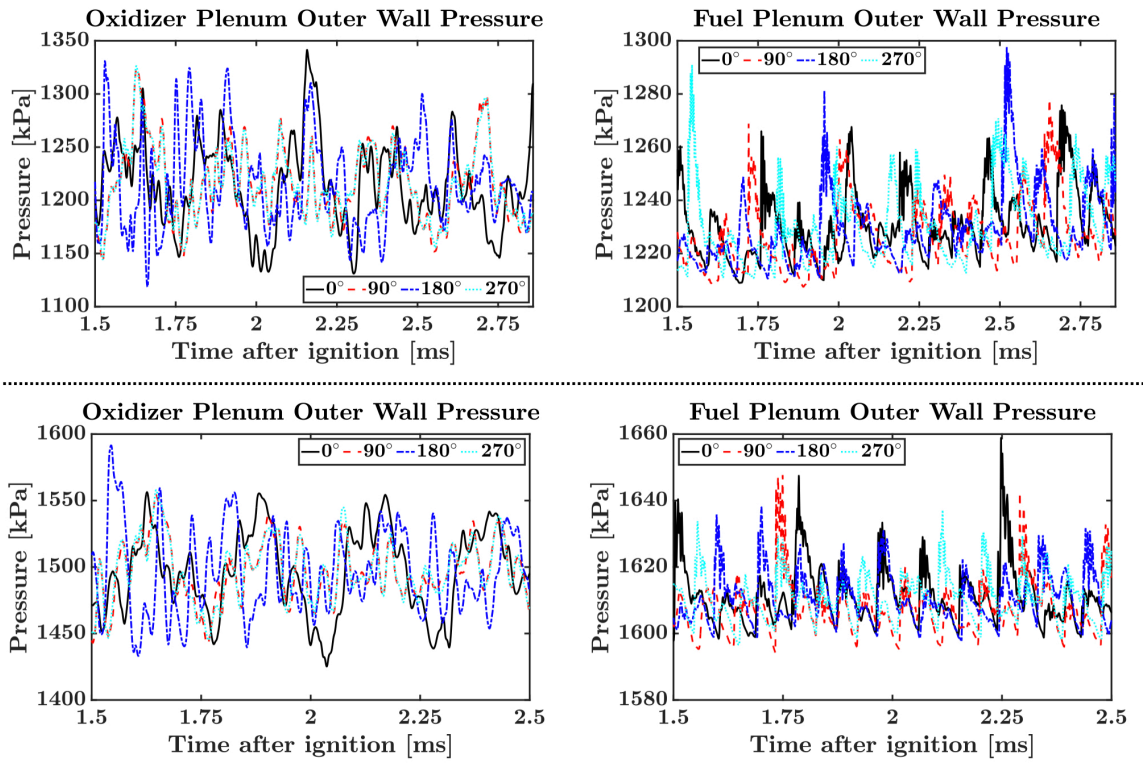

Figure 4.19: Plenum pressure fluctuations at the outer wall of the fuel and oxidizer plenums during steady-state operation, extracted from numerical simulations, for the (top row) nominal case and (bottom row) high mass flow rate case. The numerical probe is placed at a central position in the axial direction.

ture fraction [29], and the unmixedness factor (defined in Sec. 4.2.2) are shown in Fig. 4.20. With similar operating equivalence ratios, the temperature and mixture fraction profiles are nearly identical, but the increased high-temperature gas exists beyond 7.5 mm in the high mass flow rate case. This suggests increased deflagration which is continuous throughout the wave cycle, whereas detonation heat release is momentary. This deflagration occurs at the fill height of the injectors and introduces higher-temperature combustion products ahead of the wave, an outcome of the weaker counter-propagating wave system. This is further reinforced by the normalized heat release profile, where a large fraction of the heat release is confined beyond 10 mm in the nominal case but is more distributed within the first 17.5 mm with

the high mass flow rate case. This upstream shift of the heat release rate fraction is due to increased deflagration and a weaker detonative heat release in relation to the energy release sustained by deflagration. The unmixedness factor χ shows increased jet unsteadiness which is of higher magnitude and extends further into the detonation chamber than in the nominal flow rate case. This unsteadiness is attributed to the counter-propagating wave system which limits jet development and the fill height of the injectors. Further, the intensity of the opposing wave collisions may more effectively suppress the injectors and lead to increased jet flapping behavior.

In addition, the chamber-averaged profiles of volumetric heat release rate and mixture fraction [29] phase-averaged within 2° sectors 5° ahead and 5° behind the wave front reveal interesting differences in the bifurcation of combustion between deflagration and detonation. For both cases, there is a well-distributed heat release structure ahead of the detonation wave, peaking along the mid-channel radial position at a value of 10 MW/m^3. On the other hand, 5° behind the wave front, the peak heat release increases by nearly an order of magnitude and shifts towards the inner wall, and is primarily confined between the 10-15 mm height. The heat release ahead of the wave corresponds to deflagrative combustion in the form of mixture preburning whereas the heat release immediately behind the wave is attributed to high-pressure detonative combustion. Deflagration spans the majority of the combustion chamber while detonation resides near the inner wall due to the increased fuel concentration. Further, it exhibits a stand-off height of about 10 mm from the base of the combustion chamber. In the nominal case, detonations are stronger, featuring an energy release maximum of nearly 100 MW/m^3 at the 15 mm axial height while the peak is at approximately 70 MW/m^3 between the 12.5 mm to 15 mm axial for the high mass flow rate case. In contrast, deflagrative heat release is more pronounced in the high mass flow rate case with a more distributed arrangement from a height of 10 mm to nearly 25 mm. The counter-propagating wave pairs in the high mass flow rate

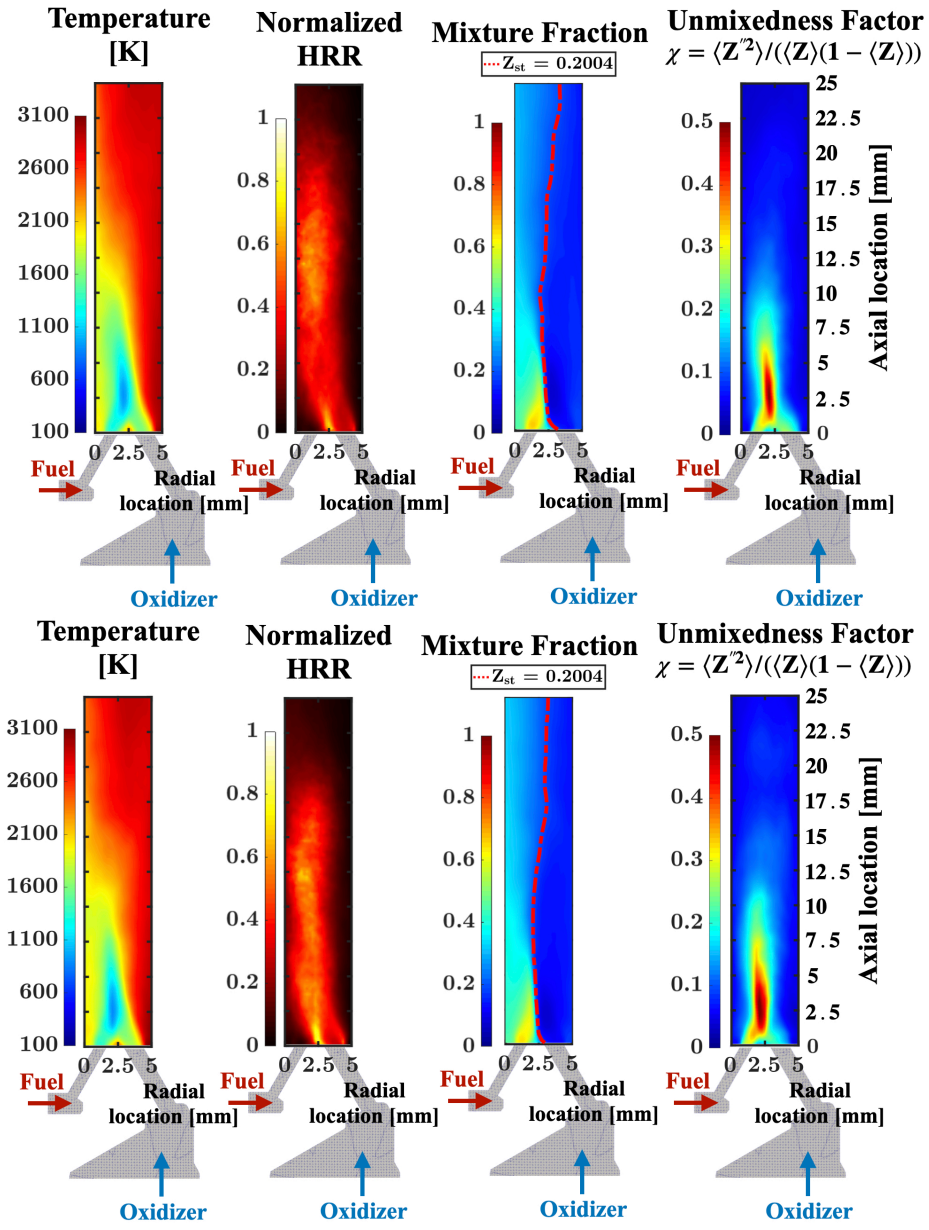

Figure 4.20: Temporally-averaged profiles of temperature, normalized heat release rate, mixture fraction, and unmixedness factor during steady-state operation for (top row) the nominal case and (bottom row) the high mass flow rate case. The dashed red isoline of mixture fraction (middle right) highlights the stoichiometric region within the detonation channel.

case lead to increased secondary combustion and contribute to weaker and slower detonation waves. This is evident in the mixture fraction profiles, where there remains an increased amount of residual fuel at locations downstream ($>$ 12.5 mm height) in the high mass flow rate case in comparison to the nominal case. The counter-

propagating wave mode supports a slow and distributed heat release process but ensures complete combustion of the available reactant mixture by the exit of the RDE. Ahead of the detonation wave, the mixture fraction distributions are similar in structure for both cases, although the nominal case exhibits a taller reactant fill height with increased fuel penetration into the chamber as expected. The increased mixture fraction values beyond the 15 mm height in the high mass flow rate case are also observed here.

The temporally-averaged exit plane (76 mm combustion chamber height) profiles of O_2 and CO_2 mass fraction and mixture fraction [29] for the nominal and high mass flow rate cases are illustrated in Fig. 4.22. In both cases, there is residual fuel entrainment near the inner wall coinciding with the fuel injector. Similarly, there are pockets of oxidizer near the outer wall, but the concentrations are minimal. The residual propellants increase noticeably with the high mass flow rate case, identifying increased incomplete combustion and mixing. Further, there is reduced oxidation of fuel to CO_2 in the high mass flow rate case as well. Notably, 97.8% of the fuel is converted to product or intermediate gases in the nominal case, whereas this parameter drops to 94.6% in the high mass flow rate case. Intermediate and product gas fractions may fluctuate due to reverse reactions as the gases are convected towards the exit. Additional methods for quantifying the percentage of the injected fuel mass that is partially oxidized, as opposed to fully oxidized, would be beneficial for future analysis.

The next set of sections details various studies performed using the AFRL RDRE as a platform to investigate analysis techniques, mesh effects, and ignition methodologies.

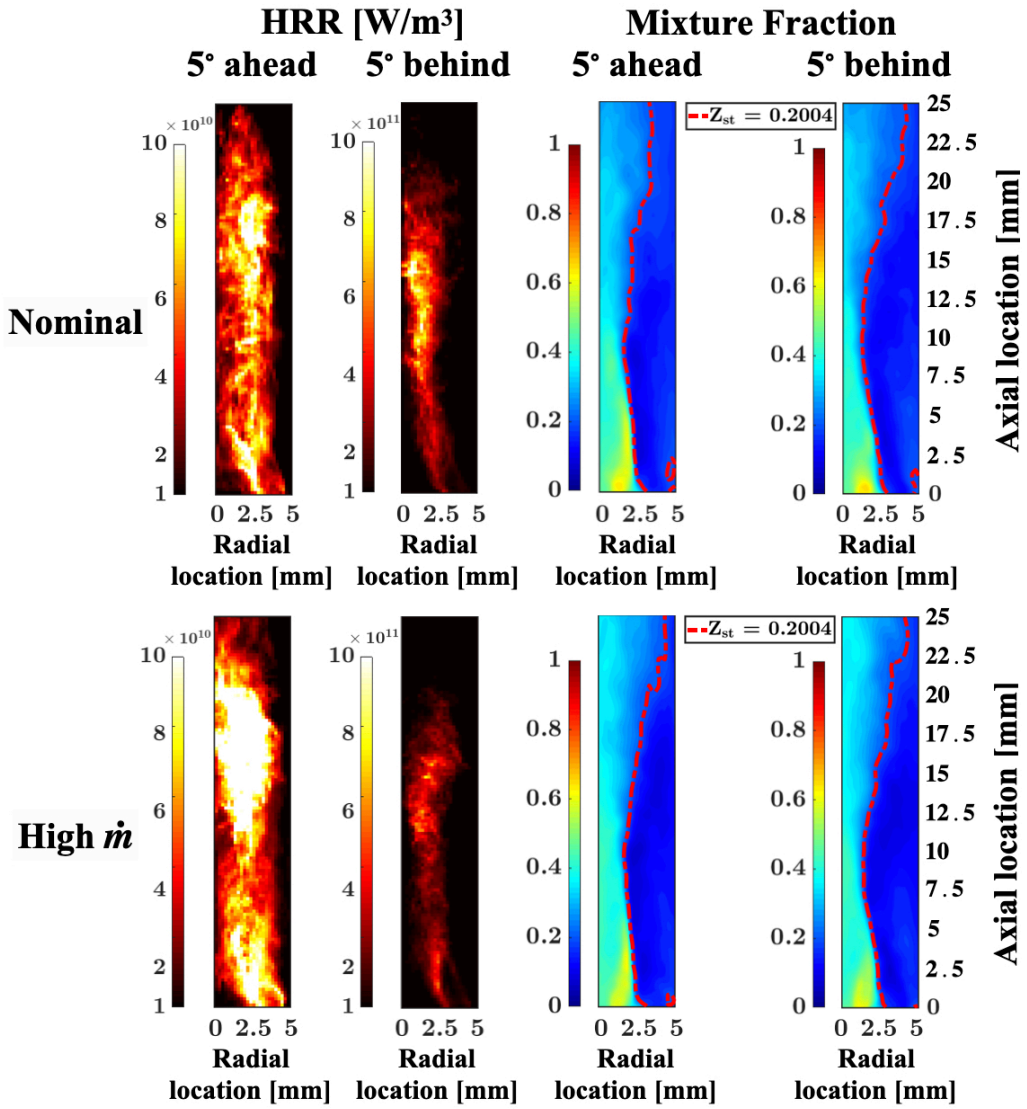

Figure 4.21: Profiles of volumetric heat release rate (far and middle left) and mixture fraction (far and middle right) for (top row) the nominal case and (bottom row) the high mass flow rate case, phase-averaged at different locations relative to the wave front–5° ahead and 5° behind–and temporally-averaged during steady-state operation. The dashed red isoline of mixture fraction highlights the stoichiometric region within the detonation channel.

4.3.2.1 Heat release partitioning

In order to partition the heat release (HR) within the RDE into either the detonation or deflagration modes, two methods can be employed. The first is a simple analytical approach based on the observed wave speed of the operating mode. The

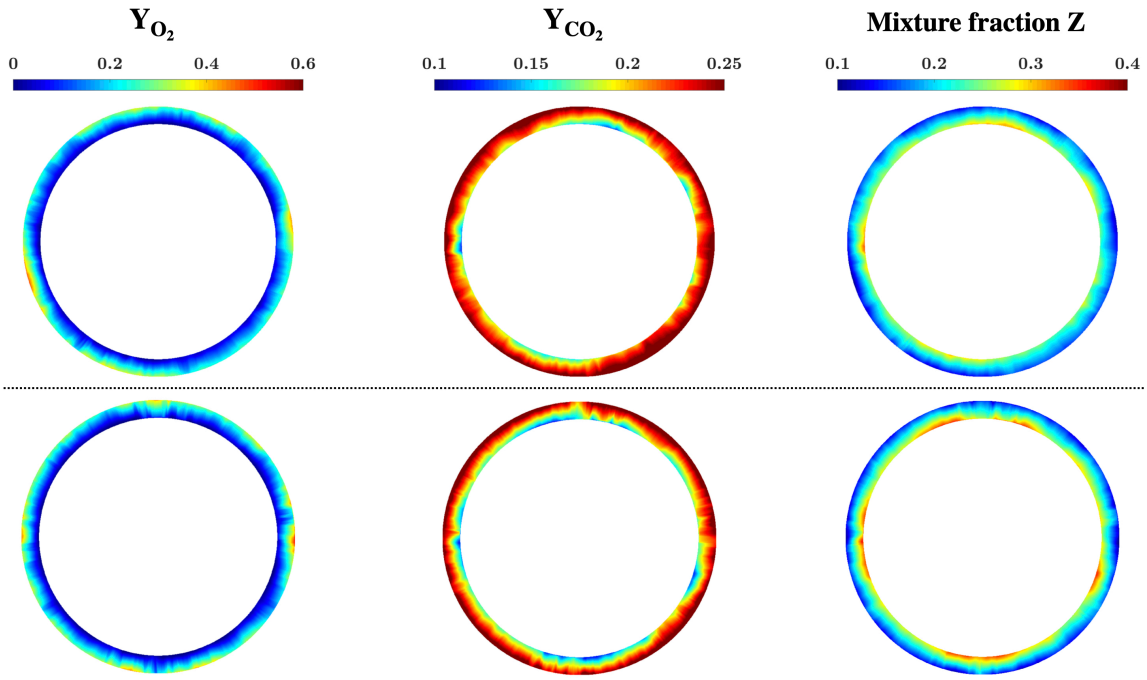

Figure 4.22: Temporally-averaged profiles of O_2 and CO_2 mass fraction and mixture fraction at the exit plane of the RDE combustion chamber for the (top row) nominal and (bottom row) high mass flow rate cases.

following relation provides the analytical expression for detonation wave speed:

$$u_{wave} = \sqrt{2(\gamma^2 - 1)(q_{theo} + c_P T)} \tag{4.5}$$

where q_{theo} is the theoretical heat release associated with detonation. For ideal methane/oxygen mixtures For an observed average wave speed, $u_{wave,sim}$, a reduced heat associated with detonation can be computed. For the nominal and high mass flow rate cases, this results in a detonative heat release fraction of 22.7% and 14.6%, respectively.

The second method relies on the heat release partitioning model described by Burr and Paulson [39]. Using a modified thermodynamic cycle shown on the left of Fig. 4.23, the heat release can be partitioned into three components: heat release due to 1) parasitic deflagration q_1, 2) detonation q_2, and 3) post-detonation deflagration

q_3. The entrainment of post-detonation gases in the reactant fill region and the subsequent parasitic deflagration has two critical consequences on the properties of the detonation wave. First, deflagration consumes a portion of the propellants in the reactant mixture, which cannot be combusted by the detonation wave. Second, the entrainment of post-combustion gases and deflagration raise the temperature of the reactant mixture ahead of the detonation wave, raising the effective sound speed ahead of the wave. This leads to a decrease in the wave Mach number and the effective compression across it, as seen in Sec. 3.3. Thus, the heat release component q_1 is heat release ahead of the wave that diminishes wave strength (*parasitic* combustion) and q_2 is heat release sufficiently behind the wave (beyond the sonic plane) that doesn't support wave propagation (*commensal* combustion) [39, 48, 53]. While this heat release past the sonic plane does not support the detonation wave, it does contribute to achieving complete combustion [39, 139]. These components of heat release can be extracted from numerical simulations using a detonation surface plot of the volumetric heat release rate depicted on the right of Fig. 4.23.

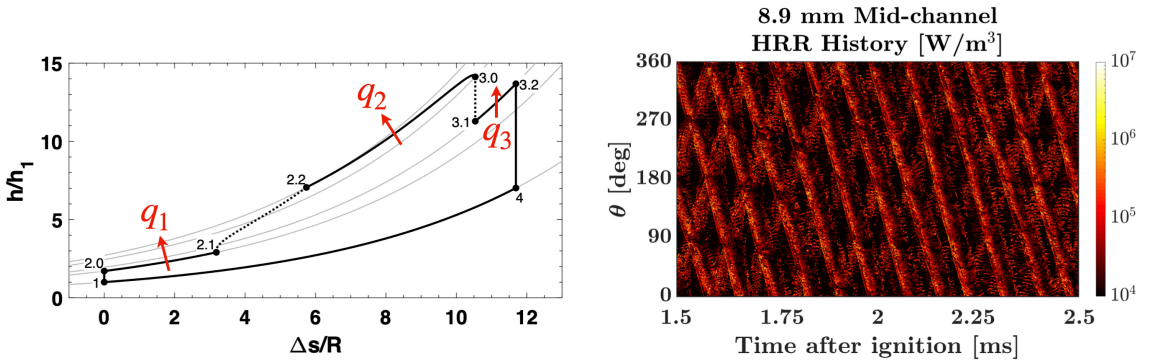

Figure 4.23: (Left) Thermodynamic cycle of heat distribution model adapted from Ref. [39] and (right) a detonation surface plot constructed from the volumetric heat release rate at a height of 8.9 mm within the combustion chamber for the nominal flow rate case.

In the volumetric heat release rate detonation surface plot at a nominal height of 8.9 mm in the combustion chamber, the heat release can be separated into the

q_1, q_2, and q_3 components. At a given time, the wave front location of each wave is marked using the pressure-based detonation surface plot shown in Fig. 4.16. For this application, the region contributing to q_1 is defined from 5° ahead of the wave up to the wave front. q_2 is the region from the wave front to the mean sonic plane distance behind the wave. Finally, q_3 is the region from the mean sonic plane of a given wave up to the 5° ahead of the next consecutive wave (or the same wave in a single-wave system). q_1 and q_3 contribute to the deflagrative heat release and q_2 represents the detonative heat release. A line integral of the volumetric heat release rate detonation surface plot about a given wave produces the partition of q_1, q_2, and q_3, and this process is averaged in time and across all waves in the system. The mean one-dimensional thermodynamic profiles in the wave reference frame for the nominal case are shown in Fig. 4.24. Here, the wave front is identified by the rapid increase in the pressure profile of the upper right plot. Using the mean wave speed, the flow velocity and the Mach number in the wave reference frame are outlined in the lower center of Fig. 4.24. The sonic plane is situated where the Mach number in the wave reference frame recovers to the sonic condition: a distance of 0.705 cm or 11.3° behind the wave for the nominal case. Using this physical partition, the heat release is divided into 2.5% parasitic deflagration HR (q_1), 81.0% post-detonation deflagration HR (q_3), and 16.5% detonation HR (q_2). This heat release fraction is informative of the heat release support from detonation. A similar method can be extended to the high mass flow rate case and other cases with counter-propagating waves but special care is required to ensure a robust spatial wave partitioning algorithm during counter-propagating wave interactions. The development of this approach is ongoing research and would be beneficial for universal analysis.

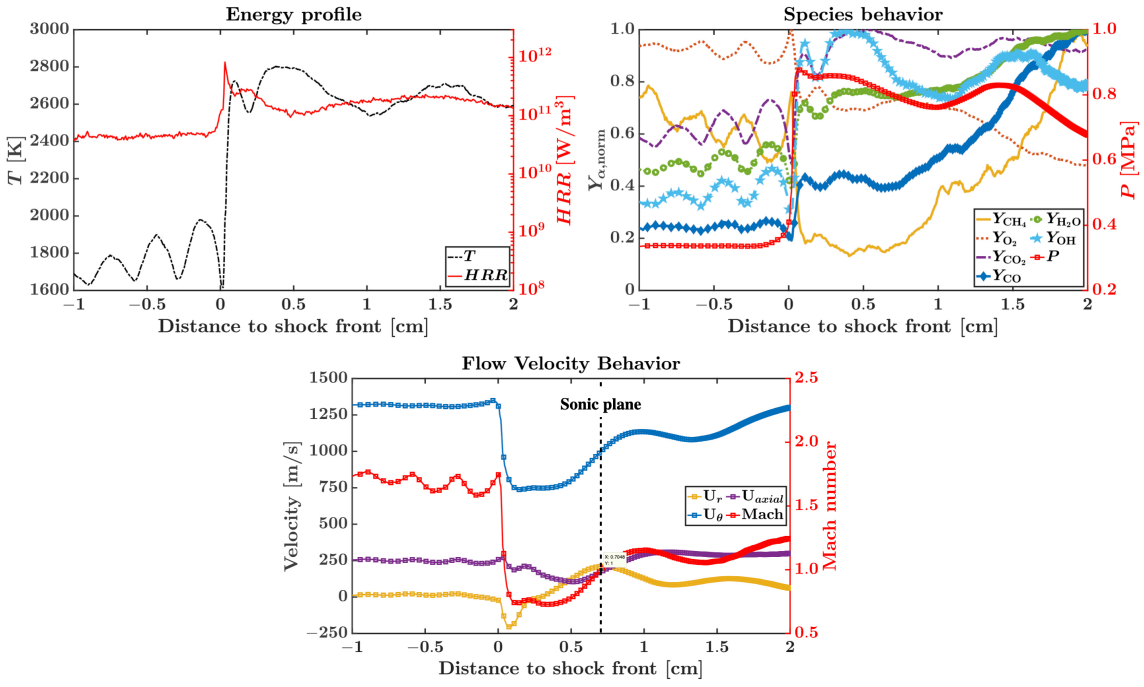

Figure 4.24: One-dimensional profiles of (top left) temperature and volumetric heat release rate, (top right) species and pressure, and (bottom center) flow velocity and Mach number in the wave reference frame for the nominal flow rate case, temporally averaged across all waves during the steady-state period.

4.3.2.2 Mesh resolution effects

The effect of the mesh resolution on the operating mode of the RDRE is quantified through the use of the coarse and fine meshes with resolutions of 200 μm and 100 μm, respectively, to simulate the nominal flow rate case (results of the high mass flow rate case not shown here). The unwrapped profiles of pressure and temperature along the mid-channel plane are shown in Fig. 4.25 for the coarse and fine meshes during an instance of steady-state operation. As shown earlier (see Tab. 4.3), the fine mesh results in 2 co-rotating waves whereas the coarser mesh produced two pairs of counter-propagating waves. The peak pressure region of the wave front shifts toward the injection plane with the coarse mesh, signifying a lower fill height and different injection dynamics. In the fine mesh simulation, the detonation wave stands tall, with

a primary detonation height in the 10-20 mm height region. The counter-propagating wave system results in a parabolic injector profile (as seen in the temperature plot) with a fill height of approximately 10 mm. With the fine mesh, a triangular injector profile is observed which extends more than 15 mm into the combustion chamber with narrower injector columns. Furthermore, the counter-propagating operating mode in the coarse mesh results in an oblique shock wave that leads ahead of the forward-leaning detonation wave, whereas the fine mesh results in a more planar detonation wave and oblique shock wave. As expected, the finer mesh reveals more turbulent structures and flow complexity.

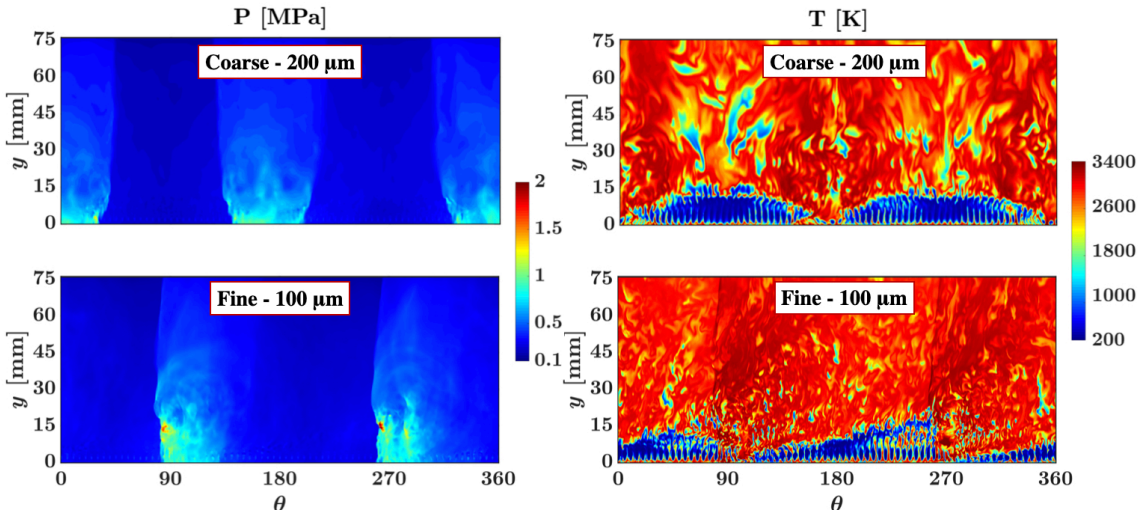

Figure 4.25: Instantaneous profiles of pressure (left column) and temperature (right column) along the RDRE combustion chamber mid-channel plane unwrapped and projected onto two dimensions for the (top row) coarse and (bottom row) fine meshes. The nominal flow rate case is displayed here.

Figure 4.26 shows the time-averaged exit plane (76 mm combustion chamber height) profile of mixture fraction and the out-of-plane velocity in the fuel injector cross-section. The fuel consumption efficiency difference is notable with a greater than 10% reduction in residual fuel by the exit plane of the RDE. While 97.8% of the fuel is converted to product or intermediate gases in the fine mesh case, only 85.2% is consumed in the coarse mesh case due to the galloping wave mode. Fur-

ther, the residual fuel is largely entrained near the inner wall but can extend up to the mid-channel location in the coarser mesh simulation. Apart from the influence of resolution on detonation propagation and mixing, the injector response is also affected. A cross-section of the fuel injector out-of-plane velocity shows that the higher resolution results in a significantly more realistic mean flow profile as expected. In a rocket-type RDE with micronozzle injectors, the resolution is crucial as it affects the effective injector discharge coefficient. With narrow micronozzles and increased plenum pressures, highly compressible flow with suppressed mixing is encouraged. An increased discharge coefficient has the effect of diminished nozzle efficiency, which can affect the recovery process of the injectors and their ability to maintain the target flow rate. The differences in the operating condition between the two mesh representations can be attributed to these numerical effects.

Due to the GPU-accelerated scalability of the UMReactingFlow solver with large meshes and chemical mechanisms, additional studies were performed where a 25° sector of the RDRE geometry, spanning five pairs of injectors, was progressively resolved down to a 20 μm resolution from the 200 μm coarse mesh. This represents a near-DNS level resolution and provides an opportunity to study the detonation-turbulence interaction in a stratified mixture. The detonation wave solution in the DNS-level mesh is compared to a coarse mesh solution of 200 microns. Figure 4.27 shows a sector of the RDRE combustion chamber mesh, along with pressure and dilatation profiles, as the detonation wave passes through the near-DNS level region. Here, the triple point dynamics, the reflected shock structures, and the compressibility of the flow are observable. The benefits of a highly-refined mesh surrounding the detonation wave are immeasurable. Adaptive mesh refinement architectures to represent complex geometries are an active area of research and are currently being investigated.

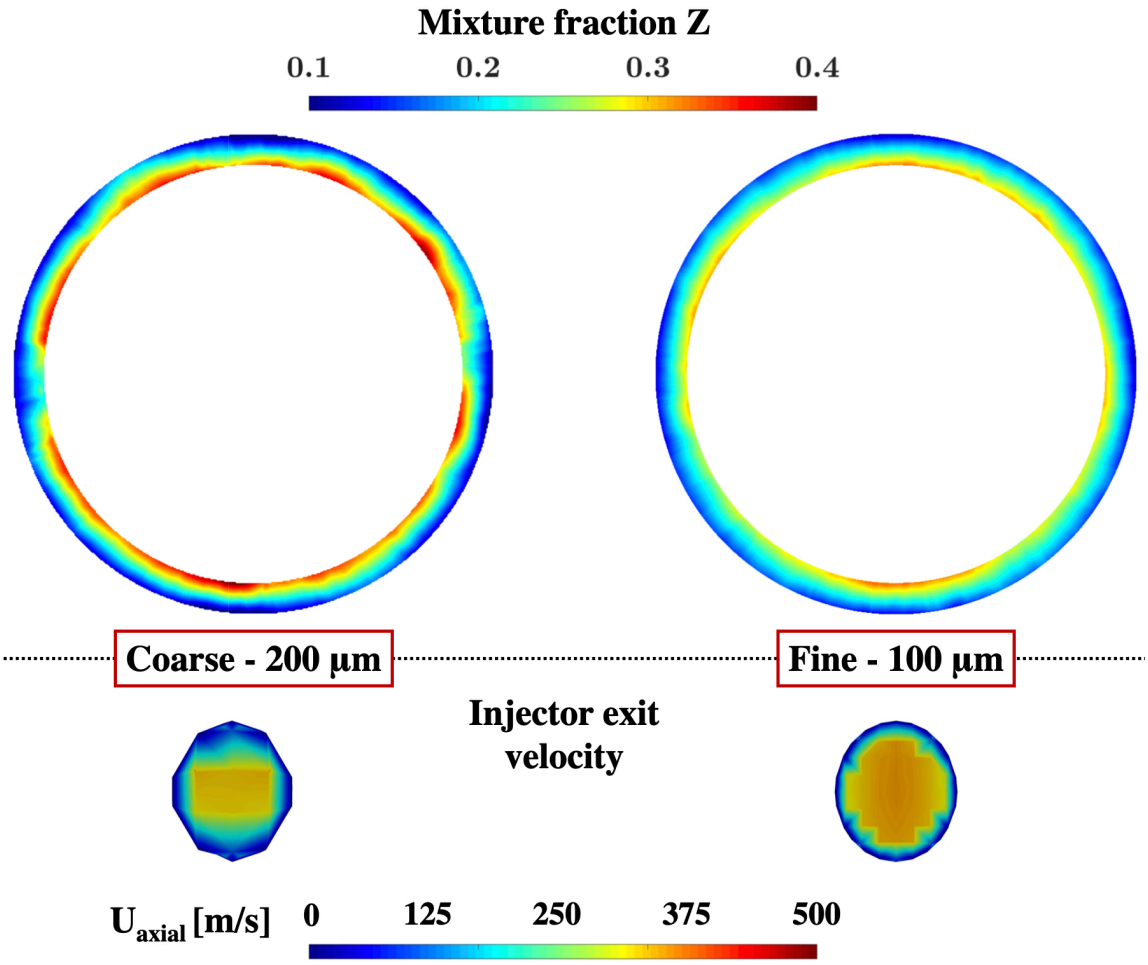

Figure 4.26: Temporally-averaged profiles of (top) mixture fraction and axial (bottom) injector velocity for the (left) coarse and (right) fine meshes. The nominal flow rate case is displayed here.

4.3.2.3 Wave multiplicity and ignition method effects

One of the most intriguing aspects of RDE operation is wave multiplicity and direction [e.g., 44, 247, 281]. For a given design and operating condition, there is no comprehensive understanding of the number of waves formed. Moreover, the direction of these waves is not predictable *a priori*. When the detonation process is initiated using some ignition source, several waves are formed, which then coalesce over several cycles to form the steady-state flow structure. For a given configuration, the number of waves is generally reproducible [242], although some studies have shown

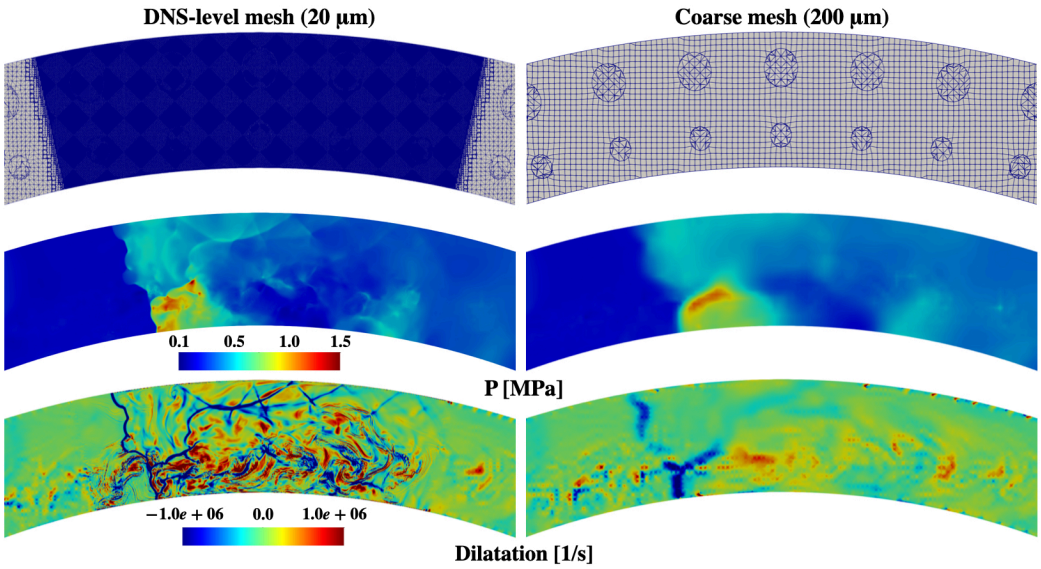

Figure 4.27: Comparison of the detonation wave structure within the RDRE channel with the (left column) near-DNS level mesh and (right column) coarse mesh in terms of (top row) mesh structure, (middle row) pressure profile, and (bottom row) dilatation rate.

that hysteresis effects may be present, especially when transitioning between two different operating conditions [28, 48]. While several studies show that the initiation mechanism does not change the number of waves [e.g., 28], there are also studies that indicate dependence on initiation [332]. Interestingly, Ref. [280] has shown that RDE reaches a steady state that is independent of the initiation procedure, measured as energy introduced into the system for ignition.

As part of the Model Validation for Propulsion workshop, an effort was made to standardize the ignition method so as to not encourage a preferential direction or number for the detonation waves that emerge. As seen earlier in Sec. 4.3.2, a high-energy homogeneous ignition kernel results in a chaotic flow path that evolves to form a detonation wave system due to instabilities cultivated by turbulence. However, in the high mass flow rate case, the simulations produced two pairs of counter-propagating waves whereas the experiments sustained three co-rotating waves (with secondary waves). Along with the implications of the numerical representation of the RDE,

the short-time simulations ($\mathcal{O}$(10 ms)) of these systems may not capture all mode transitions observed in experiments ($\mathcal{O}$(100 ms)). To study if a given mass flow rate and equivalence ratio can support multiple operating modes, the high mass flow rate case was ignited with three ramp profiles (each ramp profile constructed as explained in Sec. 4.2) spaced uniformly in the azimuthal direction of the combustion chamber. The result of the a) homogeneous ignition kernel and b) three ramp profiles are elucidated in Fig. 4.28. In both of these trials, the injector jets were developed through cold flow for 0.5 ms. Ignition within a quiescent region of propellants filled to 5 mm resulted in a similar steady-state solution but extended the length of the initial transient regime due to the homogeneous propellant mixture that strengthened the initial wave passage.

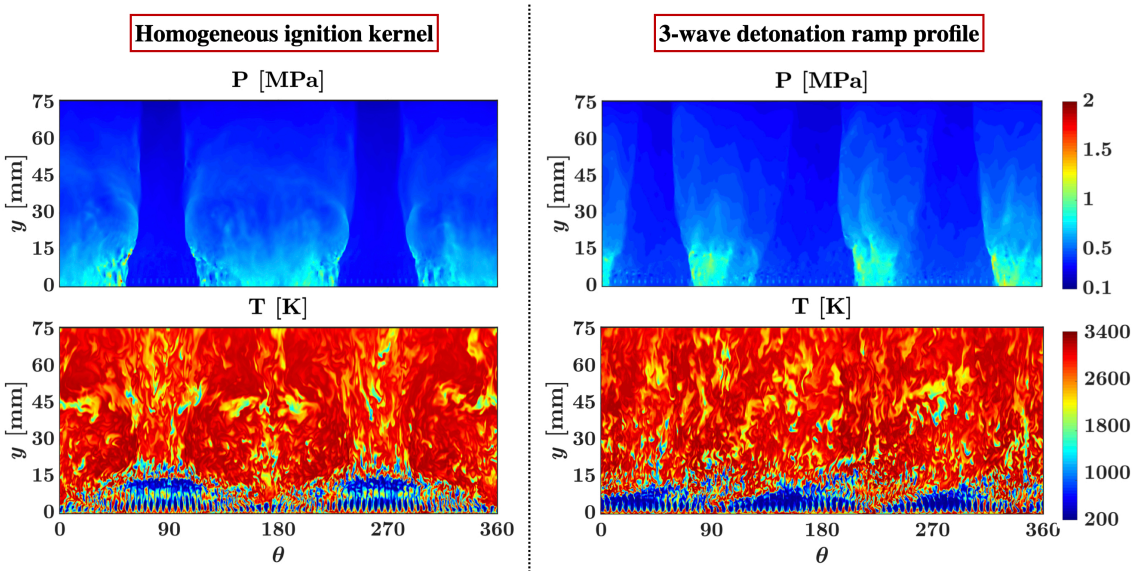

Figure 4.28: Instantaneous profiles of pressure (top row) and temperature (bottom row) along the RDRE combustion chamber mid-channel plane unwrapped and projected onto two-dimensions for solutions generated using (left column) a homogeneous ignition kernel and (right column) three detonation ramp profiles. The high mass flow rate case is simulated here.

With a homogeneous ignition kernel, four waves of similar strength operate stably within the combustion chamber, reinforced by wave collisions. With linear detonation

ramp profiles, the operating condition quickly settles on 3 co-rotating waves, spaced approximately 120° apart. In the temperature plot, triangular injector refresh profiles shorter in height than the parabolic refresh profile developed by the single ignition kernel are observed. It is known that the number of waves is found to be related to the refill height h, which is the distance that fresh mixtures travel axially before the azimuthally-moving detonation wave is encountered. Thus, an increased number of co-rotating waves results in a reduced fill height. With the counter-propagating wave mode, there is a stratified refill region, with two bands of cold gas separated by a high-temperature product gas. This is due to an interaction between the fuel and oxidizer injectors as they respond differently to the counter-propagating wave system. With the ramp profile ignition method, there is increased acoustic noise in the post-shock reaction zone, with secondary waves shed off the primary system. Further, the mean chamber pressure at the 8.9 mm height increases by approximately 3.3% to 0.608 MPa. Additionally, the reduced impedance of a co-rotating wave mode and fewer individual waves within the system results in a wave speed increase of approximately 3% to 1225 m/s.

Thus, the numerical operating mode of the RDE is a function of many factors, ranging from the numerics to the initialization method. The number of waves an RDE sustains is related to the refresh time of the injectors, and whether the injection scheme or operating condition can provide a sufficiently mixed reactant gas to support a given number of detonation waves within the domain. While the homogeneous ignition kernel initially spawns a chaotic field and requires time for the waves to coalesce and reduce in number, an initialization with a fixed number of ramp profiles can establish a stable number of waves with a wave solution different from the single ignition kernel method.

4.3.3 Study conclusions

The revised numerical representation of the AFRL RDRE, revision B, was investigated at a nominal and high mass flow rate. In particular, a finer cell resolution of 100 μm was employed throughout the feed plenums, injectors, and combustion chamber. While the operating conditions are similar to those evaluated in Sec 4.2, the increased cell resolution enabled by the GPU-accelerated UMReactingFlow solver allowed for additional analysis of the mean flow profile and operating characteristics. Additionally, as part of the Model Validation for Propulsion effort, supplemental experimental data was available for direct comparison. Here, the nominal flow rate established a co-rotating wave mode with two waves. On the other hand, the high mass flow rate established two pairs of counter-propagating waves of equal strength. The wave collisions reinforced the wave strength and resulted in a stable operating mode. The counter-propagating waves result in injector dynamics with increased jet flapping behavior and a more distributed heat release profile. Heat release through detonation is of a similar order to heat release through deflagration, which occurs continuously throughout the wave cycle. Further, while the deflagration far from the detonation wave does not support the wave itself, it does contribute to achieving complete combustion. Nevertheless, the nominal flow rate case converts nearly 3% more fuel input to the system to either intermediate or product combustion gases.

Through a partitioning of the system heat release [39, 48], a method for computing the heat release contribution through detonation as opposed to parasitic and post-detonation deflagration was outlined. Here, the fraction of heat release in detonation was notably low, highlighting that deflagration which occurs throughout the wave cycle contributes significantly to the overall heat release. However, this secondary combustion may be required to operate an RDE stably.

The high-resolution revised numerical representation enables a series of mesh resolution and ignition methodology studies. A comparison between a coarse and fine

resolution mesh of the nominal mass flow rate case revealed a different operating mode. While certain operational parameters, such as mean chamber pressure, may be similar, the coarse mesh settled on two pairs of counter-propagating waves whereas the fine mesh resulted in two co-rotating waves. Similarly, the use of two different ignition methodologies in the high mass flow rate case showed that at the same propellant feed rate, two different steady-state operating modes can be obtained within the short-time numerical simulation timescale ($\mathcal{O}$(10 ms)). A homogeneous ignition kernel induced two pairs of counter-rotating waves while three detonation ramp profiles captured the experimental result of three co-rotating waves. Even with strong co-rotating waves, the propagation of the primary detonation waves is accompanied by additional waves that propagate at similar or lower speeds, in a different direction, and are too weak to be considered detonations. These secondary waves manifest as stable, finite-strength pressure waves rotating in the annulus and are possibly associated with a low-magnitude heat release front. They can be visualized in the unwrapped two-dimensional projections of the mid-channel plane and the pressure traces within the combustion chamber. They compete with the dynamics and properties of the primary detonation waves. At first, operation under multiple competing waves may appear erratic, but instead, their dynamics are characterized by well-defined properties (e.g., propagation speed, direction, etc.).

Secondary waves are an integral part of the operation of the RDE and contribute to the structure of the DW by shaping the stratification of fuel and oxidizer and the deflagrated regions that the primary DWs encounter. The presence of secondary waves has been associated with an acoustic coupling between the detonation wave and the propellant feed plenum that results in low-frequency amplitude modulation of wave properties [6], and can even contribute to inlet chugging [7]. As a result, the attenuation of the unsteady dynamics within the combustion chamber through the injector scheme and feed plenums can result in the formation of secondary waves.

This reinforces the differences in operating mode observed by changes in the numerical representation of the feed plenums (between revision A: Sec. 4.2 and revision B: Sec. 4.3) and the injection scheme (Sec. 4.3.2.2). While the number of waves plays a clear role in the modulation of the injectors, and hence the mixing process, its impact on thrust and efficiency is not as well understood. Although they typically serve to diminish primary detonation strength, the effect of secondary waves on overall performance, such as combustion efficiency, needs further study.

CHAPTER V

An Extension to Non-premixed Liquid-fueled RDEs

This chapter presents the application of the UMReactingFlow solver modified with a Lagrangian particle tracking algorithm to study liquid-fueled RDEs. In particular, a rotating detonation rocket engine (RDRE) supplied with a liquid fuel stream and a gaseous oxygen oxidizer stream is studied. The RDRE represented here is a modification of the gas-phase RDRE designed by the Air Force Research Laboratory (AFRL) and collaborators and was examined in Chap. IV. First, the motivation for the study of liquid-fuel RDEs is highlighted in Sec. 5.1. Section 5.2.1 discusses the numerical representation of the liquid RDE while 5.2.2 details the Eulerian-Lagrangian implementation in UMReactingFlow that enables the simulations, along with the relevant models and assumptions. Section 5.3 provides the results of the simulations and outcomes are discussed in Section 5.4. The study presented here has been authorized for public dissemination with distribution statement A: approved for public release; distribution is unlimited under PA# AFRL-2022-4573.

5.1 Motivation

For the practical realization of RDEs in aeropropulsive applications, the use of liquid fuel is necessary. In this case, the stability and efficiency of detonation-based combustors are intrinsically related to the transport of atomized liquid droplets, their evaporation, and the subsequent mixing of fuel and vapor. Since detonation velocities can be high ($1 - 3$ km/s), the time for these complex multiscale processes to occur before a wave arrives is relatively short. Hence, understanding the structure of detonation processes in multiphase systems is necessary for the design of robust RDEs.

Hayashi et al. [117] conducted two-dimensional unwrapped RDE calculations with droplet injection, and found that droplet vaporization model parameters, as well as the initial droplet diameter, play a critical role in detonation stabilization. In particular, diameters over 4 μm resulted in detonation failure. Other studies [186, 265, 267, 291] have found that the range of diameters for stable detonation formation varies with fuel and oxidizer properties, and diameters in the range of 10-20 μm provide stable detonations for hydrocarbon-oxygen detonations. In particular, the velocity deficit of the detonation wave, with regard to CJ speed, was found to increase with droplet size. However, nearly all these studies consider pure fuel/oxidizer mixtures with negligible evaporation prior to detonation impact. Experimental droplet distributions in practical systems will have significantly higher mean diameters as compared to those required for stable detonation in the numerical simulations. For instance, the experiments of Kindracki [153] suggest diameters in the range of 20-40 μm, while recent experiments from Ahmed et al. [177] of RP-2/O_2 RDEs show log-normal droplet distributions with mean diameters of 20-30 μm (based on operating conditions). The impact of such pre-evaporation has not been studied extensively.

This discrepancy in stability behavior may be attributed to a more complex process of detonation propagation. In numerical simulations, the stabilization is related

to the formation of traverse waves [117, 137, 185]. Smaller diameters allow faster vapor release through evaporation, which decreases the time to heat release. Hence, significant exothermic reaction can be expected between the shock front and the sonic plane. In practical RDEs, droplets have finite time after injection for exposure to partially reacted gas mixtures at high temperatures. The resulting heat transfer will increase droplet temperature, and some evaporation leading to a vapor cloud in the droplet vicinity. Even in two-dimensional simulations [185, 186], deflagrating burning in the contact region between fresh and reacted mixtures have been observed. This high-temperature zone provides some level of pre-evaporation for the droplets. In gas-phase configurations, the presence of recirculation regions as well as the differential recovery of the injectors [232, 235, 237] provide additional mechanisms for droplet pre-evaporation. Hence, understanding the role of the RDE geometry on the stabilization of the detonation based on such droplet preparation ahead of the wave needs to be explored.

To this end, multiphase detonations are studied in a rocket-type RDE setting using liquid rocket propellant (RP-2) and gaseous oxygen using high-fidelity three-dimensional numerical simulations. To the authors' knowledge, these simulations represent one of the first multiphase studies of a full-scale RDE with discrete injection and detailed chemical kinetics.

5.2 Simulation Configuration and Numerical Approach

5.2.1 Configuration

In the present study, two different RDRE geometries are considered: 1) Configuration A (CA) and 2) Configuration B (CB) geometries which, in their numerical representations, differ only in the injector diameters. The CA geometry is based on a methane/oxygen RDRE studied previously [237] (see Chap. IV) while the CB ge-

ometry features smaller injector diameters to increase the flow velocity through the nozzle for a given mass flow rate. The fuel and oxidizer injector diameters for CB are 0.508 mm and 0.785 mm, respectively. A cross-sectional schematic of the RDRE geometry is provided in Fig. 5.1. The fuel and oxidizer are delivered through 72 pairs of impinging injectors spread uniformly around the circumference of the annulus with a 5 mm detonation chamber. The pair of fuel and oxidizer injectors are separated by 60°. An inflow plenum supplies the oxidizer through the injectors and a large exhaust plenum is applied for numerical stability such that pressure waves are dissipated before exiting the computation domain. An aerospike nozzle center body is used to direct and accelerate flow past the exit of the combustion chamber.

In the simulations, the physical fuel injector nozzle is removed from the geometry and the liquid droplets are directly injected at the base of the combustion chamber, using a prescribed diameter and velocity distribution obtained from supplemental experimental studies. Essentially, the particles are introduced into the chamber at a nominal post-atomization state as recorded from experiments. In the present study, atomization and particle break-up are not modeled. Details of the particle implementation are provided in Sec. 5.2. This injection surface is shown in the inset image of Fig. 5.1. Liquid fuel and gaseous oxidizer mass flow rates ($\dot{m}_{fuel}$ and $\dot{m}_{oxidizer}$) are 82.5 g/s and 189.6 g/s, respectively, with a global equivalence ratio of 1.5. This represents the lower end of the $\dot{m}$ operating envelope for the RDRE. The oxidizer plenum is pressurized to total pressures of 1.2 MPa and 2.9 MPa at 300 K for the CA and CB geometries, respectively. Using imaging data from supporting experimental studies of droplet-gas interactions with identical injector configurations, the spherical RP-2 liquid droplets are injected with size distribution given by $\mu = 20$ micrometers and $\sigma = 10$ micrometers at a fixed 60 m/s velocity magnitude and temperature of 300 K. A mass flow rate boundary condition is applied on the upstream inlet to the oxidizer plenum, and the fuel mass flow rate is controlled by the injection rate of the

droplets.

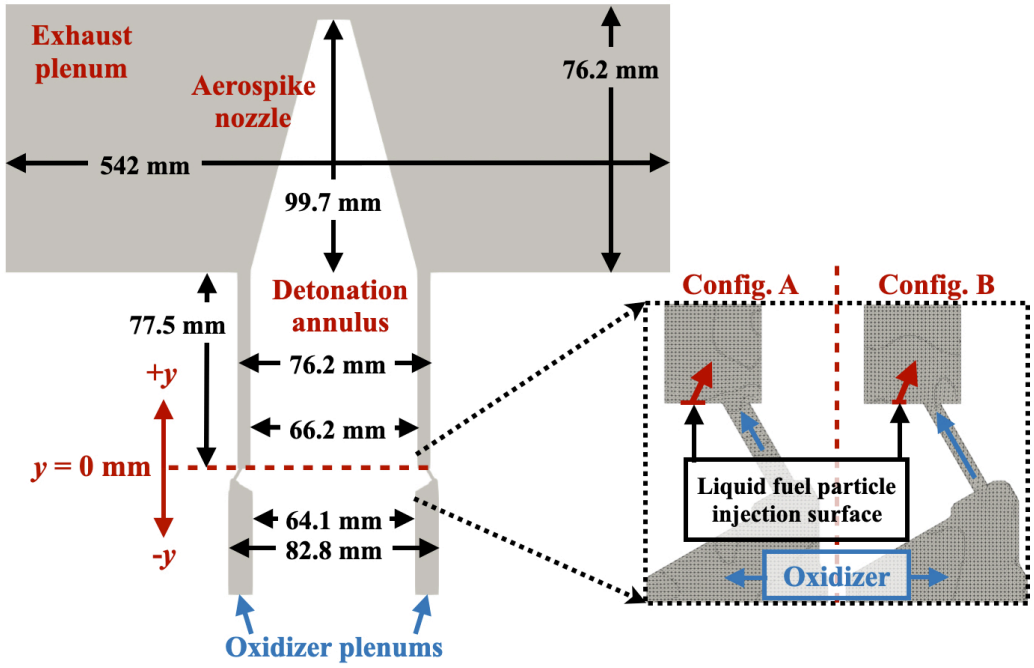

Figure 5.1: Cross-sectional schematic containing primary RDRE dimensions and a detailed view of the injector configuration in the 1) Configuration A and 2) Configuration B geometries.

5.2.2 Numerical approach

A high-fidelity Eulerian-Lagrangian approach using the compressible reactive solver UMReactingFlow was employed to study multiphase detonation. The compressible reacting Navier-Stokes equations are presented in detail in Sec. 2.2. Two-way mass, momentum, and energy coupling between the gas and liquid phases via source terms are achieved by utilizing UMCloud which solves the Lagrangian transport of droplets. Detailed chemical kinetics are computed using a GPU-accelerated chemistry library [15, 26], which enables the use of highly complex mechanisms. The combustion of RP-2/oxygen is captured by the hybrid chemistry (HyChem) 38 species, 192 reaction skeletal chemical kinetics mechanism from Xu et al. [310, 327]. The chemical mechanism has been specifically developed for use in high-temperature conditions.

The compressible Navier-Stokes equations with the Lagrangian particle source terms are described as:

$$\begin{aligned}
\frac{\partial \rho}{\partial t} + \frac{\partial \rho u_i}{\partial x_i} &= \sum M_{p\to f,j}, \\
\frac{\partial \rho u_i}{\partial t} + \frac{\partial \rho u_i u_j}{\partial x_j} &= -\frac{\partial P}{\partial x_i} + \frac{\partial \tau_{ij}}{\partial x_j} + \mathbf{F}_{p\to f}, \\
\tau_{ij} &= -\frac{2}{3}\mu \frac{\partial u_k}{\partial x_k}\delta_{ij} + \mu\left(\frac{\partial u_j}{\partial x_i} + \frac{\partial u_i}{\partial x_j}\right), \\
\frac{\partial \rho e_t}{\partial t} + \frac{\partial \rho u_j h_t}{\partial x_j} &= \frac{\partial}{\partial x_j}\lambda \frac{\partial T}{\partial x_j} + \frac{\partial \tau_{ij} u_i}{\partial x_j} + E_{p\to f}, \\
\frac{\partial \rho Y_k}{\partial t} + \frac{\partial \rho u_j Y_k}{\partial x_j} &= \frac{\partial}{\partial x_j}\rho D \frac{\partial Y_k}{\partial x_j} + \Omega_k + M_{p\to f,j},
\end{aligned} \tag{5.1}$$

where $M_{p\to f,j}$, $\mathbf{F}_{p\to f}$, $E_{p\to f}$ are the droplet species mass transfer, Eulerian-Lagrangian momentum transfer, and the Eulerian-Lagrangian energy transfer source terms, respectively. For details on the other terms in the equation, the reader is referred to the complete solver description in Sec. 2.2. The chemical reaction rates and time integration are computed using the GPU accelerated library [15] with an adaptive chemical time integration approach described in Ref. [26]. The Lagrangian system is governed by the following set of equations:

$$\begin{aligned}
\frac{d}{dt}\mathbf{x}_p &= \mathbf{u}_p, \\
\frac{d}{dt}\mathbf{u}_p &= \frac{1}{m_p}\sum \mathbf{F}_p, \\
\frac{d}{dt}T_p &= \frac{1}{m_p C_p}E_p, \\
\frac{d}{dt}m_p &= M_p,
\end{aligned} \tag{5.2}$$

where $\mathbf{x_p}$,$\mathbf{u_p}$, T_p, m_p, C_p are the droplet position, velocity, temperature, mass, and specific heat, respectively. The force ($\mathbf{F}_p$), energy change (E_p), and mass change (M_p) on the droplet are given by:

$$
\begin{aligned}
\mathbf{F}_D &= \frac{m_p Re_p Cd_p}{\tau_p} \left(\mathbf{u}_f - \mathbf{u}_p \right), \\
E_p &= hA(T_i - T_c) + Q_{lat}, \\
M_p &= -\pi D Sh \mathcal{D} \rho_v \ln \left(1 + \frac{\chi_{v,s} - \chi_{v,c}}{1 - \chi_{v,s}} \right),
\end{aligned}
\tag{5.3}
$$

where, Re_p, Cd_p, τ_p, $\mathbf{u_f}$ are the droplet Reynolds number, drag coefficient, relaxation time, and fluid velocity, respectively. The heat transfer coefficient, droplet area, gas temperature, and latent energy are denoted h, A, T_c, and Q_{lat}, respectively. Note that the liquid phase supports the latent heat of vaporization, i.e., the droplet cools as it undergoes evaporation. In other words, the Eulerian-Lagrangian energy transfer source term $E_{p \rightarrow f}$ does not include the latent energy Q_{lat}. The evaporation parameters: droplet diameter, Sherwood number, mass diffusivity, vapor density, and RP-2 concentration are identified by D, Sh, $\mathcal{D}$, ρ_v, and χ, respectively. The heat transfer coefficient is calculated using a Ranz-Marshall model [249] and the evaporation model is a Spalding model detailed in Miller et al. [190]. The traditional Schiller and Naumann's formulation for Stokes drag (valid for higher Reynolds numbers) was utilized [259]; this drag model was found to exhibit only a slight difference from several non-linear models by Cheatham and Kailasanath [54] in the interaction of a 10 μm droplet with a propagating detonation wave.

Adiabatic and no-slip wall boundary conditions are used. An unstructured mesh resolution of 200 μm is employed from the upper oxidizer plenum through to the end of the combustion chamber. The resolution is relaxed to 400 μm within the lower oxidizer plenum, around the aerospike exit nozzle, and the outflow plenum. The full-scale calculations of RDEs generally do not resolve the shock-detonation structure fully due to computational cost, which is typical of similar studies [61, 263]. For instance, the gas-phase simulations of Pal et al. [214] use grid sizes of 125-250 μm

for hydrogen/air detonations and those of Prakash et al. [237] use 100-200 μm for methane/oxygen detonations.

Past studies [237, 257] of non-premixed detonation have shown that due to finite mixing, the detonation process is highly non-ideal with broad reaction zones and induction lengths that are approximately an order of magnitude greater than the ZND expectation. Thus, this prevents very fine scales from being generated and these resolutions are still able to capture the essential dynamics of the detonation wave. Also, the ideal induction region can be longer than $\mathcal{O}(100\ \mu\text{m})$ for hydrocarbon mixtures [175]. The mesh in the present study has approximately 32.3 million control volumes for both the CA and CB geometries.

5.3 Simulation Results and Discussion

The simulation of multiphase RDRE is initiated using a method similar to gas-phase systems [17, 237]. Following a well-developed injector flow, a single high-energy ignition kernel is used to ignite a 5 mm tall stoichiometric RP-2/O_2 mixture region. The highly unsteady flow is allowed to evolve for 1.0 ms. The multiphase system proved more difficult to stabilize detonation waves within than gas phase systems. The system mode is highly dependent upon the dispersion and evaporation characteristics of the liquid fuel droplets, controlled by the droplet injection velocity and diameter. In both cases, a secondary weak perturbation (consisting of three kernels) following the initial ignition was required to establish detonation. Another 1.0 ms was simulated until statistically-stationary flow with a stable number of waves is obtained. An additional 0.5 ms is used for detailed system analysis.

Initially, the combustion chamber is filled with air at heated conditions (1 atm and 500 K) to encourage the evaporation of liquid fuel into the gaseous state. The liquid fuel and gaseous oxidizer is allowed to develop for 0.25 ms. At this point, the first 5 mm of the combustion chamber is filled with stoichiometric RP-2/O_2 mixture,

with a single high energy ignition kernel (with reaction products) at 4 MPa and 3000 K to ignite the detonation.

The multiphase system proved more difficult to ignite compared to gas phase systems with a tendency of the system to reside in a steady deflagration mode. The system mode is highly dependent upon the dispersion and evaporation characteristics of the liquid fuel droplets. In the current study, this is controlled by the injection velocity and diameter of the droplets, as the injected particles must penetrate the oxidizer stream and be carried downstream into the hotter parts of the chamber. Here, evaporation is encouraged and a mixture of sufficient quality can be prepared for detonation. If the particles do not enter the oxidizer jet shear layer, the particles become entrained in a recirculation zone at the base of the combustion chamber. Thus, the currently prescribed fixed droplet distribution supported the penetration of the liquid fuel stream into the combustion chamber. The droplet size and velocity distribution due to detonation-liquid column interactions can be best estimated through experimental measurements because a fundamental understanding of and associated models for liquid column breakup in supersonic reacting flows are limited. The combustion processes and the operating mode within the RDE are highly sensitive to this boundary condition prescribed for the liquid fuel droplets.

5.3.1 Macroscopic features

The Configuration A and B cases were simulated and steady-state detonation propagation with multiphase reactant injection was established. In comparison to previously-studied gas-phase systems, the wave structure at this point is very chaotic with multiple weak waves (below the sonic speed) moving in either azimuthal direction. As a result, an additional perturbation was applied with three weak kernels (0.7 MPa and 1500 K) spaced uniformly at the base of the combustion chamber. This flow is simulated for another 1.0 ms until steady-state detonation waves were observed.

The operating mode of the Configuration A and B RDREs is visualized in Fig. 5.2; in a so-called detonation surface plot: the pressure trace at the mid-channel location 8.9 mm from the base of the combustion chamber (corresponding to the height of experimental pressure probes) is tracked as a function of time. Following the weak perturbation, three waves were enforced in both directions, forcing existing pressure waves and fast flames to coalesce. Ultimately, the waves in the clockwise direction dominated, establishing three co-rotating waves for both cases. In order to study the effect of the number of perturbation kernels used, a single weak kernel was also explored, resulting in the same steady-state mode with three co-rotating waves. A rendered visualization of the three co-rotating waves in case CA and CB are provided in Figs. 5.3 and 5.4. Here, the shear-induced deflection of the liquid fuel droplets due to the azimuthal acceleration provided by the detonation waves at the base of the combustion chamber is visible.

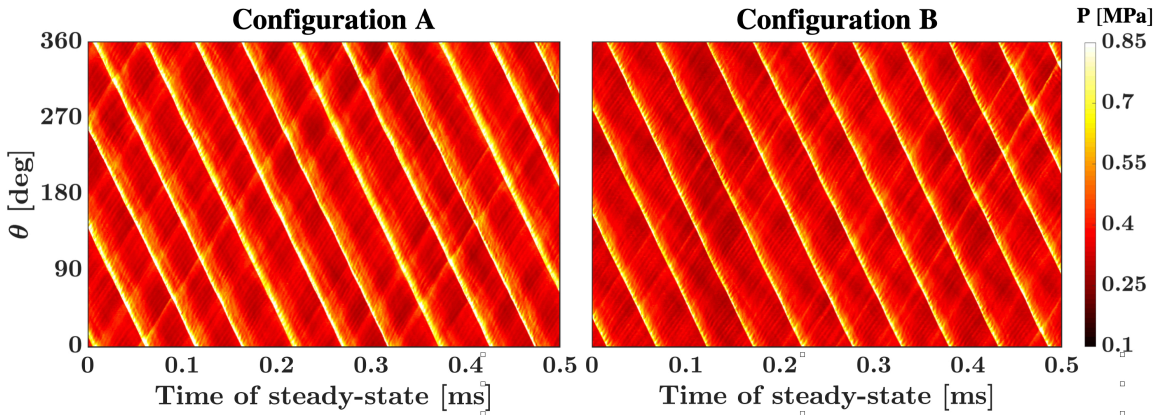

Figure 5.2: Detonation surface plots for the (left) CA and (right) CB cases under steady-state operation, identifying three clockwise co-rotating waves in both geometries. The surface plot is constructed using the pressure trace along the midchannel position at a height of 8.9 mm from the base of the combustion chamber.

An overview of each case is given in Tab. 5.1. Under steady-state operation, the system exhibits a wave speed of 1429 m/s in both cases, approximately 57% of the CJ speed of RP-2/O_2 detonation at $\phi = 1.5$. This is an interesting result because

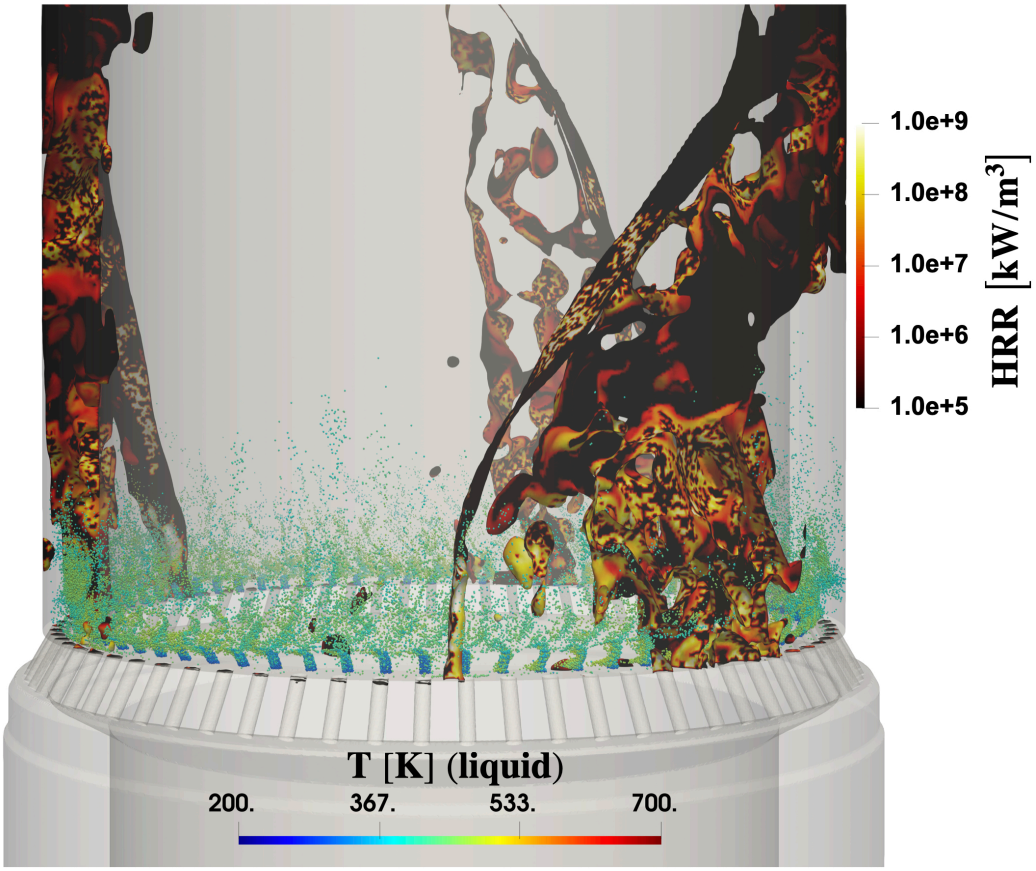

Figure 5.3: Three-dimensional view of the 3 clockwise co-rotating detonation waves in the Configuration A geometry under steady-state operation, highlighting the deflection of fuel droplets due to shear induced by the propagating detonation waves. The liquid particles are colored by temperature and the wave fronts, identified by isocontours of pressure, are colored by heat release rate.

Table 5.1: Multiphase RDRE case overview.

Case	**CA**	**CB**
$\dot{m}_{total}$ [g/s]	284	255
Global ϕ	1.43	1.69
# of waves	3 CW	3 CW
Wave speed [m/s]	1429	1429
Thrust [N]	462.6	407.9
I_{sp} [s]	165.7	163.1

while the mass flow rates between the cases are the same, the plenum values and axial pressure profile of Fig. 5.9 are notably different. Furthermore, the detonation surface plot shows that the waves in case CB are more compact, with a lower peak

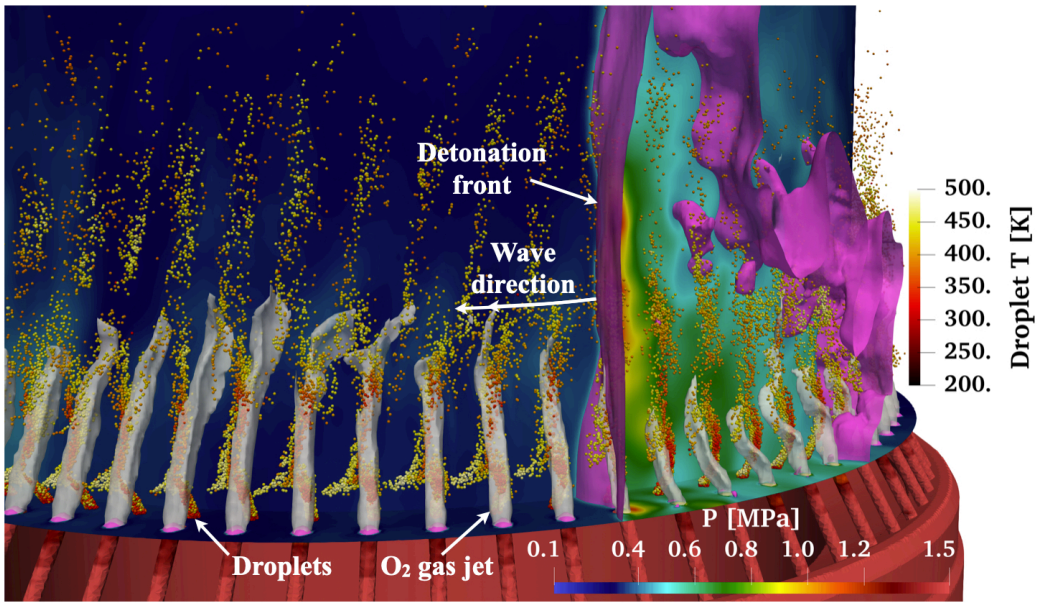

Figure 5.4: Three-dimensional close-up view of the detonation front passing through the column of fuel droplets and oxidizer jets in the Configuration B geometry. Here, the minimal suppression of the oxidizer jet and the dispersion of the fuel droplets are visible. The detonation front is identified by the pink isosurface based on the gas phase pressure. The droplets are colored by the temperature while the oxidizer jet column is shown in white.

pressure and shorter reaction zone. In both cases, there are counter-propagating pressure waves that are time-varying in strength. These waves are "shed" off of the primary wave system and reinforced through collisions with other waves. A two-dimensional projection of pressure, liquid particle number density, equivalence ratio, and particle azimuthal velocity along the mid-channel plane is provided in Fig. 5.5, revealing interesting features. In the pressure profiles, it is clear that the waves in case CA are thicker. The peak pressure along the detonation front is also more limited in case CB, with case CA exhibiting sharper inflection points and increased wave front corrugation. The wave structure and oblique shock wave angles are similar in both cases.

The particle number density profiles show that particles are carried up to 20-25 mm into the combustion chamber before being completely evaporated, with the distance traveled greater in case CB. The particle count, which also reveals the particle

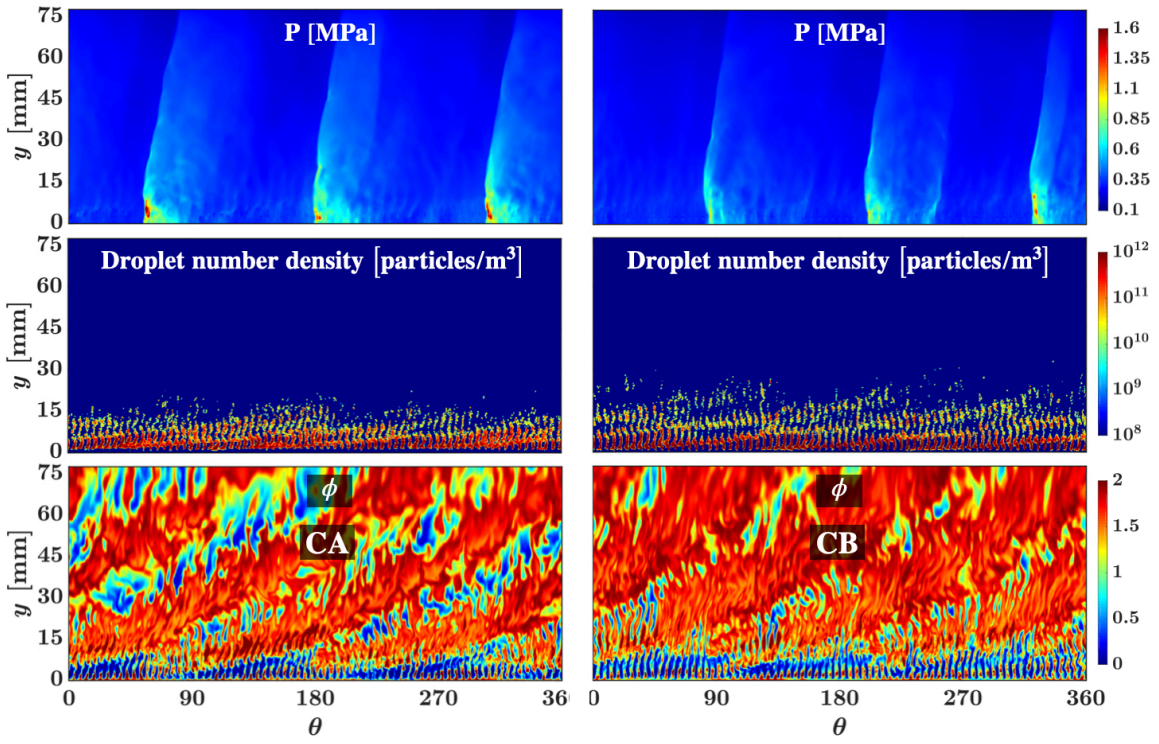

Figure 5.5: Two-dimensional projects of (top row) pressure, (second row) particle number density, (third row) equivalence ratio, and (bottom row) azimuthal particle velocity along the mid-channel plane for the (left column) CA and (right column) CB cases.

spatial distribution, has a triangular shape, maximized at some point in between adjacent waves. This is the location at which residence under high-temperature post-detonation conditions was sufficient to evaporate the particles into gaseous fuel. This is confirmed by the equivalence ratio profile, where there is a significant increase in richer mixtures downstream of the maximum of the particle distribution triangle. As the oxidizer injector recovers, this freshly-evaporated fuel is mixed and convected downstream. Near the bottom of the chamber, the regions of sparsity in droplet count can be associated with rich evaporated fuel. The particle count profile also illustrates distinct regions within the triangular recovery profile: 1) an inner region of very lean gas-phase mixture exists in conjunction with high droplet counts; 2) a buffer region of very rich gas mixture due to freshly evaporated fuel; and 3) sparse (generally larger)

particles that continue to heat up and evaporate as they are convected downstream. The buffer region is more pronounced in case CB, observed as voids (low particle count) within the triangular particle count profile. The equivalence ratio profiles show that the oxidizer injector in case CB recovers very quickly due to the stiffness of the injector and high feed pressure. Thus, the quick recovery of the oxidizer jet is able to convect and mix newly injected particles into the post-detonation mixture more effectively, allowing them to take advantage of the high temperatures and evaporate. In essence, the particles in case CA need to travel further downstream to gain enough energy to evaporate, whereas the evaporation process is more distributed and begins closer to the chamber bottom in case CB. The increased evaporation at lower heights could explain the compactness of the detonation waves in this case, where particles accelerated into the post-detonation mixture use the high energy region as a source, thereby limiting the thickness of the reaction zone region.

The particle azimuthal velocity curves of Fig. 5.5 show that particles are rapidly accelerated in the direction of the passing detonation wave due to shear forces. Due to the inertia of the droplets, the influence of the detonation wave extends well behind the reaction zone. The droplet azimuthal velocity becomes less correlated with the detonation wave within recirculation zones - where evaporation is occurring. In case CA, positive velocities opposite the wave propagation direction are observed within the sparse particle regions only. In case CB, the positive velocities are seen within the particle count voids within the refill region as well as the sparse particle sections.

Figure 5.6 outlines the recovery cycle of the oxidizer injector between two consecutive waves. This timescale is denoted $\bar{\tau}$ and is approximately 52.2 μs for both cases due to the similar wave speeds. The wave arrives at the injector just after a given time τ_0, and the injector fully recovers by $\tau_0 + \bar{\tau}$. At $\tau_0 + \frac{1}{5}\bar{\tau}$, the oxidizer stream in case CA is fully cut off. A pressure pulse is observed feeding back into the oxidizer plenum as the flow unchokes momentarily. On the other hand in case CB, the oxidizer

column is briefly dispersed but begins to reestablish almost immediately. The injector column remains choked throughout the entire process, and no detonation feedback into the oxidizer nozzle is observed. This is ensured by the significantly higher oxidizer feed pressure with similar detonation strengths. During fully-developed flow, the oxidizer column in the CB geometry extends further into the combustion chamber and is highly underexpanded as it enters the channel.

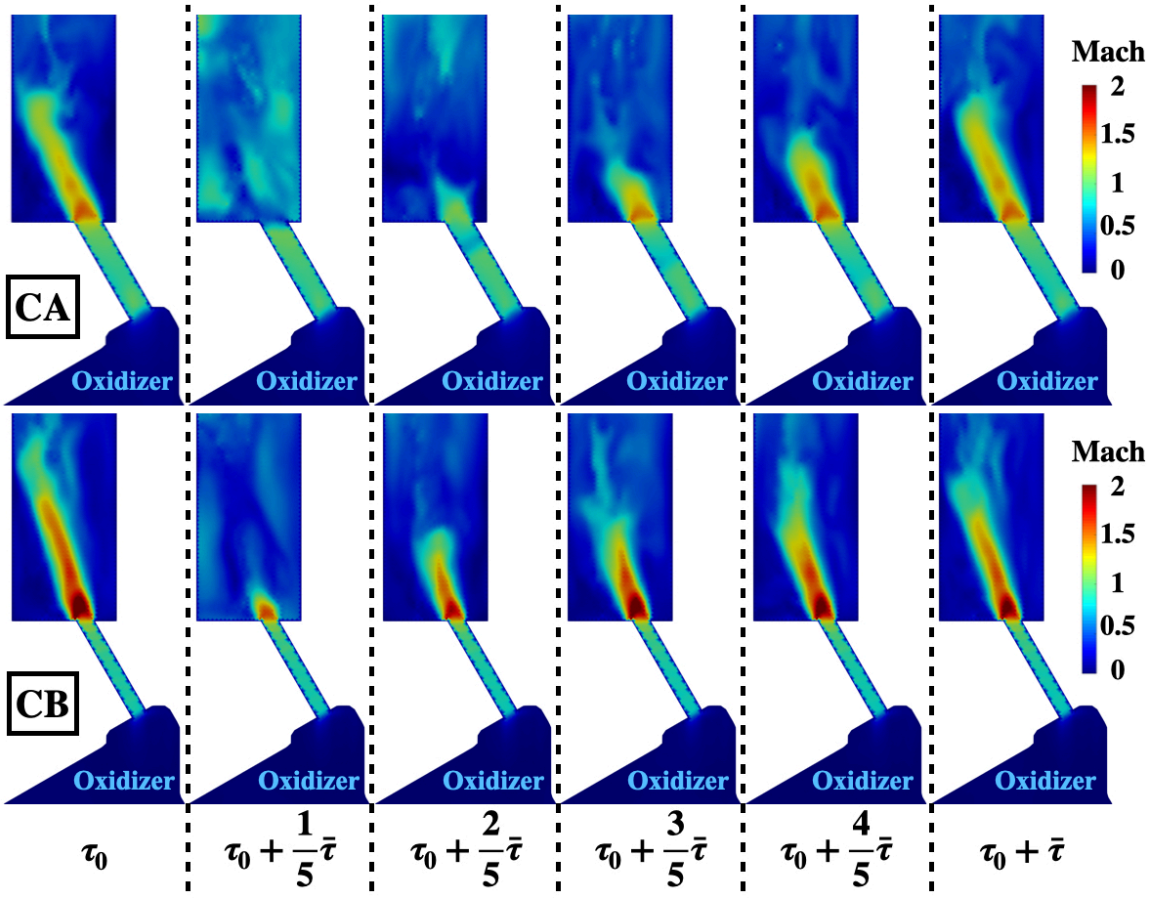

Figure 5.6: Evolution of Mach number during a single injector cycle for the (top row) CA and (bottom row) CB cases, highlighting the stiffness of CB oxidizer injector. $\bar{\tau}$ represents the average time scale between consecutive waves.

5.3.2 Unconditional statistics

To quantify the statistical properties of the RDE flow field, unconditional time averages of different quantities are discussed here. Figure 5.7 outlines the evolution of injector properties during the time between two consecutive waves, denoted $\bar{\tau}$ and is approximately 52.2 μs for both cases due to the similar wave speeds. These properties represent the flow conditions at the nozzle-center location near the exit plane of the oxidizer injector. The average profiles are obtained over multiple RDRE cycles and eight oxidizer injectors separated by 45° around the circumference. The oxidizer injector in case CB is largely unperturbed by the passing detonation wave. As the wave passes, the time evolution of the injector cross-section (not shown here) illustrates that the oxidizer column is briefly dispersed, but begins to reestablish almost immediately. The injector nozzle remains choked throughout the wave cycle and no detonation feedback into the oxidizer nozzle is observed. On the other hand, the CA injector experiences a two-step recovery: the velocity partially recovers by $0.3\bar{\tau}$ and fully recovers by approximately $0.5\bar{\tau}$. Alternatively, the CB injector flow velocity remains the same as the fully-developed value throughout the wave cycle. Importantly, the CB injector's exit temperature is nearly 50 K higher than the CA injector. Although both injectors expand into the channel, this results in droplets interacting with a warmer oxidizer jet. The boiling temperature of RP-2 liquid is estimated at 475.35 K, and this 50 K increase in flow velocity serves to limit the cooling of 300 K droplets as they penetrate the oxidizer shear layer. This supports the increased gaseous fuel converted through evaporation observed at lower chamber heights in Fig. 5.5.

The RP-2 liquid fuel droplets are injected at the prescribed post-atomization size distribution and fixed velocity in the present study. This assumption of fixed velocity is acceptable since the increased pressure due to detonation occurs across a short timescale, and the increased inertia of the fuel droplets ensures limited disruption

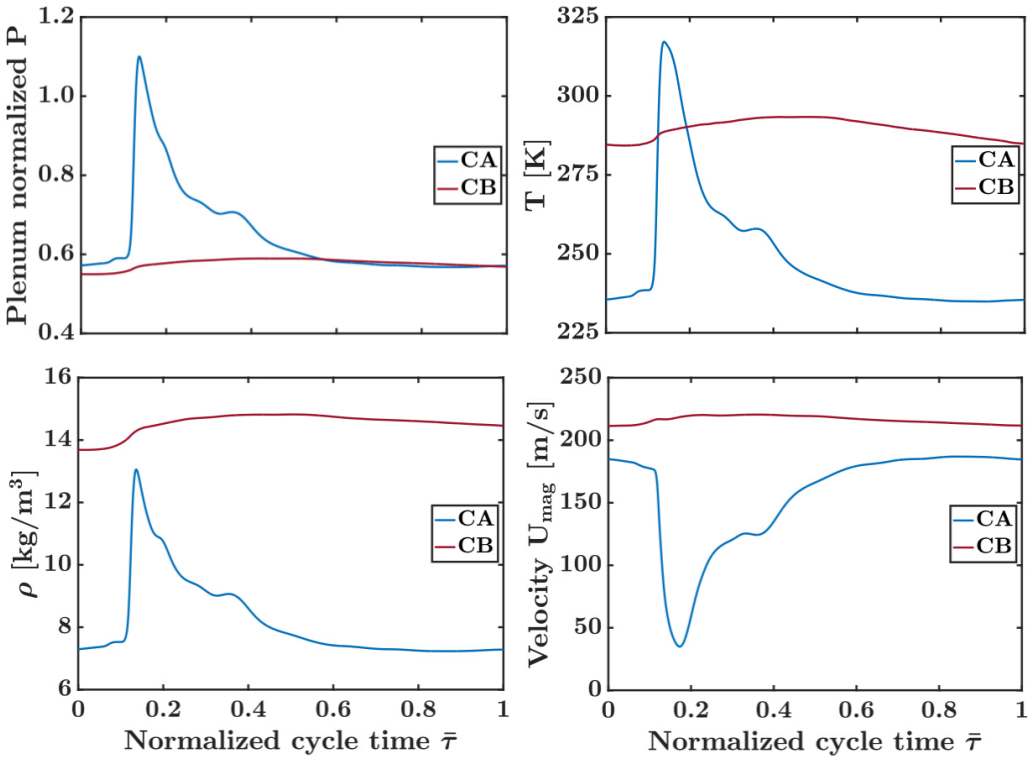

Figure 5.7: Oxidizer injector response (pressure, temperature, density, and velocity magnitude) comparison during a single injector response cycle between the CA and CB cases.

to the liquid stream during the wave cycle. In both cases, the average evaporation rate achieves the target fuel mass flow rate within 0.28% and 0.43% difference for the CA and CB cases, respectively. The volume-weighted ensemble-averaged droplet temperature for cases CA and CB are 397.9 K and 390.3 K, respectively. The time-resolved variation of these parameters during steady-state operation is highlighted in the time-history profiles in Fig. 5.8.

The axial pressure profile along the outer wall of the combustion chamber is given in Fig. 5.9. The pressure distribution in case CA is roughly 11.3% higher on average than the baseline pressures in case CB. In case CA, the pressures are relatively flat until their peak at 5 mm from the base of the combustion chamber, then rapidly decline by 12.5 mm height. Following this point, the pressures gradually decay towards the exit, following a curvature similar to case CB. However, based on Fig. 5.5,

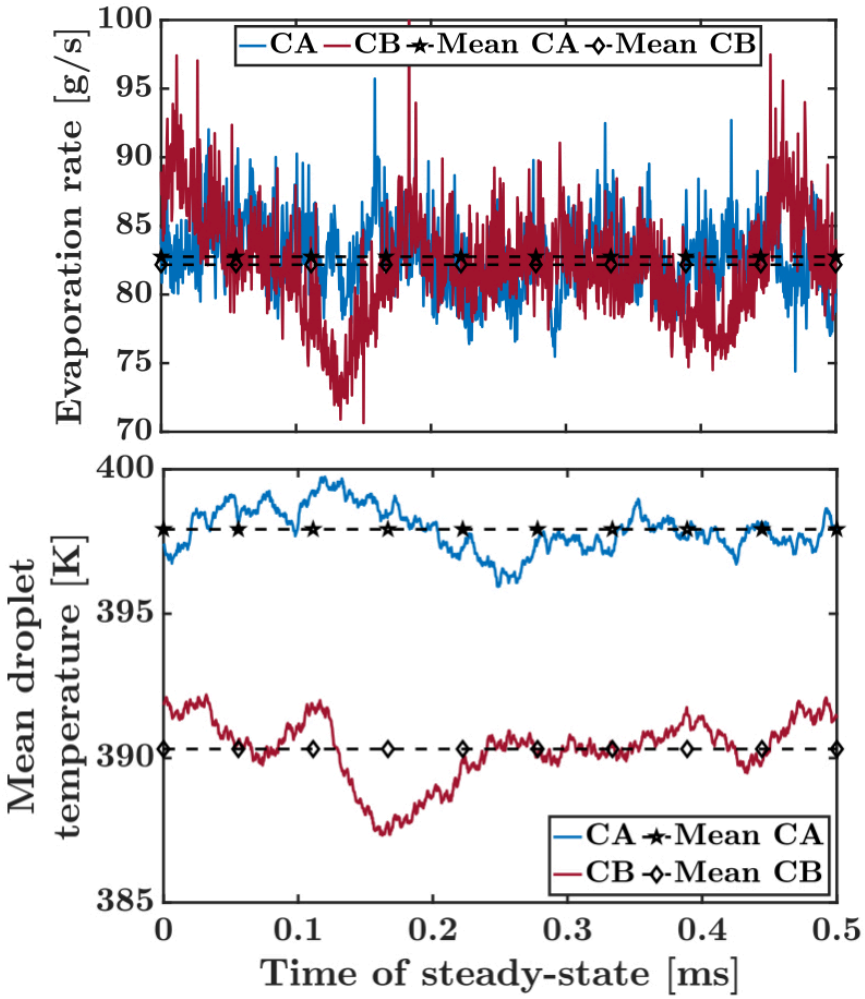

Figure 5.8: Evaporation rate (top) and volume-weighted ensemble-averaged droplet temperature (bottom) for the CA and CB cases during steady-state operation.

the primary detonation front in case CB exists farther downstream, reinforced by an oxidizer injector column that is taller and the onset of evaporation at a location lower in the combustion chamber, leading to the larger plateau in the axial pressure profile.

The axial pressure profile along the outer wall of the combustion chamber for case CB is given in Fig. 5.9. The CB geometry with liquid spray RP-2 injection has been experimentally studied at the same operating conditions ($\phi = 1.5$ and $\dot{m}_{total} =$ 272 g/s) and the pressure at three CTAP locations, 8.9 mm, 28.6 mm, and 65.3 mm from the base of the combustion chamber, were compared. The simulation captured

the CTAP measurements and the general pressure decay profile very well, with a relative error of 0.9%, 7.2%, and 3.9% at the three locations, respectively. In general, the experiment observed between 4-7 waves, with speeds ranging from 900 to 1200 m/s. These increased number of waves may correspond to the chaotic weak-wave mode obtained following the initial ignition process. However, with an increased number of waves, the associated wave speed is expected to be lower. The numerical simulation's pressure profile is relatively flat until the peak pressure at the 7.5 mm location. Beyond this point, there is a rapid decline until about 17.5 mm height, then a gradual decay towards the exit of the combustion chamber. The high pressure near the base of the chamber is influenced by the detonation strength, the post-choke injector pressure, and the acoustic effects of rapid evaporation. As a result, the effects of an individual phenomenon are difficult to isolate.

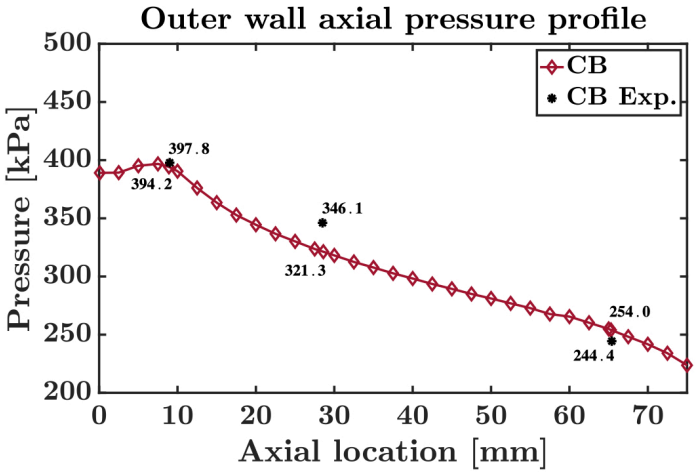

Figure 5.9: Axial pressure profiles along the outer wall for the CA and CB cases, along with experimental data at 3 CTAP locations: 8.9 mm, 28.6 mm, and 65.3 mm from the base of the combustion chamber. The experimental trial corresponds to case CB.

Figure 5.10 shows the azimuthally and temporally-averaged contours of mixture fraction (Z) and heat release rate near the base of the combustion chamber, constructed using the near-wave front conditions only. The outer wall and oxidizer injector are on the right side of these profiles. Here, clear differences in the mixture

fraction distribution are observed between the CA and CB cases. In both cases, there are three distinct recirculation zones: 1) near the lower inner wall restricted by the oxidizer injector; 2) near the lower outer wall limited by the oxidizer injector jet; and 3) downstream location where fuel particles are dispersed by the oxidizer injector. The lower outer wall recirculation zone traps more fuel in case CB due to the narrower oxidizer jet. The stoichiometry line of the downstream recirculation zone starts around the 10 mm height in both cases, but the concentration of high Z is shifted from 15 mm in case CA to greater than 20 mm in case CB. These features are reflected in the normalized heat release contours where the majority of energy release is limited to regions below the stoichiometric limit. In case CA, the heat release occurs within 7.5 mm with the primary detonation front residing around the 5 mm height. In case CB, the heat release profile is more elongated up to and beyond the 10 mm height, with peak heat release around the 7.5 mm location. Energy release primarily occurs along the intersection of the fuel particles and oxidizer stream, and above the oxidizer jet where fuel particles are convected. Moreover, the heat release profile is shifted towards the inner wall in case CB.

The time-averaged droplet properties provide insight into the combustion characteristics. The heat release profile is directly reflected by the particle density profile. A concentration on the order of 10^{10}-10^{11} droplets per cubic meter results in a slightly lean mixture that supports detonation. These regions are primarily observed downstream of the oxidizer injector and near the inner wall and represent locations where turbulent mixing aided by the oxidizer jet shear increases the evaporation of the particles. Following detonation, the particles are convected further downstream where exposure to high-temperature gases results in complete evaporation of the remaining particles and results in the high Z patch above the 15 mm height. In the temperature profile (not shown here), there is a distinct region of nearly 1500 K cooler gas at this height due to the heat transfer from the gas to the liquid during the rapid evaporation

process. The particle diameter profile on the far right of Fig. 5.10 shows that droplet diameters are generally smaller in case CB; the droplets are between 5-10 microns in the primary heat release region in case CA whereas they are below 5 microns in case CB. This can be attributed to the stiffness of the oxidizer jet and its increased ability to disperse and mix injected droplets. Temperature profiles show hotter gas near the base of the combustion chamber in case CB, which serves to decrease the size of droplets prior to impinging with the oxidizer jet itself.

One-dimensional average profiles of flow properties constructed from the wave front at the 8.9 mm chamber height are provided in Fig. 5.11. The profile of the CA case features a cooler gas ahead of the wave by approximately 200 K, supported by the increased heat release in case CB at this height. Similar peak temperatures of 3000 K are achieved but are lower than the ideal post-detonation state by nearly 700 K. The compactness of the wave in the CB case is visible here: the temperature quickly decays to the pre-detonation value within 0.5 cm from the shock front, whereas it takes 2 cm for this to occur in the CA case. This is attributed to the oxidizer injectors which supply cool gas into the chamber almost immediately after the passing detonation wave in case CB. A similar rapid decay in the heat release rate curve is also seen in the CB case. This is confirmed by the distance of the detonation wave front to the sonic plane, which is shorter in the CB case by 0.4 mm. Notably, the heat release rate beyond the sonic plane is nearly an order of magnitude higher in case CB than case CA. The pressure profiles in the right image of Fig. 5.11 are similar, with case CA exhibiting a higher peak value by 0.1 MPa, although similar wave front exothermicity is seen. Similar to the thermodynamic properties, the species mass fractions also recover to pre-detonation conditions faster, with fuel largely replenished by the sonic plane. Using a heat release segmentation process described by Burr and Paulson [39], a detonation-to-deflagration heat release fraction for cases CA and CB are 43% and 26%, respectively. Much of the heat release occurs in the deflagration mode away

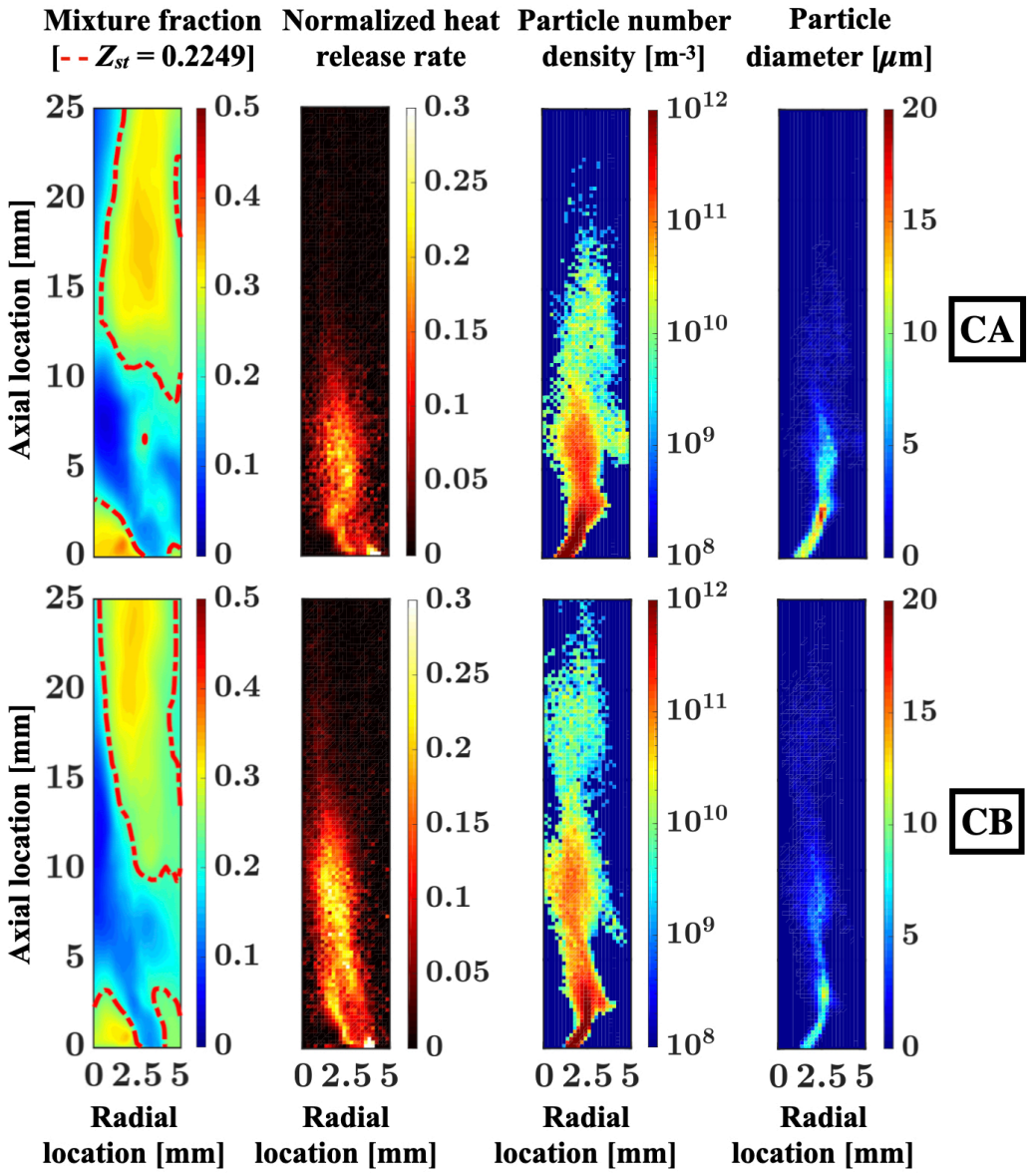

Figure 5.10: Azimuthally and temporally-averaged (far left) mixture fraction, (left) normalized heat release rate, (right) particle number density, and (far right) particle diameter profiles at the wave front for the (top row) CA and (bottom row) CB cases. The isoline of mixture fraction outlines the stoichiometric region within the detonation channel.

from the detonation wave in case CB.

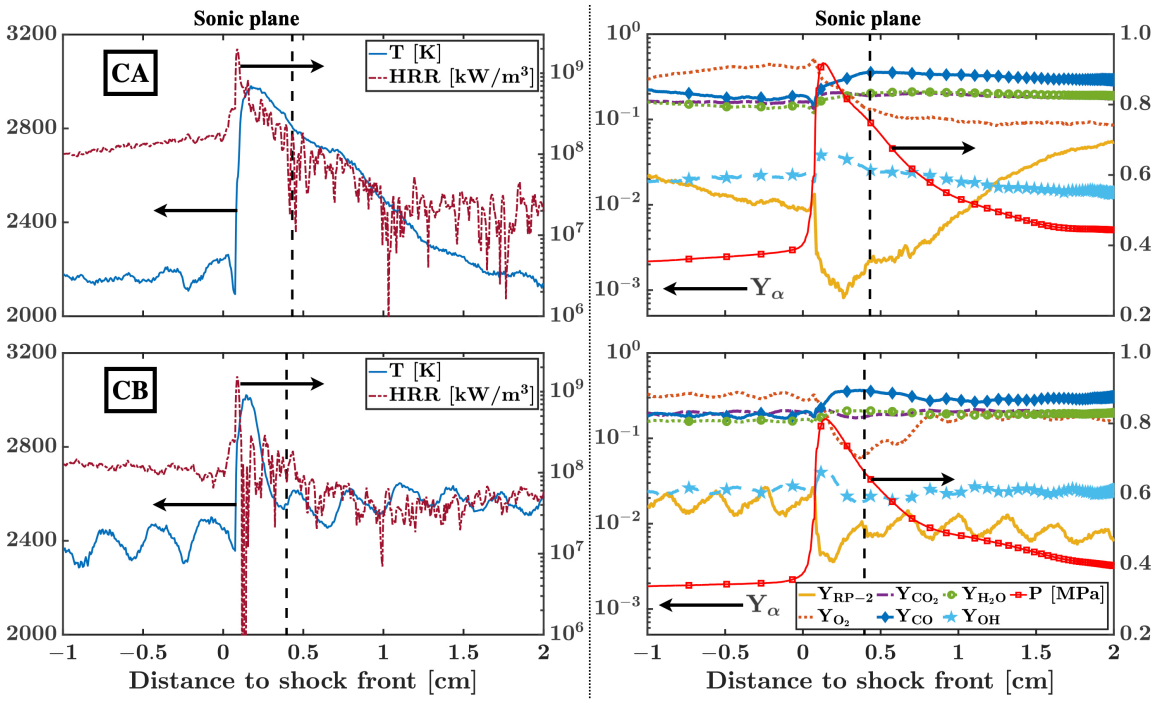

Figure 5.11: Wave-front and temporally averaged one-dimensional profiles of (left) temperature and heat release rate and (right) primary species and pressure for the (top row) CA and (bottom row) CB cases. The mean sonic plane location is given by the dashed vertical line for each case.

5.3.3 Conditional statistics

Conditional statistics of droplet parameters provide insight into the particle dispersion and evaporation characteristics between the two cases. The top row of Fig. 5.13 illustrates the probabilistic correlation between droplet temperature and diameter ensemble-averaged during steady-state operation. On the bottom row, the conditional averages of droplet temperature conditioned on diameter and the droplet diameter conditioned on temperature with reference to the spread of the averages are provided. The joint PDFs are similar for both cases, but there is a higher fraction of the droplets around the mean diameter and at high temperature, just below the boiling point of liquid RP-2 at standard conditions. The peak correlation occurs at a higher diameter in case CB, suggesting that larger droplets are heated more effectively, in part due to interactions with the oxidizer injector. Both profiles feature a

tail stemming towards cooler temperatures and smaller diameters, but the increased fraction in case CB shows that a greater fraction of particles exist in a partially heated state. Conditional averages of droplet diameter conditioned on temperature highlight that droplet diameter is negatively correlated with its temperature and begins to rapidly decay once heated to about 375 K. Droplet temperatures are slightly higher in case CA than CB for low droplet diameters (< 10 μm), suggesting increased residence time of smaller droplets prior to evaporation.

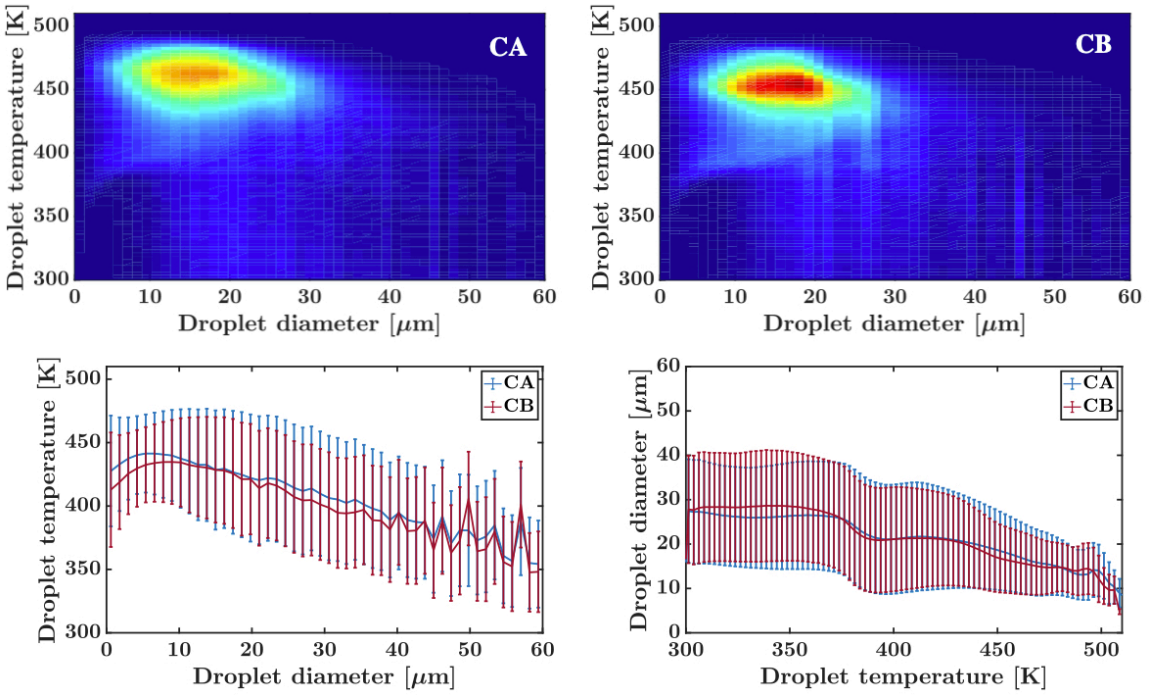

Figure 5.12: Average distributions of (left column) droplet diameter and temperature for the (top left) CA and (bottom left) CB cases. Conditional averages of (top right) droplet temperature conditioned on diameter and (bottom right) droplet diameter conditioned on temperature. The boiling point of liquid RP-2 is 475.75 K at standard conditions.

Furthermore, conditional averages of droplet diameter and number density in carrier gas temperature and mixture fraction space, shown in the top row of Fig. 5.13, highlight key properties of the droplet dynamics within case CB. Additionally, the average radial and axial position of the droplets conditioned on the carrier gas temper-

ature and mixture fraction are provided on the bottom row, allowing for correlations between droplet diameter/number density and droplet position. The largest concentration of droplets exists within rich flows at the base of the combustion chamber and the mid-channel location, as expected. This basin around a mixture fraction of 0.4, denoted by region A in the figure, accumulates mixture fraction due to the steady evaporation of droplets. The larger droplet size and low chamber heights suggest that these are freshly injected particles. The oxidizer injector which impinges above this physical location enforces a recirculation zone. The droplet density decays moving towards warmer temperatures and locations more downstream (heights of 5-10 mm from the base of the combustion chamber). Here, the mixture fraction is also reduced to near stoichiometry. Thus, droplets are moving farther upstream in order to evaporate, and the converted fuel gas mixes with the oxidizer flow. This "bulb" in the profile, denoted by region B, is shifted towards the outer wall and at locations beyond the 10 mm height. Consequently, the droplet density is fairly sparse here, with the lowest observed diameters due to evaporation, reinforced by hot gas recirculation and deflagration above the wave height.

The characteristic peak in the temperature occurs near the stoichiometric mixture fraction, but a curved parabolic distribution is observed even for nominally fast chemistry. There is a small increase in droplet density and size here. This may be attributed to droplets that exist at the primary detonation front. A peculiar feature is seen on the left boundary of the distribution, at low mixture fractions with very large droplets. The droplet density is relatively sparse in this section, named region C. These large droplets are likely entrained within a recirculation zone caused by the injector recovery process. The inertia of these droplets prevents them from becoming ejected from the recirculation zone easily by the passing detonation wave. Thus, they exist within cooler temperatures near the inner wall and at heights above 15 mm in the chamber. In general, the stiff oxidizer injector dynamics of case CB lead to

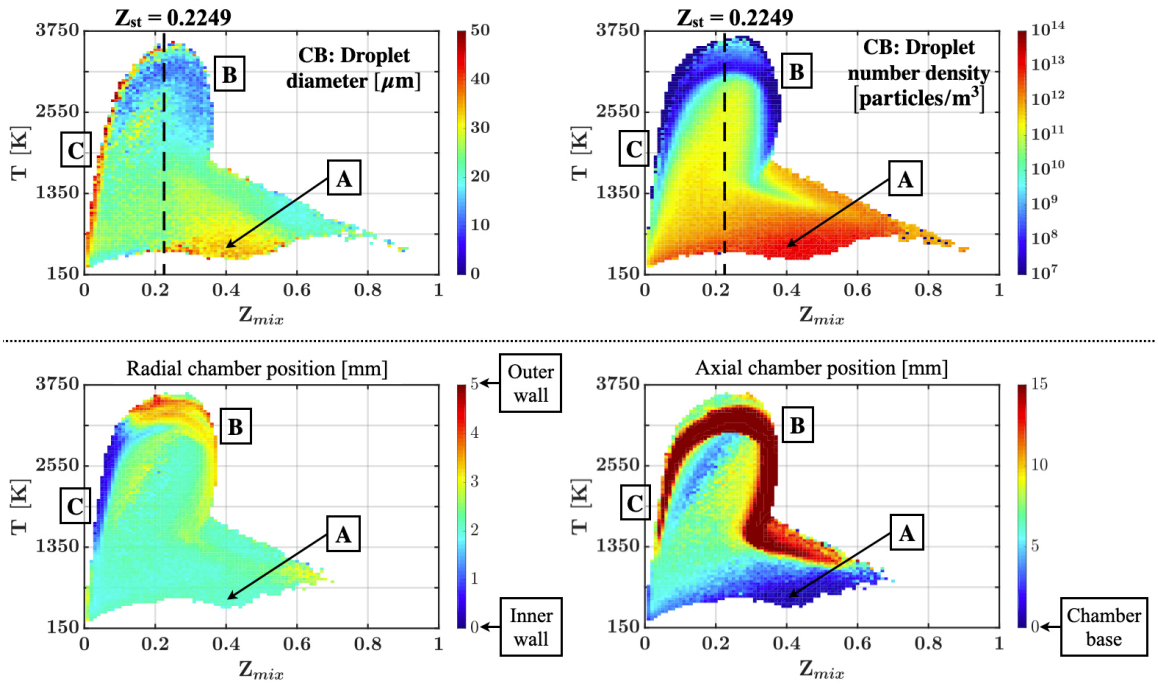

Figure 5.13: (Top row) Two-dimensional conditional averages of (top left) droplet diameter and (top right) droplet number density conditioned on gas-phase temperature and mixture fraction. (Bottom row) Conditional averages of droplet position in the radial (bottom left) and axial (bottom left) directions in the combustion chamber cross-section conditioned on gas-phase temperature and mixture fraction.

stratification within the combustion chamber and enforce the trajectory of particle evolution from cool liquid droplets to detonable fuel/oxidizer mixture.

5.4 Chapter Summary

Novel high-fidelity numerical simulations of a liquid rocket propellant-fueled RDRE were conducted using two different injector geometries, demonstrating stable operation with multiphase detonations in a practical three-dimensional configuration. The jointly-developed Eulerian-Lagrangian flow solver provided detailed insight into the physical mechanisms important in the detonation environment. Further, knowledge of stable ignition of a liquid-fueled RDE was obtained, and the differences from past

gas-phase simulations were highlighted. The two cases achieved similar steady-state behavior with three co-rotating waves with a propagation speed of 1429 m/s. However, the injector dynamics result in a different detonation wave structure and droplet dynamics. In particular, the stiff injectors in configuration B rapidly recover following wave passage, resulting in waves that are highly compact yet move at detonation-like speeds, vastly different from wave modes observed in gas-phase systems. This compactness is enforced by the injector recovery, as well as droplets that act as a heat sink to the passing detonation wave, moving the sonic plane closer to the wave front and limiting the broadness of the reaction zone. The injector dynamics lead to differences in the droplet motion, where the injector recovery enforces recirculation zones and the droplet trajectory in its evolution from injection to detonatable mixture. Most importantly, the penetration of the injected particles is crucial in their ability to be evaporated, where droplets that are not carried downstream are entrained within a recirculation zone at the base of the chamber. This can quench detonation and result in a chaotic, deflagration-like mode. The present study represents an important step to understanding the multiphase detonations crucial to practically realizing these systems.

Current ongoing work aims to address shock-induced droplet breakup and its effects. Currently, canonical numerical studies are being completed to develop the shock-induced break-up and non-linear drag models for use in the regimes observed in RDEs [27, 177]. There is a lack of models in the literature applicable to supersonic flow. Adequate calibration of the break-up model is necessary because the amount of droplet shattering estimated by detonation-induced break-up will effectively control the vapor available for subsequent detonations and secondary (parasitic/commensal) combustion between the detonation waves. For this reason, the current work does not consider a break-up model and can be considered a worst-case scenario where there is no increase in liquid fuel surface area due to droplet shattering; this would

increase the evaporative mass transfer rate of RP-2 from liquid to vapor and limit fuel available for detonative energy release. Additionally, Zhao and Zhang [342] found that the inclusion of a droplet break-up model tuned for high-pressure vaporizing sprays, ReitzKHRT, resulted in indistinguishable profiles of arithmetic and Sauter mean diameters along the axial length of the combustor when the initial distribution's mean diameter d_0 was 20 μm. Similarly, minimal differences in detonated fuel fraction and wave speed were observed below a mean initial droplet diameter of 50 μm.

In the full-scale simulations performed here, the initial droplet distribution (velocity and size) was prescribed at the post-atomization state following jet interactions (as measured by the experiments). Although there is spatial variation in the droplet size, the mean diameter of $d_0 = 20$ μm is well within the regime where Ref. [342] did not observe appreciable effects of droplet break-up on detonative performance or fuel vapor available for combustion. Future work aims to incorporate additional droplet mechanisms observed in canonical studies, such as shock-induced droplet breakup and non-linear drag estimation models tailored for use in high-speed flows.

CHAPTER VI

Modeling for RDE Performance Estimation

This chapter describes a macroscopic view of rotating detonation engine performance. In the preceding chapters, the numerical studies have outlined that detonations in non-premixed RDEs do not exhibit ZND-like behavior, with a mixture of both detonation close to the wave and deflagration in regions far from the wave front. The non-idealities are due to the thermoacoustic instabilities within the RDE system, dependent upon the coupling of the pressure and heat release fluctuations within the combustor [3, 4, 316]. In order to use detonation engines for practical applications, it is necessary to reliably estimate performance characteristics such as thrust/specific impulse over a range of operating conditions and geometric designs. Due to the inherent physics complexity, computational models are too expensive, and conducting large numbers of experiments is also not practically feasible. Hence, techniques that allow limited data to inform surrogate models that can predict performance over the entire operational map would be invaluable. Existing reduced-order models have been shown to predict performance metrics reasonably accurately but require expert tuning of model parameters. To this end, a multi-fidelity modeling framework is proposed for developing surrogate models with predictive capability using limited data sets. This framework is demonstrated on the well-studied AFRL radial hydrogen/air RDE. First, the motivation for the predictive modeling of RDE performance is high-

lighted in Sec. 6.1. Section 6.2 outlines the data sources ranging from experimental campaigns, numerical simulations, and reduced-physics models. The multi-fidelity modeling framework is introduced in Sec. 6.3 and is demonstrated in Sec. 6.4. Additionally, Bayesian calibration of the reduced-physics model is performed to tune the model for the current application in Sec. 6.5. The conclusions of the modeling framework and its advantages and limitations are summarized in Sec. 6.7. The modeling approach presented here is published in Ref. [238].

6.1 Motivation

In order to use detonation engines for practical applications, it is necessary to reliably estimate performance characteristics such as thrust/specific impulse over a range of operating conditions and geometric designs. Due to the intrinsic physics complexity of RDEs, computational models are inherently expensive, and cannot be used to map the entire set of input conditions. Similarly, conducting large numbers of experiments is also not practically feasible. The focus of this work is to develop a methodology for characterizing RDE performance using a sparse set of experimental and/or high-fidelity computational data.

The main challenge in the prediction of device performance is the influence of the injection design on the detonation wave strength. In practical RDEs, fuel and oxidizer are injected through discrete ports that are uniformly spaced around the circumference. The injected feed streams mix through turbulence created by the shear layer. Since the detonation waves move at high speeds (> 1 km/s), there is finite time available for mixing. Moreover, the passage of the detonation wave may temporarily block injectors, which leads to a time-varying unsteady mass flow rate through each port. When the fuel-oxidizer mixture is spatially stratified, the detonation strength is reduced [232, 237]. However, this may also reduce the blockage experienced by the injectors thereby increasing the time available for injection and

mixing. Consequently, the performance of the device cannot be easily determined and require some experimental or high-fidelity data to understand the injector response and mixing characteristics [52, 232, 257]. However, the range of scales involved as well as the extreme pressure and temperatures inside the system make extensive computational or experimental studies limited in scope.

In a general sense, a sparse set of experimental data, high-fidelity simulation data, and more inexpensive computational models will be available. In this regard, there exist reduced-order models [139, 156, 272] based on thermodynamics or simplified flow features. These approaches have been shown to predict performance metrics reasonably accurately but require expert tuning or calibration of an appreciable number of model parameters [139]. Most importantly, many of the model parameters cannot be directly extracted from experiments or simulations but have to be inferred through expert input based on other sources of data, such as detonation height or exit flow imaging.

To make the best use of such disparate information sources, some form of data fusion is necessary. The key question is how to combine such information to improve predictions of some well-defined quantities of interest, such as thrust as a function of operating conditions. In this regard, different approaches are feasible as shown in Fig. 6.1. Data from simulations/experiments could be used to calibrate model parameters, either deterministically (regression fitting) or statistically (Bayesian calibration). There are two challenges here. First, the data (pressure measurements, exit velocity, etc.) may not be sensitive to the choice of certain model parameters, which will result in poor calibration. In other words, a wide range of combinations of model parameters will be able to reproduce the data. Second, the calibration using data from certain operating conditions may not guarantee that the model is predictive at other operating conditions [34, 194, 207]. Hence, such calibration will not necessarily increase predictive accuracy and may not be universal in nature.

An alternative approach is the multi-fidelity method for constructing surrogate models that can predict performance characteristics [222]. Here, instead of calibrating the model parameters of the lower-fidelity reduced-order model to make it more accurate, the output of this model with nominal parameters is used along with experimental and detailed computational results to improve the predictive capability of a performance map.

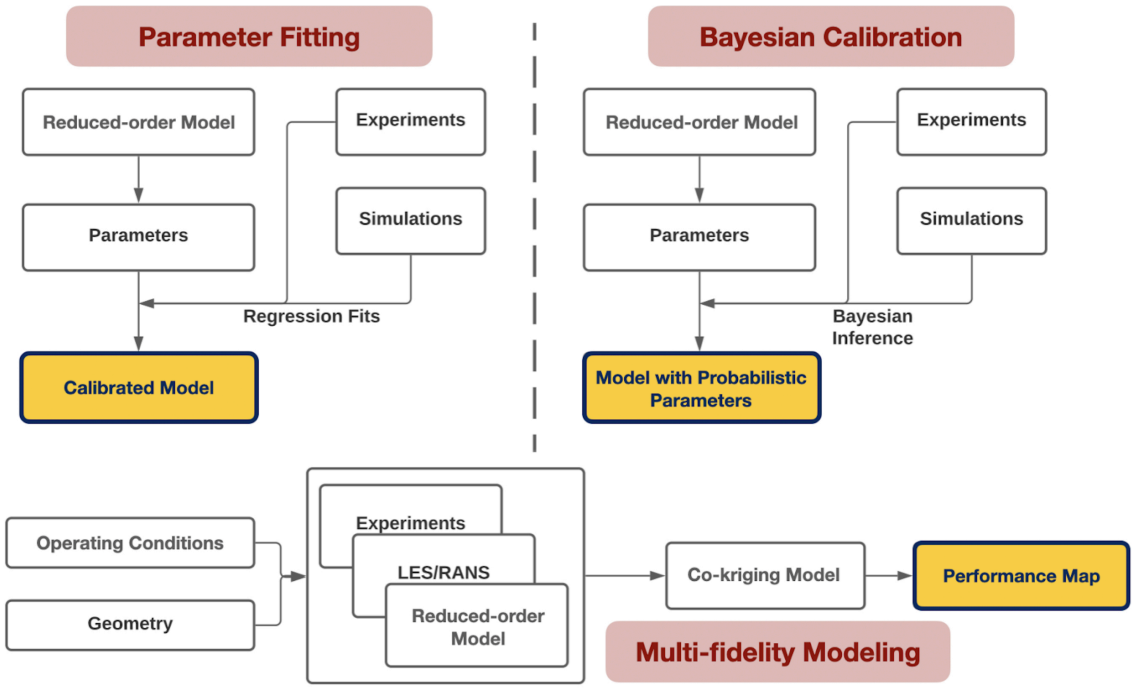

Figure 6.1: Outline of different approaches to predicting the performance of a combustion device: regression fitting, Bayesian calibration, and multi-fidelity modeling.

In summary, Fig. 6.1 shows the different approaches to predicting performance:

- Regression fitting or expert tuning: Here, model parameters are chosen to best reproduce experimental data, and such tuning is based on a small subset of the data. There is no guarantee that the model parameters can be used under other operating conditions.

- Bayesian calibration recasts the calibration problem as a statistical process, and the data is used to estimate the distribution of model parameters that can reproduce this data. Here, an initial estimate of the range of parameter values is used to generate an *a priori* distribution function, which is updated through the Bayes theorem using the experimental data. Here, the model parameters could be simultaneously varied, with the output being the *posteriori* distribution of model parameters. Once calibrated, the model can be estimated using parameter values that correspond to the mean of the distribution function (which is similar to the regression fitting procedure), or the distribution can be used to generate a spread of predictions, which reflect the uncertainty in model parameters.

- The multi-fidelity approach relates the predictions at different model levels into creating a single surrogate model constructed via recursive co-Kriging.

In multi-fidelity modeling, the function determination is recast as a machine learning problem through the method of Kriging [285]. The surrogate model is developed from co-Kriging [108, 147] of solutions from function evaluations of the numerical and experimental data sets, in combination with reduced-order models [36]. The reduced-order model, serving as the lowest fidelity informant, can span the parameter space more cost-efficiently. The co-Kriging architecture given in Ref. [147] describes an auto-regressive scheme for s-levels of fidelity in the output. The correction of Le Gratiet and Garnier [108] reorganizes the problem under the assumption that the design data sets have a nested structure. At each fidelity level t, the problem reduces to an ordinary Kriging problem. As a result, the recursive approach involves the inversion of s covariance matrices of size $n_t \times n_t$ rather than a single covariance matrix that scales with the levels of fidelity s. This multi-fidelity approach reduces the total number of numerical simulations needed by several orders of magnitude. Gaussian process approach is used to initially assign an uncertainty at each data point in the

surrogate model. Such uncertainties are estimated based on existing techniques for model errors [34, 195] and statistical errors [208, 289].

Machine learning-based surrogate modeling approaches have been demonstrated within fluid mechanics [31, 70, 155] effectively. In the present study, the computationally-efficient multi-fidelity modeling approach is extended to the performance prediction of rotating detonation engines. The goal here is to develop an integrated package that can be used to obtain performance metrics with uncertainty for a given set of design parameters. Here, the concept of multi-fidelity information fusion can be used to create a single response surface used for design purposes. Further, the solution prediction incorporates uncertainty quantification and provides metrics for gauging solution confidence. For this demonstration, a model RDE, the Air Force Research Laboratory (AFRL) representative 6-inch combustor [244] will be utilized, illustrated in Fig. 6.2 using data from high-fidelity numerical simulations. This configuration has been studied experimentally and numerically [56, 61, 255, 258]. As a result, multiple data sets across a range of operating conditions (mass flow rate and global equivalence ratio) are available for application in the multi-fidelity framework. In the current work, the prediction of device-specific thrust across a range of flow rates is constructed.

6.2 RDE Modeling Data Sources

In the proposed methodology, inexpensive reduced-order models will be used to "estimate" more expensive experimental and simulation data using the multi-fidelity modeling framework. The end goal is to estimate specific thrust as a function of air mass flow rate. For this purpose, three different data sources and models will be used. The experimental data is considered the highest-fidelity data source, and thrust data are treated as having a fixed measurement uncertainty. Detailed numerical simulations, which solve the compressible flow equations, will be considered medium-fidelity

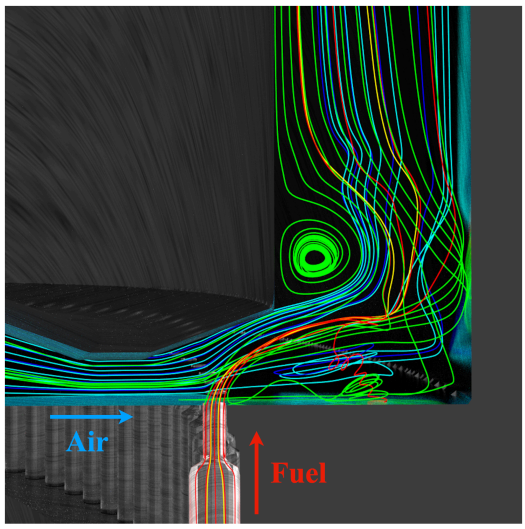

Figure 6.2: Injector configuration of the AFRL 6-inch diameter RDE with pathlines highlighting the mixing process from past numerical simulations. Adapted from Ref. [258].

data. Finally, the thermodynamic model for estimating thrust will be considered the reduced-physics lowest-fidelity model. Below, details of the experimental configuration, simulation methods, and the reduced-order model are described in more detail.

6.2.1 Experimental data

The AFRL 6-inch diameter RDE operated by hydrogen/air has been extensively studied [244, 245, 247]. The detonation chamber has an inner diameter of 138.7 mm, an outer diameter of 153.9 mm, and a combustion chamber width of 7.6 mm. The height of the annulus is 101.6 mm. The fuel and air streams are injected from separate plenums located upstream of the detonation chamber. The fuel enters the chamber through 120 discrete injectors with a diameter of 0.89 mm, whereas the air enters radially through a 123 mm diameter slot with a height of 1.78 mm. An illustration of the injection scheme is given in Fig. 6.3. A constant area combustion chamber open to the atmosphere is employed, with no exit nozzle constriction in

these studies. Further details of the experimental configuration and the measurement techniques can be found in Ref. [244]. The experimental campaign contains a large set of individual studies. There, the focus was on understanding the effect of mass flow rates on detonation structure, which is obtained by varying the total pressure of the fuel and air feed plenums upstream of the detonation chamber. The pressure is varied such that the overall mass flow rates correspond to a global equivalence ratio. The cases with an equivalence ratio of 1.0 and air injector area ratio of 0.2 are extracted for the one-dimensional multi-fidelity approach (corresponding to experimental cases 1.2.2, 2.2.2, 3.2.2, and 4.2.2 in Ref. [244]). In the two-dimensional extension, the cases also vary in equivalence ratio, ranging from approximately 0.8 to 1.3 (corresponding to experimental cases x.x.2 in Ref. [244]). The experimental data represents the highest-fidelity data source.

6.2.2 Detailed numerical simulations

Detailed simulations of RDE physics are applied to study the detonation wave behavior and the fuel and oxidizer injector dynamics within full-scale systems. These simulations serve as the medium-fidelity solutions in the multi-fidelity framework. The in-house compressible flow solver, UMReactingFlow, was employed to perform these simulations, with numerics similar to those described in Sec. 2.2 but without GPU-based acceleration of solver routines. In these numerical simulations, a hydrogen/air detailed chemical mechanism with 9 species and 19 reactions was applied [192].

The simulation domain is depicted in Fig. 6.3. The mesh is clustered in the near-injector and combustion chamber region to fully resolve fuel-air mixing and detonation processes. The mesh size is 200 micrometers from upstream of the fuel injector to throughout the detonation chamber. The resolution is relaxed to 400 micrometers in the upstream fuel and air feed plenums and progressively coarsened in the exhaust plenum to dissipate out any waves. A total of approximately 45 million

control volumes are present within the entire domain. In other investigations, it was found that additional refinement of the mesh did not change the macroscopic results significantly [258]. Further, non-ideal detonations in non-premixed practical systems lead to broader reaction zones, distributed along the azimuthal direction. The walls are represented adiabatically with a no-slip boundary condition. The inflow boundary is prescribed using a constant mass flow rate, with fluid properties interpolated from within the fluid domain similar to the simulations in Chaps. IV and V. Since the flow in the chamber is dominantly supersonic due to the detonation waves and the choked injectors, additional refinement is not given in the near-wall region.

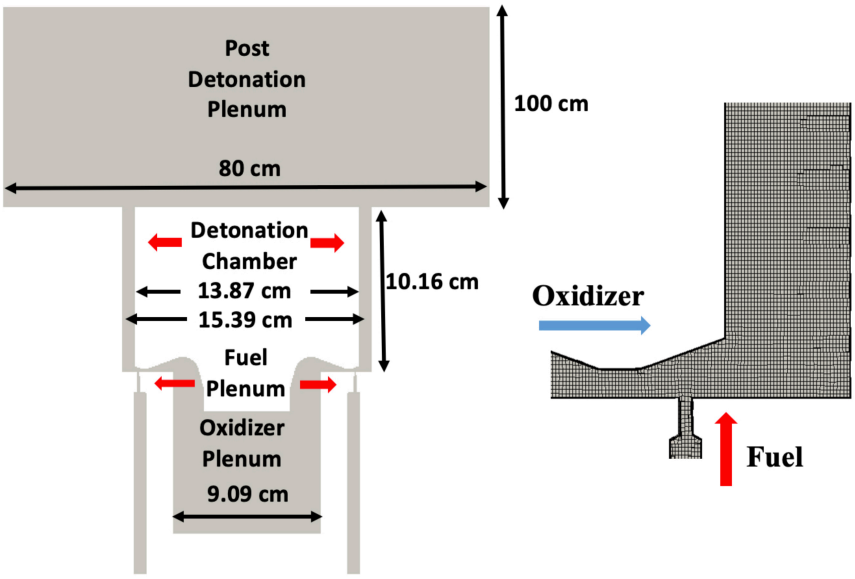

Figure 6.3: (Left) Computational geometry of the AFRL 6-inch diameter RDE with primary dimensions and (right) visualization of the computational mesh near the fuel injector and air inlet.

The simulation is run for approximately 15 detonation cycles to ensure statistical stationarity, after which data is collected for 10 cycles. Three different cases are used in the multi-fidelity modeling process, outlined in Tab. 6.1. The numerical cases 1, 2, and 3, correspond to cases 2.2.2, 3.2.2, and 4.2.2 in Ref. [244], respectively. The steady-state detonation wave structure for cases 1, 2, and 3 are depicted in Fig. 6.4.

Table 6.1: Details of the numerical simulations at the $\phi = 1.0$ condition, corresponding to cases 2.2.2, 3.2.2, and 4.2.2 in Ref. [244].

Case	**1**	**2**	**3**
$\boldsymbol{\phi}$	1.01	0.99	1.03
$\boldsymbol{P_{0,air}}$ **[kPa]**	266	509	705
$\boldsymbol{P_{0,fuel}}$ **[kPa]**	337	632	881
$\boldsymbol{\dot{m}_{air}}$ **[kg/s]**	0.32	0.62	0.83
$\boldsymbol{\dot{m}_{fuel}}$ **[g/s]**	9.5	18	25
Number of waves	1	2	2
Wave speed [m/s]	1884	1837	1877
Specific thrust [N-s/kg]	994	1229	1370
Specific impulse [s]	3486	4383	4803

6.2.3 Reduced-physics model formulation

RDEs are complex devices that require cost- and time-intensive experiments or simulations to be performed to accurately characterize their performance. Because of this, reduced-order models are attractive options when it comes to designing RDEs. These low-fidelity models use physics-based approximations to provide predictions to performance quantities of interest and are able to investigate a wide range of operating conditions due to the low cost of the model compared to full-scale RDE simulations or experimental trials.

A relevant thermodynamic model which will be used for the subsequent analysis in this paper was the reduced-order model developed by Kaemming et. al [139]. The model couples the reactant injection process with the thermodynamic processes within the chamber, focusing on the bifurcation of combustion modes (detonation and deflagration). This is performed through a balance of pressure and mass flow through the system. The model finds a chamber static pressure (denoted by $P_{3.2}$)

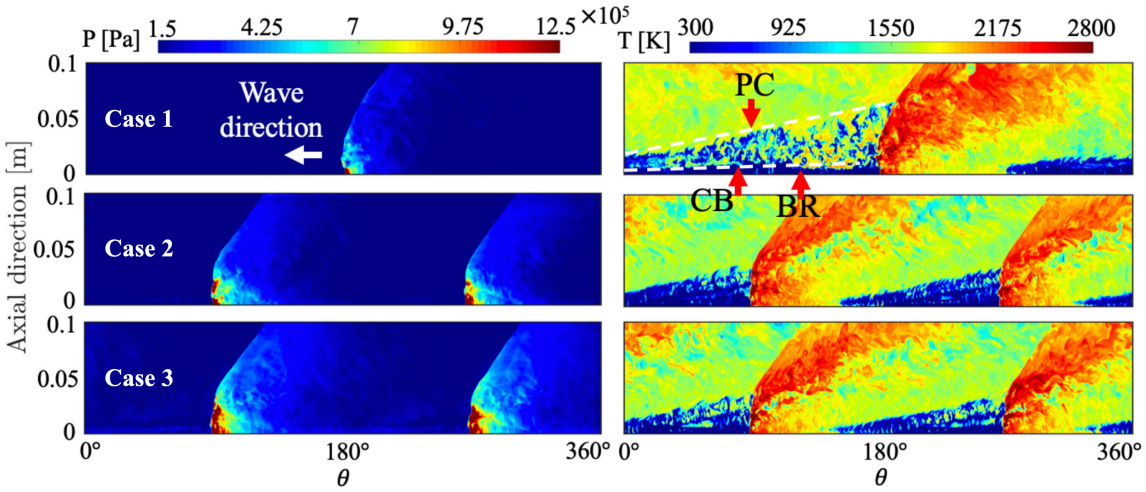

Figure 6.4: Unwrapped views of (left) pressure and (right) temperature at the mid-channel plane for (top row) case 1, (middle row) case 2, and (bottom row) case 3. The flow profiles show one, two, and two waves for cases 1, 2, and 3, respectively along with the fresh reactant buffer region (BR), contact burning (CB) surface, and parasitic combustion (PC) ahead of the wave.

such that mass conservation was enforced through the inlet and outlet of the RDE model. There are three main components: the inlet model, the thermodynamic cycle model, and the exit flow model. The inlet flow model computes the time-varying mass flow rate across the inlet for a given plenum stagnation pressure. Conversely, the exit flow model consists of computing an exit mass flow rate given the detonation pressure rise effects. The flow within the RDE was divided into three streams with their corresponding subscripts given in parentheses: detonation (a), detonation plus shock (b), and deflagration (c). The feed plenum conditions are named station 2, the pre-detonation mixed chamber condition is denoted station 3.2, the post-combustion states are at station 3.4, the post-shock compressed states are at station 3.6, and the exit conditions are given as station 8.

6.2.3.1 Inlet flow

An inlet flow model is used to determine the properties of the reactant gas and flow rates in the presence of a detonation wave within the chamber. The feed plenum conditions are fixed, and the flow is assumed to pass injectors with given flow performance characteristics. The injector flow rate is a time-varying function of the chamber pressure due to detonation. An empirical pressure decay rate of the chamber pressure was computed as:

$$\begin{aligned} \tau_{drop} &= \alpha/\tau_{factor} \\ k &= -ln(1-b)/\tau_{drop} \\ P_{3.4}(t)/P_{3.2} &= 1 + [(P_2/P_1)_{Det} - 1]e^{-kt} \end{aligned} \tag{6.1}$$

where α is an empirically-calibrated pressure drop factor of 0.00005, τ_{factor} is a pressure decay correction factor typically set to 1, b is the pressure drop of 80%, and $P_{3.2}$ is the chamber pressure estimate based on the inlet flow. The time-dependent detonation chamber pressure provides a time-dependent mass flow rate based on the mass flux equation given as:

$$\frac{\dot{w}(t)}{dA_{inj}} = C_w \frac{P_{t2}\sqrt{\gamma}}{\sqrt{RT_{t2}}} M_{inj}(t) \left(1 + \frac{\gamma - 1}{2} M_{inj}^2(t)\right)^{-(\gamma+1)/2(\gamma-1)} \tag{6.2}$$

where the C_w is the injector mass discharge coefficient and the time-dependency of the injection Mach number is defined by the feed system's total pressure to combustion chamber pressure ratio:

$$M_{inj}^2(t) = \frac{2}{\gamma - 1}\left[\left(\frac{P_{t2}}{P_{3.4}(t)}\right)^{(\gamma-1)/\gamma} - 1\right] \tag{6.3}$$

where M_{inj}^2 is limited to unity once the critical pressure ratio is achieved. Consequently, the reactant's axial flow velocity is defined as:

$$V_{refresh}(t) = \frac{\dot{w}(t)}{\rho A_{eff}} \tag{6.4}$$

where A_{eff} is the axial flow area of the combustor and ρ is the density of the mixed reactants due to the computed combustion chamber conditions. A portion of the reactants is consumed by deflagration based on the flame speed V_{flame} at chamber conditions. During the injector recovery process, the amount of deflagrated flow was given by:

$$\dot{w}_{deflag} = \int \dot{w}(t) \frac{V_{flame}}{V_{refresh}} dt \tag{6.5}$$

and the amount of inflow available for detonation is:

$$\dot{w}_{det} = \int \dot{w}(t) dt - \dot{w}_{deflag} \tag{6.6}$$

As a result, the effective equivalence ratio available for detonation (and consumed through deflagration) was computed. The height of the detonation wave was also computed based on the refresh and flame speeds as:

$$h_{det} = \int \left[V_{refresh}(t) - V_{flame} \right] dt \tag{6.7}$$

6.2.3.2 Thermodynamic cycle

Given the effective chamber pressure conditions from the inlet flow model, the combustion process was then computed. The model first calculated detonation properties using the ZND detonation model. Then, the post-detonation state 3.4a was computed and its total temperature was given by Eqn. 6.8:

$$T_{t3.4a} = T_{3.2}\left(\frac{T_2}{T_1}\right)_{Det} + \frac{1}{2C_p}(a_{3.4a}^2 - V_{Det}^2 + V_X^2) \tag{6.8}$$

where V_{Det} refers to the Chapman-Jouget wave speed and V_X represents the axial gas velocity within the combustor, induced by the expansion of gases from the injection scheme. The detonation plus shock stream conditions were computed via oblique shock relations where it was assumed that the turning angle was fixed as $\theta = 60^\circ$. Then, the post-shock conditions for this stream were given by the relations in Eqns. 6.9 and 6.10:

$$\frac{T_{3.6b}}{T_{3.4a}} = \frac{\left[2\gamma M_{3.4a}^2 sin^2(\theta) - (\gamma - 1)\right]\left[(\gamma - 1)\, M_{3.4a}^2 sin^2(\theta) + 2\right]}{(\gamma + 1)^2\, M_{3.4a}^2 sin^2(\theta)} \tag{6.9}$$

$$\frac{P_{3.6b}}{P_{3.4a}} = \frac{2\gamma M_{3.4a}^2 sin^2(\theta) - (\gamma - 1)}{\gamma + 1} \tag{6.10}$$

where $M_{3.4a} = \frac{V_{Det}}{a_{3.4a}}$. The deflagration stream was computed under the assumption of constant pressure combustion so that $P_{3.4c} = P_{3.2}$. This stream was then assumed to pass through a normal shock so that the post-shock properties were given as:

$$\frac{T_{3.6c}}{T_{3.4c}} = \frac{\left[2\gamma M_{3.4c}^2 - (\gamma - 1)\right]\left[(\gamma - 1)\, M_{3.4c}^2 + 2\right]}{(\gamma + 1)^2\, M_{3.4c}^2} \tag{6.11}$$

$$\frac{P_{3.6c}}{P_{3.4c}} = \frac{2\gamma M_{3.4c}^2 - (\gamma - 1)}{\gamma + 1} \tag{6.12}$$

$$T_{t3.6c} = T_{3.6c} + \frac{1}{2C_p}(V_{3.6c}^2 - V_{Det}^2 + V_X^2) \tag{6.13}$$

where $M_{3.4c} = \frac{V_{Det}}{a_{3.4c}}$ and the post-shock gas velocity, $V_{3.6c}$, was given as:

$$V_{3.6c}^2 = a_{3.6c}^2 M_{3.6c}^2 = a_{3.6c}^2 \left[\frac{(\gamma - 1)\, M_{3.4c}^2 + 2}{2\gamma M_{3.4c}^2 - (\gamma - 1)}\right] \tag{6.14}$$

The deflagrated flow was assumed to mix with the detonation and detonation plus shock streams. This mixed stream, denoted by state 3.6d, consisted of weighted averages of the three streams, and its thermodynamic properties are given by the relations in Eqns. 6.15 and 6.16:

$$h_{t3.6d} = Y_c h_{t3.6c} + (1 - Y_c)\left[(1 - Y_b)\, h_{t3.6a} + Y_b h_{t3.6b}\right] \tag{6.15}$$

$$\Delta s_{3.6d} = Y_c \Delta s_{3.6c} + (1 - Y_c)\left[(1 - Y_b)\, \Delta s_{3.6a} + Y_b \Delta s_{3.6b}\right] \tag{6.16}$$

where state 3.6a is identical to state 3.4a since the pure detonation stream does not experience any changes due to shocks. Y_c refers to the mass fraction of the mixed flow from the deflagrated stream and Y_b represents the fraction of the detonated flow which passes through the oblique shock.

The detonation, detonation plus shock, and mixed streams were then isentropically accelerated to the exit at station 8 to provide the exit state conditions which are used for calculating the exit mass flow rate.

6.2.3.3 Exit flow model

The exit flow model is based on the assumption that all streams are choked at the combustor exit. However, in choked conditions, the different exit streams have different properties and velocities. As a result, an exit flow distortion is computed as:

$$\delta = \frac{V_{8,max} - V_{8,min}}{V_{8,avg}} = \frac{V_{8,max} - V_{8,min}}{a_8} \tag{6.17}$$

where the minimum, maximum, and average axial velocities at the exit plane of the RDE are from the different streams. The choked flow assumption results in $V_{8,avg} = a_8$, the speed of sound. The linear variation of the Mach number at the exit flow is given in terms of the distortion:

$$M(x) = \delta x + (1 - \delta/2) \tag{6.18}$$

where x is the normalized circumferential distance within a single wave structure. As highlighted by Ref. [139], typical compound flow nozzles cannot be used for RDE flow streams due to their mixed subsonic and supersonic nature. As a result, mass and momentum correction factors can be computed assuming a distorted isentropic flow

relative to a uniform sonic flow. The mass flow correction factor is given as:

$$\frac{\dot{w}}{\dot{w}*} = \frac{\int_0^1 M(x)/((1+((\gamma-1)/2)M(x)^2)^{(\gamma+1)/2(\gamma-1)}dx}{((\gamma+1)/2)^{-(\gamma+1)/2(\gamma-1)}} \tag{6.19}$$

and the momentum correction factor:

$$\frac{w\dot{V}}{\dot{w}V*} = \frac{\int_0^1 M(x)^2/((1+((\gamma-1)/2)M(x)^2)^{\gamma/(\gamma-1)}dx}{((\gamma+1)/2)^{-\gamma/(\gamma-1)}} \tag{6.20}$$

The correction factors are applied to the computed exit mass flows and momentum. This mass flow rate is then compared to the one obtained via the inlet flow model, and $P_{3.2}$ is updated until convergence on the mass flow rates is found. A schematic of the model loop is provided in Figure 6.5. Correction factors for 1) the percentage of detonation flow processed by an oblique shock (state 3.6b), 2) the percentage of the deflagrated flow mixed with the detonated flow (state 3.6d), 3) amounts of non-axial momentum in the detonated and deflagrated flows, and 4) axial velocity distortion in the exit flow are inputs parameterized as functions of the ratio of the detonation height to the combustion chamber height. These correlations are obtained from Ref. [139]. The reader is encouraged to read Ref. [139] for complete details of model development and validation to experiments and computational data.

The aforementioned model was recreated for this analysis, based on the governing equations and assumptions from Ref. [139], but is not identical in the choice of the tunable model parameters. A nominal set of model parameters were used, and these were not extensively calibrated for the demonstration of multi-fidelity surrogate modeling. Thermodynamic state updates and chemical equilibrium calculations were performed using the open-source Cantera software package for chemistry [103] with a 9 species, 19 reaction hydrogen/air chemical kinetics model [192]. The detonation

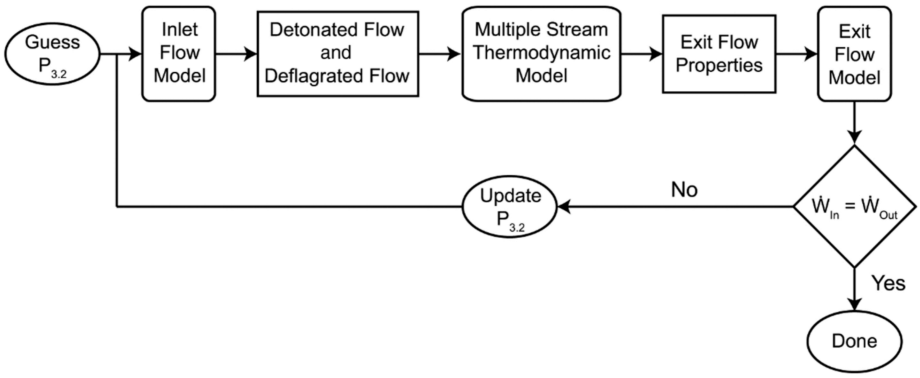

Figure 6.5: Schematic of iterative design loop used in the RDE reduced-order model. Image reproduced from Ref. [139].

properties are computed using the GALCIT Shock and Detonation Toolbox [47]. To validate the code, specific thrust and impulse values were obtained at a range of equivalence ratios and compared to data from [139]. The results are provided in Fig. 6.6. The results are in reasonable agreement with the experimental data as the general trends are captured, with the differences minimized at higher equivalence ratios. The discrepancies exist due to different parameters being used in the current model.

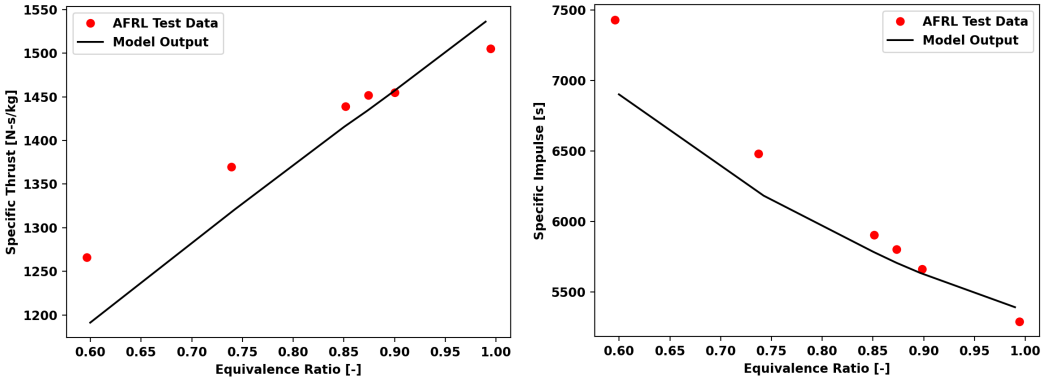

Figure 6.6: (Left) Specific thrust and (right) specific impulse versus equivalence ratio using the reduced-order model framework with comparisons to AFRL experimental data [139].

This concludes the discussion of the disparate information sources describing the operational characteristics of the AFRL 6-inch radial RDE. These data sources will be applied in the construction and demonstration of the multi-fidelity framework in

the next section.

6.3 Multi-fidelity Framework Description

In order to utilize the computationally efficient reduced-order model results in conjunction with the high-fidelity simulation data, a multi-fidelity modeling framework could be used. The purpose of the multi-fidelity model is to use information from the low-fidelity reduced-order model results to allow predictions to be made in the high-fidelity model where simulations or experiments were not conducted. One common example of constructing a multi-fidelity model in this manner is via the use of recursive Gaussian processes (GP) [108, 147]. This involves finding a constant correlation coefficient ρ such that:

$$f_t(x) = \rho f_{t-1}(x) + \delta_t(x) \tag{6.21}$$

where $f_t(x)$ and $f_{t-1}(x)$ are Gaussian processes modeling the data at fidelity levels (t) and $(t-1)$, respectively. The correlation coefficient ρ describes the correlation between the outputs of the two fidelity levels. This formulation implies the following relation between the two fidelity levels t and $(t-1)$:

$$cov\{f_t(x), f_{t-1}(x')|f_{t-1}(x)\} = 0, \forall x \neq x' \tag{6.22}$$

Statistically, Eqn. 6.22 implies that no additional information about $f_t(x)$ can be learned from $f_{t-1}(x')$ for any $x \neq x'$ [223].

An extension of the autoregressive Gaussian process framework can be formed by instead considering a nonlinear correlation coefficient such that:

$$f_t(x) = z_{t-1}(f_{t-1}(x)) + \delta_t(x) \tag{6.23}$$

where z_{t-1} is a function which maps the lower fidelity output $f_{t-1}(x)$ to the higher fidelity output $f_t(x)$. This framework was proposed in [223] and allows for more flexibility than the linear autoregressive scheme described above. Equation 6.23 can be recast in the following way:

$$f_t(x) = g_t(x, f_{*t-1}(x)) \tag{6.24}$$

where g_t is a Gaussian Process given as:

$$g_t \sim \mathcal{GP}(f_t|0, k_t((x, f_{*t-1}(x)), (x', f_{*t-1}(x')); \theta_t)) \tag{6.25}$$

The non-linear framework considers a covariance kernel for g_t which can be represented in the following way:

$$\begin{aligned} k_{t_g} &= k_{t_\rho}(x, x'; \theta_{t_\rho}) \cdot k_{t_f}(f_{*t-1}(x), f_{*t-1}(x'); \theta_{t_f}) \\ &+ k_{t_\delta}(x, x'; \theta_{t_\delta}) \end{aligned} \tag{6.26}$$

where k_{t_ρ}, k_{t_f}, and k_{t_δ} are covariance functions of the squared exponential form with $\{\theta_{t_\rho}, \theta_{t_f}, \theta_{t_\delta}\}$ being hyperparameters which are learned via maximum-likelihood estimation using the provided training data.

The flexibility of the non-linear framework makes it suitable for the purpose of

this study where the true functional form of the RDE performance metrics is high-dimensional and is not known. Thus, the non-linear framework from [223] was used to generate multi-fidelity predictions given low-fidelity results from the reduced-order model coupled with high-fidelity experimental data. Results from this framework are provided in the following section.

6.3.1 Validation of multi-fidelity algorithm

The non-linear multi-fidelity framework described in the previous section was implemented and applied against a few toy problems. First, the code was validated against the example from [223] where the low-fidelity model was given as $f_l(x) = sin(8\pi x)$, and the high-fidelity model was given as $f_h(x) = (x - \sqrt{2})f_l^2(x)$. Separate fits were generated using a standard Gaussian process and the non-linear multi-fidelity framework. Results for the standard Gaussian process and multi-fidelity fits are provided in Figs. 6.7 and 6.8, respectively.

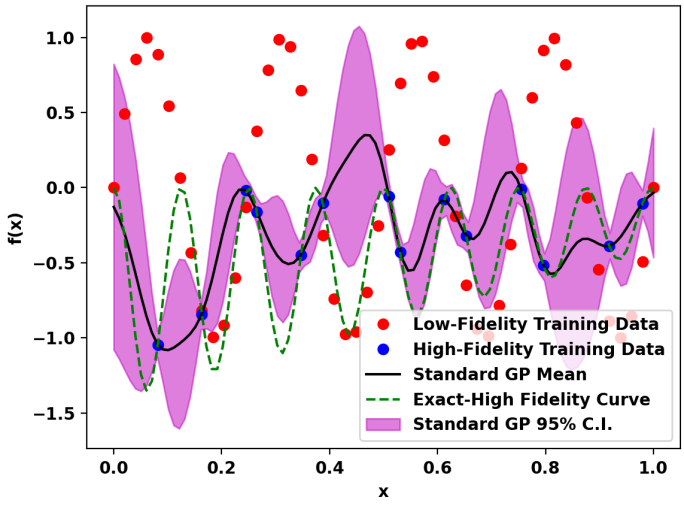

Figure 6.7: Obtained curve fit using standard Gaussian process on high-fidelity data using $f_l(x)$ and $f_h(x)$ from [223].

The results from Figs. 6.7 and 6.8 are consistent with those shown in Ref. [223], thereby validating the code. Additionally, the advantage of the multi-fidelity framework is apparent from these results since the obtained mean is nearly indistinguishable

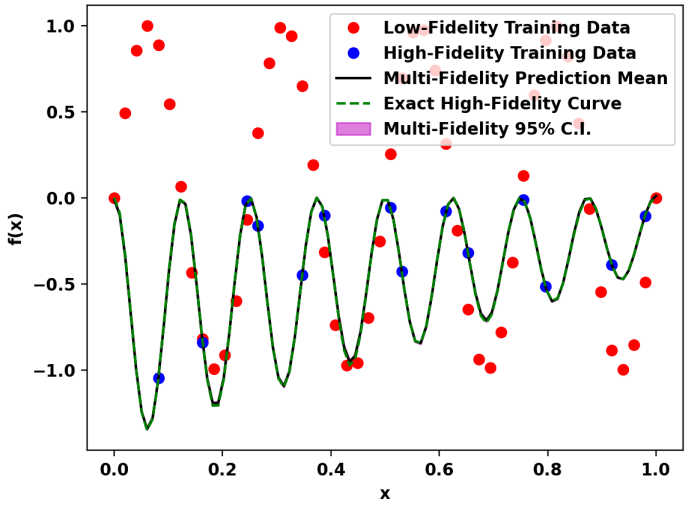

Figure 6.8: Obtained curve fit using multi-fidelity framework using $f_l(x)$ and $f_h(x)$ from [223].

from the exact high-fidelity curve, and the confidence in the prediction is much higher when compared to the results from the standard Gaussian process fit.

6.4 Multi-fidelity Performance Estimation Results

6.4.1 One-dimensional surrogate model

The non-linear multi-fidelity framework described in the previous section was implemented using the open-source GPy package and applied to the RDE framework to develop performance surrogate fits [107]. Specifically, the model was used to generate a multi-fidelity fit to estimate specific thrust as a function of mass flow rate data since thrust is a primary quantity of interest for characterizing RDE performance. To demonstrate the benefits of the multi-fidelity framework over a single-fidelity Gaussian Process, a sequence of fits was constructed using data from three fidelity levels. The low-fidelity data was represented by results using the reduced-order model described in Sec. 6.2.3. The medium-fidelity data was represented by numerical simulation data. Lastly, high-fidelity data was represented by experimental results from [244]. It was found that additional data points were needed in order to provide reasonable multi-

fidelity fits due to the sparsity of the high-fidelity data, so the experimental data was augmented with three linearly interpolated points. Results are provided in Fig. 6.9. As a pre-processing step, the input data was normalized by the ensemble minimum and maximum such that the data outputs are between 0 and 1. The final fit (mean and variance) was transformed back to the original operating space. Data from all information sources were initially applied a Gaussian noise of 10%, but it was found to have a minimal effect on the results and the confidence interval in combination with data normalization.

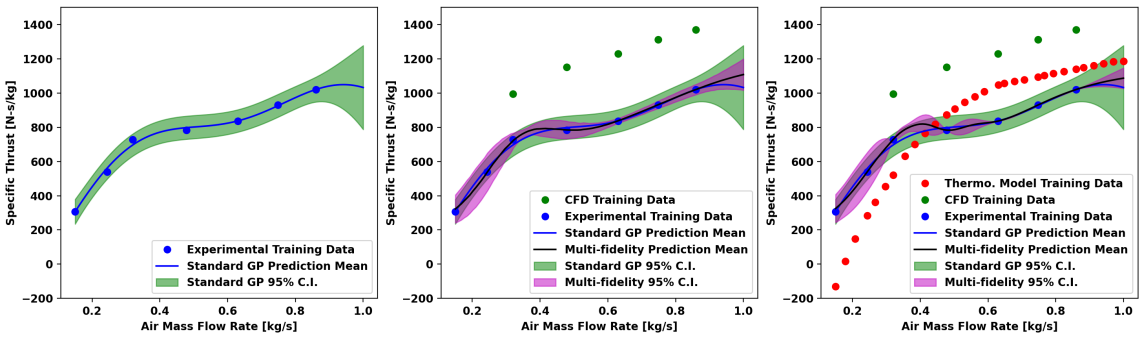

Figure 6.9: Comparison between specific thrust predictions generated (left) solely using a standard Gaussian process fit of high-fidelity data, (middle) a multi-fidelity fit using medium- and high-fidelity data, and (right) a multi-fidelity fit using low-, medium-, and high-fidelity data.

Figure 6.9 shows some interesting trends in the obtained thrust predictions. On the left plot of Fig. 6.9, the standard Gaussian process using high-fidelity experimental data is presented. The center plot of Fig. 6.9 shows the two-level fit using medium-fidelity numerical simulation data. Finally, the right plot of Fig. 6.9 provides the multi-level fit using the low-fidelity reduced-physics model along with the medium- and high-fidelity data sources. This progression illustrates the utility of the multi-fidelity framework in uncertainty reduction. Although the predicted mean profiles do not differ significantly for the different fits–biasing towards the highest fidelity data source available–the surrogate model possesses increasingly tight confidence intervals

as more data is incorporated into the fits. Further, the solution is very smooth, which is typically the result of fitting using a Gaussian process at each fidelity level.

In the multi-fidelity fit, there are features preserved from earlier fits, such as the inflection at low mass flow rates. The error at low mass flow rates is marginally increased in the multi-level fits as there is a lack of medium-fidelity data in this regime, and the reduced-physics model predicts non-physical negative thrusts–a limitation of the model when the bluff body exit of the RDE may not choked. Nevertheless, the multi-fidelity fit has a slightly narrower error interval than the two-level fit. At high mass flow rates above 0.86 kg/s, the surrogate model confidence interval becomes fairly narrow as the low-fidelity data is introduced. This demonstrates a feature of the multi-fidelity approach: the correlation between fidelity levels increases solution confidence in extrapolation regions, based on a correlation between the low- and high-fidelity data in regions where the two exist simultaneously. Within the mass flow rate range where all three data sets reside (between 0.4-0.86 kg/s, for instance) the confidence interval in the surrogate model is highly constrained.

Note that below a mass flow rate of 0.35 kg/s, device thrust increases sharply with mass flow, but the increase is more gradual at higher mass flow rates. One detonation wave was observed for the majority of the experimental conditions considered here. However, Ref. [244] notes that two detonation waves were generated at the highest mass flow rate of 0.86 kg/s. Prior numerical simulations [236, 256] have shown that as the mass flow rate is increased, the detonation wave strengthens leading to higher baseline pressure in the combustor as well as faster wave speeds. As a result, the thermal efficiency of the system increases, which is reflected in the rapid increase in thrust. However, past a critical flow rate, the wave structure does not change significantly, but secondary waves emanate from the primary detonation structure [237]. If the flow rate is increased further, these secondary waves will cause wave splitting, which will spawn weaker primary detonation waves. With further increase in mass

flow, this process is repeated. For the purpose of this study, the change in the thrust behavior due to wave dynamics is a physical feature that needs to be captured by the multi-fidelity fitting procedure.

The advantage of the multi-fidelity framework is that the model is able to use information from multiple data sources to improve predictions, even if the data sources have some inherent error and/or are not calibrated to the desired test case. Therefore, one can seed high-fidelity data (representing high confidence) with data from a low-cost, low-fidelity model (of lower confidence), and the multi-fidelity fit will produce predictions with reduced uncertainty due to the extra information provided by the low-fidelity model.

6.4.2 Two-dimensional surrogate model

The multi-fidelity framework could also be extended to multiple dimensions. To demonstrate this, a surrogate model for the specific thrust as a function of both air mass flow rate and equivalence ratio is generated with an air injector area ratio of 0.2. A two-level, two-dimensional multi-fidelity fit was constructed using the reduced-order model from Ref. [139] as the low-fidelity data and experimental results from [244] as the high-fidelity data. Again, it was found that additional data points were necessary for proper fits so the experimental data was augmented with three interpolated additional data points in air mass flow rate space for each equivalence ratio: 0.8, 1.0, and 1.3. Figs. 6.10-6.12 contain results comparing the two-level multivariate fit to a standard GP fit using the experimental campaign data.

As shown in Figs. 6.10 and 6.11, the generated mean prediction surfaces are fairly similar to one another and are able to closely predict the specific thrust outputs as desired. The multi-fidelity surrogate model captures more curvature in the response surface than the standard GP fit. Further, Fig. 6.12 shows that the uncertainty in the multi-fidelity predictions is reduced when compared to the standard GP fit which

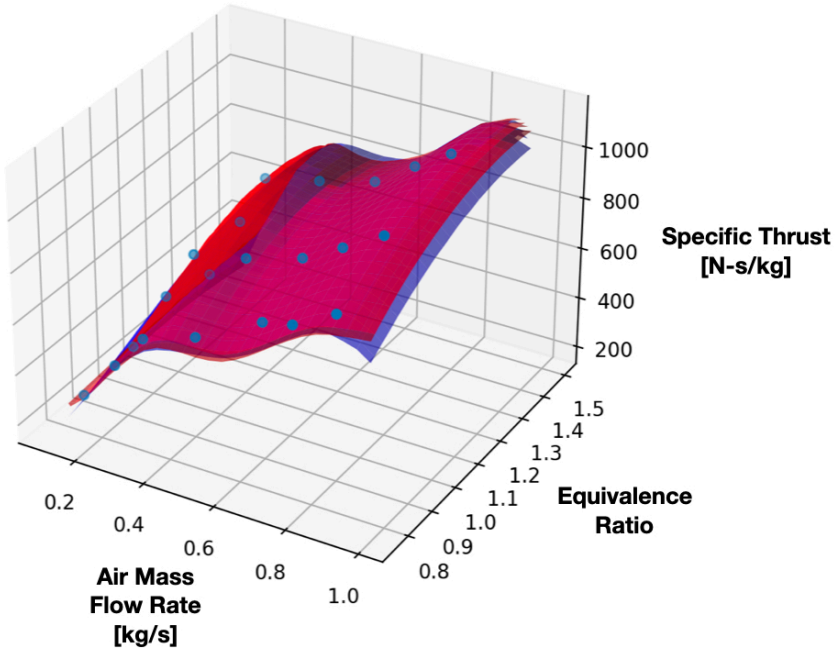

Figure 6.10: Isometric view of the response surface generated by the two-dimensional multi-fidelity fit (red) and standard GP fit (blue) as a function of air mass flow rate and equivalence ratio. The high-fidelity data is represented by the circular blue data points for context.

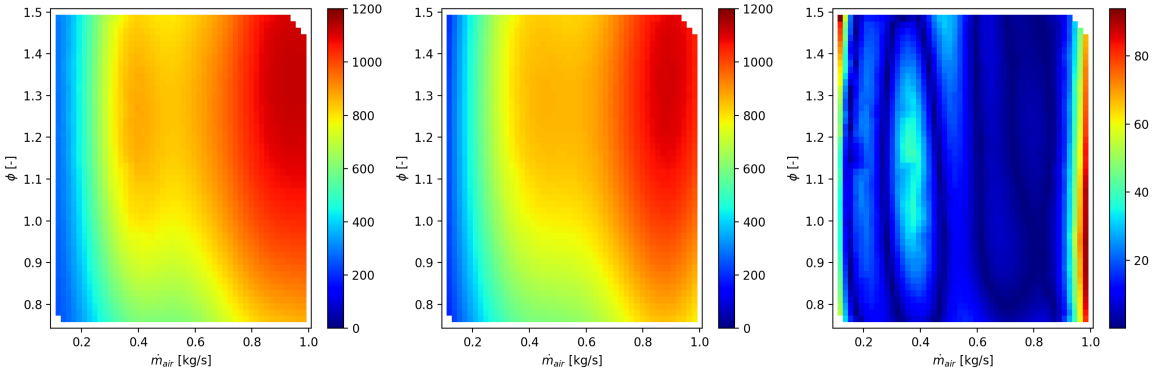

Figure 6.11: Two-dimensional contour plots of (left) the multi-fidelity prediction mean, (middle) standard GP prediction mean, and (right) absolute difference between the multi-fidelity and standard GP predictions. The color bar represents the specific thrust values in $\left[\frac{N-s}{kg}\right]$.

is consistent with the behavior seen for the one-dimensional fits. Likewise, the left plot in Fig. 6.12 shows that the uncertainty of the multi-fidelity fit shrinks near the high-fidelity data as desired. This again highlights how the multi-fidelity fit is able

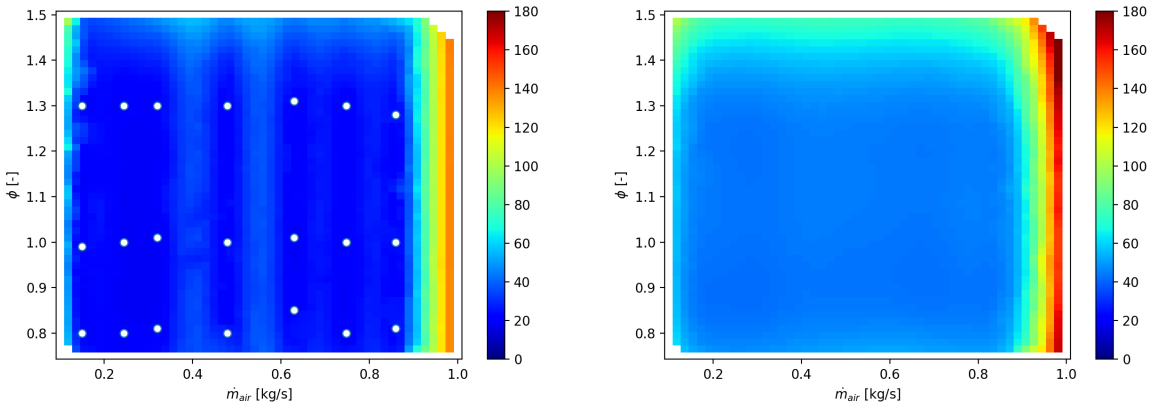

Figure 6.12: Two-dimensional contour plots of the 95% confidence interval half-width (1.96σ) of the (left) multi-fidelity prediction and (right) standard GP prediction. The color bar represents the specific thrust values in $\left[\frac{N-s}{kg}\right]$. The high-fidelity data is represented by the circular white data points in the left plot for context.

to use information from multiple data sources to increase confidence in predictions compared to a single-fidelity fit.

A part of the motivation of the multi-fidelity data fusion process is to inform researchers of where additional experiments or numerical simulations are needed to capture the dynamics of the data. Thus, additional higher fidelity points can be added in regions where the confidence interval in model predictions needs to be improved during an iterative design process. In a high-dimensional problem like RDE performance estimation, the true functional form of the performance map is unknown, and the quality of the fit is solely assessed through the width of the confidence interval. Of note, a typical hierarchical structure for the operating envelope spanned by the highest to lowest fidelity level is not strictly required in the multi-fidelity approach. While this structure is beneficial, in practical applications, the widest range in operating space is often encompassed by the lowest fidelity data source, and the operating range spanned by the high-fidelity data may not represent a subset of the medium-fidelity source (as is seen here).

6.5 Bayesian Calibration of the Reduced-Physics Model

This next section represents the Bayesian calibration of model parameters as an alternative approach to multi-fidelity modeling, as described in Fig. 6.1 and Sec. 6.1. In contrast to regression fitting, the calibration problem is recast as a statistical process, and high-fidelity data is used to estimate the distribution of model parameters that can reproduce this data (ground truth). Here, the hyper-parameters of the reduced-physics thermodynamics model of Ref. [139] are calibrated against the experimental campaign data of Ref. [244]. For brevity, this reduced-order model will henceforth be referred to as the Kaemming et al. model and the experimental campaign data set will be denoted the Rankin et al. data.

The Kaemming et al. model contains settings for the operational and geometric properties of the RDE. Additionally, several model parameters exist. Within the scope of this calibration, the primary tunable parameters will consist of 1) the percentage of detonated flow processed by the secondary shock Y_b, 2) the percentage of the deflagrated flow that is mixed with the detonated flow Y_c, 3) amount of non-axial momentum in the detonated flow ζ_{det}, 4) amount of non-axial momentum in all deflagrated flows ζ_{defl}, 5) forward flow coefficient of the air injector $C_{w,f,air}$, and 6) forward flow coefficient of the fuel injector $C_{w,f,fuel}$. On the other hand, other model parameters are set to nominal values: velocity distortion in the exit flow of 120%, detonation lateral relief of 1.2, detonation wave pressure decay time correction factor τ_{factor} of 1, oblique shock turning angle θ of 60°, nozzle stream thrust coefficient C_s of 0.9, and a bluff body exit nozzle coefficient of $C_{w,8}$ of 0.985. Hence, the model features a set of $N_{param} = 6$ model parameters given as $\psi = \{Y_b, Y_c, \zeta_{det}, \zeta_{defl}, C_{w,f,air}, C_{w,f,fuel}\}$. The primary parameters defining the operating condition are the air mass flow rate $\dot{m}_{air}$ and the equivalence ratio ϕ. The objective of the model is to predict the quantities of interest (QoI): air plenum pressure $P_{2,air}$, fuel plenum pressure $P_{2,fuel}$, and specific thrust $F_N/\dot{m}_{air}$.

The Rankin et al. experimental data set spans multiple air injector area ratios ($A_{air}/A_{ch} = \{0.1, 0.2, 0.39\}$), air mass flow rates ($\dot{m}_{air} = \{0.15, 0.32, 0.63, 0.86\}$ kg/s), and equivalence ratios ($\phi \approx \{0.8, 1.0, 1.3\}$). To ensure that the model's assumptions are valid across the calibration data set, the experimental data set is restricted to the air mass flow rates of 0.32 kg/s and above. Furthermore, Rankin et al. observed that two propagating detonation waves exist at the air mass flow rate of 0.86 kg/s and equivalence ratios of stoichiometry and above. However, due to the sparsity in experimental data and possible hysteresis effects in the wave splitting phenomenon, the highest mass flow rate condition is also removed. Thus, the experimental data set used for calibration consists of air mass flow rates of 0.32 kg/s and 0.63 kg/s only.

Prior to the description and application of the Bayesian approach, the current representation of the Kaemming et al. is described. In order to sample the Kaemming et al. model a large number of times ($> \mathcal{O}(10^6)$ evaluations), the model evaluation must be optimized for this application and its associated computational cost reduced.

6.5.1 Surrogate for the reduced-physics model

The computational cost associated with each evaluation of the current implementation of the Kaemming et al. model (with Cantera and the Shock and Detonation Toolbox) is intractable for a large number of evaluations. Thus, an artificial neural network (ANN) surrogate model for the Kaemming et al. reduced-physics model is trained. The neural network approach learns a set of weights and biases and as a series of matrix computations, offers fast evaluation times. As seen in Fig. 6.10, the specific thrust response surface through experimental and model data is fairly smooth. Thus, the reduced-order model may be a good candidate for replacement with an ANN.

To represent a surrogate for the full Kaemming et al. model, the ANN features eight inputs: six hyper-parameters described by ψ, $\dot{m}_{air}$, and ϕ. The three outputs are

the QoI: $P_{2,air}$, $P_{2,fuel}$, and $F_N/\dot{m}_{air}$. The development of an optimal ANN architecture is not within the scope of this work and is an active area of research. A simple feedforward ANN is employed here, with four hidden layers each with $\{8, 10, 7, 5\}$ neurons. The hyperbolic tangent sigmoid function is used for the hidden layer activations. The Levenberg-Marquardt backpropagation algorithm was used for parameter optimization [111, 178]. The full ANN architecture is depicted in Fig. 6.13.

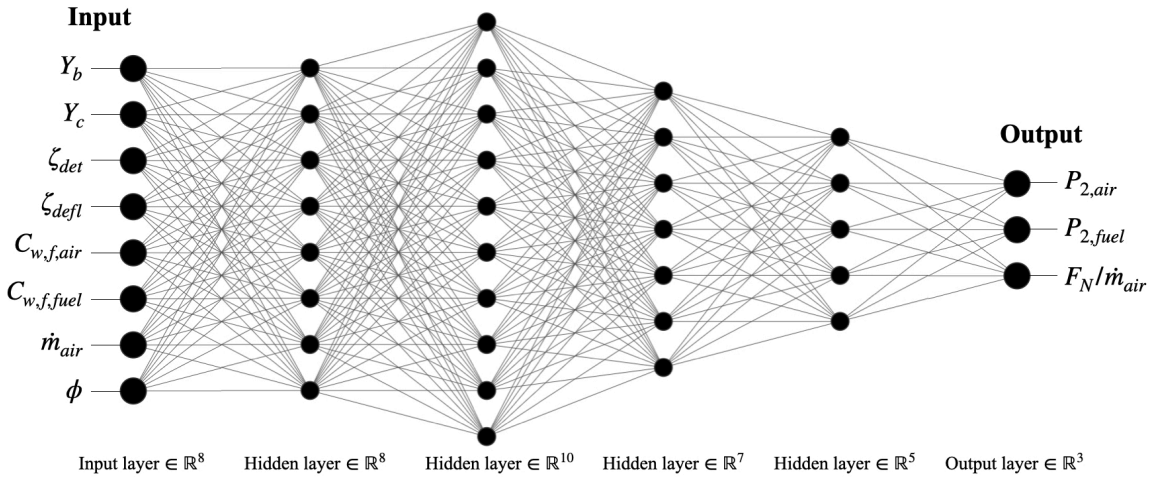

Figure 6.13: Illustration of the ANN architecture as a surrogate for the Kaemming et al. model, where the inputs consist of the six hyper-parameters $\psi = \{Y_b, Y_c, \zeta_{det}, \zeta_{defl}, C_{w,f,air}, C_{w,f,fuel}\}$, $\dot{m}_{air}$, and ϕ, and the outputs are the QoI: $P_{2,air}$, $P_{2,fuel}$, and $F_N/\dot{m}_{air}$.

Three ANNs are trained, one for each air injector area ratio because the response surface of each air injector area ratio may be sufficiently distinct. A data set of approximately 120,000 samples are generated for each area ratio, where the model parameters are randomly selected from a uniform distribution with a minimum and maximum given in Tab. 6.2. Similarly, the equivalence ratio is selected from a uniform distribution with range $\{0.75, 1.4\}$ to allow for some variation in the queried equivalence ratio range of $\{0.8, 1.35\}$. The air mass flow rate is selected from a uniform distribution as well, and the range varies based on the air injector area ratio. For an area ratio of 0.1, a range of $\{0.1, 0.37\}$ kg/s is selected, while for area ratios of 0.2 and

0.39 utilize a range of $\{0.1, 0.68\}$ kg/s (again, with some buffer to allow for variation in queried mass flow rate). These bounds in air mass flow rate are selected such that the full set of data (with one propagating detonation wave) from the Rankin et al. experimental campaign can be represented through the ANN surrogate model. The neural networks are implemented with the MATLAB Deep Learning Toolbox [294]. Here, the samples were randomly shuffled with 60% used for training, 20% set aside for validation to monitor overfitting, and 20% extracted for testing. All inputs and outputs were normalized between -1 and 1 before training. The results of the training procedure are shown in Fig. 6.14. Here, the validation set converges to a stable MSE within 400 epochs for each ANN, and the values are of a similar order for the ANNs for area ratios of 0.2 and 0.39. Further, the comparison of the testing set predictions versus ground truth shows correlation R-values of nearly 1. The ANN trained on the lowest area ratio of $A_{air}/A_{ch} = 0.1$ exhibits the lowest correlation, as it also featured the largest converged MSE. Thus, the low area ratio case features dynamics that are more difficult to capture.

Due to a direct correlation between the mass flow rate/equivalence ratio and the fuel/air plenum pressures, the ANNs are able to predict these QoI ($P_{2,air}$ and $P_{2,fuel}$) very closely in comparison to the original Kaemming et al. model and as a result, not shown here. However, increased errors are observed in the prediction of the specific thrust. In order to quantify the errors in specific thrust prediction imposed by the ANN, the error is mapped in air mass flow rate and equivalence ratio space. The error profile in specific thrust is shown in Fig. 6.15. These percent errors are averaged across all data points in the testing data set for each area ratio. The percentage error profiles show reasonable results, with the greatest error observed in the ANN trained for $A_{air}/A_{ch} = 0.1$, as expected based on previous results. However, it must be noted that the greatest errors are seen at air mass flow rates between the discrete values tested in the Rankin et al. experimental campaign (for one detonation wave:

Table 6.2: Kaemming et al. [139] model parameters to be calibrated: $N_{param} = 6$; Gaussian prior assumed mean and standard deviation.

Model parameter	**Description**	**Min.**	**Max.**	$\boldsymbol{\mu}$	$\boldsymbol{\sigma}$ **(% of** $\boldsymbol{\mu}$**)**
$\boldsymbol{Y_b}$	% of detonated flow processed by the secondary shock	0	1	0.5	0.15 (30%)
$\boldsymbol{Y_c}$	% of the deflagrated flow that is mixed with the detonated flow	0	1	0.5	0.15 (30%)
$\boldsymbol{\zeta_{det}}$	amount of non-axial momentum in the detonated flow	0	0.5	0.25	0.075 (30%)
$\boldsymbol{\zeta_{defl}}$	amount of non-axial momentum in all deflagrated flows	0	0.5	0.25	0.075 (30%)
$\boldsymbol{C_{w,f,air}}$	air injector forward flow coefficient	0.5	1.2	0.85	0.1062 (12.5%)
$\boldsymbol{C_{w,f,fuel}}$	fuel injector forward flow coefficient	0.5	1.2	0.85	0.1062 (12.5%)

$\dot{m}_{air} = \{0.15, 0.32, 0.63\}$ kg/s). The error is reduced for these discrete air mass flow rates of interest, with errors with 5% for the $A_{air}/A_{ch} = 0.1$ ANN and within 2% for the $A_{air}/A_{ch} = 0.2$ and $A_{air}/A_{ch} = 0.39$ ANNs. These error maps for each ANN will be later applied as model errors in the Bayesian optimization framework. This

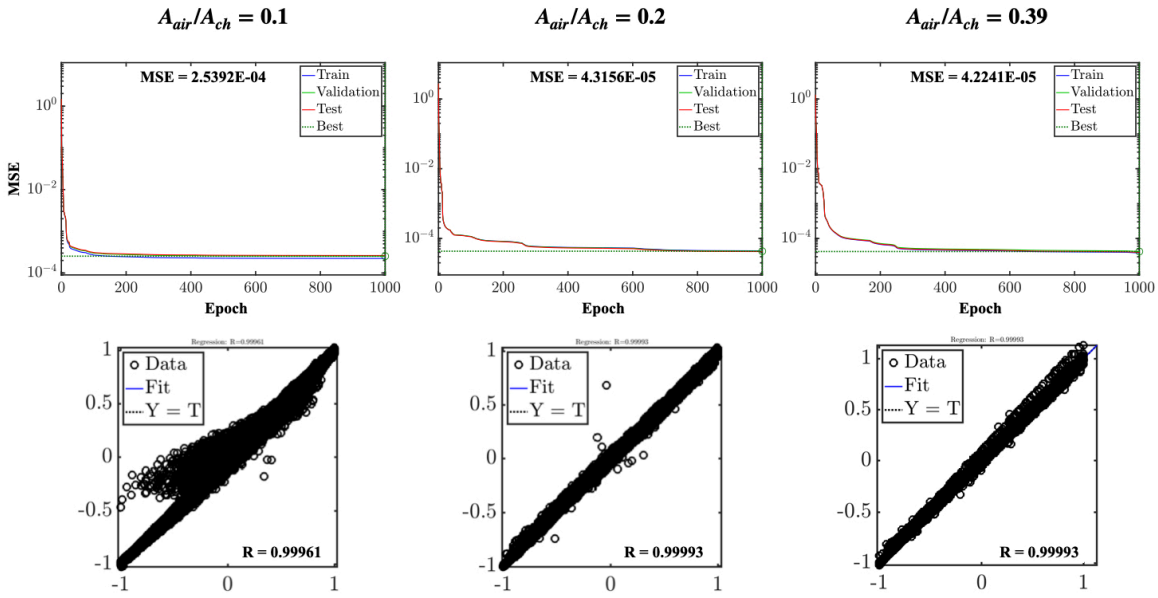

Figure 6.14: (Top row) Convergence of mean-squared error (MSE) for each ANN with the training, validation, and testing data sets as a function of epoch with the best validation MSE quantified within the plots. (Bottom row) Scatter plots showing the predictions on the y-axis versus the ground truth on the x-axis using the testing data set for each ANN, with the regression R-value quantified within the plots. The left column represents the ANN for $A_{air}/A_{ch} = 0.1$, middle column represents the ANN for $A_{air}/A_{ch} = 0.2$, and the right column represents the ANN for $A_{air}/A_{ch} = 0.39$.

concludes the discussion of the development of the ANN-based surrogate model. The ANN surrogate model offers 3-4 orders of magnitude speed-up in time to solution compared to the original Kaemming et al. model. As a result, the trade-offs in prediction error are acceptable in exchange for the model evaluation speed-up vital to the Bayesian optimization process, and the model error is accounted for during optimization.

6.5.2 Bayesian inference

With the ANN-based surrogate model of the Kaemming et al. reduced-physics model, the model's parameters will be calibrated to estimate the QoI across the range of mass flow rates and equivalence ratios given in the Rankin et al. experimental data

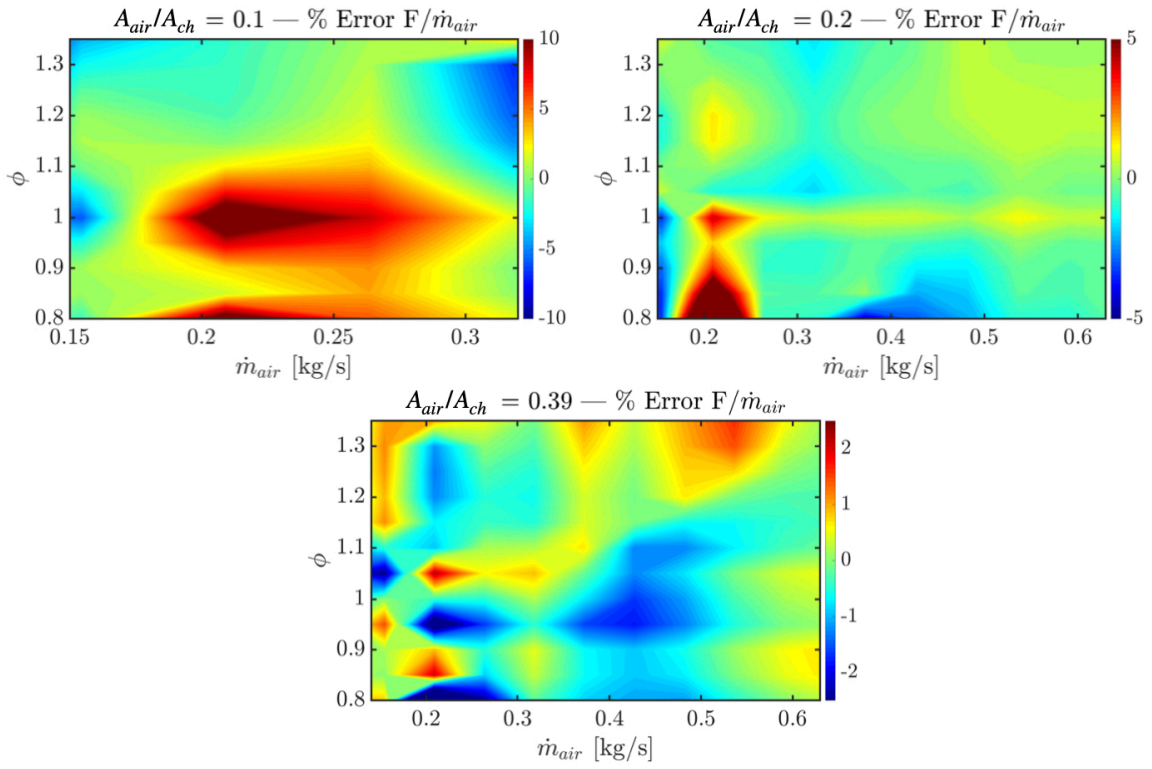

Figure 6.15: Average percent error map in specific thrust between the ANN prediction and the original Kaemming et al. model computed across the testing data set for (top left) $A_{air}/A_{ch} = 0.1$ ANN, (top right) $A_{air}/A_{ch} = 0.2$ ANN, and (bottom center) $A_{air}/A_{ch} = 0.39$ ANN. The color bars represent percentage errors.

set. For a given set of operating conditions χ and model parameters ψ, the model output provides the QoI as $\mathcal{G}(\psi, \chi) = \{P_{2,air}, P_{2,fuel}, F_N/\dot{m}_{air}\}_{\mathcal{G}}$ and similarly, the corresponding experimental data is given by $\mathcal{D}(\chi) = \{P_{2,air}, P_{2,fuel}, F_N/\dot{m}_{air}\}_{\mathcal{D}}$. In essence, the calibration process is an optimization problem that seeks to minimize the following error function:

$$E_{\{\psi,\chi\}} = \sum_{\chi} ||\mathcal{G}(\psi, \chi) - \mathcal{D}(\chi)|| \tag{6.27}$$

over different solution vectors for ψ. However, it must be noted that the solution vector ψ is not constant for the set of operating conditions. Additionally, it would be beneficial to elucidate the correlations between the different model parameters and

their relative importance in the model output. For these reasons, the computationally efficient Bayesian optimization procedure is used here over a more complex and costly regression analysis method. Since the objective function $f(\psi, \chi)$ which prescribes the relationship between the operating conditions χ and model parameters ψ and the QoI is unknown, the Bayesian approach treats the solution vector of model parameters as random variables and places a prior joint-distribution over the parameter set. Determination of the unknown function $f(\psi, \chi)$ is difficult to perform due to its computational cost which scales with the degrees of freedom. The objective function f is assumed to be continuous over the operational space and takes some unknown form. The prior joint-distribution is ascribed to capture assumptions or beliefs about the model parameters. With model evaluations, the prior is updated to form the posterior distribution of model parameters. Through a sequential process, the posterior distribution defines the acquisition function that determines the next query point in parameter space. The Bayesian optimization process is an area of active research and has been extensively detailed in several publications [34, 89, 101, 193, 198, 209]. Furthermore, the approach was successfully applied by Fiévet et al. to a one-dimensional model for the pseudoshock characteristics of a scramjet isolator and demonstrated improved ability in capturing the QoI in comparison to a genetic algorithm approach [84].

Bayesian inference is a statistical inference method that provides a distribution of random variables, i.e., through probability distribution functions (PDFs), instead of a single expectation value for all the model parameters. As more data is added, the optimization is recursively improved using the previous joint distribution of parameters as the initial guess. In the end, the posterior distribution of model parameters captures both the model and measurement uncertainties and incorporates all the information contained by the data and models and their respective uncertainties. Specifically, the Bayesian inference approach determines the posterior distribution of the set of model parameters conditioned on experimental data. Recalling the previous definitions, for

a model output $\mathcal{G}(\psi, \chi)$ given set of operating conditions χ and model parameters ψ, the relation between the experimental data $\mathcal{D}(\chi)$ and the model is given as:

$$\mathcal{D}(\chi) = \mathcal{G}(\psi, \chi) + \epsilon \tag{6.28}$$

where the error term ϵ encapsulates both the uncertainty in the model and the measurement uncertainties of the experimental data. In the present study, due to the use of the ANN-based surrogate for the Kaemming et al. model, the model error is computed as a function of χ using the specific thrust error response shown in Fig. 6.15 and with error maps for the air and fuel plenum pressures. Additionally, the measurement error is added to form the error term. The measurement component of the error is assumed to be a normally distributed random variable with a nominally fixed standard deviation of 1% for the mass flow rates of air and fuel, 2% for the equivalence ratio, 1% for the pressure measurements, and 5% for the specific thrust measurements from Ref. [244]. The Bayesian inference procedure is summarized by the evaluation of Bayes' theorem through three discrete steps:

1. Construct the prior joint-distribution for all N_{param} model parameters ψ assuming a Gaussian distribution for each parameter based on existing knowledge. This results in a density function $\Omega(\psi)$.

2. Compute the likelihood function that determines the probability that a given set of model parameters ψ sampled from the prior distribution describes the experimental data $\mathcal{D}$. This distribution function is denoted $\Omega(\mathcal{D}|\psi)$.

3. Determine the posterior conditional distribution $\Omega(\psi|\mathcal{D})$ through Bayes' theorem:

$$\Omega(\psi|\mathcal{D}) = \frac{\Omega(\mathcal{D}|\psi)\Omega(\psi)}{\Omega(\mathcal{D})} \tag{6.29}$$

The posterior distribution has a few key features [84]. The maximum a poste-

riori (MAP) represents the most probable solution and is indicative of both the likelihood and the accuracy. The mean of the posterior minimizes the squared error computed from the maximum-likelihood estimate (MLE), whereas the median minimizes the absolute error. If a uniform random distribution is used to represent the prior, the MAP is equivalent to the MLE, whereas they are distinct when the priors are Gaussian.

There exist many approaches to defining the prior distribution of model parameters and the likelihood function [25, 145]. In the present study, the prior distribution is assumed to be Gaussian in form, and the likelihood function is similarly based on a Gaussian function [34, 209, 314] due to the assumed distribution of the error term ϵ.

6.5.2.1 Selection of prior joint-distribution

The prior distribution of parameters must be selected so as to not bias the posterior. As given by Bayes' theorem, the posterior distribution is a product of the prior distribution and the likelihood function. Consequently, a prior with a narrower width than anticipated will artificially limit the support of the posterior. In the present study, the prior PDF is assumed to be Gaussian with the mean and standard deviation determined from authors' assumptions of nominal values, as given in Tab. 6.2. The parameters are assumed to be randomly distributed and independent, without any assumed cross-correlation between the parameters ($\rho = 0$). As a result, the prior joint-distribution is an N_{param}-dimensional jointly Gaussian distribution that is simply the product of the individual Gaussian distributions. The standard deviations are set to be sufficiently large so as to not limit support of the prior. Fiévet and co-workers determined that additionally increasing the standard deviation by a factor of two did not affect the MAP or the optimization procedure significantly [84]. Further, it must be noted that the model parameters of the Kaemming model related to the combustion process are constrained from 0 and 1 for physical relevancy, while

the flow coefficients can exceed 1 (up to 1.2). As a result, the Gaussian distributions are trimmed to enforce this constraint. The marginal prior PDFs of the model parameters are shown in Fig. 6.16. As described earlier, the calibration is performed for corresponding experimental cases where the exit flow is choked and a positive specific thrust value is computed, i.e., experimental cases with an air mass flow rate greater than a critical value of approximately 0.25 kg/s. Figures 6.17, 6.18, and 6.19 outline the model predictions $\mathcal{G}(\Omega(\psi))$ for the QoI with model parameters sampled from the prior distribution $\Omega(\psi)$ for the 15 experimental cases where positive specific thrust is predicted. The model predictions for specific thrust do not capture the QoI well in any of the cases and the experimental data is often well outside one standard deviation from the model prediction mean. The predictions for plenum pressure more closely match the experimental values, but the true values are still generally outside one standard deviation from the model prediction mean. The goal of the calibration process is to constrain and adjust the PDF, given the experimental data on net thrust and plenum pressure alongside the inlet blockage ratio and discharge coefficients.

6.5.2.2 Likelihood function and maximum likelihood estimate

The likelihood function is used to determine the probability that a model parameter solution vector ψ yields a model output $\mathcal{G}(\psi, \chi)$ at the given operating conditions χ that predicts the experimental data $\mathcal{D}(\chi)$ within the error margins. This function effectively models the distribution function for the error term ϵ that accounts for both the model and measurement uncertainties. The experimental data is incorporated in the likelihood function as a vector of model outputs $\mathcal{D}(\chi) = \{P_{2,air}, P_{2,fuel}, F_N/\dot{m}_{air}\}$ with standard deviations $\sigma(\chi) = \{\sigma_{P_{2,air}}, \sigma_{P_{2,fuel}}, \sigma_{F_N/\dot{m}_{air}}\}$. To this end, the likelihood density function for ψ assumes a Gaussian form [34, 209, 314] and is computed as:

$$\Omega(\mathcal{D}|\psi) = \prod_{\chi=1}^{\beta} \prod_{i=1}^{\theta} \frac{1}{\sqrt{2\pi}\sigma_i(\chi)} \exp\left(- \frac{\big(\mathcal{D}_i(\chi) - \mathcal{G}_i(\psi, \chi)\big)^2}{2\sigma_i^2(\chi)} \right) \tag{6.30}$$

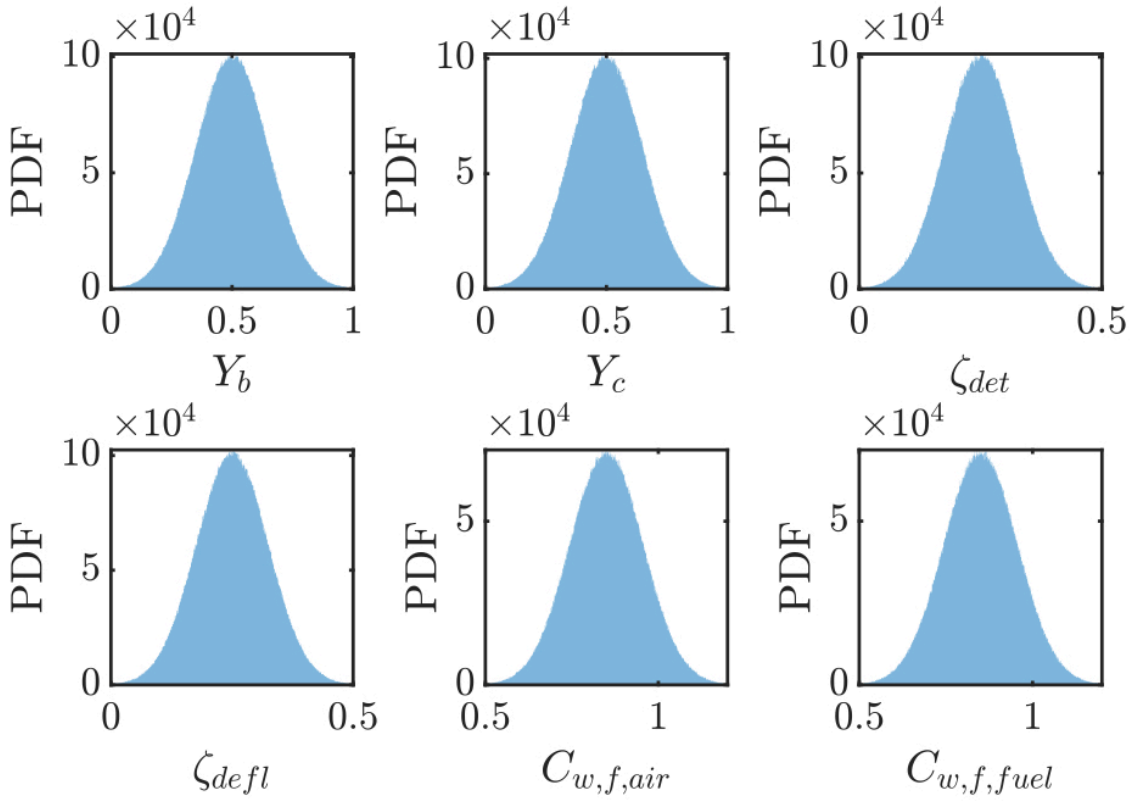

Figure 6.16: Gaussian prior distributions of the Kaemming et al. ANN surrogate model to be calibrated with $N_{param} = 6$.

and the corresponding log-likelihood is given as:

$$\log\left(\Omega(\mathcal{D}|\psi)\right) = \sum_{\chi=1}^{\beta}\sum_{i=1}^{\theta} -\log\left(\sigma_i(\chi)\right) - \frac{1}{2}\log(2\pi) - \frac{\left(\mathcal{D}_i(\chi) - \mathcal{G}_i(\psi,\chi)\right)^2}{2\sigma_i^2(\chi)} \tag{6.31}$$

where β is the number of experimental cases and θ represents the number of QoI. The standard deviations in the likelihood function are a summation of the experimental measurement uncertainties and the ANN surrogate model errors in the present study.

6.5.2.3 Evaluation of the posterior distribution

In the evaluation of the posterior, if the difference between the experimental data and model outputs $\mathcal{D}_i(\chi) - \mathcal{G}_i(\psi,\chi)$ is a linear function of the model parameter vector ψ, the joint-likelihood function has a Gaussian form and the joint-posterior

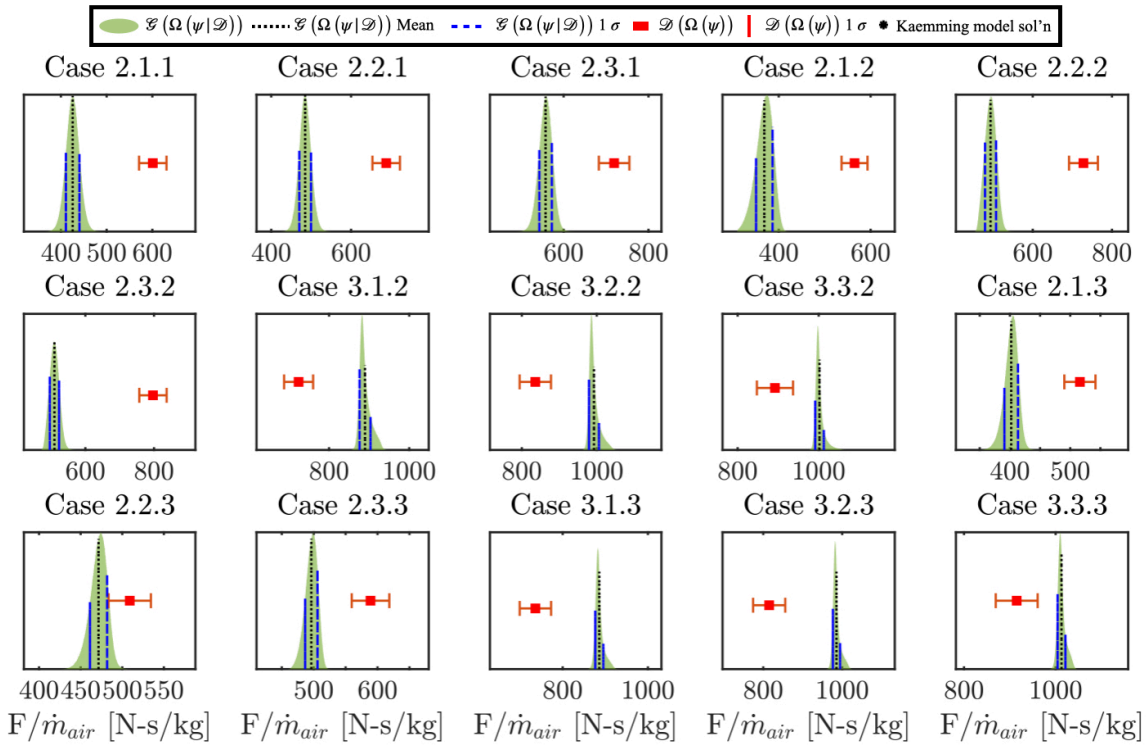

Figure 6.17: PDF of model predictions of specific thrust using the model prior distributions for the 15 experimental cases from Ref. [244] above the critical air mass flow rate of ~0.25 kg/s.

distribution is simply the product of the joint-prior and joint-likelihood distributions, as described earlier. However, in the present study, the model is a highly non-linear function of the model parameters ψ and the effect of the parameters on the outputs is not clearly discernible. For this reason, the posterior distribution is computed using a Markov chain Monte Carlo (MCMC) method [34, 296]. Specifically, the Goodman and Weare affine-invariant MCMC sampling procedure [102] is employed, which has been implemented in the open-source GWMCMC package of Grinstead [110]. The primary selections in the MCMC sampling procedure are the number of Markov chains, N_{chain}, and the number of samples per Markov chain, N_{sample}. In the present study with $N_{param} = 6$, 1024 independent Markov chains ($N_{chain} = 1024$) with 20,480 elements each ($N_{sample} = 20480$) are used. The model evaluations during the MCMC sampling procedure were executed in parallel over 128 cores to accelerate the execution of the

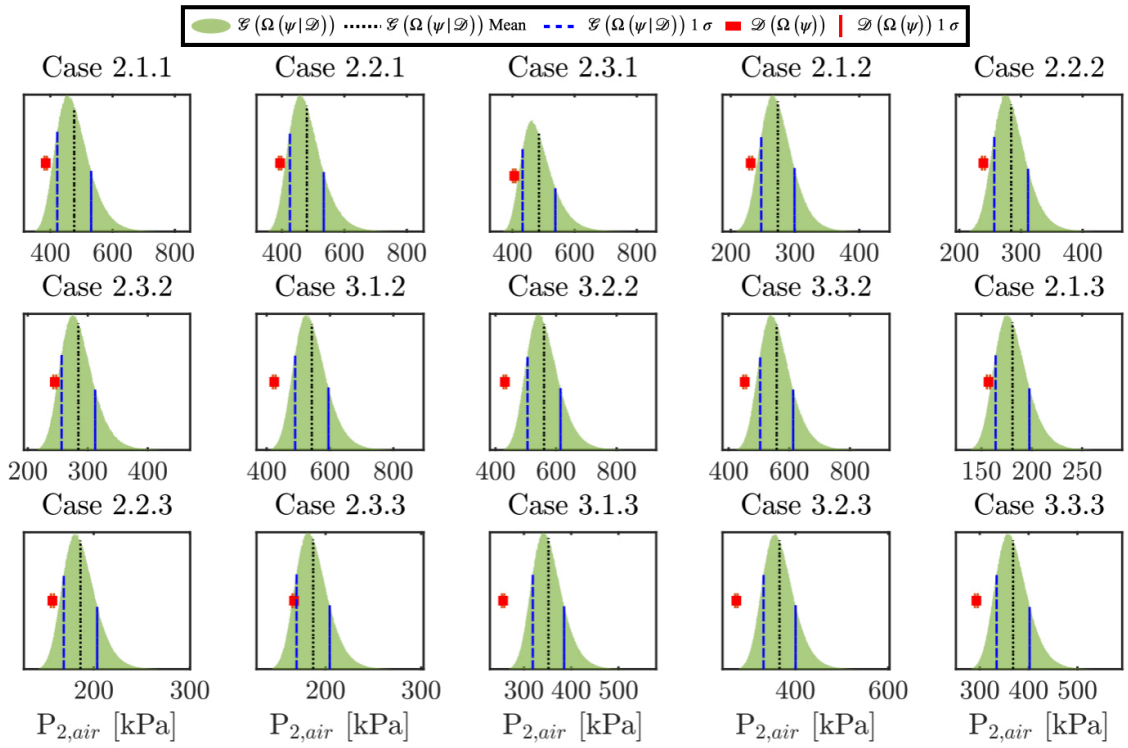

Figure 6.18: PDF of model predictions of air plenum pressure using the model prior distributions for the 15 experimental cases from Ref. [244] above the critical air mass flow rate of ~0.25 kg/s.

ANN-based surrogate model even further.

The primary outcome of the calibration procedure is to obtain a posterior with narrower support compared to the prior; this highlights that the experimental data provided information for the posterior distribution of model parameters to converge based on model constraints. The posterior distribution is computed using the 15 cases within the experimental data set $\mathcal{D}(\chi)$ where the air mass flow rate is above the critical value (~0.25 kg/s) to ensure positive thrusts are predicted and below an air mass flow rate of 0.86 kg/s where two detonation waves were seen at equivalence ratios of stoichiometry and higher. The Kaemming et al. model is sensitive to wave number as an input, and all the cases studied here were restricted to those exhibiting a single detonation wave. The mean and standard deviation of the posterior distributions are given in Tab. 6.3. For all six parameters, the mean of the posterior distributions have

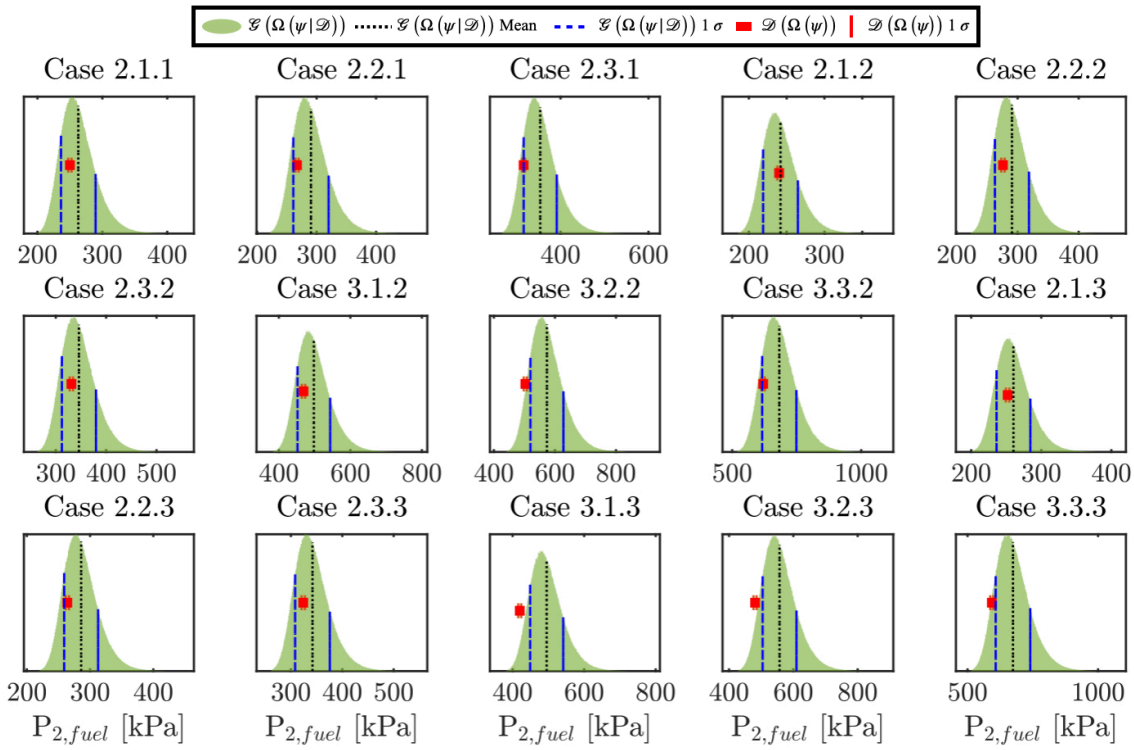

Figure 6.19: PDF of model predictions of fuel plenum pressure using the model prior distributions for the 15 experimental cases from Ref. [244] above the critical air mass flow rate of ~0.25 kg/s.

converged, and the standard deviations are narrower than the prior. However, for ζ_{det}, the posterior standard deviation is of the same order as the mean. To understand the behavior further, the marginal PDFs of the posteriors are provided in comparison to the prior PDFs in Fig. 6.20. The PDF provides a better view of the convergence characteristics. For the air and fuel forward flow coefficients, the convergence is very clear, with a posterior that has substantially settled on a mean value with very narrow support. The posterior for ζ_{defl} resembles the Gaussian distribution that was initially assumed, with slightly narrow support in the posterior. For the two mixing coefficients Y_b and Y_c, the posteriors have moved towards the bounds of physical validity with the former converging towards 0 and the latter approaching 1. However, the support of the posterior appears to be similar to the prior, and the reduction in standard deviation may be attributed to the constraints on the parameters themselves. Similarly, the

ζ_{det} has approached 0, but with very narrow support similar to the flow coefficients. The mixing coefficients Y_b and Y_c are mutually exclusive, but the data is suggesting that the amount of detonated flow processed by a secondary shock is minimal and the amount of deflagrated flow mixed with the detonated flow is high. According to the model formulation in Eqn. 6.15, as Y_c approaches 1, the second term of the equation goes to 0; the mixing contribution of Y_b is irrelevant. Thus, the data do not provide information about Y_b as Y_c is computed to be > 0.75. The amount of non-axial momentum in the detonation flow is near zero and data does not provide information to shift the amount of non-axial momentum in all deflagrated flows. In conjunction with the model dynamics, the experimental data set does not provide information on the probable values of ζ_{defl}, and possibly Y_b as well. Further, it is possible that this parameter is not universal among the experimental data so no convergence of the posterior is possible.

Table 6.3: Statistics of the Gaussian prior distribution and the posterior distribution conditioned on the experimental cases.

Model parameter	$\boldsymbol{\Omega(\psi) : \mu}$	$\boldsymbol{\Omega(\psi) : \sigma}$	$\boldsymbol{\Omega(\psi\|\mathcal{D}) : \mu}$	$\boldsymbol{\Omega(\psi\|\mathcal{D}) : \sigma}$
$\boldsymbol{Y_b}$	0.5	0.15	0.1252	0.0916
$\boldsymbol{Y_c}$	0.5	0.15	0.8708	0.0852
$\boldsymbol{\zeta_{det}}$	0.25	0.075	0.0084	0.0080
$\boldsymbol{\zeta_{defl}}$	0.25	0.075	0.2281	0.0745
$\boldsymbol{C_{w,f,air}}$	0.85	0.1062	1.0891	0.0048
$\boldsymbol{C_{w,f,fuel}}$	0.85	0.1062	0.9220	0.0039

In order to further analyze the converged posterior distributions with the Gaussian prior PDFs, two-dimensional marginal PDFs in a 6×5 lower triangular matrix are highlighted in Fig. 6.21. An analysis of the autocorrelation of the Markov chain for

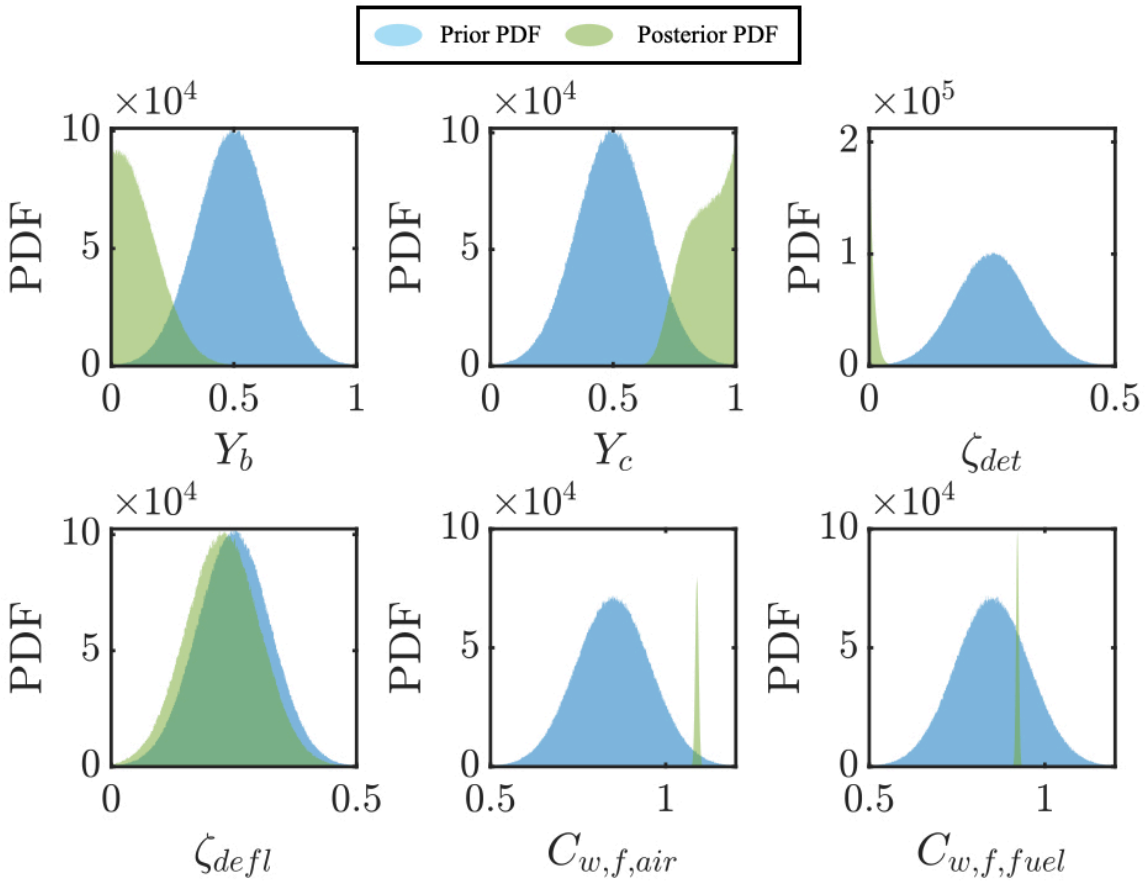

Figure 6.20: Comparison of the posterior PDF with the prior distributions of the hyper-parameters of the Kaemming et al. ANN surrogate model.

this calibration showed that the samples within each chain were decorrelated from the initial sequence after an average of approximately 1741 samples. As a result, each Markov chain featured more than 10 statistically independent samples, for a total effective sample size of approximately 10,845 samples across the entire model sampling process.

The shape of the joint posterior PDF provides detailed insight into the Bayesian inference process and the cross-correlation between model parameters. The joint posterior PDFs with circular or elliptical structures with the major and minor axes aligned with the grid directions indicate that the two parameters are not highly correlated. Further, a more circular pattern suggests that the spread of the parameters

is nearly identical. Uncorrelated parameters highlight that changing one parameter does not require a simultaneous change in another to ensure the model outputs are within the margin of error. The narrow support of the flow coefficients shows that they are generally uncorrelated with the other parameters, as the distributions of the other parameters are generally mapped to the same value of the flow coefficients. The Gaussian-like structure of ζ_{defl} results in a "clipped" circular two-dimensional PDF with the mixing parameters, and highly "squeezed" joint distribution with ζ_{det} due to its narrow support. The lack of parametric structure in the joint-distributions shows that the parameters are largely exclusive, and describe different aspects of RDE operation within the system. Further, the structure of Eqns. 6.15 and 6.16 remove the effectiveness of the data in describing Y_b as Y_c approaches one. In contrast, Bayesian optimization approaches in Refs. [84] and [131] have obtained parametric functional relationships between model parameters that allowed a reduction in model parameters.

Finally, the marginal posterior distributions of the model hyper-parameters can be used to predict the QoI and compare the solutions with experimental data. A comparison of model QoI predictions with the posterior distribution of parameters (in red) and the prior distributions of parameters (in green) is visualized in Figs. 6.22, 6.23, and 6.24. Here, the model predictions of the QoI have very narrow support, due in part to the narrow support of the flow coefficients and ζ_{det}. In general, for cases with an air mass flow rate of 0.32 kg/s (case indices of the form 2.x.x), the posterior improved predictions of specific thrust. However, for cases with an air mass flow rate of 0.63 kg/s (case indices of the form 3.x.x), the model prediction of thrust remains in the vicinity of the mean of the estimates using the prior distributions, but now with narrower support. On the other hand, the prediction of air and fuel plenum pressure notably improved for all cases, with the model prediction residing within one standard deviation of the experimental data for a majority of the 15

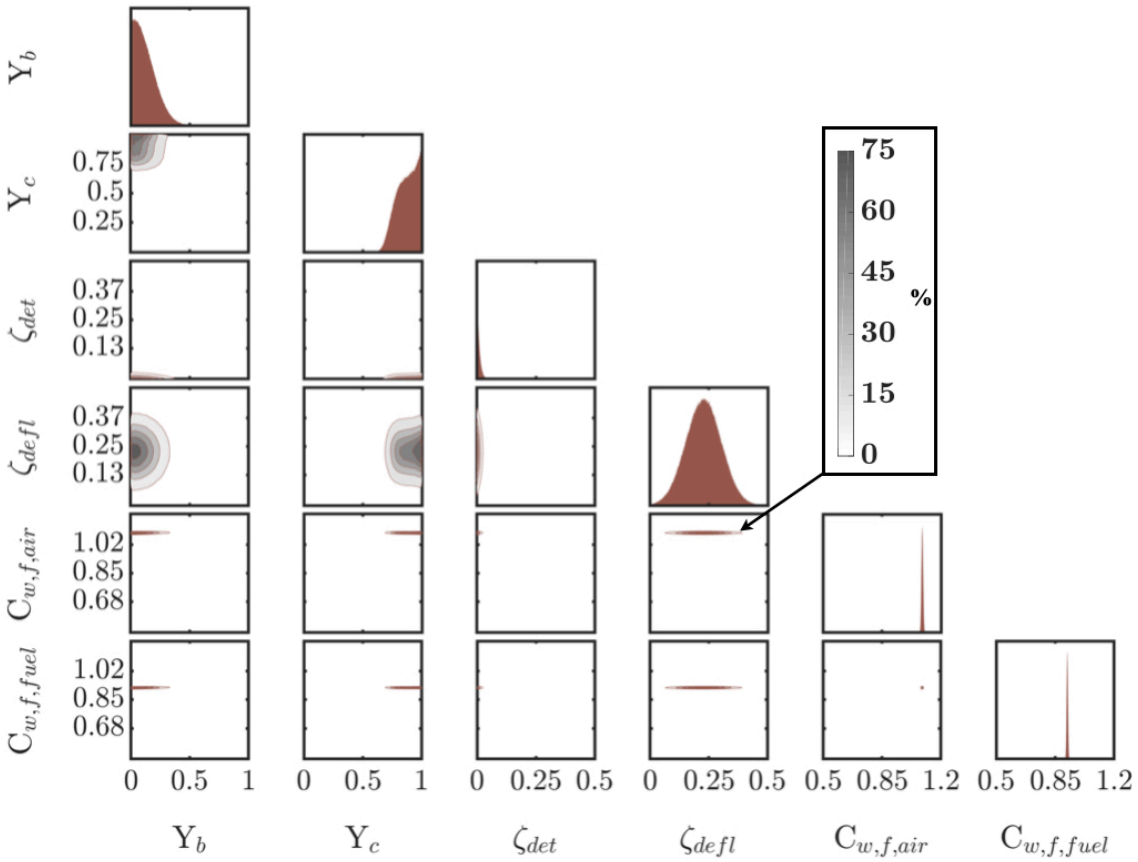

Figure 6.21: Posterior distributions and cross-correlations between the $N_{param} = 6$ parameters for the calibration performed on the Kaemming et al. ANN surrogate model. The contour lines on the joint PDFs are given at every 15% of the cross-correlation distributions' maximum value.

cases. It appears that through convergence on a few parameters, namely the flow coefficients, the model was able to improve specific thrust prediction when the prior distributions of parameters underestimated the specific thrust. However, for cases where the estimations overestimated the specific thrust, there are limited avenues for "reducing" system performance to match the experimental data. The model appears very stiff in its dynamics as the six parameters within ψ are varied. Thus, the six parameters studied here are unable to change the model dynamics to capture the experimental data. For future studies, other model components, such as heat release (as a representative of combustion efficiency) may need to be calibrated to further

improve model predictions of experimental data. However, this exercise of Bayesian calibration highlights that the experimental data must contain information to inform the model, and subsequently, the model needs to be sufficiently malleable through the choice of calibration parameters to capture the experimental data.

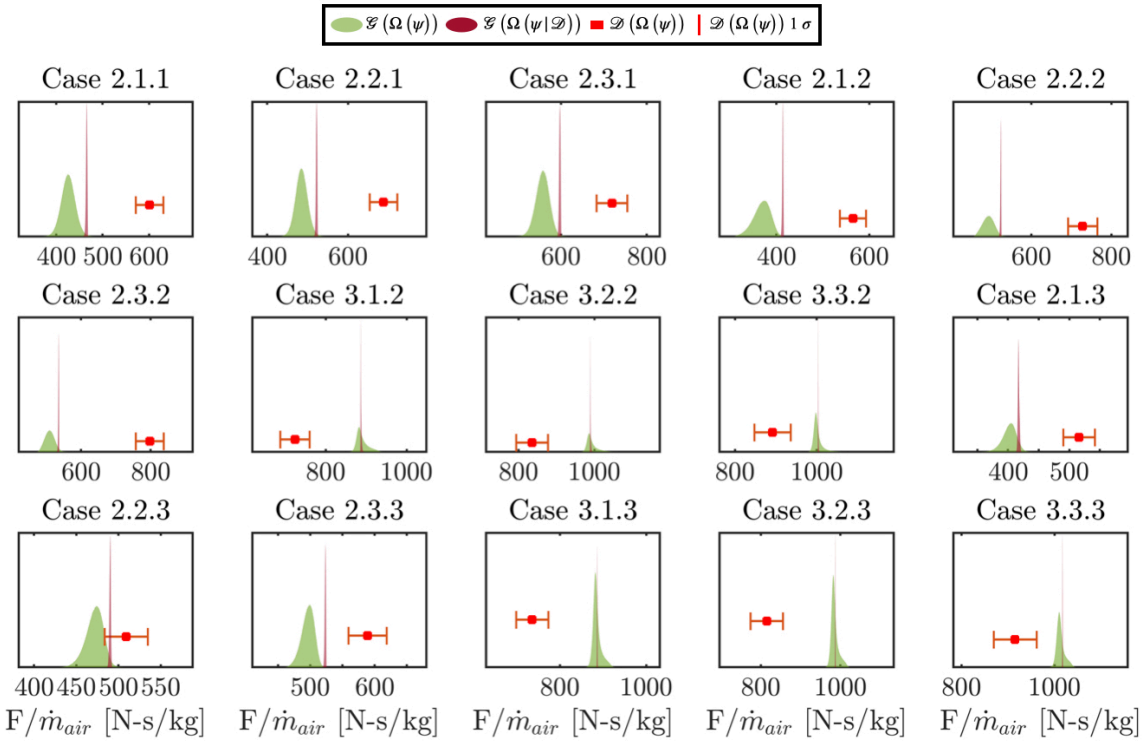

Figure 6.22: PDF of model predictions of specific thrust using the model posterior distributions for the 15 experimental cases from Ref. [244] above the critical air mass flow rate of ~0.25 kg/s.

6.6 Multi-fidelity Performance Estimation with Calibrated Low-Fidelity Model

The capabilities of both the multi-fidelity data fusion and Bayesian calibration can be combined to increase the robustness of the modeling approach. In the following section, the one- and two-dimensional surrogate models for performance estimation are updated with the calibrated Kaemming et al. model. Illustrated in Fig. 6.25, the

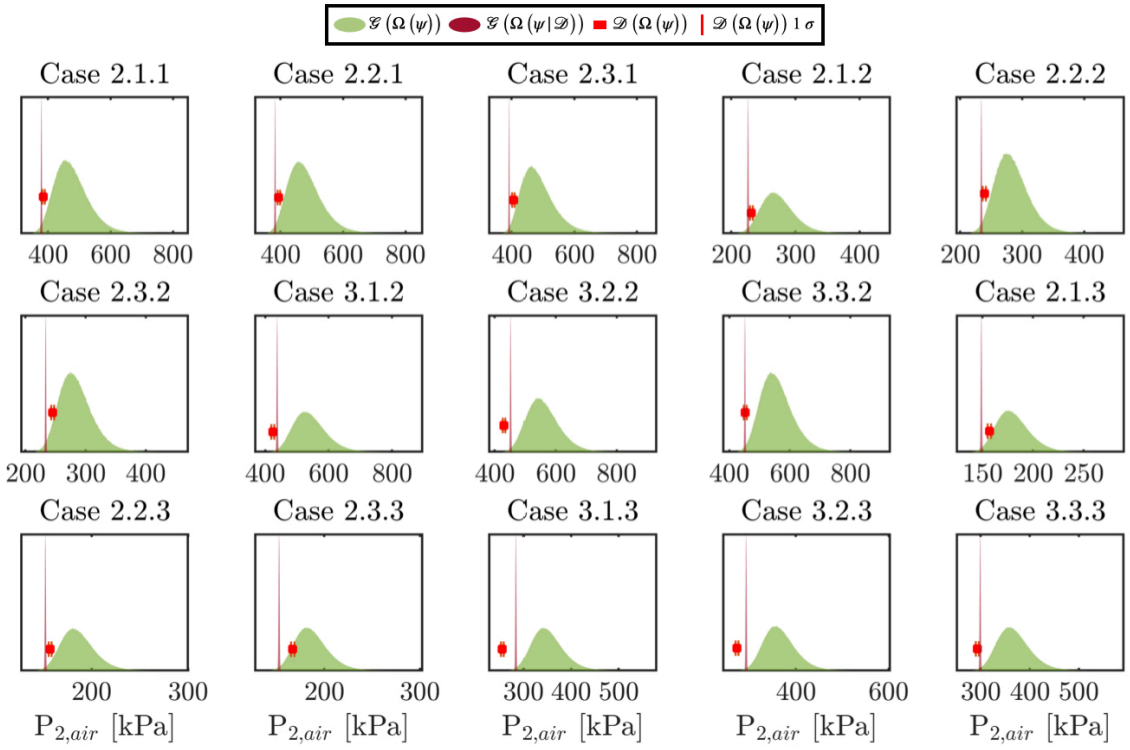

Figure 6.23: PDF of model predictions of air plenum pressure using the model posterior distributions for the 15 experimental cases from Ref. [244] above the critical air mass flow rate of ~0.25 kg/s.

use of the calibrated reduced-physics model results in different dynamics in the confidence interval. For the one-dimensional fit, the confidence interval is substantially tighter and more uniform across the full range of air mass flow rates. The "bulges" in confidence interval at low equivalence ratios are also improved and exhibit marked improvements over the standard GP fit. In the two-dimensional response surface, the multi-fidelity fit features additional curvature in the high equivalence ratio region. This results in lower response surface variance for high air mass flow rates with the trade-off of slightly increased variance for high equivalence ratios. Overall, the calibrated reduced-physics model is able to represent the experimental data more accurately, and this is reflected in the quality of the multi-fidelity performance map. Thus, the ideal modeling framework is a joint approach that combines the Bayesian

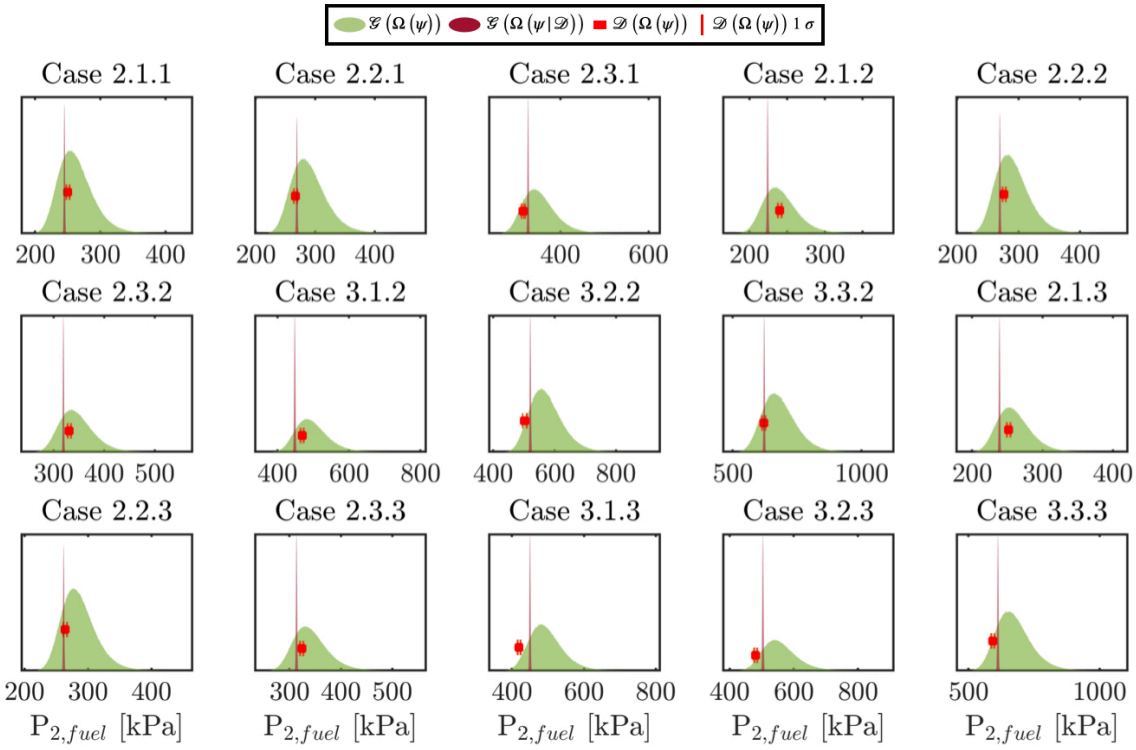

Figure 6.24: PDF of model predictions of fuel plenum pressure using the model posterior distributions for the 15 experimental cases from Ref. [244] above the critical air mass flow rate of ~0.25 kg/s.

calibration of model parameters with the multi-fidelity data fusion method.

6.7 Chapter Summary

In order to use detonation engines for practical applications, it is necessary to reliably estimate performance characteristics such as thrust/specific impulse over a range of operating conditions and geometric designs. Due to the inherent physics complexity, computational models are inherently expensive, and cannot be used to map the entire set of input conditions. Similarly, conducting large numbers of experiments is also not practically feasible. Hence, techniques that allow limited data to inform surrogate models, which can then predict performance over the entire operational map would be invaluable. To this end, the multi-fidelity modeling approach

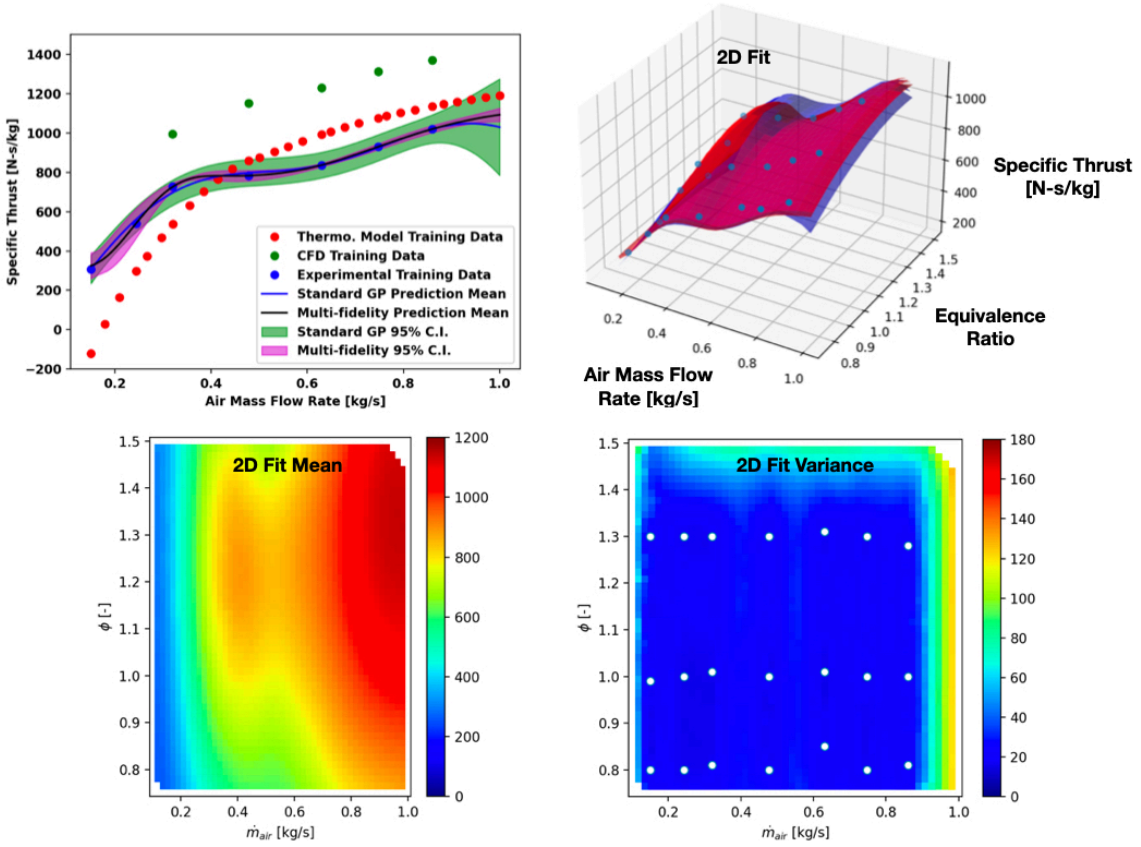

Figure 6.25: Multi-fidelity data fusion results with calibrated Kaemming et al. model. (Top left) One-dimensional multi-fidelity fit of specific thrust as a function of air mass flow rate. (Top right) Isometric view of the response surface of the multi-fidelity fit of specific thrust as a function of air mass flow rate and equivalence ratio. (Bottom left) Two-dimensional contour plot of the multi-fidelity fit of specific thrust as a function of air mass flow rate and equivalence ratio. (Bottom right) Two-dimensional contour plot of the 95% confidence interval half-width (1.96σ) of the multi-fidelity fit of specific thrust as a function of air mass flow rate and equivalence ratio. The color bars in the lower row represent specific thrust values in $\left[\frac{N-s}{kg}\right]$.

is an attractive method for developing a surrogate model for predictive performance using limited data sets. Here, instead of calibrating the model parameters of the lower-fidelity reduced-order model, the output of this model with nominal parameters is used along with sparser experimental and detailed computational results to improve the predictive capability of a performance map.

A multi-fidelity framework was developed and tested on available RDE data to test its ability to evaluate performance metrics. A reduced-order model using the methodology described in [139] was used to generate low-fidelity data. It was found that augmented data points were necessary to generate a reasonable multi-fidelity fit. For the augmented low-fidelity data, the multi-fidelity results produced predictions with a higher degree of confidence when compared to standard Gaussian process regression results. It was also found that adding data from additional fidelity levels yielded fits with progressively tighter error bounds. Further investigation into how the data sparsity and distribution affect the model outputs is ongoing and is detailed in Ref. [238]. Bayesian calibration of a set of hyper-parameters of the reduced-order model was performed, which provided limited improvement in predictive capability due to stiffness in the model's ability to capture the experimental data. While the multi-fidelity framework is the more comprehensive approach for data assimilation, a joint approach where a calibrated reduced-physics model is used in concert with the multi-fidelity model (as the low-fidelity data source) to improve the robustness of surrogate model predictive capability. The present study represents an important initial assessment of multi-fidelity information fusion in the evaluation of high-dimensional turbulent reacting systems.

CHAPTER VII

Summary, Conclusions, and Future Directions

7.1 Chapter Summaries

To reduce the environmental impact of aeropropulsion and expand the capability of high-speed propulsion devices, step changes in thermal efficiency and fuel burn, particulate emissions, and device thrust-to-weight ratio are of paramount importance. This fundamental efficiency improvement may be realized through detonation-based combustion, in contrast to the traditional deflagration-based combustion found in gas turbine engines and rocket combustors today. Pressure-gain combustion devices offer an increase in the total pressure of the system, which can be used to extract work with a lower required pre-compression of reactants and reduced system pressure losses. In particular, the rotating detonation engine (RDE) is a realization of pressure-gain combustion, where a propagating detonation wave confined within a combustion chamber produces shock-based compression with rapid chemical heat release. Due to the high wave speeds, such devices can convert a large mass of reactants within small volumes, thereby providing an increased thrust density over deflagrative combustion devices and leading to compact and unconventional propulsion system designs. Furthermore, continuous operation ensures interoperability with existing propulsion systems. However, the unsteady flow field within an RDE is one of the most complex environments characterized by multi-scale physics and extreme tem-

peratures and pressures. The operational characteristics of an RDE are determined by an equilibrium between large- and small-scale processes within the combustor. A fundamental understanding of this multiscale coupling is required to realize RDEs for practical applications, such as in gas turbines, rockets, and scramjets. The complex flow field within an RDE is fraught with non-idealities, ranging from incomplete propellant mixing and stratification, unsteady injector dynamics, secondary combustion, and multiple detonation waves. These non-idealities diminish practical system performance and define its operational characteristics. The literature review of RDEs and detonative propulsion is outlined in Chap. I. An understanding of the unsteady environment in detonating flows and practical RDEs is required to design and operate these devices.

The objective of this dissertation is to interrogate these non-idealities of practical detonations with gaseous and multiphase propellants from a numerical perspective. The root cause of non-ideal phenomena is the non-premixed injection scheme used in practical RDEs to ensure safety and operability. A range of computational tools, such as direct numerical simulation, high-fidelity massively parallel compressible flow solvers, and data-driven methods, are used to investigate detonating flows and are detailed in Chap. II. In particular, UTCOMP–a high-order, structured grid flow solver– is used for canonical configurations and UMReactingFlow–an unstructured mesh solver–is used for complex and large full-scale RDE geometries. The flow structure within canonical detonating flows is analyzed, as well as in full-scale RDEs with gaseous and liquid fuel injection of high-order hydrocarbon fuels. The novelty of this work is in the development and application of computational tools to provide detailed insight into these harsh environments, where experimental diagnostics and macroscopic performance parameters are limited in capability. Computationally intensive subroutines for the convective and reaction stages are offloaded to the GPU using in-house CUDA-based modules for compatibility with heterogeneous computing

platforms. The solver was adapted with its current form jointly developed over the course of this dissertation. The details are provided in Ref. [26], along with details of the GPU-based chemistry treatment (UMChemGPU) by Barwey and Raman in Ref. [15]. The GPU-accelerated solver provides an order of magnitude reduction in solver time-to-solution compared to a CPU-only approach.

These numerical simulations represent some of the highest fidelity computational studies of rotating detonation combustors, with an elevation in the number of modeled degrees of freedom originating from increased cell resolution, larger full-scale computational domains, detailed chemical kinetics for hydrocarbon mixtures with an increased number of species and reaction steps, and extended simulation times. Further, the simulations of the liquid-fuelled RDE represent one of the first computational studies of self-sustaining multiphase detonation in a three-dimensional full-scale domain. The massively parallel GPU-accelerated flow solver enables these computations and was jointly developed over the course of the work detailed in the dissertation.

The outcomes from the studies in this dissertation help shape the community's current understanding of reacting flows within detonation engines. In Chap. III, the simulations of canonical detonating flows using the UTCOMP solver isolates and interrogates the effects of small- and large-scale processes, such as mixture stratification due to discrete injection and propellant preburning. Additionally, in the full-system simulations of Chap. IV, the detonation structure, its coupling with the injector response and plenum dynamics, and overall combustion processes and bifurcation into detonation and deflagration are interrogated and characterized. This approach is extended to the study of multiphase detonation in Chap. V. The merit of numerical simulations is their ability to evaluate changes in these mechanisms as the operating condition and/or design is varied. Further, to advance the realization of RDEs, a modeling framework for data fusion from multiple disparate information sources, such as numerical simulations, experiments, and reduced-physics models, with uncer-

tainty quantification is proposed and demonstrated on a characteristic RDE design in Chap. VI.

Key conclusions derived from the numerical effort on understanding non-idealities in detonating flows are provided in Sec. 7.2. Finally, challenges and recommendations for continued research are provided in Sec. 7.3.

7.2 Conclusions

The practical realization of rotating detonation engines (RDEs) requires an increased understanding of non-ideal phenomena. Prior experiments and numerical investigations have shown that RDEs operate under mixing-limited conditions leading to spurious losses, best characterized by reduced wave speeds and minimal or lack of pressure gain (through methods such as EAP [140], for instance). These losses manifest as non-idealities such as incomplete propellant mixing and stratification, unsteady injector dynamics, secondary combustion, and multiple detonation waves. The operating mode of an RDE is achieved through a balance between the small- and large-scale processes (see Fig. 1.10). The goal of this dissertation was to 1) develop an understanding of the non-idealities within RDEs and their effects on device operation, 2) contribute high-fidelity data on detonation physics and RDE operation to the community, and 3) establish a framework for assimilation of numerical and experimental data and reduced-physics models for RDE performance estimation. Thus, the work contained within this dissertation can be segmented into three parts: I) fundamental physics of canonical detonating flows; II) simulations of full-scale, non-premixed RDEs; and III) macroscopic RDE performance estimation. The workflow is visualized and outlined in Fig. 7.1.

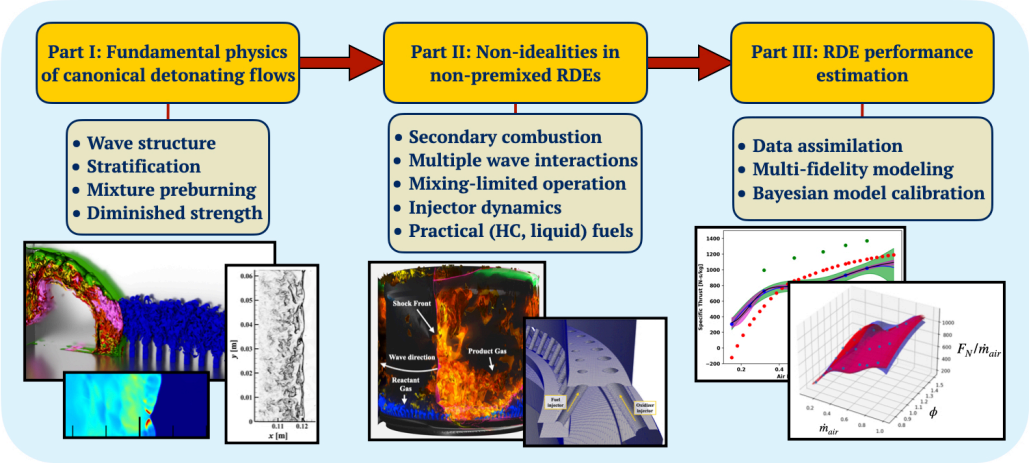

Figure 7.1: Outline of the three components of the dissertation in an effort to increase the community's understanding of detonating flows.

7.2.1 Part I: Fundamental physics of canonical detonating flows

Near-DNS simulations of canonical detonating flows have allowed for the non-idealities to be isolated in simplified geometries and interrogated in detail. It was found that the detonation structures are multi-dimensional in nature. The shock front and reaction zone of an unsteady detonation wave are typically closely coupled, reinforced by triple point collisions as the fundamental three-shock structure traverses the domain. However, with discrete injection, the reaction zone broadens in time due to the fluctuating acoustic impedance of the mixture ahead of the wave. This leads to instantaneous wave galloping. The complex reaction zone consists of multiple pressure waves and density gradients. The fluctuating wave does not completely consume the available fuel/oxidizer mixture, and turbulent mixing driven by the vortices stemming off of the triple points and the three-shock region serve to mix the intermediary gases and ensure more complete combustion. In turn, the practical reaction zone is thicker and the detonation wave is of lower strength than the ideal ZND solution through a homogeneous mixture. This behavior reflects those observed in the experimental campaigns.

Fuel stratification introduces additional density and composition gradients (not typically aligned with the direction of wave propagation) in the flow field. The wave front becomes highly corrugated due to shearing forces generated as the detonation wave passes through fuel-rich and fuel-lean regions. Both the size of these turbulent structures and the node length of the wave front corrugation are proportional to the length scale of stratification. The size of these turbulent structures stemming off the triple points and concentration boundaries is proportional to the stratification length scale, and this affects the post-detonation mixing and deflagrative combustion of residual products. Detonation properties such as pressure rise and detonation cell size – a product of the small-scale triple point and transverse/Mach wave interactions – are directly controlled by the stratification length scale. In relation to RDE performance, a smaller mixture stratification size leads to greater combustion efficiency, but a lower average total pressure rise in comparison to a larger stratification length scale. Overall, the physical structure of the detonation wave front is highly dependent upon the distribution of the fuel and oxidizer. Deflagration ahead of the detonation wave, termed *parasitic* combustion, is known to be present due to the interaction between fresh and product gases. This weakens the shock front with considerable unburnt fuel downstream of the shock front that continues to burn in a slow and distributed heat release process termed *commensal* combustion. The parasitic combustion alters the upstream gas composition and lowers the wave Mach number thereby affecting wave characteristics. Thus, parasitic combustion ahead of the wave leads to commensal combustion behind the wave, indicating that it, along with mixture inhomogeneity, is the root cause of combustion efficiency loss across the detonation wave.

7.2.2 Part II: Non-idealities in non-premixed RDEs

The AFRL rocket-type RDE (RDRE) was used as a test bed to study the small- and large-scale processes within practical RDEs with non-premixed injection schemes.

These simulations promoted the development of new techniques for the analysis of RDEs, such as the visualization of operating modes through a detonation surface plot, time-averaged profiles of the combustion chamber relative to the wave front location, time-averaged exit flow profiles, quantification of the bifurcation of combustion into detonation and deflagration, and statistical perspectives on the combustion processes. These analysis methods have been the baseline in the community for the evaluation of a given RDE design. Furthermore, these numerical simulations represent some of the highest fidelity computational studies of full-scale rotating detonation combustors, with an advancement in the number of modeled degrees of freedom in the form of increased cell resolutions, larger full-scale computational domains, detailed chemical kinetics for hydrocarbon mixtures with enhanced complexity, and extended simulation times. The massively parallel GPU-accelerated flow solver enables these computations and was jointly developed over the course of the work detailed in the dissertation.

Across a range of operating conditions of the AFRL RDRE, different operating modes were observed with either co-rotating or counter-propagating wave pairs, and this, in turn, affected the amount of parasitic combustion present through a first-order effect. The injector refresh profile is affected by counter-propagating or secondary waves which increase the amount of deflagration at the base of the combustion chamber. With strong co-rotating waves, the injector profile is triangular rather than parabolic (in the counter-propagating case), and expels the hot gas which can lead to autoignition of mixtures and secondary combustion. The reactant fill and detonation height adjust to the number of waves present within the system. An increased number of waves, either co-rotating or counter-propagating, reduces the strength and speed of the individual waves, while the chamber pressure profile is fixed by the feed plenum conditions and the injector flow path. Recirculation zones between the impingement points of injector columns and near the wall can lead to increased deflagration. In fact, statistical analysis showed that the amount of heat released due to deflagration

is of a similar order to that released by detonation, since deflagration occurs at nearly all times throughout the wave cycle but detonative energy release is momentary. Statistical and time-averaged analysis of the combustion processes showed that while all of the primary heat release occurs within the base of the combustion chamber, there is still unburnt fuel and oxidizer that escape the detonation region. In other words, the detonation wave is unable to process all the fuel-oxidizer mixture available. As a result, partially oxidized fuel is carried downstream in a relatively high-temperature gas, where subsequent oxidation to CO_2 occurs. This is mainly due to the weak detonation wave with a diminished pressure rise, which affects the net amount of work that can be extracted from the system. In fact, the observed wave speeds were approximately 50% the CJ speed for a given methane-oxygen mixture, along with a wave front peak pressure of approximately 30% the von Neumann pressure.

The wave energies spatially fluctuate, with large variations in local wave speed and flow compression. The fraction of heat release in detonation was notably low in practical systems, highlighting that commensal combustion that occurs throughout the wave cycle and far from the wave front contributes significantly to the overall heat release. The thermal efficiency gain of an RDE is realized through increased detonation efficiency, which can be inconsistent with the overall combustion efficiency of the system. Thus, small-scale processes and secondary processes within the RDE combustor affect how heat is released within the system, and thereby the realizable efficiency benefit of detonative propulsion. However, this secondary combustion may be required to operate an RDE stably. A change in the operating mode following a revision of the plenum geometry highlights that the plenum dynamics and the injector response predominantly affect the balance between the small- and large-scale processes. The operating mode is a result of the manifestation and propagation of stochastic instabilities. Multiple stable operating modes are possible through different ignition methods within the short-time limit of numerical simulations.

Novel numerical simulations of a liquid-fueled RDRE illustrated that the operating modes of multiphase systems are vastly different from wave modes observed in gas-phase systems. The waves are highly compact yet move at detonation-like speeds. This compactness is enforced by the injector recovery process, as well as droplets that act as a heat sink to the passing detonation wave, moving the sonic plane closer to the wave front and limiting the broadness of the reaction zone. The injector dynamics lead to differences in the droplet motion, where the injector recovery enforces recirculation zones and the droplet trajectory in its evolution from injection to detonatable mixture. Additionally, the droplet trajectory uncovers the spatial locations along with the wave phase-relative position where liquid particles undergo evaporation. The penetration of the injected particles is paramount in their ability to be evaporated, where droplets that are not carried downstream are entrained within a recirculation zone at the base of the chamber. This can quench detonation and result in a chaotic, deflagration-like mode. The combustion processes and the operating mode within the RDE are highly sensitive to the boundary condition prescribed for the liquid fuel droplets. The merit of numerical simulations is their ability to evaluate changes in these mechanisms as the operating condition and/or design is varied.

7.2.3 Part III: RDE performance estimation

In order to use detonation engines for practical applications, it is necessary to reliably estimate performance characteristics such as thrust/specific impulse over a range of operating conditions and geometric designs. The numerical simulations highlight that the small- and large-scale processes are important in the operation of the RDE, as they control wave stability and both detonation and combustion efficiency. However, elucidating the propulsive performance of the device from the small-scale processes is challenging, chiefly because the operating mode of the RDE does not provide a direct link to its propulsive performance as improvements in the detona-

tion structure and mixing quality do not produce improvements in thrust/specific impulse of the same order. Further, multiple non-unique operating modes can provide similar performance. For this reason, the operating mode cannot be determined *a priori*. Computational approaches, especially the high-fidelity techniques described here, are inherently expensive and cannot map the full operating envelope. Similarly, large numbers of experiments are also not practically feasible. To this end, the multi-fidelity modeling approach is an attractive method for developing a surrogate model for an unknown function of predictive performance using limited and disparate data sets. The multi-fidelity fit of an unknown high-dimensional function yielded a solution with a tighter confidence interval than a standard Gaussian process fit.

In essence, the modeling approach establishes a pathway to link input RDE operating conditions to the propulsive performance of the device. Further, the multi-fidelity approach offered a pathway for uncertainty quantification of the key quantities of interest, necessary in an iterative design process. While Bayesian calibration of key hyperparameters of a reduced-physics model can improve its predictive capability, stiffness in the model dynamics can limit this improvement. Thus, a proposed solution combines the Bayesian calibration of a reduced-order model along with its application in a multi-fidelity framework to maximize the robustness and predictive capability of the surrogate model. This workflow provided for increased tightness in the confidence interval of the multi-fidelity surrogate model. In the design of experiments, multi-fidelity modeling is a recursive framework that can inform researchers where additional experiments or numerical simulations are needed to capture the system dynamics. Additional high-fidelity data simulations/experiments can be commissioned and the surrogate model is recursively evaluated as new data is available, such as within a design optimization loop.

The numerical analysis conducted in this work provides unprecedented insight and understanding of the non-idealities in practical detonation engines and the coupling

between small- and large-scale processes. The details gleaned from numerical simulations can drive enhancements to RDE design, such as through the minimization of pressure losses and detonation flashback into the feed plenums, ideal placement of recirculation zones to aid mixing, and optimal exit flow configurations to ensure combustion chamber isolation. Furthermore, the merit of numerical simulations is clear in their ability to generate high-fidelity data sets for the community, and provide avenues for analysis not possible even with state-of-the-art experiments. The summary points are:

- High-fidelity numerical simulations have provided unprecedented insight into the physics of detonating flows and RDE combustors.
- Non-idealities due to non-premixed injection result in detonation waves with diminished strength and propagation speed with a broader spatial structure than the ZND expectation.
- Parasitic combustion ahead of the wave results in commensal combustion behind the wave; a majority of the heat release within the RDE may result from these deflagrative combustion processes ($> 60\%$) as opposed to detonation. Deflagrative energy release occurs through a slow and distributed process.
- Parasitic and commensal combustion, while decreasing the achievable thermal efficiency, may improve operability and the overall combustion efficiency of the system due to the complex interaction of unsteady turbulent mixing and detonation wave propagation.
- Multiple competing detonation and secondary waves influence the flow structure by altering local heat release and fuel-oxidizer mixing. Secondary waves are integral to RDE operation.
- While the small-scale processes are important in the stability of the RDE and

dictate how heat is released within the system, variations at the small scale do not produce propulsive performance changes of the same order. The operating mode cannot be determined *a priori* as it is a manifestation of the equilibrium between small- and large-scale processes.

7.3 Future Challenges and Research Recommendations

There remain several pathways for continued research needed to increase the technology readiness level of the RDE concept, which are outlined below. These range from investigations of different physical aspects of detonation engines to improvements to the numerical tools and methods used in their analyses.

7.3.1 Physics-based pathways

7.3.1.1 Feed plenum dynamics

The operating mode of the RDE represents a balance between the small- and large-scale processes, such as the injector response rate and dynamics. Even with stiff injectors, detonation pressure fluctuations feed back into the plenums. The short-time numerical simulations presented here did not study the low-frequency dynamics of acoustic reflections within the plenum. However, for practical realization, the attenuation of the pressure waves in the plenum and its effect on the injector recovery process is needed. In the long-time limit, these reflected pressure waves may cause unwanted disruptions in the propellant flow rate, and affect the operability of the device.

7.3.1.2 Exit nozzle effects on chamber dynamics

In the full-scale RDE numerical simulations discussed within this dissertation, a bluff body exit or simple aerospike nozzle was employed but their effect was not

adequately studied. RDEs are favored over PDEs for their continuous axial thrust and ease of integration with existing turbomachinery. Although at a high frequency, the cycle-to-cycle variation in thrust must be minimized and the thrust itself augmented through the use of exit flow control devices, such as nozzles [243]. An exit flow nozzle ensures that the exit to the combustion chamber remains choked, and controls the pressure at the exit of the combustion chamber. This can provide usable pressure gain or at least limit the system's total pressure loss. A choked combustion chamber boundary can heavily influence the dynamics within the combustion chamber, as observed in the shuttling reflective detonation engine configuration [268, 300]. Pressure reflections from the exit boundary can contaminate the flow field and lead to vastly different operating modes with an increased number of waves, multiple competing waves, and deflagration-to-detonation transition events. As the RDE is a highly-coupled device, changes in the chamber dynamics will thereby affect injector and plenum dynamics. Nozzle effects may significantly affect the behavior and operability of RDEs.

7.3.1.3 NOx and particulate emissions of RDEs

The RDE flow field is characterized by extreme temperatures within the combustion chamber. These conditions can encourage NOx formation which is highly sensitive to temperature. However, NOx generation also requires increased residence times which may be limited in general due to the highly unsteady flow and high wave propagation speeds. The limited NOx and O_2 emission measurements of [77] suggest that NOx emission may be low (< 30 ppm). In the presence of parasitic and secondary combustion at high temperatures and increased residence times within recirculation zones, the formation of nitrogen oxides may be promoted. Further, in multiphase RDEs, the rapid evaporation and partial oxidation of fuels may encourage NOx and carbon particulate formation. A detailed understanding of the NOx and

particulate generation process in RDE flow environments is required.

7.3.1.4 Models for multiphase detonation

The use of liquid fuels is necessary to integrate RDEs in aeropropulsive applications. These liquid fuels are generally high-order hydrocarbons, such as jet fuels and rocket propellants (kerosene derivatives). Liquid fuels possess higher energy densities and provide safety and operability benefits. The novel high-fidelity numerical simulations of a liquid rocket propellant-fueled RDRE presented within the dissertation are an initial step to understanding multiphase detonation. Current ongoing work aims to address shock-induced droplet breakup and its effects. Currently, canonical numerical studies are being completed to develop the shock-induced break-up and non-linear drag models for use in the regimes observed in RDEs [27, 177]. There is a lack of models in the literature applicable to supersonic flow. Adequate calibration of the break-up model is necessary because the amount of droplet shattering estimated by detonation-induced break-up will effectively control the vapor available for subsequent detonations and secondary (parasitic/commensal) combustion between the detonation waves. Non-linear drag estimation and evaporation models tailored for use in high-speed flows are also needed for the study of multiphase detonations.

7.3.2 Numerics-based pathways

7.3.2.1 Embedded boundary approach

The simulations of full-scale RDEs within this dissertation utilized an unstructured mesh framework. However, in the embedded boundary (EB) approach to PDE discretizations, the computational mesh is uniform and block-structured. Irregular computational domains can cut through this structured mesh to represent complex geometries. For instance, in the AMReX software framework [340, 341], each cell in the mesh is denoted as regular, cut, or covered, and the traditional finite volume-

based discretization methods can be adapted to incorporate the irregular cell shapes. The advantage of a block-structured mesh is the use of high-order numerics, like that of the UTCOMP solver, to increase solution accuracy and better capture turbulence and shocks within minimal dissipation.

7.3.2.2 Adaptive mesh refinement

As described throughout the dissertation, the numerical simulation capability of detonating flows is heavily limited by the spatial resolution restrictions imposed by computational costs and resources. Local refinement of the mesh surrounding the detonation wave would better resolve the shock compression and induction zone, with a more accurate representation of the detonation chemistry. In Sec. 4.3.2.2, the amount of flow detail and turbulent structures revealed by a DNS-level mesh sector within a full-scale geometry was fascinating. However, this resolution is intractable for the full combustion chamber even with current state-of-the-art computing resources with GPU acceleration. However, a high-resolution mesh that tracks the motion of the detonation wave and provides local refinement would offer invaluable insight. Traditionally, gradient-based tagging algorithms are used to inform where the mesh needs to be refined. However, a physics-guided clustering approach proposed by Barwey [13] to identify and track regions in the flow field with stiff chemical kinetics and turbulent features is a promising solution.

7.3.2.3 Hybrid numerical schemes

Hybrid schemes provide a compromise between the diffusive nature of shock-capturing schemes and unstable central schemes. By using a central scheme for the convective fluxes in smooth regions of the flow, turbulent structures and the turbulent energy cascade are more accurately resolved. The variable scheme consists of a local shock sensor that is used to determine a linear combination of both

schemes to ensure a continuous spatial transition between the schemes. Typically, these are dilatation-based parameters [71, 138, 191]. However, the aforementioned physics-guided clustering approach [13] may be a viable alternative.

7.4 Closing Remarks and Outlook

The dissertation work provides a comprehensive overview of detonating flows and non-ideal mechanisms of interest to the RDE community. The capability and availability of computational tools can significantly increase the understanding of complex phenomena within high-dimensional systems, such as RDEs. However, computational tools still contain gaps in predictive capability as demonstrated in Chaps. IV- VI, such as in the estimate of the operating modes (number, direction, and speed of the waves) and pressure/thrust outputs. The numerical simulations are short-time studies compared to experimental campaigns and may not capture all mode transitions. A comprehensive approach to model validation needs to be defined. This model validation will require an understanding of measurement errors, numerical mesh and algorithm effects, quantitative state measurements of the domain boundaries (inflow and exit), and validation of chemical kinetic mechanisms at the operating conditions observed within RDEs. Alongside the pathways outlined in Sec. 7.3.2, this will provide the opportunity to better understand the interplay between small- and large-scale processes and the establishment of the operating mode (wave number and speed, secondary waves).

The massively parallel GPU-accelerated codes have demonstrated that new realms in computation capability have been unlocked in the past few years, ranging from the solution of problems with increased degrees of freedom or fast turnaround times for simulations of reduced complexity. With the concurrent transition to exascale computing [2], this capability will continue to flourish, as long as combustion software and codes adapt to GPU-centric, heterogeneous architectures. Coupled with multi-

fidelity design frameworks, the design process can be automated where the surrogate model can be optimized through the autonomous selection of additional numerical simulations that best tightens the confidence intervals, and recursively update the multi-fidelity surrogate model as new data becomes available. Further, this process can be completed on the HPC so multiple numerical simulations can be evaluated at the same time. This recursive workflow is outlined in Fig. 7.2.

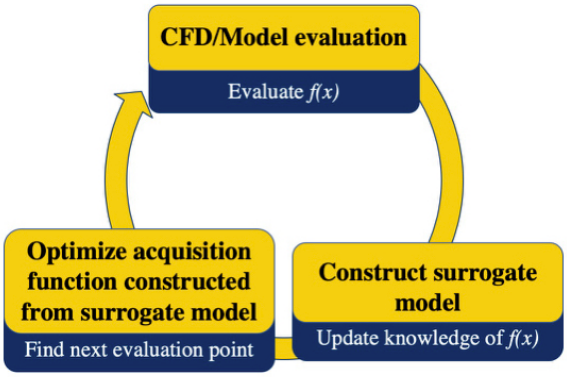

Figure 7.2: Flow chart of the Bayesian design optimization process.

Current research and development efforts of aeropropulsion devices are driven by an insistence on enhanced capability with a reduced environmental impact and increased sustainability. The RDE is a promising technology for providing the step-change in thermal efficiency and fuel burn, particulate emissions, and device thrust-to-weight ratio needed to address this demand.

APPENDIX

APPENDIX A

Analysis Procedures for Detonation Wave Statistics

This section outlines the analysis procedures used to post-process the simulation data and extract averaged quantities and wave statistics.

A.1 Conditional averaging procedure

The conditional average of properties in mixture fraction and pressure space is obtained on a volume-weighted basis. The averaging is performed using data from just ahead of the wave front surface to 1.5 cm behind the front. Initially, the shock front surface is reconstructed by identifying the wave location in the direction normal to wave propagation at every point in the transverse plane. The wave location is determined by finding the location where the local pressure exceeds a threshold pressure, tuned to 40% greater than the ambient pressure of 0.5 atm. This threshold pressure was found to consistently determine the pressure rise associated with the traveling detonation wave while disregarding the pressure variations ahead of the wave. At every snapshot, the wave front surface is represented as a collection of cell center locations that approximate the "true" shock surface location, as illustrated in

Fig. A.1. At every cell center along the wave front surface, data extending 1.5 cm behind wave front in the streamwise direction (identified by the blue-shaded region in Fig. A.1) is collected for averaging. The conglomeration of data from all wave surface locations and all snapshots is utilized for averaging on a cell volume-weighted basis.

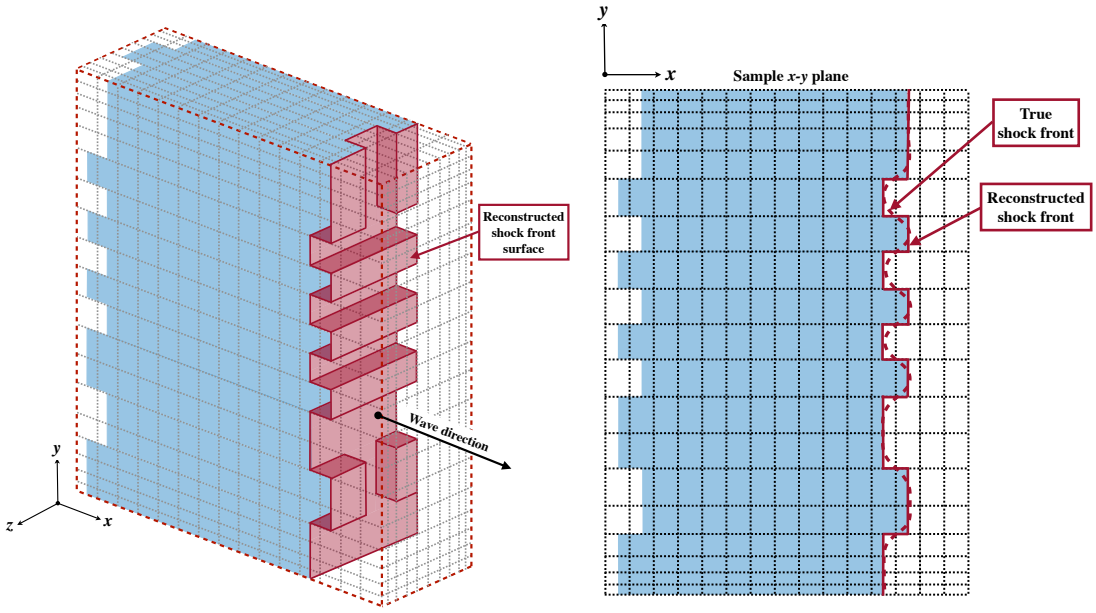

Figure A.1: Schematic of the shock front surface reconstruction procedure at a given snapshot in (left) three dimensions and (right) two dimensions using a single plane in the depthwise direction. The cells extending 1.5 cm behind the shock front at each shock-normal and spanwise location (shaded in blue) are used for volume-weighted averaging.

A.2 Shock-normal profile extraction

The one-dimensional shock-normal profiles are computed in the laboratory-fixed reference frame. Note that the one-

dimensional profiles show the variation of properties as a function of distance from the shock front along the surface-normal direction. As described above, at every snapshot, the wave front surface is represented as a collection of cell center locations that approximate the "true" shock surface location, and each of these points is characterized by a cross-sectional area that is equivalent to the discretized elemental area

of the reconstructed shock surface. As shown in Fig. A.2, a surface normal vector at every point on the wave front surface is determined based on a gradient local to that surface element. The gradient is computed primarily using central differencing and directional differencing near the boundaries.

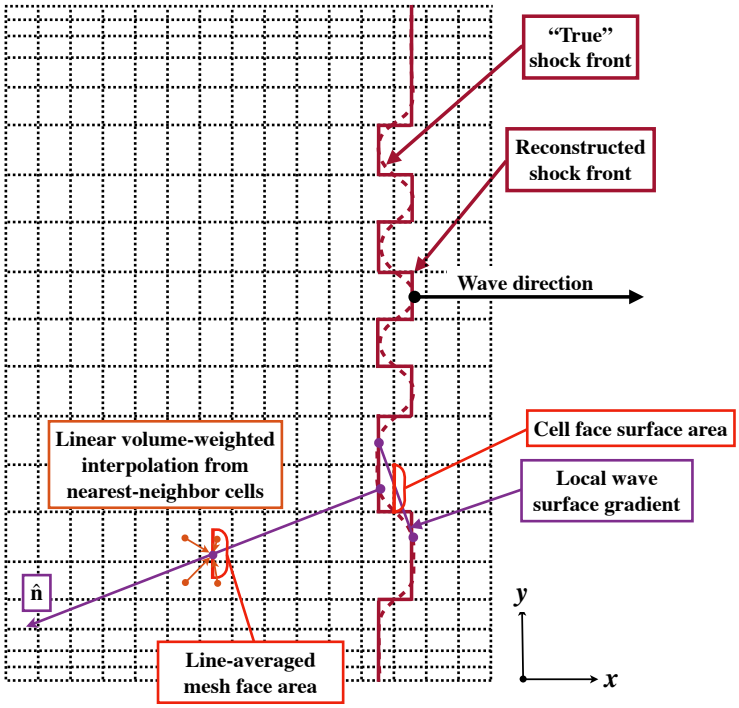

Figure A.2: Schematic of the extraction of the local shock-normal one-dimensional profile based on a local shock-front normal gradient. The schematic is projected in two-dimensions but the surface normal vector and one-dimensional profile can span all three dimensions.

After the surface reconstruction, a one-dimensional normal profile along this surface normal vector is extracted behind the wave using linear nearest-neighbor volume-weighted interpolation from the three-dimensional cell center data. A representative mesh surface area is also extracted along these one-dimensional vectors, where the resulting line-averaged mesh face area (influenced by the nearest-neighbor cell volumes) is assigned to be the aforementioned cross-sectional area. Subsequently, averaging is performed about these one-dimensional profiles for every spatial location across the shock front surface, for every snapshot of data, weighted by the cross-sectional area.

Each one-dimensional profile at every location across the wave front surface, at every time step, is used to obtain this averaged profile, as displayed in Fig. A.3. Hence, the averaging is temporal and spatial in nature. The output of this above procedure is essentially a surface-averaged one-dimensional shock normal profile. In the wave-fixed reference frame, this process essentially makes the front planar (shown in Fig. A.3) and the one-dimensional profiles can be aligned. This method is later used in Sec. 3.2.3.4 when computing heat release and combustion efficiency parameters tracked with wave position.

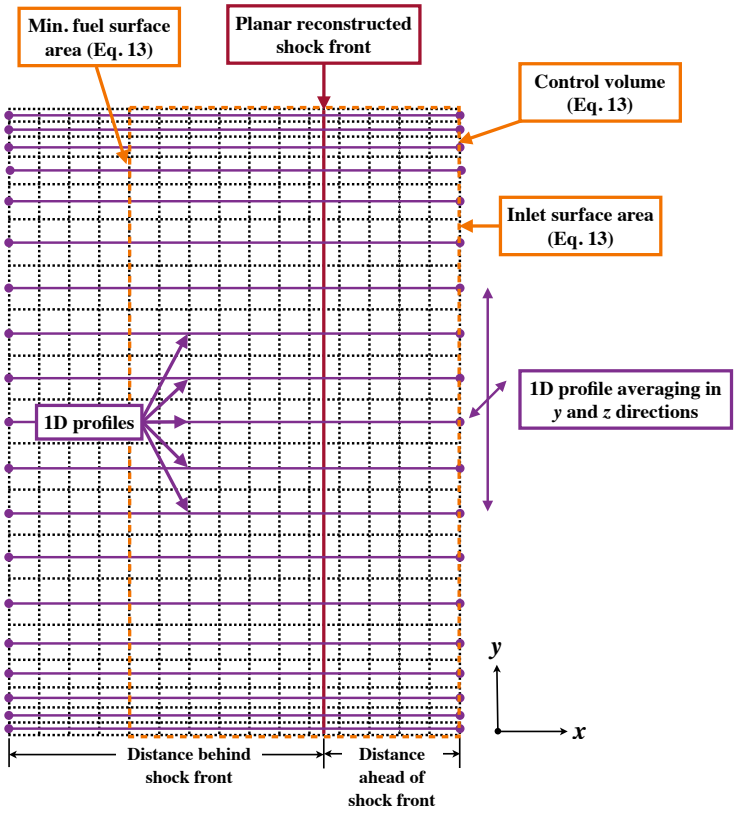

Figure A.3: Schematic of the planar shock front with one-dimensional profiles corresponding to each element aligned to the shock location on the reconstructed shock front surface. The schematic is given for a single two-dimensional plane but extends similarly to all depthwise planes.

A.3 Instantaneous wave velocity computation

The wave speed is calculated using the surface normal direction across the shock-front surface, outlined in Fig. A.4. At the subsequent snapshot (output at a temporal spacing of $\Delta t_{\text{snapshot}} = 250$ ns), the intersection of the wave front surface at time $t+\Delta t_{\text{snapshot}}$ with this previously-determined surface normal line at time t is computed to the nearest grid point. The Euclidean distance between this intersection point at time $t + \Delta t_{\text{snapshot}}$ and cell center (which the surface normal points from) at the preceding snapshot is calculated. Thus, although the primary wave front motion is in the x direction, this algorithm accounts for wave front motion in the y/z directions. With $\Delta t_{\text{snapshot}} = 250$ ns, the wave front location travels between 8-12 grid points between snapshots. Furthermore, when the wave front is not aligned with the x direction, the Euclidean distance is not solely multiples of the grid resolution in the x directions. The grid resolution in the x and y/z directions are not equal in the core region.

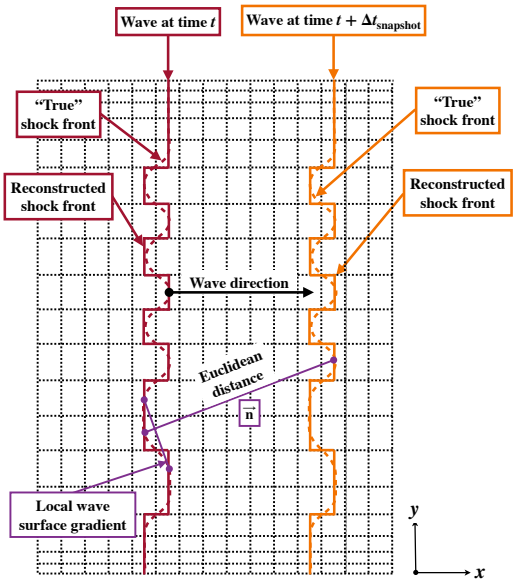

Figure A.4: Schematic of the computation of instantaneous shock front velocity in Sec. 3.2.3.1. The schematic is projected onto two-dimensions but the surface normal vector can span all three dimensions.

BIBLIOGRAPHY

BIBLIOGRAPHY

[1] Akbari, P., and M. R. Nalim (2009), Review of recent developments in wave rotor combustion technology, *Journal of Propulsion and Power*, *25*(4), 833–844, doi:10.2514/1.34081.

[2] Alexander, F., et al. (2020), Exascale applications: skin in the game, *Philosophical Transactions of the Royal Society A: Mathematical, Physical and Engineering Sciences*, *378*(2166), 20190,056, doi:10.1098/rsta.2019.0056.

[3] Anand, V., and E. Gutmark (2019), Rotating detonation combustors and their similarities to rocket instabilities, *Progress in Energy and Combustion Science*, *73*, 182–234.

[4] Anand, V., A. S. George, R. Driscoll, and E. Gutmark (2015), Characterization of instabilities in a rotating detonation combustor, *International Journal of Hydrogen Energy*, *40*(46), 16,649–16,659.

[5] Anand, V., A. St. George, R. Driscoll, and E. Gutmark (2016), Investigation of rotating detonation combustor operation with H_2-air mixtures, *International Journal of Hydrogen Energy*, *41*(2), 1281–1292, doi: https://doi.org/10.1016/j.ijhydene.2015.11.041.

[6] Anand, V., A. S. George, and E. Gutmark (2017), Amplitude modulated instability in reactants plenum of a rotating detonation combustor, *International Journal of Hydrogen Energy*, *42*(17), 12,629–12,644, doi: 10.1016/j.ijhydene.2017.03.218.

[7] Anand, V., L. Babu, and E. Gutmark (2021), Observations of DC shift and chugging in a pressurized rotating detonation combustor, *Acta Astronautica*, *187*, 362–369, doi:10.1016/j.actaastro.2021.06.019.

[8] ANSYS, Inc. (2019), Ansys® Fluent Meshing, Release 19.1.

[9] Araki, T., K. Yoshida, Y. Morii, N. Tsuboi, and A. K. Hayashi (2016), Numerical analyses on ethylene/oxygen detonation with multistep chemical reaction mechanisms: Grid resolution and chemical reaction model, *Combustion Science and Technology*, *188*(3), 346–369.

[10] Athmanathan, V., K. A. Rahman, D. K. Lauriola, J. Braun, G. Paniagua, M. N. Slipchenko, S. Roy, and T. R. Meyer (2021), Femtosecond/picosecond

rotational coherent anti-stokes raman scattering thermometry in the exhaust of a rotating detonation combustor, *Combustion and Flame*, *231*, 111,504, doi: 10.1016/j.combustflame.2021.111504.

[11] Ausserer, J., and F. Harmon (), *Integration, Validation, and Testing of a Hybrid-Electric Propulsion System for a Small Remotely Piloted Aircraft*, doi: 10.2514/6.2012-4239.

[12] Bach, E., P. Stathopoulos, C. O. Paschereit, and M. D. Bohon (2020), Performance analysis of a rotating detonation combustor based on stagnation pressure measurements, *Combustion and Flame*, *217*, 21–36, doi: https://doi.org/10.1016/j.combustflame.2020.03.017.

[13] Barwey, S. (2022), High-fidelity simulations of rotating detonation engines, Ph.D. thesis, University of Michigan.

[14] Barwey, S., and V. Raman (2021), Impact of operator splitting schemes on detonation convergence, *Bulletin of the American Physical Society*, *66*.

[15] Barwey, S., and V. Raman (2021), A neural network-inspired matrix formulation of chemical kinetics for acceleration on GPUs, *Energies*, *14*(9), 2710, doi:10.3390/en14092710.

[16] Barwey, S., S. Prakash, M. Hassanaly, and V. Raman (2021), Data-driven classification and modeling of combustion regimes in detonation waves, *Flow, Turbulence and Combustion*, *106*(4), 1065–1089, doi:10.1007/s10494-020-00176-4.

[17] Batista, A., M. Ross, C. Lietz, and W. A. Hargus (), Descending modal transition study in a rotating detonation rocket engine, in *AIAA Scitech 2021 Forum*, Paper No. AIAA-2021-0191, 2021.

[18] Batten, P., N. Clarke, C. Lambert, and D. M. Causon (1997), On the choice of wavespeeds for the hllc riemann solver, *SIAM Journal on Scientific Computing*, *18*(6), 1553–1570, doi:10.1137/S1064827593260140.

[19] Bedick, C., D. Ferguson, and P. Strakey (2019), Characterization of rotating detonation engine injector response using laser-induced fluorescence, *Journal of Propulsion and Power*, *35*(4), 827–838, doi:10.2514/1.b37309.

[20] Bennewitz, J. W., B. R. Bigler, W. A. Hargus, S. A. Danczyk, and R. D. Smith (2018), Characterization of detonation wave propagation in a rotating detonation rocket engine using direct high-speed imaging, in *2018 Joint Propulsion Conference*, Paper No. AIAA-2018-4688, doi:10.2514/6.2018-4688.

[21] Bennewitz, J. W., B. R. Bigler, J. J. Pilgram, and J. William A. Hargus (2019), Modal transitions in rotating detonation rocket engines, *International Journal of Energetic Materials and Chemical Propulsion*, *18*(2), 91–109.

[22] Bennewitz, J. W., B. R. Bigler, S. A. Schumaker, and W. A. Hargus (2019), Automated image processing method to quantify rotating detonation wave behavior, *Review of Scientific Instruments*, *90*(6), 065,106, doi:10.1063/1.5067256.

[23] Bennewitz, J. W., J. R. Burr, and C. F. Lietz (2021), Characteristic timescales for rotating detonation rocket engines, in *AIAA Propulsion and Energy 2021 Forum*, doi:10.2514/6.2021-3671, paper No. AIAA-2021-3671.

[24] Benson, C. M., J. M. Ingram, P. N. Battersby, D. Mba, V. Sethi, and A. M. Rolt (2019), An Analysis of Civil Aviation Industry Safety Needs for the Introduction of Liquid Hydrogen Propulsion Technology, doi:10.1115/GT2019-90453.

[25] Berger, J. O., et al. (1994), An overview of robust bayesian analysis, *Test*, *3*(1), 5–124, doi:10.1007/BF02562676.

[26] Bielawski, R., S. Barwey, S. Prakash, and V. Raman (2022), Highly-scalable gpu-accelerated compressible reacting solver for shock-containing flows, *Computers & Fluids*, in preparation.

[27] Bielawski, R., S. Prakash, and V. Raman (2022), Thermodynamic modeling of a rotating detonation engine through aquid-gas colliding jets impacted by a detonation wave, *Proceedings of the 28th International Colloquium on the Dynamics of Explosions and Reactive Systems (ICDERS)*.

[28] Bigler, B. R., J. R. Burr, J. W. Bennewitz, S. Danczyk, and W. A. Hargus (2020), Performance effects of mode transitions in a rotating detonation rocket engine, in *AIAA Propulsion and Energy 2020 Forum*, doi:10.2514/6.2020-3852, paper No. AIAA-2020-3852.

[29] Bilger, R. W. (1993), Conditional moment closure for turbulent reacting flow, *Physics of Fluids*, *5*(2), 436–444.

[30] Boeck, L. R., F. M. Berger, J. Hasslberger, and T. Sattelmayer (2016), Detonation propagation in hydrogen–air mixtures with transverse concentration gradients, *Shock Waves*, *26*(2), 181–192, doi:10.1007/s00193-015-0598-8.

[31] Bonfiglio, L., P. Perdikaris, S. Brizzolara, and G. Karniadakis (2017), A multifidelity framework for investigating the performance of super-cavitating hydrofoils under uncertain flow conditions, Paper No. AIAA-2017-1328.

[32] Boulal, S., P. Vidal, and R. Zitoun (2016), Experimental investigation of detonation quenching in non-uniform compositions, *Combust. Flame*, *172*, 222 – 233, doi:10.1016/j.combustflame.2016.07.022.

[33] Boyce, M. P. (2011), *Gas Turbine Engineering Handbook*, Butterworth-Heinemann, Oxford, UK.

[34] Braman, K., T. A. Oliver, and V. Raman (2013), Bayesian analysis of syngas chemistry models, *Combustion Theory and Modelling*, *17*(5), 858–887.

[35] Brand, J., S. Sampath, F. Shum, R. Bayt, and J. Cohen (), *Potential Use of Hydrogen In Air Propulsion*, doi:10.2514/6.2003-2879.

[36] Brochu, E., V. M. Cora, and N. De Freitas (2010), A tutorial on bayesian optimization of expensive cost functions, with application to active user modeling and hierarchical reinforcement learning, *arXiv preprint arXiv:1012.2599*.

[37] Brown, P. N., G. D. Byrne, and A. C. Hindmarsh (1989), Vode: A variable-coefficient ode solver, *SIAM Journal on Scientific and Statistical Computing*, *10*(5), 1038–1051, doi:10.1137/0910062.

[38] Burr, J., and K. H. Yu (2015), Shock in reactive crossflow under partial confinement, *25th International Colloquium on the Dynamics of Explosions and Reactive Systems*.

[39] Burr, J. R., and E. Paulson (2021), Thermodynamic performance results for rotating detonation rocket engine with distributed heat addition using cantera, in *AIAA Propulsion and Energy 2021 Forum*, Paper No. AIAA-2021-3682, doi: 10.2514/6.2021-3682.

[40] Burr, J. R., and K. Yu (2017), Detonation wave propagation in cross-flow of discretely spaced reactant jets, in *53rd AIAA/SAE/ASEE Joint Propulsion Conference*, p. 4908, doi:10.2514/6.2017-4908.

[41] Burr, J. R., and K. Yu (2019), Characterization of CH_4-O_2 detonation in unwrapped RDE channel combustor, Paper No. AIAA-2019-4215, doi: 10.2514/6.2019-4215.

[42] Burr, J. R., and K. H. Yu (2014), Blast wave propagation in cross-flow of detonable mixture, in *50th AIAA/ASME/SAE/ASEE Joint Propulsion Conference*, Paper No. AIAA-2014-3984, doi:10.2514/6.2014-3984.

[43] Burr, J. R., and K. H. Yu (2016), Detonation reignition within a rotating detonation engine, in *54th AIAA Aerospace Sciences Meeting*, Paper No. AIAA-2016-1202, doi:10.2514/6.2016-1202.

[44] Bykovskii, F. A., S. A. Zhdan, and E. F. Vedernikov (2006), Continuous spin detonations, *Journal of Propulsion and Power*, *22*(6), 1204–1216, doi: 10.2514/1.17656.

[45] Bykovskii, F. A., S. A. Zhdan, and E. F. Vedernikov (2008), Continuous spin detonation of hydrogen-oxygen mixtures. 1. annular cylindrical combustors, *Combustion, Explosion, and Shock Waves*, *44*(2), 150–162, doi:10.1007/s10573-008-0021-1.

[46] Bykovskii, F. A., S. A. Zhdan, and E. F. Vedernikov (2019), Continuous detonation of the liquid kerosene—air mixture with addition of hydrogen or syngas, *Combustion, Explosion, and Shock Waves*, *55*(5), 589–598, doi: 10.1134/S0010508219050101.

[47] California Institute of Technology Explosion Dynamics Laboratory (2021), Shock and detonation toolbox.

[48] Chacon, F. (2020), Non-ideal phenomena in rotating detonation combustors, Ph.D. thesis, University of Michigan.

[49] Chacon, F., and M. Gamba (2018), Development of an optically accessible continuous wave rotating detonation engine, in *2018 Joint Propulsion Conference*, Paper No. AIAA-2018-4779, doi:10.2514/6.2018-4779.

[50] Chacon, F., and M. Gamba (2019), Study of parasitic combustion in an optically accessible continuous wave rotating detonation engine, *AIAA Scitech 2019 Forum*, doi:10.2514/6.2019-0473, paper No. AIAA-2019-0473.

[51] Chacon, F., and M. Gamba (2019), OH PLIF visualization of an optically accessible rotating detonation combustor, in *AIAA Propulsion and Energy 2019 Forum*, doi:10.2514/6.2019-4217, paper No. AIAA-2019-4217.

[52] Chacon, F., and M. Gamba (2019), Detonation wave dynamics in a rotating detonation engine, in *AIAA Scitech 2019 Forum*, doi:10.2514/6.2019-0198, paper No. AIAA-2019-0198.

[53] Chacon, F., A. Feleo, and M. Gamba (2019), Impact of inlet area ratio on the operation of an axial air inlet configuration rotating detonation combustor, in *AIAA Propulsion and Energy 2019 Forum*, doi:10.2514/6.2019-4450, paper No. AIAA 2019-4450.

[54] Cheatham, S., and K. Kailasanath (2005), Numerical modelling of liquid-fuelled detonations in tubes, *Combustion Theory and Modelling*, *9*(1), 23–48, doi:10.1080/13647830500051786.

[55] Chiesa, P., G. Lozza, and L. Mazzocchi (2005), Using Hydrogen as Gas Turbine Fuel , *Journal of Engineering for Gas Turbines and Power*, *127*(1), 73–80, doi:10.1115/1.1787513.

[56] Cho, K. Y., J. R. Codoni, B. A. Rankin, J. L. Hoke, and F. R. Schauer (2016), High-repetition-rate chemiluminescence imaging of a rotating detonation engine, in *54th AIAA Aerospace Sciences Meeting*, Paper No. AIAA-2016-1648.

[57] Chong, S. T., M. Hassanaly, H. Koo, M. E. Mueller, V. Raman, and K.-P. Geigle (2018), Large eddy simulation of pressure and dilution-jet effects on soot formation in a model aircraft swirl combustor, *Combustion and Flame*, *192*, 452–472, doi:10.1016/j.combustflame.2018.02.021.

[58] Chong, S. T., V. Raman, M. E. Mueller, P. Selvaraj, and H. G. Im (2018), Effect of soot model, moment method, and chemical kinetics on soot formation in a model aircraft combustor, *Proceedings of the Combustion Institute*, doi:10.1016/j.proci.2018.06.093.

[59] Ciccarelli, G., T. Ginsberg, J. Boccio, C. Economos, K. Sato, and M. Kinoshita (1994), Detonation cell size measurements and predictions in hydrogen-air-steam mixtures at elevated temperatures, *Combust. Flame*, *99*(2), 212 – 220, doi:10.1016/0010-2180(94)90124-4.

[60] Claflin, S., E. D. Lynch, and J. Stout (2015), Rotating detonation combustion for gas turbines – modeling and system synthesis to exceed 65% efficiency goal, in *2015 University Turbine Systems Research Workshop, November 3 - 5, 2015*.

[61] Cocks, P. A., A. T. Holley, and B. A. Rankin (2016), High fidelity simulations of a non-premixed rotating detonation engine, in *54th AIAA Aerospace Sciences Meeting*, Paper No. AIAA-2016-0125, doi:10.2514/6.2016-0125.

[62] Connolly-Boutin, S., V. Joseph, H. Ng, and C. Kiyanda (2021), Small-size rotating detonation engine: scaling and minimum mass flow rate, *Shock Waves*, *31*(7), 665–674.

[63] Courant, R., and K. O. Friedrichs (1999), *Supersonic flow and shock waves*, vol. 21, Springer Science & Business Media.

[64] Dausen, D., C. Brophy, R. Wright, and J. Marder (2012), Design of an optically-accessible rotating detonation engine, in *48th AIAA/ASME/SAE/ASEE Joint Propulsion Conference & Exhibit*, p. 3944.

[65] Davidson, T. A. (1993), *A simple and accurate method for calculating viscosity of gaseous mixtures*, vol. 9456, US Department of the Interior, Bureau of Mines.

[66] Del Rosario, R. (2014), A future with hybrid electric propulsion systems: A NASA perspective, in *Turbine Engine Technology Symposium*, GRC-E-DAA-TN17600.

[67] Depperschmidt, D., R. Miller, J. Tobias, M. Uddi, A. K. Agrawal, and J. B. Stout (2019), Time-resolved PIV diagnostics to measure flow field exiting methane-fueled rotating detonation combustor, in *AIAA Scitech 2019 Forum*, Paper No. AIAA-2019-1514, doi:10.2514/6.2019-1514.

[68] Donde, P., H. Koo, and V. Raman (2012), A multivariate quadrature based moment method for les based modeling of supersonic combustion, *Journal of Computational Physics*, *231*(17), 5805 – 5821, doi:10.1016/j.jcp.2012.04.031.

[69] Driscoll, R. (2016), Investigation of sustained detonation devices: the pulse detonation engine-crossover system and the rotating detonation engine system, Ph.D. thesis, University of Cincinnati.

[70] Drozda, T. G., R. Shenoy, E. L. Axdahl, and R. A. Baurle (2019), Numerical investigation and optimization of a flushwall injector for scramjet applications at hypervelocity flow conditions, Paper No. AIAA-2019-4196.

[71] Ducros, F., V. Ferrand, F. Nicoud, C. Weber, D. Darracq, C. Gacherieu, and T. Poinsot (1999), Large-eddy simulation of the shock/turbulence interaction, *Journal of Computational Physics*, *152*(2), 517–549.

[72] Dunn, I. B., K. Thurmond, K. A. Ahmed, and S. Vasu (2018), Exploration of measuring pressure gain combustion within a rotating detonation engine, in *2018 Joint Propulsion Conference*, Paper No. AIAA-2018-4566, doi: 10.2514/6.2018-4566.

[73] Duvall, J., F. Chacon, C. Harvey, and M. Gamba (2018), Study of the effects of various injection geometries on the operation of a rotating detonation engine, in *2018 AIAA Aerospace Sciences Meeting*, Paper No. AIAA-2018-0631, doi: 10.2514/6.2018-0631.

[74] Eswaran, V., and S. B. Pope (1988), Direct numerical simulations of the turbulent mixing of a passive scalar, *The Physics of Fluids*, *31*(3), 506–520, doi: 10.1063/1.866832.

[75] Ettner, F., K. Vollmer, and T. Sattelmayer (2013), Mach reflection in detonations propagating through a gas with a concentration gradient, *Shock Waves*, *23*(3), 201–206.

[76] Feleo, A., J. France, L. W. White, and M. Gamba (2019), Evaluation of OH emission for determining operation of a rotating detonation engine, in *AIAA Scitech 2019 Forum*, Paper No. AIAA-2019-2252, doi:10.2514/6.2019-2252.

[77] Ferguson, D. H., B. O'Meara, A. Roy, and K. Johnson (2020), Experimental measurements of NOx emissions in a rotating detonation engine, in *AIAA Scitech 2020 Forum*, Paper No. AIAA-2020-0204, doi:10.2514/6.2020-0204.

[78] Fievet, R. (2018), Impact of vibrational nonequilibrium on the simulation and modeling of dual-mode scramjets, Ph.D. thesis, University of Michigan.

[79] Fiévet, R., and V. Raman (2016), Direct numerical simulation of a normal shock train with thermal nonequilibrium, in *APS Division of Fluid Dynamics Meeting Abstracts*, L5.003.

[80] Fiévet, R., and V. Raman (2018), Effect of vibrational nonequilibrium on isolator shock structure, *Journal of Propulsion and Power*, *34*(5), 1334–1344, doi: 10.2514/1.B37108.

[81] Fiévet, R., H. Koo, and V. Raman (2015), Numerical simulation of a scramjet isolator with thermodynamic nonequilibrium, in *22nd AIAA Computational Fluid Dynamics Conference*, p. 3418, doi:10.2514/6.2015-3418.

[82] Fiévet, R., S. Voelkel, H. Koo, V. Raman, and P. L. Varghese (2017), Effect of thermal nonequilibrium on ignition in scramjet combustors, *Proceedings of the Combustion Institute*, *36*(2), 2901–2910.

[83] Fiévet, R., S. J. Voelkel, V. Raman, and P. L. Varghese (2017), Numerical investigation of vibrational relaxation coupling with turbulent mixing, AIAA SciTech Forum, American Institute of Aeronautics and Astronautics, doi:10.2514/6.2017-0663.

[84] Fiévet, R., V. Raman, and A. H. Auslender (2019), Data-driven one-dimensional modeling of pseudoshocks, *Journal of Propulsion and Power*, *35*(2), 313–327, doi:10.2514/1.B37175.

[85] Fievisohn, R. T., and K. H. Yu (2016), Parametric study of an ethylene-air rotating detonation engine using an ideal model, in *54th AIAA Aerospace Sciences Meeting*, Paper No. AIAA-2016-1403, doi:10.2514/6.2016-1403.

[86] Fievisohn, R. T., K. Y. Cho, J. L. Hoke, and F. R. Schauer (2019), Experimental study of a linear RDE section coupled to an operating RDE, in *AIAA Scitech 2019 Forum*, doi:10.2514/6.2019-1251, paper No. AIAA-2019-1251.

[87] Fievisohn, R. T., J. Hoke, R. T. Battelle, C. Klingshirn, A. T. Holley, and S. A. Schumaker (2021), Closed loop integration of a rotating detonation combustor in a T63 gas turbine engine, in *AIAA Scitech 2021 Forum*, doi:10.2514/6.2021-0900, paper No. AIAA-2021-0900.

[88] Fotia, M. L., F. Schauer, T. Kaemming, and J. Hoke (2016), Experimental study of the performance of a rotating detonation engine with nozzle, *Journal of Propulsion and Power*, *32*(3), 674–681, doi:10.2514/1.B35913.

[89] Frazier, P. I. (2018), *Bayesian Optimization*, chap. 11, pp. 255–278, doi:10.1287/educ.2018.0188.

[90] Friedrich, C., and P. Robertson (2015), Hybrid-electric propulsion for aircraft, *Journal of Aircraft*, *52*(1), 176–189, doi:10.2514/1.C032660.

[91] Frolov, S., V. Aksenov, V. Ivanov, and I. Shamshin (2015), Large-scale hydrogen–air continuous detonation combustor, *International Journal of Hydrogen Energy*, *40*(3), 1616–1623, doi:https://doi.org/10.1016/j.ijhydene.2014.11.112.

[92] Frolov, S., V. Smetanyuk, V. Ivanov, and B. Basara (2021), The influence of the method of supplying fuel components on the characteristics of a rotating detonation engine, *Combustion Science and Technology*, *193*(3), 511–538.

[93] Frolov, S. M., V. Aksenov, and V. Ivanov (2015), Experimental proof of zel'dovich cycle efficiency gain over cycle with constant pressure combustion for hydrogen–oxygen fuel mixture, *International Journal of Hydrogen Energy*, *40*(21), 6970–6975, doi:https://doi.org/10.1016/j.ijhydene.2015.03.128.

[94] Frolov, S. M., V. S. Aksenov, V. S. Ivanov, S. N. Medvedev, I. O. Shamshin, N. N. Yakovlev, and I. I. Kostenko (2018), Rocket engine with continuous detonation combustion of the natural gas-oxygen propellant system, *Doklady Phys. Chemistry*, *478*(2), 31–34, doi:10.1134/S001250161802001X.

[95] Fujii, J., Y. Kumazawa, A. Matsuo, S. Nakagami, K. Matsuoka, and J. Kasahara (2017), Numerical investigation on detonation velocity in rotating detonation engine chamber, *Proceedings of the Combustion Institute*, *36*(2), 2665–2672, doi:10.1016/j.proci.2016.06.155.

[96] Gaillard, T., D. Davidenko, and F. Dupoirieux (2015), Numerical optimisation in non reacting conditions of the injector geometry for a continuous detonation wave rocket engine, *Acta Astronautica*, *111*, 334 – 344, doi: https://doi.org/10.1016/j.actaastro.2015.02.006.

[97] Gamezo, V., D. Desbordes, and E. Oran (1999), Formation and evolution of two-dimensional cellular detonations, *Combust. Flame*, *116*(1), 154 – 165, doi: 10.1016/S0010-2180(98)00031-5.

[98] Gelfand, B., S. Frolov, and M. Nettleton (1991), Gaseous detonations—a selective review, *Progress in Energy and Combustion Science*, *17*(4), 327–371, doi:https://doi.org/10.1016/0360-1285(91)90007-A.

[99] George, A. S., R. Driscoll, V. Anand, and E. Gutmark (2017), On the existence and multiplicity of rotating detonations, *Proceedings of the Combustion Institute*, *36*(2), 2691–2698.

[100] Geuzaine, C., and J.-F. Remacle (2009), Gmsh: A 3-d finite element mesh generator with built-in pre- and post-processing facilities, *International Journal for Numerical Methods in Engineering*, *79*(11), 1309–1331, doi: https://doi.org/10.1002/nme.2579.

[101] Ghanem, R., and J. Red-Horse (1999), Propagation of probabilistic uncertainty in complex physical systems using a stochastic finite element approach, *Physica D: Nonlinear Phenomena*, *133*(1), 137–144, doi:https://doi.org/10.1016/S0167-2789(99)00102-5.

[102] Goodman, J., and J. Weare (2010), Ensemble samplers with affine invariance, *Communications in applied mathematics and computational science*, *5*(1), 65–80.

[103] Goodwin, D. G., R. L. Speth, H. K. Moffat, and B. W. Weber (2021), Cantera: An object-oriented software toolkit for chemical kinetics, thermodynamics, and transport processes, doi:10.5281/zenodo.4527812, version 2.5.1.

[104] Goto, K., et al. (2021), Cylindrical rotating detonation engine with propellant injection cooling, *Journal of Propulsion and Power*, pp. 1–11.

[105] Goto, K., et al. (2021), Thrust validation of rotating detonation engine system by moving rocket sled test, *Journal of Propulsion and Power*, *37*(3), 419–425, doi:10.2514/1.B38037.

[106] Goto, K., et al. (2022), Flight demonstration of detonation engine system using sounding rocket S-520-31: Performance of rotating detonation engine, in *AIAA Scitech 2022 Forum*, doi:10.2514/6.2022-0232, paper No. AIAA-2022-0232.

[107] GPy (2012), GPy: A gaussian process framework in python, http://github.com/SheffieldML/GPy.

[108] Gratiet, L. L., and J. Garnier (2014), Recursive co-kriging model for design of computer experiments with multiple levels of fidelity, *International Journal for Uncertainty Quantification*, *4*(5), 365–386.

[109] Greenshields, C. J., H. G. Weller, L. Gasparini, and J. M. Reese (2010), Implementation of semi-discrete, non-staggered central schemes in a colocated, polyhedral, finite volume framework, for high-speed viscous flows, *International journal for numerical methods in fluids*, *63*(1), 1–21.

[110] Grinsted, A. (2022), Ensemble mcmc sampler, gitHub, https://github.com/grinsted/gwmcmc.

[111] Hagan, M., and M. Menhaj (1994), Training feedforward networks with the marquardt algorithm, *IEEE Transactions on Neural Networks*, *5*(6), 989–993, doi:10.1109/72.329697.

[112] Han, H.-S., E. S. Lee, and J.-Y. Choi (2021), Experimental investigation of detonation propagation modes and thrust performance in a small rotating detonation engine using c_2h_4/o_2 propellant, *Energies*, *14*(5), doi:10.3390/en14051381.

[113] Han, W., Y. Gao, and C. K. Law (2017), Flame acceleration and deflagration-to-detonation transition in micro- and macro-channels: An integrated mechanistic study, *Combustion and Flame*, *176*, 285–298, doi: https://doi.org/10.1016/j.combustflame.2016.10.010.

[114] Han, W., C. Wang, and C. K. Law (2019), Role of transversal concentration gradient in detonation propagation, *Journal of Fluid Mechanics*, *865*, 602–649.

[115] Hassanaly, M., V. Raman, H. Koo, and M. B. Colket (), Influence of fuel stratification on turbulent flame propagation, in *53rd AIAA Aerospace Sciences Meeting*, doi:10.2514/6.2015-0426, paper No. AIAA-2015-0426.

[116] Hassanaly, M., H. Koo, L. C. F., S. T. Chong, and V. Raman (2018), A minimally-dissipative low-mach number solver for complex reacting flows in OpenFOAM, *Computer and Fluids*, *162*, 11–25, doi: 10.1016/j.compfluid.2017.11.020.

[117] Hayashi, A. K., N. Tsuboi, and E. Dzieminska (2020), Numerical study on JP-10/air detonation and rotating detonation engine, *AIAA Journal*, *58*(12), 5078–5094.

[118] Hayashi, A. K., K. Ishii, T. Watanabe, N. Tsuboi, K. Ozawa, N. Jourdaine, E. Dzieminska, and X. Tang (2021), Experimental and numerical study on disc-RDE: Flow structure and its performances, in *AIAA Scitech 2021 Forum*, doi:10.2514/6.2021-1253, paper No. AIAA-2021-1253.

[119] Hayashi, A. K., et al. (2020), Recent experimental and numerical study on disc-type rdes, in *AIAA Scitech 2020 Forum*, doi:10.2514/6.2020-1169, paper No. AIAA-2020-1169.

[120] Hayashi, A. K., et al. (2021), 3D numerical study on flow field in disc-RDE, in *AIAA Scitech 2021 Forum*, doi:10.2514/6.2021-3665, paper No. AIAA-2021-3665.

[121] Heiser, W. H., and D. T. Pratt (2002), Thermodynamic cycle analysis of pulse detonation engines, *Journal of Propulsion and Power*, *18*(1), 68–76, doi:10.2514/2.5899.

[122] Heister, S. D., and D. P. Stechmann (2014), Survey of rotating detonation wave combustor technology and potential rocket vehicle applications, 50th AIAA/ASME/SAE/ASEE Joint Propulsion Conference, doi:10.2514/6.2014-3902.

[123] Herrmann, M., G. Blanquart, and V. Raman (2006), Flux corrected finite volume scheme for preserving scalar boundedness in reacting large-eddy simulations, *AIAA Journal*, *44*(12), 2879–2886, doi:10.2514/1.18235.

[124] Higashi, J., S. Nakagami, K. Matsuoka, J. Kasahara, A. Matsuo, I. Funaki, and H. Moriai (2017), Experimental study of the disk-shaped rotating detonation turbine engine, in *55th AIAA Aerospace Sciences Meeting*, doi:10.2514/6.2017-1286, paper No. AIAA-2017-1286.

[125] Hindmarsh, A. C. (1983), Odepack: A systemized collection of ode solvers, *Scientific computing*, pp. 55–64.

[126] Hishida, M., T. Fujiwara, and P. Wolanski (2009), Fundamentals of rotating detonations, *Shock waves*, *19*(1), 1–10.

[127] Hoke, J., R. Bradley, and F. Schauer (2008), Single-ejector augmentation of a multi-tube pulsed detonation engine, in *46th AIAA Aerospace Sciences Meeting and Exhibit*, Paper No. AIAA-2008-115.

[128] Honein, A. E., and P. Moin (2004), Higher entropy conservation and numerical stability of compressible turbulence simulations, *Journal of Computational Physics*, *201*(2), 531–545, doi:https://doi.org/10.1016/j.jcp.2004.06.006.

[129] Houim, R. W., and R. T. Fievisohn (2017), The influence of acoustic impedance on gaseous layered detonations bounded by an inert gas, *Combustion and Flame*, *179*, 185–198, doi:https://doi.org/10.1016/j.combustflame.2017.02.001.

[130] Huff, R., M. D. Polanka, M. J. McClearn, F. R. Schauer, M. L. Fotia, and J. L. Hoke (2019), Design and operation of a radial rotating detonation engine, *Journal of Propulsion and Power*, *35*(6), 1143–1150, doi:10.2514/1.B37578.

[131] Huffman, M., A. Holley, T. Kaemming, J. Hoke, S. Prakash, V. Raman, J. Shepard, A. Feleo, and M. Gamba (2022), Development of a rotating detonation engine cycle-deck calibration methodology, in *69th JANNAF Propulsion Meeting (JPM)*.

[132] Humble, J., and S. D. Heister (2021), Heterogeneous detonation physics as applied to high pressure rotating detonation engines, in *AIAA Scitech 2021 Forum*, Paper No. AIAA-2021-1027, doi:10.2514/6.2021-1027.

[133] Ishii, K., and M. Kojima (2007), Behavior of detonation propagation in mixtures with concentration gradients, *Shock Waves*, *17*(1), 95–102, doi:10.1007/s00193-007-0093-y.

[134] Ivanov, V. S., S. M. Frolov, S. S. Sergeev, Y. M. Mironov, A. E. Novikov, and I. I. Schultz (2021), Pressure measurements in detonation engines, *Proceedings of the Institution of Mechanical Engineers, Part G: Journal of Aerospace Engineering*, *235*(14), 2113–2134.

[135] Jasak, H. (2009), Openfoam: open source cfd in research and industry, *International Journal of Naval Architecture and Ocean Engineering*, *1*(2), 89–94.

[136] Jiang, G., and D. Peng (2000), Weighted eno schemes for hamilton–jacobi equations, *SIAM Journal on Scientific Computing*, *21*(6), 2126–2143, doi:10.1137/S106482759732455X.

[137] Jin, S., H. Zhang, N. Zhao, and H. Zheng (2022), Simulations of rotating detonation combustion with in-situ evaporating bi-disperse n-heptane sprays, *Fuel*, *314*, 123,087, doi:https://doi.org/10.1016/j.fuel.2021.123087.

[138] Johnsen, E., et al. (2010), Assessment of high-resolution methods for numerical simulations of compressible turbulence with shock waves, *Journal of Computational Physics*, *229*(4), 1213–1237.

[139] Kaemming, T., M. L. Fotia, J. Hoke, and F. Schauer (2017), Thermodynamic modeling of a rotating detonation engine through a reduced-order approach, *Journal of Propulsion and Power*, *33*(5), 1170–1178, doi:10.2514/1.b36237.

[140] Kaemming, T. A., and D. E. Paxson (2018), Determining the pressure gain of pressure gain combustion, in *2018 Joint Propulsion Conference*, Paper No. AIAA-2018-4567, doi:10.2514/6.2018-4567.

[141] Kailasanath, K. (2003), Recent developments in the research on pulse detonation engines, *AIAA Journal*, *41*(2), 145–159, doi:10.2514/2.1933.

[142] Kailasanath, K. (2017), Recent developments in the research on rotating-detonation-wave engines, in *55th AIAA Aerospace Sciences Meeting*, doi: 10.2514/6.2017-0784, paper No. AIAA-2017-0784.

[143] Kailasanath, K., and D. A. Schwer (2017), High-fidelity simulations of pressure-gain combustion devices based on detonations, *Journal of Propulsion and Power*, *33*(1), 153–162, doi:10.2514/1.B36169.

[144] Kailasanath, K., E. Oran, J. Boris, and T. Young (1985), Determination of detonation cell size and the role of transverse waves in two-dimensional detonations, *Combustion and Flame*, *61*(3), 199–209.

[145] Kass, R. E., and L. Wasserman (1996), The selection of prior distributions by formal rules, *Journal of the American Statistical Association*, *91*(435), 1343–1370, doi:10.1080/01621459.1996.10477003.

[146] Kee, R. J., F. M. Rupley, and J. A. Miller (1989), Chemkin-II: A fortran chemical kinetics package for the analysis of gas-phase chemical kinetics, *Tech. rep.*, United States, sAND89-8009B.

[147] Kennedy, M. C., and A. O'Hagan (2000), Interpolation of spatial data: some theory for kriging, *Biometrika*, *87*(1), 1–13.

[148] Kessler, D., V. Gamezo, and E. Oran (2011), Multilevel detonation cell structures in methane-air mixtures, *Proceedings of the Combustion Institute*, *33*(2), 2211–2218, doi:https://doi.org/10.1016/j.proci.2010.07.071.

[149] Kessler, D., V. Gamezo, and E. Oran (2012), Gas-phase detonation propagation in mixture composition gradients, *Philosophical Transactions of the Royal Society A: Mathematical, Physical and Engineering Sciences*, *370*(1960), 567–596.

[150] Khodadadi Azadboni, R., A. Heidari, L. R. Boeck, and J. X. Wen (2019), The effect of concentration gradients on deflagration-to-detonation transition in a rectangular channel with and without obstructions – a numerical study, *International Journal of Hydrogen Energy*, *44*(13), 7032–7040, doi: https://doi.org/10.1016/j.ijhydene.2019.01.157.

[151] Kindracki, J., P. Wolański, and Z. Gut (2011), Experimental research on the rotating detonation in gaseous fuels–oxygen mixtures, *Shock Waves*, *21*(2), 75–84, doi:10.1007/s00193-011-0298-y.

[152] Kindracki, J., S. Siatkowski, and B. Lukasik (2020), Influence of inlet flow parameters on rotating detonation, *AIAA Journal*, *58*(12), 5046–5051, doi: 10.2514/1.j058152.

[153] Kindracki, J., K. Wacko, P. Woźniak, S. Siatkowski, and Meżyk (2020), Influence of gaseous hydrogen addition on initiation of rotating detonation in liquid fuel–air mixtures, *Energies*, *13*(19).

[154] Knowlen, C., J. Koch, M. Kurosaka, and M. Washington (2019), Radial injector mixing effects on detonation zone position in rotating detonation engine, in *AIAA Propulsion and Energy 2019 Forum*, Paper No. AIAA-2019-4131, doi: 10.2514/6.2019-4131.

[155] Koch, J. (2021), Data-driven surrogates of rotating detonation engine physics with neural ordinary differential equations and high-speed camera footage, *Physics of Fluids*, *33*(9), 091,703.

[156] Koch, J., and J. N. Kutz (2020), Modeling thermodynamic trends of rotating detonation engines, *Physics of Fluids*, *32*(12), 126,102, doi:10.1063/5.0023972.

[157] Koo, H. (2011), Large-eddy simulations of scramjet engines, Ph.D. thesis, University of Texas at Austin.

[158] Koo, H., and V. Raman (2012), Large-eddy simulation of a supersonic inlet-isolator, *AIAA Journal*, *50*(7), 1596 – 1613, doi:10.2514/1.J051568.

[159] Koo, H., V. Raman, and P. L. Varghese (2015), Direct numerical simulation of supersonic combustion with thermal nonequilibrium, *Proceedings of the Combustion Institute*, *35*(2), 2145–2153.

[160] Kubicki, S. W., W. Anderson, and S. D. Heister (2020), Further experimental study of a hypergolically-ignited liquid-liquid rotating detonation rocket engine, in *AIAA Scitech 2020 Forum*, doi:10.2514/6.2020-0196, paper No. AIAA-2020-0196.

[161] Kurzke, J. (2009), Fundamental Differences Between Conventional and Geared Turbofans, pp. 145–153, doi:10.1115/GT2009-59745.

[162] Lee, J. H. S. (1984), Dynamic parameters of gaseous detonations, *Annual Review of Fluid Mechanics*, *16*(1), 311–336, doi: 10.1146/annurev.fl.16.010184.001523.

[163] Lele, S. K., and J. Larsson (2009), Shock-turbulence interaction: what we know and what we can learn from peta-scale simulations, in *Journal of Physics: Conference Series*, vol. 180, p. 012032, IOP Publishing.

[164] Lentsch, A., et al. (2005), Overview of current french activities on pdre and continuous detonation wave rocket engines, in *AIAA/CIRA 13th International Space Planes and Hypersonics Systems and Technologies Conference*, doi: 10.2514/6.2005-3232, paper No. AIAA-2005-3232.

[165] Leonard, B. (1979), A stable and accurate convective modelling procedure based on quadratic upstream interpolation, *Computer Methods in Applied Mechanics and Engineering*, *19*(1), 59–98, doi:https://doi.org/10.1016/0045-7825(79)90034-3.

[166] LeVeque, R. J. (2002), *Finite Volume Methods for Hyperbolic Problems*, Cambridge Texts in Applied Mathematics, Cambridge University Press, doi: 10.1017/CBO9780511791253.

[167] Levin, V. A., I. S. Manuĭlovich, and V. V. Markov (2010), New effects of stratified gas detonation, *Doklady Physics*, *55*, 28–32, doi: 10.1134/S1028335810010064.

[168] Li, C., K. Kailasanath, and E. S. Oran (1994), Detonation structures behind oblique shocks, *Physics of Fluids*, *6*(4), 1600–1611, doi:10.1063/1.868273.

[169] Lietz, C., Y. Desai, W. A. Hargus, and V. Sankaran (2019), Parametric investigation of rotating detonation rocket engines using large eddy simulations, in *AIAA Propulsion and Energy 2019 Forum*, doi:10.2514/6.2019-4129, paper No. AIAA-2019-4129.

[170] Lim, D., J. Humble, and S. D. Heister (2020), Experimental testing of an RP-2-GOX rotating detonation rocket engine, in *AIAA Scitech 2020 Forum*, doi: 10.2514/6.2020-0195, paper No. AIAA-2020-0195.

[171] Lisanti, J. C., and W. L. Roberts (Paper No. AIAA-2016-0899, January 2016), Design of an actively valved and acoustically resonant pulse combustor for pressure-gain combustion applications, doi:10.2514/6.2016-0899.

[172] Liu, Y., X. Sun, V. Sethi, D. Nalianda, Y.-G. Li, and L. Wang (2017), Review of modern low emissions combustion technologies for aero gas turbine engines, *Progress in Aerospace Sciences*, *94*, 12–45, doi: https://doi.org/10.1016/j.paerosci.2017.08.001.

[173] Liu, Z., J. Braun, and G. Paniagua (2020), Thermal power plant upgrade via a rotating detonation combustor and retrofitted turbine with optimized endwalls, *International Journal of Mechanical Sciences*, *188*, 105,918, doi: https://doi.org/10.1016/j.ijmecsci.2020.105918.

[174] Lu, F. K., and E. M. Braun (2014), Rotating detonation wave propulsion: Experimental challenges, modeling, and engine concepts, *Journal of Propulsion and Power*, *30*(5), 1125–1142, doi:10.2514/1.B34802.

[175] Lu, T., C. K. Law, and Y. Ju (2003), Some aspects of chemical kinetics in chapman-jouguet detonation: Induction length analysis, *Journal of Propulsion and Power*, *19*(5), 901–907, doi:10.2514/2.6181.

[176] Łukasik, B., A. Rowiński, A. Irzycki, and K. Snopkiewicz (2012), Study of combustion chamber with a rotating detonation, *Journal of KONES*, *19*, 313–320.

[177] Malik, V., et al. (2023), Detonation wave driven by aerosolized liquid RP-2 spray, *Proceedings of the Combustion Institute*.

[178] Marquardt, D. W. (1963), An algorithm for least-squares estimation of nonlinear parameters, *Journal of the Society for Industrial and Applied Mathematics*, *11*(2), 431–441, doi:10.1137/0111030.

[179] Masselot, D., R. Fiévet, and V. Raman (2017), Effect of equivalence ratio and turbulence fluctuations on the propagation of detonations, AIAA SciTech Forum, American Institute of Aeronautics and Astronautics, doi:10.2514/6.2017-0374.

[180] Mathews, G. C., M. G. Blaisdell, A. I. Lemcherfi, C. D. Slabaugh, and C. S. Goldenstein (2021), High-bandwidth absorption-spectroscopy measurements of temperature, pressure, CO, and H_2O in the annulus of a rotating detonation rocket engine, *Applied Physics B*, *127*(12), 1–23.

[181] Mazaheri, K., Y. Mahmoudi, and M. I. Radulescu (2012), Diffusion and hydrodynamic instabilities in gaseous detonations, *Combustion and Flame*, *159*(6), 2138–2154, doi:https://doi.org/10.1016/j.combustflame.2012.01.024.

[182] Mcbride, B., S. Gordon, and M. Reno (1993), Coefficients for calculating thermodynamic and transport properties of individual species, *Tech. Rep. NASA-TM-4513*, NASA Lewis Research Center, United States.

[183] Meng, H., Q. Zheng, C. Weng, Y. Wu, W. Feng, G. Xu, and F. Wang (2021), Propagation mode analysis of rotating detonation waves fueled by liquid kerosene, *Acta Astronautica*, *187*, 248–258, doi:https://doi.org/10.1016/j.actaastro.2021.06.043.

[184] Meng, H., Q. Xiao, W. Feng, M. Wu, X. Han, F. Wang, C. Weng, and Q. Zheng (2022), Air-breathing rotating detonation fueled by liquid kerosene in cavity-based annular combustor, *Aerospace Science and Technology*, *122*, 107,407, doi:https://doi.org/10.1016/j.ast.2022.107407.

[185] Meng, Q., M. Zhao, H. Zheng, and H. Zhang (2021), Eulerian-lagrangian modelling of rotating detonative combustion in partially prevaporized n-heptane sprays with hydrogen addition, *Fuel*, *290*, 119,808, doi:https://doi.org/10.1016/j.fuel.2020.119808.

[186] Meng, Q. ., N. . Zhao, and H. . Zhang (2021), On the distributions of fuel droplets and in situ vapor in rotating detonation combustion with prevaporized n-heptane sprays, *Physics of Fluids*, *33*(4), 043,307.

[187] Mi, X., A. J. Higgins, H. D. Ng, C. B. Kiyanda, and N. Nikiforakis (2017), Propagation of gaseous detonation waves in a spatially inhomogeneous reactive medium, *Phys. Rev. Fluids*, *2*, 053,201, doi:10.1103/PhysRevFluids.2.053201.

[188] Mi, X., E. V. Timofeev, and A. J. Higgins (2017), Effect of spatial discretization of energy on detonation wave propagation, *J. of Fluid Mechanics*, *817*, 306–338, doi:10.1017/jfm.2017.81.

[189] Mikhalkin, V. N. (1996), Thermodynamic calculation of detonation in poorly mixed gas mixtures, *Combustion, Explosion and Shock Waves*, *32*(1), 57–60, doi:10.1007/BF01992192.

[190] Miller, R., K. Harstad, and J. Bellan (1998), Evaluation of equilibrium and non-equilibrium evaporation models for many-droplet gas-liquid flow simulations, *International Journal of Multiphase Flow*, *24*(6), 1025–1055.

[191] Modesti, D., and S. Pirozzoli (2017), A low-dissipative solver for turbulent compressible flows on unstructured meshes, with openfoam implementation, *Computers & Fluids*, *152*, 14–23.

[192] Mueller, M. A., T. J. Kim, R. A. Yetter, and F. L. Dryer (1999), Flow reactor studies and kinetic modeling of the H_2/O_2 reaction, *International Journal of Chemical Kinetics*, *31*(2), 113–125, doi:10.1002/(SICI)1097-4601(1999)31:2¡113::AID-KIN5¿3.0.CO;2-0.

[193] Mueller, M. E., and V. Raman (2014), Effects of turbulent combustion modeling errors on soot evolution in a turbulent nonpremixed jet flame, *Combustion and Flame*, *161*(7), 1842–1848, doi:https://doi.org/10.1016/j.combustflame.2013.12.020.

[194] Mueller, M. E., and V. Raman (2018), Model form uncertainty quantification in turbulent combustion simulations: Peer models, *Combustion and Flame*, *187*, 137–146.

[195] Mueller, M. E., G. Iaccarino, and H. Pitsch (2013), Chemical kinetic uncertainty quantification for large eddy simulation of turbulent nonpremixed combustion, *Proceedings of the Combustion Institute*, *34*(1), 1299 – 1306.

[196] Nagayama, K., and S. Kubota (2003), Equation of state for detonation product gases, *Journal of Applied Physics*, *93*(5), 2583–2589, doi:10.1063/1.1542660.

[197] Nair, A. P., D. D. Lee, D. I. Pineda, J. Kriesel, W. A. Hargus Jr, J. W. Bennewitz, B. Bigler, S. A. Danczyk, and R. M. Spearrin (2021), Methane-oxygen rotating detonation exhaust thermodynamics with variable mixing, equivalence ratio, and mass flux, *Aerospace Science and Technology*, *113*, 106,683.

[198] Najm, H. N. (2009), Uncertainty quantification and polynomial chaos techniques in computational fluid dynamics, *Annual review of fluid mechanics*, *41*, 35–52.

[199] Nakagami, S., K. Matsuoka, J. Kasahara, Y. Kumazawa, J. Fujii, A. Matsuo, and I. Funaki (2017), Experimental visualization of the structure of rotating detonation waves in a disk-shaped combustor, *Journal of Propulsion and Power*, *33*(1), 80–88, doi:10.2514/1.B36084.

[200] Naples, A., J. Hoke, and F. Schauer (2014), Rotating detonation engine interaction with an annular ejector, in *52nd Aerospace Sciences Meeting*, Paper No. AIAA-2014-0287.

[201] Naples, A., J. Hoke, R. Battelle, and F. Schauer (2018), T63 Turbine Response to Rotating Detonation Combustor Exhaust Flow, *Journal of Engineering for Gas Turbines and Power*, *141*(2), doi:10.1115/1.4041135.

[202] Nejaamtheen, M. N., T. Y. Kim, P. K. Pavalavanni, J. Ryu, and J.-Y. Choi (2021), Effects of the dimensionless radius of an annulus on the detonation propagation characteristics in circular and non-circular rotating detonation engines, *Shock Waves*, *31*(7), 703–715, doi:10.1007/s00193-021-01065-z.

[203] Ng, K. S., D. Farooq, and A. Yang (2021), Global biorenewable development strategies for sustainable aviation fuel production, *Renewable and Sustainable Energy Reviews*, *150*, 111,502, doi:https://doi.org/10.1016/j.rser.2021.111502.

[204] Nicholls, J., R. Cullen, and K. Ragland (1966), Feasibility studies of a rotating detonation wave rocket motor, *Journal of Spacecraft and Rockets*, *3*(6), 893–898.

[205] Nordeen, C. A., D. Schwer, F. Schauer, J. Hoke, T. Barber, and B. Cetegen (2014), Thermodynamic model of a rotating detonation engine, *Combustion, Explosion, and Shock Waves*, *50*(5), 568–577, doi:10.1134/S0010508214050128.

[206] Oates, G. C. (1989), *Aircraft propulsion systems technology and design*, AIAA.

[207] Oliver, T. A., and R. D. Moser (2011), Bayesian uncertainty quantification applied to RANS turbulence models, *Journal of Physics: Conference Series*, *318*(4), 042,032.

[208] Oliver, T. A., N. Malaya, R. Ulerich, and R. D. Moser (2014), Estimating uncertainties in statistics computed from direct numerical simulation, *Physics of Fluids*, *26*(3), 035,101.

[209] Oliver, T. A., G. Terejanu, C. S. Simmons, and R. D. Moser (2015), Validating predictions of unobserved quantities, *Computer Methods in Applied Mechanics and Engineering*, *283*, 1310–1335, doi:https://doi.org/10.1016/j.cma.2014.08.023.

[210] Oran, E. S., D. A. Jones, and M. Sichel (1992), Numerical simulations of detonation transmission, *Proceedings of the Royal Society of London. Series A: Mathematical and Physical Sciences*, *436*(1897), 267–297, doi:10.1098/rspa.1992.0018.

[211] Oran, E. S., J. W. Weber, E. I. Stefaniw, M. H. Lefebvre, and J. D. Anderson (1998), A numerical study of a two-dimensional H_2-O_2-ar detonation using a detailed chemical reaction model, *Combustion and Flame*, *113*(1), 147 – 163, doi:10.1016/S0010-2180(97)00218-6.

[212] Pal, P., G. Kumar, S. Drennan, B. A. Rankin, and S. Som (2019), Numerical modeling of supersonic combustion in a non-premixed rotating detonation engine.

[213] Pal, P., G. Kumar, S. A. Drennan, B. A. Rankin, and S. Som (2019), Multidimensional numerical simulations of reacting flow in a non-premixed rotating detonation engine, in *Turbo Expo: Power for Land, Sea, and Air*, vol. 58622, p. V04BT04A050, American Society of Mechanical Engineers.

[214] Pal, P., G. Kumar, S. A. Drennan, B. A. Rankin, and S. Som (2021), Multidimensional numerical modeling of combustion dynamics in a non-premixed rotating detonation engine with adaptive mesh refinement, *Journal of Energy Resources Technology*, *143*(11), doi:10.1115/1.4050590, 112308.

[215] Pan, Z., Z. Zhang, H. Yang, M. Gui, P. Zhang, and Y. Zhu (2021), Experimental and numerical investigation on flame propagation and transition to detonation in curved channel, *Aerospace Science and Technology*, *118*, 107,036, doi:https://doi.org/10.1016/j.ast.2021.107036.

[216] Papatheodore, T. (2018), Oak Ridge Leadership Computing Facility (OLCF) Summit system overview.

[217] Paxson, D. (2017), Resonant pulse combustors: A reliable route to practical pressure gain combustion, in *International Constant Volume Detonation Combustion Workshop*.

[218] Paxson, D. E. (2018), Examination of wave speed in rotating detonation engines using simplified computational fluid dynamics, in *2018 AIAA Aerospace Sciences Meeting*, paper No. AIAA-2018-1883.

[219] Paxson, D. E., and T. Kaemming (2014), Influence of unsteadiness on the analysis of pressure gain combustion devices, *Journal of Propulsion and Power*, *30*(2), 377–383.

[220] Peng, H., W. Liu, and S. Liu (2018), Ethylene continuous rotating detonation in optically accessible racetrack-like combustor, *Combustion Science and Technology*, *191*(4), 676–695, doi:10.1080/00102202.2018.1498850.

[221] Peng, W. Y., S. J. Cassady, C. L. Strand, C. S. Goldenstein, R. M. Spearrin, C. M. Brophy, J. B. Jeffries, and R. K. Hanson (2019), Single-ended mid-infrared laser-absorption sensor for time-resolved measurements of water concentration and temperature within the annulus of a rotating detonation engine, *Proceedings of the Combustion Institute*, *37*(2), 1435–1443, doi:10.1016/j.proci.2018.05.021.

[222] Perdikaris, P., D. Venturi, J. O. Royset, and G. E. Karniadakis (2015), Multifidelity modelling via recursive co-kriging and gaussian markov random fields, *Proceedings of the Royal Society A: Mathematical, Physical and Engineering Sciences*, *471*(2179), 20150,018, doi:10.1098/rspa.2015.0018.

[223] Perdikaris, P., M. Raissi, A. Damianou, N. D. Lawrence, and G. E. Karniadakis (2017), Nonlinear information fusion algorithms for data-efficient multi-fidelity modelling, *Proceedings of the Royal Society A: Mathematical, Physical and Engineering Sciences*, *473*(2198), 20160,751.

[224] Perkins, H. D., and C. J. Sung (2005), Effects of fuel distribution on detonation tube performance, *J. of Prop. and Power*, *21*(3), 539–545, doi:10.2514/1.2253.

[225] Peschka, W., E. Wilhelm, and U. Wilhelm (2012), *Liquid Hydrogen: Fuel of the Future*, Springer Vienna.

[226] Pintgen, F., C. Eckett, J. Austin, and J. Shepherd (2003), Direct observations of reaction zone structure in propagating detonations, *Combust. and Flame*, *133*(3), 211 – 229, doi:10.1016/S0010-2180(02)00458-3.

[227] Pirozzoli, S. (2010), Generalized conservative approximations of split convective derivative operators, *Journal of Computational Physics*, *229*(19), 7180–7190, doi:https://doi.org/10.1016/j.jcp.2010.06.006.

[228] Poinsot, T., and S. Lelef (1992), Boundary conditions for direct simulations of compressible viscous flows, *Journal of Computational Physics*, *101*(1), 104–129, doi:https://doi.org/10.1016/0021-9991(92)90046-2.

[229] Pope, S. B. (2000), *Turbulent Flows*, Cambridge University Press.

[230] Powers, J. M., and S. Paolucci (2005), Accurate spatial resolution estimates for reactive supersonic flow with detailed chemistry, *AIAA Journal*, *43*(5), 1088–1099, doi:10.2514/1.11641.

[231] Prakash, S., and V. Raman (2019), Detonation propagation through inhomogeneous fuel-air mixtures, *Proceedings of the 27th International Colloquium on the Dynamics of Explosions and Reactive Systems (ICDERS)*.

[232] Prakash, S., and V. Raman (2021), The effects of mixture preburning on detonation wave propagation, *Proceedings of the Combustion Institute*, *38*(3), 3749–3758.

[233] Prakash, S., S. Barwey, M. Hassanaly, and V. Raman (2019), Data driven classification of regimes in a detonation wave, *Proceedings of the 11th Mediterranean Combustion Symposium (MCS)*.

[234] Prakash, S., R. Fievet, and V. Raman (2019), The effect of fuel stratification on the detonation wave structure, in *AIAA Scitech 2019 Forum*, paper No. AIAA-2019-1511.

[235] Prakash, S., R. Fiévet, V. Raman, J. Burr, and K. H. Yu (2020), Analysis of the detonation wave structure in a linearized rotating detonation engine, *AIAA Journal*, *58*(12), 5063–5077, doi:10.2514/1.j058156.

[236] Prakash, S., V. Raman, C. Lietz, W. A. Hargus, and S. A. Schumaker (2020), High fidelity simulations of a methane-oxygen rotating detonation rocket engine, in *AIAA Scitech 2020 Forum*, doi:10.2514/6.2020-0689, paper No. AIAA-2020-0689.

[237] Prakash, S., V. Raman, C. F. Lietz, W. A. Hargus, and S. A. Schumaker (2021), Numerical simulation of a methane-oxygen rotating detonation rocket engine, *Proceedings of the Combustion Institute*, *38*(3), 3777–3786.

[238] Prakash, S., C. Klarkowski, and V. Raman (2022), Multi-fidelity data fusion for estimating performance of rotating detonation engines, *Energy and AI*, in preparation.

[239] Qian, C., C. Wang, J. Liu, A. Brandenburg, N. E. L. Haugen, and M. A. Liberman (2020), Convergence properties of detonation simulations, *Geophysical & Astrophysical Fluid Dynamics*, *114*(1-2), 58–76, doi:10.1080/03091929.2019.1668382.

[240] Radulescu, M. I., G. J. Sharpe, C. K. Law, and J. H. S. Lee (2007), The hydrodynamic structure of unstable cellular detonations, *J. of Fluid Mechanics*, *580*, 31–81, doi:10.1017/S0022112007005046.

[241] Raman, V., S. Prakash, and M. Gamba (2023), Non-idealities in rotating detonation engines, *Annual review of fluid mechanics*.

[242] Rankin, B. A., J. P. Gore, J. L. Hoke, and F. R. Schauer (2013), Radiation measurements and temperature estimates of unsteady exhaust plumes exiting from a turbine driven by pulsed detonation combustion, in *51st AIAA Aerospace Sciences Meeting including the New Horizons Forum and Aerospace Exposition 2013*, doi:10.2514/6.2013-886, paper No. AIAA-2013-886.

[243] Rankin, B. A., J. Hoke, and F. Schauer (2014), Periodic exhaust flow through a converging-diverging nozzle downstream of a rotating detonation engine, in *52nd Aerospace Sciences Meeting*, doi:10.2514/6.2014-1015, paper No. AIAA-2014-1015.

[244] Rankin, B. A., M. L. Fotia, D. E. Paxson, J. L. Hoke, and F. R. Schauer (2015), Experimental and numerical evaluation of pressure gain combustion in a rotating detonation engine, in *53rd AIAA Aerospace Sciences Meeting*, doi:10.2514/6.2015-0877, paper No. AIAA-2015-0877.

[245] Rankin, B. A., D. R. Richardson, A. W. Caswell, A. Naples, J. Hoke, and F. Schauer (2015), Imaging of OH* chemiluminescence in an optically accessible nonpremixed rotating detonation engine, in *53rd AIAA Aerospace Sciences Meeting*, Paper No. AIAA-2015-1604, doi:10.2514/6.2015-1604.

[246] Rankin, B. A., M. L. Fotia, A. G. Naples, C. A. Stevens, J. L. Hoke, T. A. Kaemming, S. W. Theuerkauf, and F. R. Schauer (2017), Overview of Performance, Application, and Analysis of Rotating Detonation Engine Technologies, *Journal of Propulsion and Power*, *33*(1), 131–143, doi:10.2514/1.B36303.

[247] Rankin, B. A., D. R. Richardson, A. W. Caswell, A. G. Naples, J. L. Hoke, and F. R. Schauer (2017), Chemiluminescence imaging of an optically accessible non-premixed rotating detonation engine, *Combustion and Flame*, *176*, 12–22, doi:10.1016/j.combustflame.2016.09.020.

[248] Rankin, B. A., J. R. Codoni, K. Y. Cho, J. L. Hoke, and F. R. Schauer (2019), Investigation of the structure of detonation waves in a non-premixed hydrogen-air rotating detonation engine using mid-infrared imaging, *Proceedings of the Combustion Institute*, *37*(3), 3479–3486, doi:10.1016/j.proci.2018.09.036.

[249] Ranz, W., and W. Marshall (1952), Evaporation from droplets, *Chem. Eng. Prog*, *48*(3), 141–146.

[250] Rein, K. D., S. Roy, B. C. Sell, J. L. Hoke, A. W. Caswell, F. R. Schauer, and J. R. Gord (2016), Time-resolved in-situ absorption spectroscopy of a hydrogen-air rotating detonation engine using a fiber-coupled tunable laser system, in 54^{th} *AIAA Aerospace Sciences Meeting*, doi:10.2514/6.2016-1199, paper No. AIAA-2016-1199.

[251] Santavicca, D., R. Yetter, and S. Peluso (2015), Effect of mixture concentration inhomogeneity on detonation properties in pressure gain combustors, university Turbine Systems Research (UTSR) 2015 Kick-off Meeting Proceedings. https://netl.doe.gov/plp/FE0025525-Santavicca-UTSR-KickOff-20151005.pdf (2015). Accessed 2 December 2018.

[252] Sato, T. (2020), High-fidelity simulations of rotating detonation engines, Ph.D. thesis, University of Michigan.

[253] Sato, T., and V. Raman (2019), Hydrocarbon fuel effects on non-premixed rotating detonation engine performance, in *AIAA Scitech 2019 Forum*, Paper No. AIAA-2019-2023, doi:10.2514/6.2019-2023.

[254] Sato, T., and V. Raman (2020), Detonation structure in ethylene/air-based non-premixed rotating detonation engine, *Journal of Propulsion and Power*, *36*(5), 752–762.

[255] Sato, T., S. Voelkel, and V. Raman (2018), Detailed chemical kinetics based simulation of detonation-containing flows, in *Volume 4A: Combustion, Fuels, and Emissions*, ASME, doi:10.1115/gt2018-75878.

[256] Sato, T., F. Chacon, M. Gamba, and V. Raman (2021), Mass flow rate effect on a rotating detonation combustor with an axial air injection, *Shock Waves*, *31*(7), 741–751, doi:10.1007/s00193-020-00984-7.

[257] Sato, T., F. Chacon, L. White, V. Raman, and M. Gamba (2021), Mixing and detonation structure in a rotating detonation engine with an axial air inlet, *Proceedings of the Combustion Institute*, *38*(3), 3769–3776, doi: 10.1016/j.proci.2020.06.283.

[258] Sato, T., C. Van Beck, and V. Raman (2022), Effects of injection pressure on performance of non-premixed rotating detonation engines, *Combustion and Flame*, in preparation.

[259] Schiller, L. (1933), A drag coefficient correlation, *Zeit. Ver. Deutsch. Ing.*, *77*, 318–320.

[260] Schwer, D., and K. Kailasanath (2010), Numerical investigation of rotating detonation engines, AIAA/SAE/ASEE Joint Propulsion Conference, American Institute of Aeronautics and Astronautics, doi:10.2514/6.2010-6880.

[261] Schwer, D., and K. Kailasanath (2011), Numerical investigation of the physics of rotating-detonation-engines, *Proceedings of the combustion institute*, *33*(2), 2195–2202.

[262] Schwer, D., and K. Kailasanath (2011), Rotating detonation-wave engines, *Tech. rep.*, Navy Research Laboratory: Laboratory for Computational Physics and Fluid Dynamics.

[263] Schwer, D., and K. Kailasanath (2012), Feedback into mixture plenums in rotating detonation engines, *50th AIAA Aerospace Sciences Meeting including the New Horizons Forum and Aerospace Exposition*, doi:10.2514/6.2012-617.

[264] Schwer, D., and K. Kailasanath (2013), Fluid dynamics of rotating detonation engines with hydrogen and hydrocarbon fuels, *Proc. of the Combust. Inst.*, *34*(2), 1991–1998, doi:10.1016/j.proci.2012.05.046.

[265] Schwer, D. A. (2019), Multi-dimensional simulations of liquid-fueled JP-10/oxygen detonations, Paper No. AIAA-2019-4042.

[266] Schwer, D. A., and K. Kailasanath (2017), Assessment of rotating detonation engines with fuel blends, 53rd AIAA/SAE/ASEE Joint Propulsion Conference, doi:10.2514/6.2017-4942.

[267] Schwer, D. A., E. P. O'Fallon Jr., and D. Kessler (2018), Liquid-fueled detonation modeling at the US naval research laboratory, *NRL Technical Report Report No. NRL/MR/6041–18-9816*, Naval Research Laboratory, Washington, D.C., USA.

[268] Schwinn, K., R. Gejji, B. Kan, S. Sardeshmukh, S. Heister, and C. D. Slabaugh (2018), Self-sustained, high-frequency detonation wave generation in a semi-bounded channel, *Combustion and Flame*, *193*, 384–396.

[269] Shaw, I. J., J. A. Kildare, M. J. Evans, A. Chinnici, C. A. Sparks, S. N. Rubaiyat, R. C. Chin, and P. R. Medwell (2019), *A Theoretical Review of Rotating Detonation Engines*, chap. 7, London, doi:10.5772/intechopen.90470.

[270] Shepherd, J., and E. Wintenberger (2004), Thermodynamic analysis of combustion processes for propulsion systems, in *42nd AIAA Aerospace Sciences Meeting and Exhibit*, doi:10.2514/6.2004-1033, paper No. AIAA-2004-1033.

[271] Shepherd, J. E. (2009), Detonation in gases, *Proc. Comb. Inst.*, *32*(1), 83–98, doi:10.1016/j.proci.2008.08.006.

[272] Shepherd, J. E., and J. Kasahara (2017), Analytical models for the thrust of a rotating detonation engine.

[273] Shi, L., H. Shen, P. Zhang, D. Zhang, and C. Wen (2017), Assessment of vibrational non-equilibrium effect on detonation cell size, *Combustion Science and Technology*, *189*(5), 841–853.

[274] Shimizu, H., A. Hayashi, and N. Tsuboi (2001), Study of detailed chemical reaction model of hydrogen-air detonation, Aerospace Sciences Meetings, American Institute of Aeronautics and Astronautics, doi:10.2514/6.2001-478.

[275] Shu, C.-W. (2003), High-order finite difference and finite volume weno schemes and discontinuous galerkin methods for cfd, *International Journal of Computational Fluid Dynamics*, *17*(2), 107–118, doi:10.1080/1061856031000104851.

[276] Slessor, M. D., M. Zhuang, and P. E. Dimotakis (2000), Turbulent shear-layer mixing: growth-rate compressibility scaling, *J. of Fluid Mech.*, *414*, 35–45, doi:10.1017/S0022112099006977.

[277] Smith, G., Y. Tao, and H. Wang (2016), Foundational fuel chemistry model version 1.0 (ffcm-1), http://nanoenergy.stanford.edu/ffcm1.

[278] Sosa, J., R. Burke, K. A. Ahmed, D. J. Micka, J. W. Bennewitz, S. A. Danczyk, E. J. Paulson, and W. A. Hargus Jr (2020), Experimental evidence of H_2/O_2 propellants powered rotating detonation waves, *Combustion and Flame*, *214*, 136–138.

[279] Sousa, J., G. Paniagua, and E. Collado Morata (2017), Thermodynamic analysis of a gas turbine engine with a rotating detonation combustor, *Applied Energy*, *195*, 247–256, doi:https://doi.org/10.1016/j.apenergy.2017.03.045.

[280] St. George, A., S. Randall, V. Anand, R. Driscoll, and E. Gutmark (2016), Characterization of initiator dynamics in a rotating detonation combustor, *Experimental Thermal and Fluid Science*, *72*, 171–181, doi:https://doi.org/10.1016/j.expthermflusci.2015.11.002.

[281] St. George, A., R. Driscoll, V. Anand, and E. Gutmark (2017), On the existence and multiplicity of rotating detonations, *Proceedings of the Combustion Institute*, *36*(2), 2691–2698, doi:https://doi.org/10.1016/j.proci.2016.06.132.

[282] Stechmann, D. P. (2017), Experimental study of high-pressure rotating detonation combustion in rocket environments, Ph.D. thesis, Purdue U., West Lafayette, IN.

[283] Stechmann, D. P., S. D. Heister, and A. J. Harroun (2019), Rotating detonation engine performance model for rocket applications, *Journal of Spacecraft and Rockets*, *56*(3), 887–898.

[284] Stechmann, D. P., S. Sardeshmukh, S. D. Heister, and K. Mikoshiba (2019), Role of ignition delay in rotating detonation engine performance and operability, *Journal of Propulsion and Power*, *35*(1), 125–140.

[285] Stein, M. L. (2012), *Interpolation of spatial data: some theory for kriging*, Springer Science & Business Media.

[286] Subramanian, S., and J. Meadows (2020), Novel approach for computational modeling of a non-premixed rotating detonation engine, *Journal of Propulsion and Power*, *36*(4), 617–631, doi:10.2514/1.B37719.

[287] Sutton, G. P., and O. Biblarz (2010), *Rocket Propulsion Elements*, Wiley, Hoboken, NJ, USA.

[288] Taguchi, T., M. Yamaguchi, K. Matsuoka, A. Kawasaki, H. Watanabe, N. Itouyama, J. Kasahara, and A. Matsuo (2022), Investigation of reflective shuttling detonation cycle by schlieren and chemiluminescence photography, *Combustion and Flame*, *236*, 111,826, doi:10.1016/j.combustflame.2021.111826.

[289] Talnikar, C., P. Blonigan, J. Bodart, and Q. Wang (2014), Parallel optimization for large eddy simulations, *arXiv preprint arXiv:1410.8859*.

[290] Tang, Y., M. Hassanaly, V. Raman, B. Sforzo, and J. Seitzman (2019), A comprehensive modeling procedure for estimating statistical properties of forced ignition, *Combustion and Flame*, *206*, 158 – 176, doi:10.1016/j.combustflame.2019.04.045.

[291] Tangirala, V., A. Dean, O. Peroomian, and S. Palaniswamy (), Investigations of two-phase detonations for performance estimations of a pulsed detonation engine, Paper No. AIAA-2007-1173, 2007.

[292] Taylor, B., D. Kessler, V. Gamezo, and E. Oran (2013), Numerical simulations of hydrogen detonations with detailed chemical kinetics, *Proceedings of the Combustion Institute*, *34*(2), 2009–2016, doi:https://doi.org/10.1016/j.proci.2012.05.045.

[293] Taylor, B., D. Kessler, and E. Oran (2013), Estimates of vibrational nonequilibrium time scales in hydrogen-air detonation waves, in *24th International Colloquium on the Dynamics of Explosive and Reactive Systems, Taipei, Taiwan, July*, vol. 23, p. 44.

[294] The MathWorks, Inc. (2021), Matlab and deep learning toolbox, Release 2021b.

[295] Thurmond, K., S. Vasu, J. Stout, S. B. Coogan, K. A. Ahmed, I. B. Dunn, S. White, and C. Nolen (2018), MHz-rate laser spectroscopic instrument for reacting flow composition and temperature measurements inside rotating detonation engines (RDEs), in *2018 Joint Propulsion Conference*, Paper No. AIAA-2018-4687, doi:10.2514/6.2018-4687.

[296] Tierney, L. (1994), Markov Chains for Exploring Posterior Distributions, *The Annals of Statistics*, *22*(4), 1701 – 1728, doi:10.1214/aos/1176325750.

[297] Timmes, F. X. (2022), Chapman-jouget detonations.

[298] Toro, E. F. (2013), *Riemann solvers and numerical methods for fluid dynamics: a practical introduction*, Springer Science & Business Media.

[299] Toro, E. F., M. Spruce, and W. Speares (1994), Restoration of the contact surface in the hll-riemann solver, *Shock waves*, *4*(1), 25–34.

[300] Ullman, M., S. Prakash, D. Jackson, V. Raman, C. Slabaugh, and J. Bennewitz (2022), Self-excited wave dynamics in an open-closed reflective shuttling detonation combustor, *Combustion and Flame*, in preparation.

[301] Unruh, E. C., M. Spaulding, D. M. Lineberry, K. G. Xu, and R. A. Frederick (2020), Development of an optically accessible racetrack-type rotating detonation rocket engine, in *AIAA Propulsion and Energy 2020 Forum*, Paper No. AIAA-2020-3868, doi:10.2514/6.2020-3868.

[302] Vaidyanathan, R., P. K. Tucker, N. Papila, and W. Shyy (2004), Computational fluid dynamics-based design optimization for single-element rocket injector, *Journal of Propulsion and Power*, *20*(4), 705–717, doi:10.2514/1.11464.

[303] Valera-Medina, A., S. Morris, J. Runyon, D. Pugh, R. Marsh, P. Beasley, and T. Hughes (2015), Ammonia, methane and hydrogen for gas turbines, *Energy Procedia*, *75*, 118–123, doi:https://doi.org/10.1016/j.egypro.2015.07.205, clean, Efficient and Affordable Energy for a Sustainable Future: The 7th International Conference on Applied Energy (ICAE2015).

[304] Van Zante, D. E. (2015), Progress in Open Rotor Research: A U.S. Perspective, doi:10.1115/GT2015-42203, v001T01A003.

[305] Varatharajan, B., M. Petrova, F. Williams, and V. Tangirala (2005), Two-step chemical-kinetic descriptions for hydrocarbon–oxygen-diluent ignition and detonation applications, *Proceedings of the Combustion Institute*, *30*(2), 1869–1877, doi:https://doi.org/10.1016/j.proci.2004.08.181.

[306] Voelkel, S., D. Masselot, P. L. Varghese, and V. Raman (2016), Analysis of hydrogen-air detonation waves with vibrational nonequilibrium, in *AIP Conference Proceedings*, vol. 1786, p. 070015, AIP Publishing LLC.

[307] Wada, Y., and M.-S. Liou (1997), An accurate and robust flux splitting scheme for shock and contact discontinuities, *SIAM Journal on Scientific Computing*, *18*(3), 633–657, doi:10.1137/S1064827595287626.

[308] Walters, I. V., R. M. Gejji, S. D. Heister, and C. D. Slabaugh (2021), Flow and performance analysis of a natural gas-air rotating detonation engine with high-speed velocimetry, *Combustion and Flame*, *232*, 111,549, doi: https://doi.org/10.1016/j.combustflame.2021.111549.

[309] Walters, I. V., A. Lemcherfi, R. M. Gejji, S. D. Heister, and C. D. Slabaugh (2021), Performance characterization of a natural gas–air rotating detonation engine, *Journal of Propulsion and Power*, *37*(2), 292–304, doi: 10.2514/1.B38087.

[310] Wang, H., R. Xu, K. Wang, C. T. Bowman, R. K. Hanson, D. F. Davidson, K. Brezinsky, and F. N. Egolfopoulos (2018), A physics-based approach to modeling real-fuel combustion chemistry - i. evidence from experiments, and thermodynamic, chemical kinetic and statistical considerations, *Combustion and Flame*, *193*, 502–519.

[311] Wang, S., P. B. Butler, and H. Krier (1985), Non-ideal equations of state for combusting and and detonating explosives, *Progress in Energy and Combustion Science*, *11*(4), 311 – 331, doi:10.1016/0360-1285(85)90005-X.

[312] Welch, C., D. Depperschmidt, R. Miller, J. Tobias, M. Uddi, A. K. Agrawal, and S. Lowe (2018), Experimental analysis of wave propagation in a methane-fueled rotating detonation combustor, in *Turbo Expo: Power for Land, Sea, and Air*, vol. 51067, p. V04BT04A065, American Society of Mechanical Engineers.

[313] Wen, H., Q. Xie, and B. Wang (2019), Propagation behaviors of rotating detonation in an obround combustor, *Combustion and Flame*, *210*, 389–398, doi: 10.1016/j.combustflame.2019.09.008.

[314] Werman, M., and D. Keren (2001), A bayesian method for fitting parametric and nonparametric models to noisy data, *IEEE Transactions on Pattern Analysis and Machine Intelligence*, *23*(5), 528–534, doi:10.1109/34.922710.

[315] White, F. M., and J. Majdalani (2006), *Viscous fluid flow*, vol. 3, McGraw-Hill New York.

[316] Wilhite, J., R. B. Driscoll, A. C. S. George, V. Anand, and E. J. Gutmark (2016), Investigation of a rotating detonation engine using ethylene-air mixtures, in *54th AIAA Aerospace Sciences Meeting*, doi:10.2514/6.2016-1650, paper No. AIAA-2016-1650.

[317] Wintenberger, E., and J. E. Shepherd (2006), Thermodynamic cycle analysis for propagating detonations, *Journal of Propulsion and Power*, *22*(3), 694–698, doi:10.2514/1.12775.

[318] Wintenberger, E., and J. E. Shepherd (2006), Stagnation hugoniot analysis for steady combustion waves in propulsion systems, *Journal of Propulsion and Power*, *22*(4), 835–844, doi:10.2514/1.12779.

[319] Wolański, P. (2011), Rotating detonation wave stability, in *23rd international colloquium on the dynamics of explosions and reactive systems*, pp. 1–6.

[320] Wolański, P. (2015), Application of the continuous rotating detonation to gas turbine, in *Applied Mechanics and Materials*, vol. 782, pp. 3–12, Trans Tech Publ.

[321] Wolański, P. (2021), RDE research and development in Poland, *Shock Waves*, *31*(7), 623–636, doi:10.1007/s00193-021-01038-2.

[322] Wolański, P., P. Kalina, W. Balicki, A. Rowiński, W. Perkowski, M. Kawalec, and B. Łukasik (2017), Development of gasturbine with detonation chamber, in *Shock Wave and High Pressure Phenomena*, pp. 23–37, Springer International Publishing, doi:10.1007/978-3-319-68906-7_2.

[323] Wolański, P. (2013), Detonative propulsion, *Proceedings of the Combustion Institute*, *34*(1), 125–158, doi:https://doi.org/10.1016/j.proci.2012.10.005.

[324] Wu, J., P. Brown, I. Diakunchak, A. Gulati, M. Lenze, and B. Koestlin (2007), Advanced Gas Turbine Combustion System Development for High Hydrogen Fuels, pp. 1085–1091, doi:10.1115/GT2007-28337.

[325] Xie, Q., H. Wen, W. Li, Z. Ji, B. Wang, and P. Wolanski (2018), Analysis of operating diagram for H_2/air rotating detonation combustors under lean fuel condition, *Energy*, *151*, 408–419, doi:https://doi.org/10.1016/j.energy.2018.03.062.

[326] Xu, R., and H. Wang (2018), "A reduced reaction model of methane combustion: FFCMy-12," Personal communication.

[327] Xu, R., et al. (2018), A physics-based approach to modeling real-fuel combustion chemistry – ii. reaction kinetic models of jet and rocket fuels, *Combustion and Flame*, *193*, 520–537.

[328] Yamaguchi, M., K. Matsuoka, A. Kawasaki, J. Kasahara, H. Watanabe, and A. Matsuo (2019), Supersonic combustion induced by reflective shuttling shock wave in fan-shaped two-dimensional combustor, *Proc Combust Inst*, *37*(3), 3741–3747, doi:10.1016/j.proci.2018.06.210.

[329] Yamaguchi, M., T. Taguchi, K. Matsuoka, A. Kawasaki, J. Kasahara, H. Watanabe, and A. Matsuo (2021), Investigation of combustion modes and pressure of reflective shuttling detonation combustor, *Proceedings of the Combustion Institute*, *38*(3), 3615–3622, doi:10.1016/j.proci.2020.07.064.

[330] Yamashita, H., M. Shimada, and T. Takeno (1996), A numerical study on flame stability at the transition point of jet diffusion flames, *Symp. (Int.) on Combust.*, *26*(1), 27 – 34, doi:https://doi.org/10.1016/S0082-0784(96)80196-2.

[331] Yan, C., H. Teng, and H. D. Ng (2021), Effects of slot injection on detonation wavelet characteristics in a rotating detonation engine, *Acta Astronautica*, *182*, 274–285.

[332] Yao, S., and J. Wang (2016), Multiple ignitions and the stability of rotating detonation waves, *Applied Thermal Engineering*, *108*, 927–936, doi:https://doi.org/10.1016/j.applthermaleng.2016.07.166.

[333] Yi, T.-H., J. Lou, C. Turangan, B. C. Khoo, and P. Wolanski (2010), Effect of nozzle shapes on the performance of continuously-rotating detonation engine, in *48th AIAA Aerospace Sciences Meeting Including the New Horizons Forum and Aerospace Exposition*, doi:10.2514/6.2010-152, paper No. AIAA-2010-152.

[334] Yi, T.-H., J. Lou, C. Turangan, J.-Y. Choi, and P. Wolanski (2011), Propulsive performance of a continuously rotating detonation engine, *Journal of Propulsion and Power*, *27*(1), 171–181, doi:10.2514/1.46686.

[335] Yokoo, R., K. Goto, J. Kim, A. Kawasaki, K. Matsuoka, J. Kasahara, A. Matsuo, and I. Funaki (2020), Propulsion performance of cylindrical rotating detonation engine, *AIAA Journal*, *58*(12), 5107–5116.

[336] York, W. D., W. S. Ziminsky, and E. Yilmaz (2013), Development and Testing of a Low NOx Hydrogen Combustion System for Heavy-Duty Gas Turbines, *Journal of Engineering for Gas Turbines and Power*, *135*(2), doi:10.1115/1.4007733.

[337] Yusupovich, M. L. (2022), Perspectives of hydrogen fuel cells in aviation, *Texas Journal of Multidisciplinary Studies*, *6*, 140–144.

[338] Yılmaz, I., M. Ilbaş, M. Taştan, and C. Tarhan (2012), Investigation of hydrogen usage in aviation industry, *Energy Conversion and Management*, *63*, 63–69, doi:https://doi.org/10.1016/j.enconman.2011.12.032, 10th International Conference on Sustainable Energy Technologies (SET 2011).

[339] Zhang, L., T. L. Butler, and B. Yang* (2020), *Recent Trends, Opportunities and Challenges of Sustainable Aviation Fuel*, chap. 5, pp. 85–110, John Wiley & Sons, Ltd, doi:https://doi.org/10.1002/9781119152057.ch5.

[340] Zhang, W., A. Myers, K. Gott, A. Almgren, and J. Bell (2021), Amrex: Block-structured adaptive mesh refinement for multiphysics applications, *The International Journal of High Performance Computing Applications*, *35*(6), 508–526, doi:10.1177/10943420211022811.

[341] Zhang, W., et al. (2019), Amrex: a framework for block-structured adaptive mesh refinement, *Journal of Open Source Software*, *4*(37), 1370, doi:10.21105/joss.01370.

[342] Zhao, M., and H. Zhang (2021), Rotating detonative combustion in partially pre-vaporized dilute n-heptane sprays: Droplet size and equivalence ratio effects, *Fuel*, *304*, 121,481, doi:https://doi.org/10.1016/j.fuel.2021.121481.

[343] Zhao, M., D. Buttsworth, R. J. Gollan, and P. A. Jacobs (2018), Simulation of a rotating detonation ramjet model in mach 4 flow, in *21st Australasian Fluid Mechanics Conference Paper*.

[344] Zhong, Y., Y. Wu, D. Jin, X. Chen, X. Yang, and S. Wang (2019), Investigation of rotating detonation fueled by the pre-combustion cracked kerosene, *Aerospace Science and Technology*, *95*, 105,480, doi: https://doi.org/10.1016/j.ast.2019.105480.

[345] Zhou, R., and J.-P. Wang (2013), Numerical investigation of shock wave reflections near the head ends of rotating detonation engines, *Shock Waves*, *23*(5), 461–472, doi:10.1007/s00193-013-0440-0.

[346] Zhou, R., D. Wu, and J. Wang (2016), Progress of continuously rotating detonation engines, *Chinese J. of Aero.*, *29*(1), 15 – 29.